

**FABRICATION OF SUPER CAPACITOR AND PEROVSKITE-SENSITIZED
SOLAR CELL FOR THE ASSEMBLY OF PHOTO-SUPER CAPACITOR**

NG CHI HUEY

Department of Biological Functions Engineering

Graduate School of Life Science and Systems Engineering

Kyushu Institute of Technology

May 2017

**FABRICATION OF SUPER CAPACITOR AND PEROVSKITE-SENSITIZED
SOLAR CELL FOR THE ASSEMBLY OF PHOTO-SUPER CAPACITOR**

by

NG CHI HUEY

May 2017

Department of Biological Functions Engineering

Graduate School of Life Science and Systems Engineering

Kyushu Institute of Technology

ACKNOWLEDGEMENTS

I would like to express my sincerest appreciation to whom who have assisted me during my PhD study.

First and foremost, I would like to express my deepest gratitude to my supervisors from Universiti Putra Malaysia, Associate Professor Dr. Janet Lim Hong Ngee, from whom the idea of photo-super capacitor was borne, and Kyutech, Professor Dr. Shuzi Hayase. Thank you for your assistance, guidance, encouragement, and your unremitting support throughout my PhD study. I sincerely appreciate their efforts in providing suggestions and brainstorming session to solve the arisen challenges. Thanks of turning me to be a qualified PhD candidate.

In addition, I would like to thank my co-supervisors from Universiti Putra Malaysia, Professor Dr. Zulkarnain Zainal and Associate Professor Dr. Suhaidi Shafie, and examiners, Professor Dr. Tingli Ma, Associate Professor Dr. Pandey Shyam, Professor Dr. Kenji Yoshino, and Professor Dr. Zainal Abidin Talib for their valuable suggestions and discussion for the betterment of my works for their valuable suggestions and discussion for the betterment of my works. I would like to convey my gratitude to Dr. Teresa, Professor Dr. Juan Bisquet, and Mr. Hamada for their guidance and assistance in making the perovskite research work a success.

Many thanks to the staffs and technicians of Faculty of Science Universiti Putra Malaysia, Kyushu Institute of Technology, University of Nottingham Malaysia Campus, and MIMOS for the characterization works.

In addition, I would like to thank my friends and colleagues, especially Miss Lim Pei Cee, friends from Kyushu Institute of Technology, and my warm-hearted lab mates from Laboratory

441 of Universiti Putra Malaysia for their support and encouragements. Our lab441 spirits will never diminish! Thanks to Mr Takuya Morimoto, who was my tutor during my stay in Kyushu Institute of Technology.

Special thanks to my loving parents and siblings. Thanks for their understanding, unconditional love, support, and care throughout my study. Additionally, thanks Dr. Teo Siow Hwa for his encouragements and support.

My gratitude goes to the Ministry of Education (MOE) Malaysia for providing me My PhD scholarship under Program MyBrain15 and Japan Student Service Organization (JASSO) for providing me JASSO scholarship for the student exchange support program. Lastly, I would like to acknowledge the Fundamental Research Grant Scheme (01-01-16-1872FR) from the Ministry of Higher Education of Malaysia, and the Newton-Ungku Omar Fund (638600-13501) from the British Council and MIGHT and KAKENHI from the Japan Society for the Promotion of Science (JSPS) under the Grant-in-Aid for Young Scientists B (Grant Number JP16K17947) and MINECO of Spain under project MAT2016-76892-C3-1-R on the research sponsorships.

TABLE OF CONTENTS

	Page
FRONT PAGE	i
ACKNOWLEDGEMENTS	ii
TABLE OF CONTENTS	iv
LIST OF FIGURES	viii
LIST OF TABLES	xv
LIST OF ABBREVIATIONS	xvii
PUBLICATIONS AND CONFERENCES ATTENDED	xxii
ABSTRACT	xxiv
CHAPTER	
1. INTRODUCTION	
1.1 Background	1
1.2 Problem Statements/Hypothesis	6
1.3 Research Scope	9
1.4 Objectives	11
2. LITERATURE REVIEWS	
2.1 Introduction	13
2.2 Supercapacitive Materials	16
2.2.1 Types of Pseudocapacitance/Active Electrode Materials	16
2.2.2 Conducting Polymers	22
2.2.3 Types of Carbon-Based Materials	23
2.3 Evolution of Third Generation Solar Cell	25
2.4 Potential Light Responsive Materials for Perovskite Solar Cell	28
2.4.1 Working Principle of Perovskite Solar Cell	28
2.4.2 Electron Transporting Material (ETM)	30

2.4.3	Light-Harvesting Materials	31
2.4.4	Hole-Transporting Materials (HTM)	39
2.5	The Integrated Photo-Super Capacitor	39
2.6	Working Principle of Photo-Super Capacitor	40
2.7	Emerging Field of Photo-Super Capacitor	41
3.	MATERIALS AND METHODS	
3.1	Materials	46
3.2	The Bi ₂ O ₃ /MnO ₂ Symmetrical and Asymmetrical Super Capacitor	47
3.2.1	Fabrication of Bi ₂ O ₃ /MnO ₂ Electrode	47
3.2.2	Fabrication of Bi ₂ O ₃ /MnO ₂ Symmetrical Super Capacitor	48
3.2.3	Fabrication of Bi ₂ O ₃ /MnO ₂ //PyR Asymmetrical Super Capacitor	48
3.3	The rGO/ZnO/Co ₃ O ₄ //PyR (RZCo//PyR) Asymmetrical Super Capacitor	48
3.3.1	Preparation of Graphene Oxide (GO)	48
3.3.2	Preparation of rGO/ZnO/Co ₃ O ₄ (RZCo) Positive Electrode	49
3.3.3	Preparation of PPy/rGO (PyR) Negative Electrode	49
3.3.4	Fabrication of RZCo//PyR Asymmetrical Super Capacitor	49
3.4	The Perovskite Solar Cell	50
3.4.1	Perovskite Solar Cell Fabrication	50
3.5	The Photo-Super Capacitor	51
3.5.1	Fabrication of Perovskite Solar Cell	51
3.5.2	Fabrication of An Asymmetrical Super Capacitor	52
3.5.3	Fabrication of Cesium Perovskite Based Photo-Super Capacitor	52
3.6	Materials Characterizations	52

3.6.1	Super Capacitors	52
3.6.2	Perovskite Solar Cells	53
3.6.3	Photo-Super Capacitor	53
3.7	Electrochemical Measurements	54
4.	ELECTROCHEMICAL PERFORMANCES OF SUPER CAPACITORS FOR PHOTO-SUPER CAPACITOR APPLICATION	
4.1	Introduction	56
4.2	Bi ₂ O ₃ /MnO ₂ Symmetrical Super Capacitor	61
4.2.1	Material Characterizations of Bi ₂ O ₃ /MnO ₂ Pseudocapacitive Materials	61
4.2.2	Formation Mechanism of Bi ₂ O ₃ /MnO ₂ Materials	64
4.2.3	The Charging and Discharging Mechanism of Bi ₂ O ₃ /MnO ₂ Electrode	66
4.2.4	Electrochemical Performances of Pseudocapacitor Under The Influences of Temperatures	67
4.3	Bi ₂ O ₃ /MnO ₂ //PyR Asymmetrical Super Capacitor	75
4.3.1	Electrochemical Measurement of Bi ₂ O ₃ /MnO ₂ //PyR Asymmetrical Super Capacitor	75
4.4	RZCo//PyR Asymmetrical Super Capacitor	77
4.4.1	Material Characterizations of RZCo Cathodic Materials	77
4.4.2	Electrical Conductivity	82
4.4.3	Electrochemical Performances of RZCo//PyR Asymmetrical Super Capacitor	82
4.4.4	Influence of Graphene Oxide Concentration on Supercapacitive Performances	88
4.4.5	Electrochemical Performances of Asymmetrical Super Capacitor Under Temperature Influence	89
4.4.6	Electrochemical Comparison Between As-Fabricated Asymmetrical Super Capacitor and KEMET Commercial Super Capacitor	92

4.5	Conclusion	94
5.	INTEGRATION OF CESIUM-BASED PEROVSKITE SOLAR CELL TOWARDS THE FABRICATION OF PHOTO-SUPER CAPACITOR	
5.1	Introduction	97
5.2	Performance Evaluation of Perovskite Solar Cells at Low Humidity Condition	102
5.2.1	Crystallographic Study	102
5.2.2	Energy Level Diagram	102
5.2.3	Effect of Iodide Inclusion on The Performance of Perovskite Solar Cells	104
5.2.4	Stability Investigation of Perovskite Solar Cells With Different HTM Contacts Upon Encapsulation	109
5.3	Towards The Integration of Photo-Super Capacitor	110
5.3.1	Materials Characterizations of Perovskite Solar Cells	111
5.3.2	Photovoltaic Performances of The Fabricated Perovskite Solar Cells	112
5.3.3	Materials and Electrochemical Measurements of Asymmetrical Super Capacitor	118
5.3.4	Electrochemical Performances of Assembled Photo-Super Capacitor	120
5.3.5	Working Mechanism of Photo-Super Capacitor	121
5.4	Conclusion	123
6.	CONCLUDING REMARKS AND RECOMMENDATIONS FOR FUTURE RESEARCH	
6.1	Conclusions	125
6.2	Recommendations for Future Works	127
	REFERENCES	129
	APPENDICES	147

LIST OF FIGURES

Figure		Page
2.1	Schematic diagram of charging/discharging mechanism of EDLC	14
2.2	Basic schematics of a pseudocapacitor comprises MnO ₂ active materials, a current collector, a separating membrane with Na ₂ SO ₄ electrolyte	14
2.3	Ragone plot of various electrochemical devices	15
2.4	A two-electrode configuration of the PPy/GO/ZnO super capacitor. Polypyrrole is denoted as PPy, graphene oxide as GO, and zinc oxide as ZnO	19
2.5	(a) Galvanostatic charge/discharge cycles of PPy, PPy/GO, and PPy/GO/ZnO at a current density of 1 A/g. (b) Specific capacitance of PPy, PPy/GO, and PPy/GO/ZnO at various current densities. (c) Prepared super capacitor connected in series lighting up an LED circuit, and (d) super capacitor bent at 90° lighting up an LED circuit. Polypyrrole is denoted as PPy, graphene oxide as GO, and zinc oxide as ZnO	20
2.6	Cyclic voltammograms of (a) PEDOT and (b) PProDOT-Et ₂ thick films (60C/cm ²) on Pt disc (0.1cm diameter) in 0.5M LiClO ₄ /MPN solution at the scan rate of 2 and 0.5mV/s. (c) Complex plane impedance plots of PEDOT and PProDOT-Et ₂ thick films (60C/cm ²) on Pt disc (0.1cm diameter) measured at 0.4V vs. Ag/Ag ⁺ in 0.5M LiClO ₄ /MPN solution. Inset: the corresponding linear relations between Z'' and 1/(2πf) for the two films	23
2.7	Cyclic voltammetric characteristics of activated carbon recorded in three-electrode cell at 5 mV/s	25
2.8	Progression of photovoltaic devices	27
2.9	Schematic of perovskite-coated TiO ₂ and Al ₂ O ₃ , illustrating electron and hole transfer	29
2.10	Schematic diagram and energy band gap diagram of architecture perovskite solar cell	30
2.11	(a) Photovoltaic performance of optimized planar heterojunction perovskite solar cells where CH ₃ NH ₃ PbI _{3-x} Cl _x (blue box) and CH ₃ NH ₃ PbI ₃ (yellow box) cells were both measured under 100 mW/cm ² AM1.5 simulated sunlight. (b) Diffusion lengths (L _D) of optimized planar heterojunction perovskite solar cells where the errors quoted predominantly	34

	arise from perovskite film thickness variations, which are ± 35 nm for the triiodide perovskite films and ± 40 nm for the mixed halide perovskite films	
2.12	Solar cell configuration and performance. (a) Scheme and (b) J–V curves of the two different cell configurations analyzed: Thin film (TF), left, and nanostructured (NS), right	34
2.13	Transport and recombination parameters vs voltage: recombination resistance, R_{rec}	35
2.14	(a) J-V curves under AM1.5 illumination of devices made with different concentrations of perovskite precursor. Inset/EQE spectrum of the best device, with the shaded area representing the part of the EQE most likely originating from P3HT. (b) UV-Vis spectra of the perovskite layers used in the devices of (a), deposited on a dense layer of TiO_2	36
2.15	(a) Absorbance over time of thin films of CsPbI_3 and CsPbI_2Br , measured at 675 and 625 nm respectively, when exposed to a slow flow of air at 50% RH. The slight increase in the absorbance of the CsPbI_2Br film is not yet fully understood. XRD spectra before and after 270 min of heating at 85 C in 20-25% RH for (b) CsPbI_2Br and (c) MAPbI_2Br . The reference powder pattern for CsPbI_3 (cubic phase) is from Trots and Myagkota; the MAPbI_3 (tetragonal phase) powder pattern is from a crushed single crystal. X-ray absorbance due to the Kapton film is seen below $2\Theta = 10^\circ$; the $\text{PbI}_{2-x}\text{Br}_x$ peak position is indicated by a diamond	37
2.16	(a) Schematic of stand-alone self-powered system consisting of four series-wound DSSCs, three series-wound flexible SCs, and one LED. (b) Leakage current curve of three series-wound SCs charged at 0.5 mA to a potential of 2.4 V and kept at 2.4 V for 5000 s, indicating a small leakage current. Inset is the voltage profile for three SCs in series when being charged by four DSSCs in series	42
2.17	The power pack device comprises a perovskite based solar cell and a polypyrrole-based super capacitor	44
2.18	(a) Schematic illustration of the printable perovskite solar cell based photo-super capacitor. (b) The voltage response of the perovskite solar cell during photocharge and galvanostatic discharge of super capacitor at different current densities in dark	44
4.1	FESEM images of (a) Bi_2O_3 after hydrothermal process, (b) MnO_2 , and (c) $\text{Bi}_2\text{O}_3/\text{MnO}_2$ nanocomposite, along with (d) TEM image, (e) HRTEM, and (f) SAED of $\text{Bi}_2\text{O}_3/\text{MnO}_2$ nanocomposite. Inset of Figure 4.1d shows the encapsulation of 2D MnO_2 ultrathin sheet over Bi_2O_3 particles	62

4.2	(a) XRD profile and (b) FTIR spectrum of blank Ni foam, Bi ₂ O ₃ , MnO ₂ , and Bi ₂ O ₃ /MnO ₂ , and (c) Raman spectroscopies of Bi ₂ O ₃ , MnO ₂ , and Bi ₂ O ₃ /MnO ₂	63
4.3	XPS analysis of (a) wide scan of Bi ₂ O ₃ , MnO ₂ , and Bi ₂ O ₃ /MnO ₂ , and narrow scan of (b) Bi4f, (c) Mn2p, and (d) O1s. The MnO ₂ is postulated to be Mn ⁴⁺ because it has a different binding energy of 4.6 eV, which is the closest to the theoretical value of 4.8 eV, as determined from the Mn3s plot, as shown in Figure A.3	65
4.4	Plausible growth of Bi ₂ O ₃ /MnO ₂ on nickel foam substrate during hydrothermal process. It shows that the MnO ₂ nanosheet is compactly covering the Bi ₂ O ₃ sphere after calcination	66
4.5	(a) Cyclic voltammogram, (b) galvanostatic charge/discharge, (c) Nyquist plot, and (d) life cycle of Bi ₂ O ₃ /MnO ₂ super capacitors at different temperatures	69
4.6	(a) Ragone plot of Bi ₂ O ₃ /MnO ₂ super capacitor at temperatures of 0, 30, and 60 °C, while (b) EIS and (c) life cycle of Bi ₂ O ₃ /MnO ₂ super capacitor at various defrosting periods (30, 60, and 120 min) after being cooled at 0 °C for 1 hour. The EIS of Bi ₂ O ₃ /MnO ₂ super capacitor was measured from starting frequency of 100 kHz to ending frequency of 0.01 Hz.	71
4.7	FESEM images of Bi ₂ O ₃ /MnO ₂ (a) before life cycle at 30 °C and (b)–(d) after life cycle measurements at 0 °C, 30 °C, and 60 °C, respectively	72
4.8	(a) Cyclic retention comparison between Bi ₂ O ₃ /MnO ₂ , MnO ₂ , and Bi ₂ O ₃ super capacitors. (b) Nyquist plots of Bi ₂ O ₃ /MnO ₂ super capacitor after life cycle performances at room temperature. Figure 4.8(a) shows an image of a light emitting diode (LED) lighted by the Bi ₂ O ₃ /MnO ₂ super capacitor. The active electrode possesses an active surface area of 1 cm ²	74
4.9	Assignment of positive and negative electrodes determine through three-electrodes cyclic voltammetry System. The CV curves of (a) Bi ₂ O ₃ /MnO ₂ positive and (b) PyR negative electrodes. The pseudo-rectangular Bi ₂ O ₃ /MnO ₂ and PyR voltammograms are prominent at 0-1 V and -0.2-0.4 V potential range, respectively, giving an overall potential window of 1.6 V. PyR refers to polypyrrole and reduced graphene oxide	75
4.10	(a) Specific capacitance obtained through cyclic voltammogram at the scan rate of 100 to 2 mV/s, (b) galvanostatic charge/discharge from current density of 2 mA/cm ² to 20 mA/cm ² , and (c) capacitive retention of Bi ₂ O ₃ /MnO ₂ /PyR asymmetrical super capacitor	76

4.11	FESEM images of (a) ZCo positive electrode and (b) RZCo positive electrode	78
4.12	The growth of (a) ZCo and (b) RZCo on graphite sheet. The eventual particle size of ZCo was dependent on the presence of GO. The graphite sheet acted as a current collector for the as-assembled super capacitor	79
4.13	(a) XRD profile and (b) FTIR spectrum of RZCo positive electrode. Inset shows the magnified XRD peaks of RZCo positive electrode	80
4.14	XPS analysis of (a) wide scan, (b) Zn2p, (c) Co2p, (d) O1s, and (e) C1s of RZCo positive electrode	81
4.15	Cyclic voltammograms of (a) PyR and (b) RZCo electrodes at various potentials range	83
4.16	(a) Nyquist plot, (b) ragone plot, and (c) life retention of ZCo//PyR and RZCo//PyR asymmetric super capacitor. Inset shows the magnified high frequency region and the life cycle was measured at current density of 2 mA/cm ² . The energy and power density of as-fabricated asymmetric super capacitors were compared against the KEMET commercial super capacitor	86
4.17	Plot of specific capacitance of asymmetric super capacitor versus GO concentrations. The specific capacitance results were extracted from cyclic voltammetric. Inset is the tabulated results of asymmetric super capacitor with various GO concentrations	88
4.18	Plot of specific capacitance of asymmetric super capacitor with rGO and asymmetric super capacitor without rGO at different current densities from 2 mA/cm ² to 20 mA/cm ² . The area of each electrode is 1 cm ² . The specific capacitance results were extracted from galvanostatic charge/discharge profile	89
4.19	(a) Nyquist plot, (b) life cycle of asymmetric super capacitor at different operating temperatures (0 °C, 30 °C, and 60 °C)	90
4.20	Reversibility performance of RZCo//PyR asymmetric super capacitor (a) at various temperatures and (b) at various defrosting time. The specific capacitance was extracted from galvanostatic charge/discharge profile measured at 2mA/cm ² , whereas the cyclic retention was calculated upon 1000 continuous charge/discharge measurement	92
4.21	FESEM images of RZCo positive electrode under (a) cold (0 °C) and (b) hot condition (60 °C)	92
4.22	Electrochemical measurements of (a) cyclic voltammetry at scan rate of 2 mV/s, (b) galvanostatic charge/discharge at current density of 2 mA/cm ² ,	94

	(c) EIS, and (d) life cycle of as-fabricated and KEMET commercial super capacitor	
5.1	XRD patterns of glass/CsPbBr _{3-x} I _x , where the amount of iodide varies as $x = 0, 0.1, 0.2,$ and 0.3 in molar ratio	103
5.2	Normalized (a) absorption and (b) photoluminescence of CsPbBr _{3-x} I _x , where x is $0, 0.1, 0.2,$ and 0.3 molar ratio, and (c) band gap energy	104
5.3	Schematic energy level diagram of FTO/TiO ₂ /CsPbBr _{3-x} I _x /HTM/Au, where x is $0, 0.1, 0.2$ or 0.3 perovskite solar cell, employing HTM as either <i>Spiro</i> -OMeTAD or P3HT/MoO ₃ . The band gap of each perovskite is also indicated	104
5.4	J-V measurements (a) under simulated AM 1.5G sun light of 100 mW cm^{-2} irradiance, and (b) under dark. (c) EQE for glass/FTO/c-TiO ₂ /mp-TiO ₂ /CsPbBr _{3-x} I _x /Spiro-OMeTAD/Au solar cells, where x varies in $0, 0.1, 0.2,$ and 0.3 molar ratio. (d) Enlarged EQE spectrum of CsPbBr _{3-x} I _x perovskite solar cells shows the red-shifted EQE onsets	106
5.5	The V_{oc} behaviour is represented in the energy level diagrams for perovskite solar cells with narrow (a) or wide band gaps (E_g) (b) and (c) of absorber and different HTMs, such as <i>Spiro</i> -OMeTAD/Au in (a) and (b) or deeper work function (W_F) as P3HT/MoO ₃ /Au in (c). The conduction band (E_c), valence band (E_v), Fermi level of electrons (E_{Fn}) and holes (E_{Fp}) were indicated. The MoO ₃ layer creates a dipole (Δ) at the interface, reducing the vacuum level energy (E_{vac})	107
5.6	J-V measurements (a) under simulated AM 1.5G sun light of 100 mW cm^{-2} irradiance, and (b) under dark. (c) EQE for glass/FTO/c-TiO ₂ /mp-TiO ₂ /CsPbBr _{3-x} I _x /P3HT/MoO ₃ /Au solar cells, where x varies in $0, 0.1, 0.2,$ and 0.3 molar ratio	108
5.7	Stability test of CsPbBr _{3-x} I _x devices ($x = 0, 0.1, 0.2,$ and 0.3 molar ratios). Figures show the cell parameters of (a) J_{sc} , (b) FF, (c) V_{oc} , and (d) efficiency as a function of time	110
5.8	Digital photographic image of as-fabricated CsPbBr _{3-x} I _x perovskite solar cells where $x=0, 0.1, 0.2,$ and 0.3	112
5.9	(a) Cross section of ITO/c-TiO ₂ /m-TiO ₂ /CsPbBr _{3-x} I _x /HTM and (b-e) top view surface morphology of ITO/CsPbBr _{3-x} I _x perovskite solar cells in the molar ratios of 0 (b), 0.1 (c), 0.2 (d), and 0.3 (e)	112
5.10	(a) J-V performances of CsPbBr _{3-x} I _x solar cell under 1sun illumination and in dark, (b) Nyquist plot and (c) Bode phase diagram of CsPbBr _{3-x} I _x solar cell under 1sun illumination measured at near open-circuit voltage. The solar cells were measured under 1sun illumination (solid lines) and in dark	114

(dotted lines) for J-V test. The complete set of perovskite solar cell for both measurements is composed of ITO/c-TiO₂/m-TiO₂/CsPbBr_{3-x}I_x/*Spiro-OMeTAD* and PEDOT:PSS as the counter electrode. The electrochemical impedance spectroscopy was measured from a starting frequency of 1 MHz to an ending frequency of 0.1 Hz

5.11	Stability performances of CsPbBr _{3-x} I _x perovskite solar cells where (a) corresponds to the V _{oc} , (b) FF, (c) J _{sc} , and (d) PCE. For the stability test, the perovskite solar cells were stored in dark in a humidity control desiccator after 1sun illumination test for 168 hours	116
5.12	Stability performance of CsPbBr _{2.9} I _{0.1} perovskite solar cell under exposure to UV and moisture (>80% RH). The CsPbBr _{2.9} I _{0.1} perovskite solar cell is potential to be employed for photo-super capacitor application	117
5.13	(a) FESEM image, (b) RAMAN spectroscopy, and (c) EDX spectrum of RZCo active material deposited on a graphite sheet	119
5.14	(a) Galvanostatic charge discharge, (b) Nyquist plot, and (c) cyclic retention of PEDOT:PSS-assisted RZCo//PyR super capacitor in a swagelok. RZCo is representing reduced graphene oxide/zinc oxide/cobalt oxide, while the PyR is representing the polypyrrole/reduced graphene oxide. The electrochemical impedance spectroscopy was calculated from starting frequency of 100 kHz to an ending frequency of 0.01 Hz	119
5.15	(a) Photovoltage response and (b) photocurrent response of CsPbBr _{2.9} I _{0.1} perovskite solar cell in the presence of illumination and in dark condition. (c) galvanostatic charge/discharge of integrated asymmetrical super capacitor in dark condition	121
5.16	Charging mechanism of photo-super capacitor. Positive electrode/cathode represents PEDOT:PSS-assisted RZCo, while negative electrode represents PyR. RZCo is denoted as reduced graphene oxide, zinc oxide, and cobalt oxide, while PyR stands for polypyrrole and reduced graphene oxide	122
5.17	(a) Discharging of photo-super capacitor and (b) magnified alignment of charges along the electrode and electrolyte interface of electric double layer capacitor (EDLC)	123
A.1	FESEM image of Bi ₂ O ₃ particle before hydrothermal process	147
A.2	Elemental maps of Ni, Mn, O, and Bi elements for Bi ₂ O ₃ /MnO ₂	147
A.3	XPS analysis: determination of oxidation state of MnO ₂ from Mn3s plot	148

A.4	The cyclic voltammogram of KEMET commercial super capacitor at 2 mV/s and the inset shows the XRD profile of KEMET commercial super capacitor. The XRD profile shows that the KEMET commercial super capacitor is composed of graphitic carbon based material	149
A.5	(a) Raman spectroscopy and (b) FESEM images of polypyrrole/reduced graphene oxide (PyR) negative electrode. Inset shows the magnified PyR materials	149
B.1	Magnified FESEM images of CsPbBr _{3-x} I _x perovskite materials on ITO conductive glass, where x=0, 0.1, 0.2, and 0.3	151
B.2	A three electrodes coupled photo-super capacitor. The sharing electrode of PEDOT:PSS assisted RZCo electrode is acted as the counter electrode for the perovskite solar cell and simultaneously being a positive electrode for the super capacitor	152

LIST OF TABLES

Table		Page
2.1	Potential active materials applied for super capacitor applications	21
2.2	Typical conductivities of various conducting polymers	22
2.3	The advantages and disadvantages of perovskite materials employed in most reported works	32
2.4	Summary of mono- and alloyed-halide perovskite solar cells	38
2.5	A summary on the integration of a photovoltaic device and an energy storage device	45
4.1	Tabulated energy and power density, and specific capacitance of Bi ₂ O ₃ /MnO ₂ super capacitors, extracted from galvanostatic charge/discharge (CD) at 2 mA/cm ²	72
4.2	Electrochemical performances of present and reported super capacitor studies under temperature influences or at room temperature	73
4.3	Electrochemical performances of Bi ₂ O ₃ /MnO ₂ symmetrical super capacitor and Bi ₂ O ₃ /MnO ₂ //PyR asymmetrical super capacitor. The Bi ₂ O ₃ /MnO ₂ is assigned as the positive electrode, while the PyR is the negative electrode for the asymmetric configured super capacitor. The specific capacitance is obtained from galvanostatic charge/discharge	77
4.4	Electrical conductivity measurements performed on (a) ZCo, and (b) RZCo graphite sheets positive electrode	82
4.5	Tabulated results of energy and power density of as-fabricated asymmetrical super capacitor against KEMET commercial super capacitor at scan rate of 2mV/s	86
4.6	Comparison of electrochemical performances of RZCo//PyR asymmetrical super capacitor against the reported zinc cobalt based super capacitor in the literatures	87
4.7	Tabulated results for EIS and life cycle of RZCo//PyR asymmetrical super capacitor at 0 °C, 30 °C, and 60 °C. EIS was performed from starting frequency of 100 kHz to an ending frequency of 0.01 Hz, while the life cycle was performed at current density of 2 mA/cm ²	90
5.1	Photovoltaic parameters of the CsPbBr _{3-x} I _x solar cells (<i>x</i> varies between 0, 0.1, 0.2, and 0.3 in molar ratio) with <i>Spiro</i> -OMeTAD as the HTM. The	106

	photocurrent calculated from the integration of the EQE curves is also added	
5.2	Photovoltaic parameters of the CsPbBr _{3-x} I _x solar cells (<i>x</i> varies between 0, 0.1, 0.2, and 0.3 in molar ratio) with P3HT as the HTM. The photocurrent calculated from the integration of the EQE curves is also added	108
5.3	Electron lifetimes of the mixed halides solar cells under 1sun illumination. The electron lifetimes are calculated based on Equation (3.5)	114
A.1	General information of a graphite sheet and a nickel foam	148
A.2	Electrochemical performances of Bi ₂ O ₃ /MnO ₂ symmetrical super capacitor, Bi ₂ O ₃ /MnO ₂ //PyR and RZCo//PyR asymmetrical super capacitor. The Bi ₂ O ₃ /MnO ₂ and RZCo are assigned as the positive electrode, while the PyR is the negative electrode for the asymmetric configured super capacitor. The specific capacitance is obtained from galvanostatic charge/discharge. (The bold column is the super capacitor used for photo-super capacitor)	150
A.3	General information and specifications of KEMET commercial super capacitor (KEMET Part Number: FT0H105ZF)	150
B.1	Specifications and prices comparison between FTO and ITO conductive glass. Data were extracted from Techinstro®. TCO represents transparent conductive oxide	151

LIST OF ABBREVIATIONS

<i>Spiro-OMeTAD</i>	2,2',7,7'-tetrakis(N,N-di-p-ethoxyphenylamino)-9,9'-spirobifluorene
P	Poly[[2,5-bis(2-octyldodecyl)-2,3,5,6-tetrahydro-3,6-dioxopyrrolo[3,4-c]pyrrole-1,4-diyl]-alt-[[2,2'-(2,5-thiophene)bis-thieno[3,2-b]thiophen]-5,5'-diyl]]
TiO ₂	Titanium dioxide
PProDOT-Et ₂	Poly(3,3-diethyl-3,4-dihydro-2H-thieno-[3,4-b][1,4]dioxepine)
HTM	Hole transport mobility
HI	Hysteresis index
ATO	Anodic titanium oxide
KMnO ₄	Potassium permanganate
Bi ₂ O ₃	Bismuth oxide
H ₂ SO ₄	Sulphuric acid
H ₃ PO ₄	Phosphoric acid
H ₂ O ₂	Hydrogen peroxide
HCl	Hydrogen chloride
Na ₂ SO ₄	Sodium sulphate anhydrous
NapTS	Toluene-4-sulfonic acid sodium salt
Zn(NO ₃) ₂ ·6H ₂ O	Zinc nitrate hexahydrate
Co(NO ₃) ₂ ·6H ₂ O	Cobalt (II) nitrate hexahydrate
NH ₄ Cl	Ammonium chloride
FTO	Fluorine-doped tin oxide
ITO	Indium tin oxide
mp-TiO ₂	Mesoporous titanium dioxide
PbBr ₂	Lead (II) bromide
PbI ₂	Lead (II) iodide

CsBr	Cesium bromide
Li-TFSI	Bis (trifluoromethane) sulfonimide lithium salt
TBP	4-tert-butylpyridine
TTIP	Titanium (IV) tetraisopropoxide
DMF	Dimethylformamide
LiClO ₄	Lithium perchlorate
GO	Graphene Oxide
AACVD	Aerosol assisted chemical vapour deposition
XPS	X-ray photoelectron spectroscopy
XRD	X-ray diffraction
FTIR	Fourier transform infrared spectroscopy
FESEM	Field Emission Scanning Electron Microscope
TEM	Transmission electron microscopy
UPS	Ultraviolet Photo-Electron Spectroscopy
CV	Cyclic voltammetry
EIS	Electrochemical impedance spectroscopy
J-V	Current density-voltage
EQE	External quantum efficiency
rGO	Reduce graphene oxide
PPy	Polypyrrole
Co ₃ O ₄	Cobalt oxides
Ni(OH) ₂	Nickel hydroxide
NiO	Nickel oxide
Li	Lithium
Zn	Zinc

PANI	Polyaniline
MnO ₂	Manganese dioxide
RuO ₂	Ruthenium oxide
ZnO	Zinc oxide
SAED	Selected area electron diffraction
2D	2-Dimensional
3D	3-Dimensional
RZCo	Reduced GO/zinc oxide/cobalt oxide
PyR	Polypyrrole/reduced GO
ZCo	Zinc oxide/cobalt oxide
EIS	Electrochemical impedance spectroscopy
ESR	Equivalent series resistance
R _{ct}	Charge transfer resistance
CsPbBr ₃	Cesium lead bromide
LUMO	Lowest unoccupied molecular orbital
HOMO	Highest occupied molecular orbital
MgO	Magnesium oxide
PSC	Perovskite solar cell
VB	Valence band
CB	Conduction band
TCO	Transparent conductive oxide
ETL	Electron transporting layer
HTM	Hole transporting material
PVA	Polyvinyl alcohol
KOH	Potassium hydroxide

LED	Light emitting diode
PLQY	Photoluminescence quantum yield
V_{oc}	Open-circuit voltage
J_{sc}	Short circuit current
FF	Fill factor
TF	Thin film
NS	Nanostructure
$CsPbI_3$	Cesium lead iodide
$FAPbI_3$	Formamidinium lead iodide
R_{rec}	Recombination resistance
MoO_3	Molybdenum trioxide
$MAPbI_3$ or	Methylammonium lead iodide
$CH_3NH_3PbI_3$	
$MAPbX_3$ or	Methylammonium lead halide
$CH_3NH_3PbX_3$	
EDLC	Electric double layer capacitor
DSSC	Dye-sensitized solar cell
PCE	Power conversion efficiency
Bi_2O_3/MnO_2	Bismuth oxide/manganese oxide
RH	Relative humidity
PEDOT:PSS	Poly(3,4-ethylenedioxythiophene) polystyrene sulfonate
SWCNT	Single-walled carbon nanotubes
MWCNT	Multiwalled carbon nanotubes
IPCE	Photo-to-electrical current conversion efficiency
Al_2O_3	Aluminium oxide or alumina

P3HT	Poly(3-hexylthiophene)
C_E	Specific capacitance per unit electrode active area
SCE	Saturated calomel electrode
YD2-o-C8	Donor- π -bridge-acceptor zinc porphyrin dye
D- π -A	Donor- π -bridge-acceptor
PMMA	Polymethylmethacrylate

LIST OF PUBLICATIONS

Papers published in referred journals

1. **Ng C.H.**, Lim H.N., Hayase S., Zainal Z., Shafie S. and Huang N.M. (2017). Capacitive Performance of Graphene-Based Asymmetric Supercapacitor. *Electrochimica Acta*. **229**: 173-182.
2. **Ng C.H.**, Ripolles T.S., Hamada K., Teo S.H., Lim H.N., Bisquert J. and Hayase S. (2018). Tunable Open Circuit Voltage by Engineering Inorganic Cesium Lead Bromide/Iodide Perovskite Solar Cells. *Scientific Reports*. **8**: 2482.
3. **Ng C.H.**, Lim H.N., Hayase S., Zainal Z., Shafie S., Lee H.W. and Huang N.M. (2018). Cesium Lead Halide Inorganic-Based Perovskite-Sensitized Solar Cell for Photo-Supercapacitor Application under High Humidity Condition. Accepted at *ACS Applied Energy Materials*. DOI: 10.1021/acsaem.7b00103.
4. **Ng C.H.**, Lim H.N., Hayase S., Zainal Z., Shafie S. and Huang N.M. (2018). Effects of Temperature on Electrochemical Properties of Bismuth Oxide/Manganese Oxide Pseudocapacitor. Accepted at *Industrial & Engineering Chemistry Research*. DOI: 10.1021/acs.iecr.7b04980
5. **Ng C.H.**, Lim H.N., Hayase S., Harrison I., Pandikumar A. and Huang N.M. (2015). Potential Active Materials for Photo-Supercapacitor: A Review. *Journal of Power Sources*. **296**: 169-185.

List of involvement/attended seminars/workshops/conferences

1. Workshop on Princeton Applied Research Instruments at Physics Department, University of Malaya on 19th June 2014. (Participant)
2. International Materials Technology Conference & Exhibition (IMTCE) 2014, Organised by Institute of Materials, Malaysia (IMM) on 13th-16th May 2014 at Putra

- World Trade Centre, Kuala Lumpur, Malaysia. (Committee Member and Poster Presenter)
3. X-Ray Photoelectron Spectroscopy Workshop, Organised by Nano-semiconductor technology on 10th March 2015 at MIMOS Berhad. (Participant)
 4. Workshop and Hands On Training in Photoelectrochemistry and Dye-Sensitized Solar Cells on 20th May 2015, held at High Impact Research (HIR) Building, University of Malaya. (Participant)
 5. Participated in Young Scientists Network Malaysia: 2nd Creative Science Writing Competition 2015 Organised by Akademik Malaysia. (Consolation Prize)
 6. DropSens Miniaturized Electrochemistry Seminar, Organised by Metrohm Malaysia on 19th April 2016. (Participant)
 7. 10th International Materials Technology Conference & Exhibition (IMTCE) Organised by Institute of Materials, Malaysia (IMM) on 16th-19th May 2016 at Putra World Trade Centre, Kuala Lumpur, Malaysia. (Committee Member and Oral Presenter)
 8. Elsevier Publishing Connect Workshop on 13th June 2016 at Auditorium Faculty of Educational Studies. (Participant)
 9. Workshop on Increasing the Impact of Research: Strategies and Practical Guidelines for Universities and Research Institutions, Organised by Perpustakaan Sultan Abdul Samad School of Graduate Studies Center for Academic Development on 1st March 2017. (Participant)
 10. UPM-KYUTECH Joint Seminar on Solar Technology at Faculty of Engineering, Universiti Putra Malaysia on 9th March 2017. (Participant)
 11. Public Seminar from Kyushu Institute of Technology, Japan at Bilik Saintis Gemilang, Universiti Putra Malaysia on 10th March 2017. (Participant)
 12. Public Seminar from Kyushu Institute of Technology, Japan at Bilik Saintis Gemilang, Universiti Putra Malaysia on 16th November 2017. (Participant)

ABSTRACT

The coupling of a solar cell with a super capacitor is gaining interest owing to its superior photo-to-electrical conversion efficiency and its in-situ energy storage ability for green and sustainable energy development. In this work, the electrochemical performances of the fabricated super capacitor and perovskite solar cell were individually measured for the fabrication of a photo-super capacitor.

A $\text{Bi}_2\text{O}_3/\text{MnO}_2$ based symmetrical and asymmetrical super capacitor were fabricated. The symmetrical super capacitor could charge up to 1.0 V, which gave a specific capacitance of 136.4 F/g at a scan rate of 2 mV/s. The power and energy densities of the bismuth-based symmetrical super capacitor were 51.8 W/kg and 7.1 Wh/kg, respectively and were improved to 25.6 Wh/kg and 115.3 W/kg when a $\text{Bi}_2\text{O}_3/\text{MnO}_2$ positive electrode was integrated to a polypyrrole/reduced graphene oxide (PyR) negative electrode. It thus proven the feasibility of an asymmetrical super capacitor to promote the performance of a super capacitor. The dissatisfying stability performance of the $\text{Bi}_2\text{O}_3/\text{MnO}_2//\text{PyR}$ asymmetrical super capacitor (60% capacitance retained) prompted for screening of other pseudocapacitive materials. An asymmetrical super capacitor comprising a positive cobalt oxide/zinc oxide/reduced graphene oxide electrode (RZCo) and a negative polypyrrole/reduced graphene oxide electrode was then fabricated. A wide operational potential range for the RZCo//PyR asymmetrical super capacitor resulted in a high specific capacitance of 470.8 F/g, as opposed to the $\text{Bi}_2\text{O}_3/\text{MnO}_2$ symmetrical super capacitor of 136.4 F/g and 144.1 F/g for the bismuth-based asymmetrical super capacitor, at a scan rate of 2mV/s, additionally exhibited 1.6-fold higher in energy and power densities, which fulfilling the criteria as the energy storage device for the photo-super capacitor.

Perovskite solar cells were fabricated from a series of cesium based halide mixtures perovskite harvesting materials, denoted as $\text{CsPbBr}_{3-x}\text{I}_x$, where $x = 0-0.3$. An optimum iodide concentration of $\text{CsPbBr}_{2.9}\text{I}_{0.1}$ perovskite solar cell with an efficiency of 3.9% was fabricated. The solar cell achieved an open circuit voltage of more than 1.0 V and a fill factor of 64% by employing *Spiro-OMeTAD* as a hole transporting material with enhanced stability. The performances of the $\text{CsPbBr}_{2.9}\text{I}_{0.1}$ solar cell with P3HT/ MoO_3 hole transporting material was also investigated. The deeper HOMO and shallower LUMO level of the hole and electron transporting materials, respectively has achieved high V_{oc} of 1.23 V, but with lower power conversion efficiency of 2.51% due to reduction in the J_{sc} , implies an additional charge loss processes at the interface of perovskite/HTM. In high humidity of more than 80 percent, the perovskite solar cell comprising $\text{CsPbBr}_{2.9}\text{I}_{0.1}$ achieved an efficiency of 0.46%. The perovskite solar cell retains 70% of its original efficiency after a week storage in dark and 33% efficiency retained under UV and air exposure at a high relative humidity of more than 80% for 24 hours. The integration of the perovskite solar cell and the asymmetrical super capacitor enabled simultaneous photoconversion and charge storage within the photo-super capacitor. The photovoltage and photocurrent measurements were successfully performed, evidencing that the photo-super capacitor was responsive to light illumination. Referred to the photovoltage measurement, zero voltage was presented at the first 50 s without the shine of light. Subsequently, the photovoltage was abruptly shot up to ~80 mV and continue increasing to 90 mV for 100 s in the presence of light, and was then decreases drastically when light was switched off. To further proof the energy conversion and storage of the photo-super capacitor, the photocharged integrated device was galvanostatically discharged in dark at the current of 0.1 mA. As the integrated device reaches the cut off potential of 0.07 V, the discharging process took place in dark with the connection of only super capacitor's electrodes, thus shows the workability of the photo-super capacitor. To enable practical application, improvizations

such as optimizing thickness of each active layer and encapsulation of the photo-super capacitor are needed to prevent electrolyte loss.

CHAPTER 1

INTRODUCTION

1.1 Background

The photo-super capacitor is a green energy device which utilizes the non-depletable solar energy as the prime energy source for photo-to-electrical conversion, subsequently storing of energy within the energy storage devices such as batteries, capacitors, and the super capacitors. Considerable attention has been allocated on the progression of solar energy conversion and electric energy storage to cope the raising energy demands in daily lives, to minimize the usage of non-renewable energy resources, and to use the harvested solar energy during night when an energy storage device is integrated to an energy conversion device (Xu *et al.*, 2014). The present existing photo-super capacitor are composed of dye-sensitized solar cell (DSSC)-battery or DSSC-super capacitor. When a DSSC was incorporated to a lithium ion battery, the power pack device was charged up to 3 V in 8 min and exhibited a total energy conversion and storage efficiency of 0.82%, which is considerably low (Guo *et al.*, 2012). To improve the power output performance of the photo-super capacitor, a silicon based photo-super capacitor where the energy conversion device composed of titania based DSSC, while the super capacitor composed of silicon wafer was therefore integrated and rendered an overall efficiency of 2.1% (Cohn *et al.*, 2015). In 2017, a photo-super capacitor made up of DSSC and polypyrrole/reduced graphene oxide super capacitor achieved a specific capacitance retention of 70.9% after 50 consecutive charge discharge cycles at a current density of 5 mA/cm² (Lau *et al.*, 2017). Nevertheless, DSSC-based photo-super capacitor suffered from low charging voltage owing to low open circuit voltage obtained from the DSSC, consequently led to low energy density of photo-super capacitor. In addition, self-discharging of photo-super capacitor

could restrain the charge storage ability of the photo-super capacitor. The reason of self-discharging is owing to the energy storage device has certain internal resistance, which in turn consume energy. Additionally, the electrons of the solar cell part flows back to the cathode of the energy storage part and thus recombination between electrons and holes occur. Hence, prioritizing materials used for energy conversion and storage devices is important for energy harvest and storage surge.

So far, the super capacitor has been overriding all kinds of energy storage devices owing to its high power density (2-10 kW/kg), fast charging/discharging, and longer lifespan (10^4 - 10^6 cycles) properties (Vidyadharan *et al.*, 2014; Xia *et al.*, 2012; Xie *et al.*, 2013). Super capacitor is classified into two classes, namely the electric double layer capacitor (EDLC) and pseudo-capacitor. The distinctive feature between EDLC and pseudo-capacitor solely relies on their charging mechanisms where the EDLC electrode materials are electrochemically inactive and dependence on its accumulation of charges at the electrode/electrolyte interface; whereas the occurrence of faradaic reaction on pseudo-capacitor enables the storage of charges during charging and discharging process (Chen *et al.*, 2014; Y. Cheng *et al.*, 2013; Lim *et al.*, 2013; Lim *et al.*, 2014; Wang *et al.*, 2012). The EDLC materials such as carbonaceous materials are profound in establishing a cyclic stability, whereas the pseudo-capacitive materials comprise transition metal oxides with multi-oxidative transition states and conducting polymer are of high capacitive spices in the energy storage family. The transition metal oxides are profound in their oxidation and reduction reversibility over the wider potential range which is favorable in the super capacitor application.

Relentless efforts have been done to maximize the super capacitor performances. The limitations of a symmetrical super capacitor such as low overall power and energy density hence prompted the switching of the symmetric configuration of the super capacitor to

asymmetric configuration ascribed to narrower potential range applied (Wang *et al.*, 2012). An asymmetrical super capacitor is made up of the combination of a battery-type faradaic cathode and a capacitor-type anode that is able to increase the potential window range, subsequently, maximizes the operation voltage of asymmetrical super capacitor (Luan *et al.*, 2013; Ng *et al.*, 2017; Tang *et al.*, 2013) and increases the energy density of the energy storage device (Fan *et al.*, 2011; Lin *et al.*, 2014). The occurrence of redox reaction with or without the non-Faradaic reaction and EDL (electrostatic adsorption/desorption) on either of the electrodes, respectively, clearly distinguishes the difference between an asymmetric and symmetric configuration of super capacitor (Ng *et al.*, 2015; Wang *et al.*, 2013).

In an effort to increase the surface area of active materials, tailoring nanostructure electrode is essential as it renders shorter ion insertion/desorption diffusion path to enable efficient charge and mass transfer without compromising its double layer capacitance (Luan *et al.*, 2013). In addition, the merit point of binder-less electrode is credited to its excellence in charge transportation (Luan *et al.*, 2013), in order to minimize the supercapacitive resistance and “dead volumes” in electrode materials (Fan *et al.*, 2011; Liu *et al.*, 2011). All in all, the key features to attain high performance super capacitor are large surface area, controlled pore size, layer stacking, and distribution of electrode materials (Brownson *et al.*, 2011). These merit points thus revealed that super capacitor is the most considerable candidate for photo-super capacitor association upon integrated with the photovoltaic device.

Taking into consideration of the energy conversion device, owing to the high fabrication cost of the first generation silicon solar cells, focus has therefore diverted to the second-generation thin-film semiconductors (copper indium gallium diselenide) and third-generation DSSCs, which have good cost effectiveness and easy fabrication methods without compromising their

high efficiency performances. The efforts to incorporate three-dimensional (3D) perovskite light harvester materials ($\text{CH}_3\text{NH}_3\text{PbX}_3$) into DSSCs produced efficiencies of 3.1% and 3.8% for $X = \text{Br}$ and $X = \text{I}$, respectively, in 2009 (Kojima *et al.*, 2009). These undesirable efficiencies were ascribed to the ionic crystal of organolead halide perovskite, which is highly soluble in a polar solvent, and subsequently affected the stability in a liquid electrolyte-based sensitized solar cell (Park, 2015a). In addition, the leakage of electrolyte was the main encumbering issue in stabilizing the photovoltaic performances of DSSCs. Thus, in an effort to curb the energy conversion limitation, the focus has switched to the fabrication of perovskite solar cells, where a solid hole transporting material (HTM) is used instead of liquid electrolyte, with the goal of achieving a higher stability relative to DSSCs.

The excellent ability of perovskite solar cells to convert solar energy to electrical energy is unquestionable based on the evidence of the organic-inorganic methylammonium lead iodide perovskite solar cell ($\text{CH}_3\text{NH}_3\text{PbI}_3$ or MAPbI_3), which has a high efficiency of 15% (Xing *et al.*, 2013; Xu *et al.*, 2014). $\text{CH}_3\text{NH}_3\text{PbI}_3$ is excellent at producing optimal band gaps, high absorption coefficients, and long-range exciton diffusion lengths (Choi *et al.*, 2014; Xing *et al.*, 2013). In addition, photovoltaic (PV) cells with a power conversion efficiency (PCE) of 19% and certified PCE of 20% were reported in 2014 (Park, 2015b; Yakunin *et al.*, 2015). Many studies and investigations on the performances of perovskite solar cells are still ongoing in the effort to surpass this PCE of 20%, as well as to establish a stable performance for a perovskite solar cell, in an effort to eliminate costly silicon PV cells (Boix *et al.*, 2014). The perovskite solar cell has been expected to be the next most promising light harvesting PV device compared to silicon-based photovoltaic cells and DSSCs, owing to its price effectiveness and high efficiency. To the best of our knowledge, the most suitable light absorbing material band gap for a single junction solar cell is 1.4 eV, according to the Shockley-Queisser limit curve

(Shockley and Queisser, 1961). $\text{CH}_3\text{NH}_3\text{PbI}_3$ has an energy band gap of ~ 1.55 eV, which surpasses the optimum band gap range of 1.1–1.4 eV (Kitazawa *et al.*, 2002; Wang *et al.*, 2014). Hence, solar cells with a high open circuit voltage (V_{oc}) such as those that incorporate bromide-based perovskite solar cells with a V_{oc} of ~ 1.5 eV (Kulbak *et al.*, 2016; Xu *et al.*, 2015) are highly desirable for electrochemical reactions and a high-energy photon absorber in a system with spectral splitting in order to widen the solar absorption ability (Edri *et al.*, 2013; Rühle *et al.*, 2009).

Despite perovskite solar cell has achieved impressive PCE of 22.1% in 2016 (Sun *et al.*, 2017), however, its low stability performance under operative conditions is apparently the main barrier for commercialization purpose. The $\text{CH}_3\text{NH}_3\text{PbX}_3$ perovskite material is highly sensitive to moisture, ultraviolet light (UV), and thermal stress where irreversible degradation and decomposition happen when the perovskite material is exposed to moisture. A thin film of $\text{CH}_3\text{NH}_3\text{PbI}_3$ thermally degrades to PbI_2 at >85 °C (Sutton *et al.*, 2016). Relentless efforts such as using cross-linking additives, compositional engineering, and encapsulation have been done to mitigate photo-instability of perovskite solar cells. However, this approach increases the overall solar cell's fabrication cost and device complexity. Replacing an organic methylammonium cation with an inorganic cesium cation is an approach to decelerate degradation process. CsPbBr_3 and CsPbI_3 are compositionally stable up to their melting point (>460 °C). At room temperature, CsPbBr_3 crystallizes in orthorhombic phase and it transitioned to tetragonal phase at 88 °C. At 130 °C, the orange cubic perovskite phase is formed. Conversely, an orthorhombic non-perovskite (yellow phase) CsPbI_3 is stable at room temperature. When it is heated >300 °C, the orthorhombic non-perovskite CsPbI_3 perovskite structure consequently transitioned to cubic perovskite phase (black phase). However, the CsPbI_3 is unstable in black perovskite phase in ambient condition and rapidly reverse to non-perovskite

yellow phase. (Sutton *et al.*, 2016). Hence, engineering mixed-halide perovskite materials is envisioned to be able to improve its absorption ability, stability, and subsequently the performance of the solar cell.

Though a photovoltaic device (perovskite-sensitized solar cell) accomplishes high energy conversion efficiency, however, its inability to store the converted energy, thus requires an additional energy storage device such as a super capacitor for a storage system, in addition to serve as the main power delivery output in most applications such as optoelectronic devices (Bagheri *et al.*, 2014). Considerable attention and efforts have been underway to improve and achieve a strikingly high efficiency, capacitance, and storage ability of a photo-super capacitor by studying and extensively investigating and analyzing the utility of active materials and preparation methods. Overall, the compatibility of active materials is the primary factor ensuring a striking performance for a photo-super capacitor due to the synergic effect of each material, which increases the conversion efficiency of the perovskite solar cell by suppressing electron recombination and simultaneously providing a surge of electrons for storage in the reservoir of the super capacitor, proving the concept of the energy storage system. In this works, the electrochemical performances of super capacitor and perovskite based solar cell were individually being studied towards the coupling of photo-super capacitor. Voltage and current response measurements were performed, thus proved the energy conversion and storage concept of photo-super capacitor.

1.2 Problem Statement/Hypothesis

The depletion of fossil fuels and natural resources has urgently called for green energy substitution. The utilization of solar cell or energy storage device solely cannot be the best solution to minimize energy wastage or to replace the usage of non-replenishing resources as

the solar cell could not store energy by its own and the energy storage device still require the sparking of electrical power for energy generation. Herein, the integration of an energy storage and conversion device (photo-super capacitor) as a wholly solar generated power-back device is envisaged to becoming the next energy saver for most optoelectronic applications by applying the energy converting, storage, and delivery system; without any usage of non-renewable sources. The conventional photo-super capacitor was composed of DSSC-battery or DSSC-super capacitor. However, the limitations of present technologies aforementioned are low efficiencies of traditional DSSC and hybrid organic solar cells, leakage of electrolyte, and low storage capacity of the energy storage device. Thus, the super capacitor is employed as the energy storage and power output device for the photo-super capacitor as it bridges the performances gap between the battery and capacitor featuring with fast charging/discharging properties. The electrode materials and super capacitor's configuration are important features for high performing super capacitor.

In realizing the integration of the solar generated power-pack device, firstly, a bismuth oxide/manganese oxide ($\text{Bi}_2\text{O}_3/\text{MnO}_2$) symmetrical super capacitor was fabricated and was tested through various electrochemical measurements. The limitation of the symmetrical $\text{Bi}_2\text{O}_3/\text{MnO}_2$ super capacitor, which could only charge up to 1.0 V led to low energy and power densities of 7.1 Wh/kg and 51.8 W/kg, respectively. The energy density performance is proportional to the cell voltage of the super capacitor, which is tunable when both of the super capacitor electrodes are composed of different active materials. Thus, to overcome the limitation of the bismuth-based symmetrical super capacitor, a $\text{Bi}_2\text{O}_3/\text{MnO}_2$ positive electrode was integrated to a polypyrrole/reduced graphene oxide (PyR) negative electrode. The $\text{Bi}_2\text{O}_3/\text{MnO}_2//\text{PyR}$ asymmetrical super capacitor exhibited 3.6-fold and 2.2-fold higher in energy and power densities, respectively when the potential window of the asymmetrical super

capacitor was extended to 1.6 V. Despite the electrochemical performances of the bismuth-based asymmetrical super capacitor have been improved, however the cyclic stability is the next shortcoming that needed prompt addresses. The $\text{Bi}_2\text{O}_3/\text{MnO}_2//\text{PyR}$ super capacitor could only retain 60% of its original capacitance after 1000 continuous charge/discharge cycles, implies the incompatibility of positive and negative active materials. The non-sustaining cyclic performance of the $\text{Bi}_2\text{O}_3/\text{MnO}_2//\text{PyR}$ super capacitor has urged for the next screening of potential active materials that contribute for high capacitance without compromises its cyclic stability. The incorporation of small amount of reduced graphene oxide (rGO) to the hybrid zinc oxide (ZnO) and cobalt oxide (Co_3O_4), in short denoted as RZCo as the positive super capacitor electrode has significantly enhanced the stability performance (1.4-fold increment) upon coupled to a PyR negative electrode.

For the energy conversion device, a highly performing perovskite solar cell is not solely relying on the power conversion efficiency, but also emphasizing on the surface morphology, interfaces of each layer, and stability of the devices. Getting a well-coated and compact film are truly important for efficient charge extraction and delivery system. Thus far, the racing efficiency of a perovskite solar cell is said to be achieved and is still forwarding (efficiency leap), however, the stability performance of the perovskite solar cell is still far left behind, especially under high humidity influence. As per discussed in most literature reports, the organic perovskite material, for instance, methylammonium lead iodide ($\text{CH}_3\text{NH}_3\text{PbI}_3$) is highly vulnerable and prone to materials degradation. The solutions over the stability issue are (i) substituting the organic based perovskite material (methylammonium-based) to an inorganic material (cesium-based), and (ii) varies the halides composition.

Switch to the case in a tropical country with humidity >80% relative humidity (RH), the inorganic perovskite light harvester will be the best choice for solar cell synthesis. The degradation of methylammonium precursor was observed (color of solution turned from colorless to dark brown) during stirring process, which shows the unsuitability of $\text{CH}_3\text{NH}_3\text{PbI}_3$ to be used for perovskite material in an ambient condition. In my work, a series of $\text{CsPbBr}_{3-x}\text{I}_x$ perovskite materials in the molar ratio of 0, 0.1, 0.2, and 0.3, respectively were synthesized, which not merely enhance the morphological perovskite surface, as well as enhancing its stability performances.

The inaccessibility of the equipment such as the metal evaporator and glove box is one of the encumbers during the fabrication of the solar cells. The metal evaporator is used to prepare the counter electrode or back contact of the solar cell. Due to inaccessibility of the evaporator, a PEDOT:PSS is spin coated as the counter electrode to replace the metal counter electrode. In addition, due to inaccessible glove box, the solar cell fabrication process was conducted in ambient condition, which accelerate the degradation process.

1.3 Research Scope

There are six chapters in total in this thesis, which comprises the Introduction (Chapter 1), Literature review (Chapter 2), Materials and methods (Chapter 3), Results and discussion (Chapter 4 and 5), and Conclusion and recommendations (Chapter 6). Generally, the physical and material properties of the catalysts/active materials used were carried out through X-ray diffraction (XRD), X-ray photoelectron spectroscopy (XPS), fourier-transform infrared spectroscopy (FTIR), field emission scanning electron microscope (FESEM), transmission electron microscopy (TEM), and RAMAN spectroscopy.

A systematic research background (Chapter 1) is presented, which includes an introductory to the super capacitor such as the classification and kinds of super capacitors, as well as the advantageous and disadvantageous of the super capacitor, followed by the discussion on the photovoltaic devices. The history and development of the photovoltaic device, especially the third generation photovoltaic devices (DSSC and perovskite solar cell) are briefly included. Lastly, we will look into the integration of both devices for photo-super capacitor application. Additionally, problem statements and objectives are included in Chapter 1. Chapter 2 is about the thorough literature reviews on the topics which cover the super capacitor, solar cell, and photo-super capacitor; while chapter 3 is reporting on the methodologies of each device's fabrication, characterizations, and measurements.

The results and discussion section is presented in Chapter 4 and 5 where chapter 4 is reporting on the performances of the super capacitors; while chapter 5 is focusing on the photovoltaic device (perovskite solar cell) and towards the emergence of the photo-super capacitor. Firstly, the performances of a symmetrical super capacitor were studied through various electrochemical characterizations such as the cyclic voltammetry (CV), galvanostatic charge discharge, electrochemical impedance spectroscopy (EIS), and cyclic stabilities. The dissatisfactory capacitive performance of the symmetrical super capacitor thus led to the coupling of an asymmetric configured super capacitor, which widen the cell voltage with improved energy and power density performances for photo-super capacitor application.

Chapter 5 presents the photovoltaic performances of the $\text{CsPbBr}_{3-x}\text{I}_x$ perovskite solar cell ($x = 0, 0.1, 0.2, \text{ and } 0.3$) evaluated through photocurrent density-photovoltage (J-V) curves, EIS, and stability of the perovskite solar cells. It shows that the perovskite solar cell performs the best when $x=0.1$. The $\text{CsPbBr}_{2.9}\text{I}_{0.1}$ perovskite solar cell is still performing the best even at high

humidity >80% RH. The champion cell was then integrated to the asymmetrical super capacitor for photo-super capacitor application. Conclusions are drawn in Chapter 6, accompanied with recommendations for further improvisation in achieving a highly efficient and stable photo-super capacitor.

1.4 Objectives

The aim of this project is to devise and develop a photo-super capacitor by studying the electrochemical and photovoltaic performances of super capacitor and perovskite solar cell respectively. In line with the increasing demand of energy, the use of renewable, green and clean energy is important for energy sustaining purpose. In this regards, the solar energy, which is one of the most cost effective renewable resources should be fully utilized in most applications. While the efficiency race is still progressing, the stability of the perovskite solar cell should not be compromised though. Thus, the focus of this work is to investigate and evaluate stability of the perovskite solar cell, especially at a high humidity influence. The next objective of this project is to validate the improved charge extraction and power conversion efficiency of the halide mixture solar cell upon the addition of small amount of iodide into the bromide matrix, as well as to examine the morphology of the perovskite surface after the inclusion of iodide.

Apart from the solar cell, the performances of the super capacitor as the primary energy storage and output device are also being investigated. In this context, the energy storage capacity and the rate of power output are essentially important for the photo-super capacitor application. Prioritize the electrode materials for capacitance, energy, and power densities surge for the super capacitor is an objective to be achieved. Attaining a highly reversible and sustainable

super capacitor is the next objective to achieve. The super capacitor with high recyclability fits the criteria for practical use and commercialization.

CHAPTER 2

LITERATURE REVIEWS

2.1 Introduction

The need for an endless renewable energy supply, typically through the utilization of solar energy in most applications and systems, has driven the expansion, versatility, and diversification of marketed energy storage devices. The evolution of the energy storage devices from batteries, conventional capacitors, and finally the high performing super capacitors have attracted considerable attention. Generally, super capacitors have been categorized into two types, which are the EDLC and faradaic super capacitor (or pseudocapacitor). The distinctive charging mechanism differs the both devices, as manifested in Figure 2.1 and 2.2. The electric double layer capacitance arises from the separation of ionic and electronic charges in the electrode and electrolyte interface (Ng *et al.*, 2015). The charging and discharging mechanism of an EDLC super capacitor is described in Figure 2.1. The charge storage in EDLC is highly reversible without compromising its cycling stabilities. By applying voltage to the facing electrodes, the positive ions and negative ions respectively move and adsorb on the surface of negative and positive electrodes, gives rise to its capacitance value. Conversely, ions detached from the electrode during the discharging process. Whilst, reversible faradaic reactions take place on the electrode materials for a Faradaic super capacitor (Wang *et al.*, 2012) through electrosorption, intercalation process, and oxidation-reduction process (Figure 2.2).

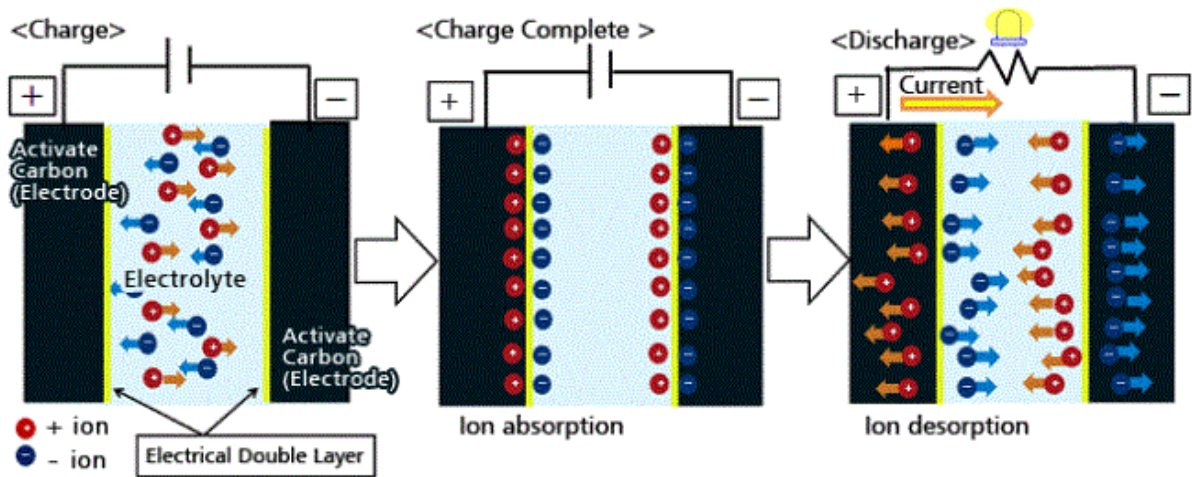


Figure 2.1 Schematic diagram of charging/discharging mechanism of EDLC. Adapted from <http://www.murata.com/products/capacitor/edlc/techguide/principle>.

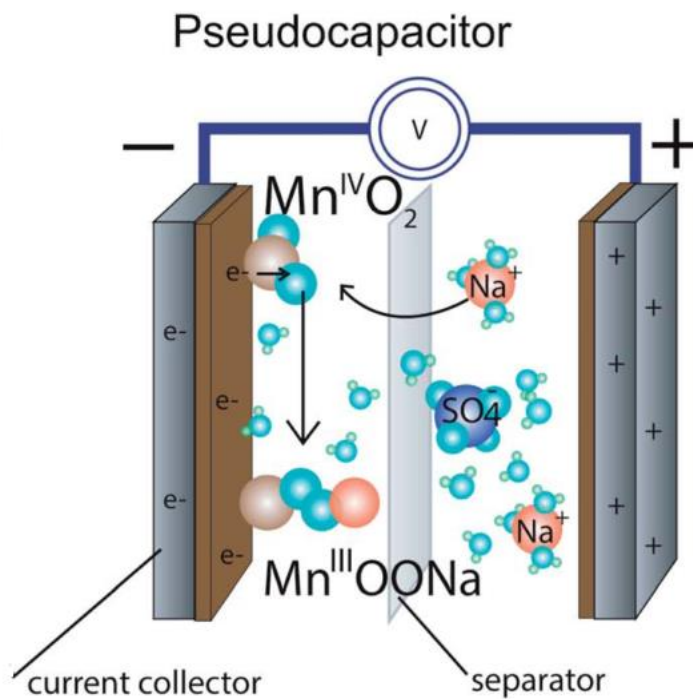


Figure 2.2 Basic schematics of a pseudocapacitor comprises MnO_2 active materials, a current collector, a separating membrane with Na_2SO_4 electrolyte. Adapted from (Jost *et al.*, 2014)

Super capacitor or electrochemical capacitor bridges the critical performance gap between the conventional capacitor and battery owing to its high power density performance than a battery and higher energy density than a conventional capacitor (Nithya and Sabari, 2016; You *et al.*,

2014), as illustrated in Figure 2.3. Super capacitor possesses fast charging/discharging properties and long life cyclic performance (>100000 cycles), which is highly suitable for power back systems, hybrid electrical vehicles, and portable electronics (Gan *et al.* 2015). Additionally, it has been used in memory backups, uninterruptible power supplies, consumer electronics, and braking systems. Nevertheless, the main shortcoming of the super capacitor is its limited energy density (Jampani *et al.*, 2010). Attaining high energy density performance is a criterion for large scale commercial applications, which drives focuses towards the engineering of the electrode materials, usage of non-aqueous electrolytes with wider electrochemical stability, and the electrodes configuration of a super capacitor such as the asymmetrical super capacitor (Nithya and Sabari, 2016).

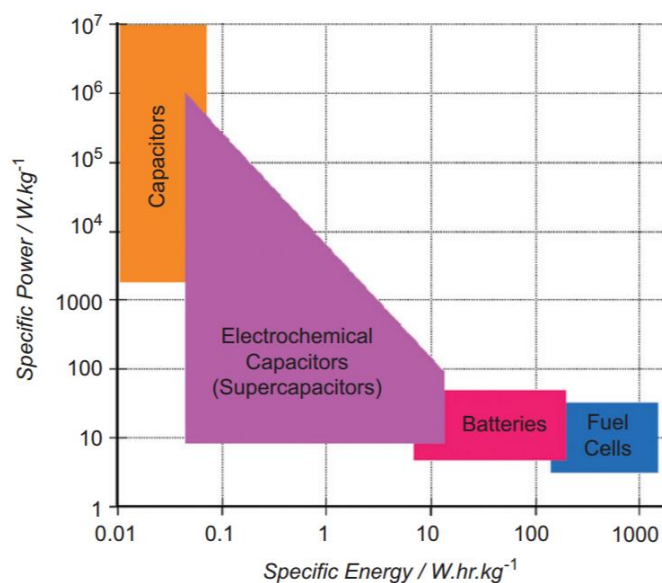


Figure 2.3 Ragone plot of various electrochemical devices. Adapted from (Hall and Bain, 2008)

The paradigm shift for energy sustainability advancement is further achieved through the idea of integrating an energy conversion and storage device, taking the advantageous of fully utilizing solar energy for chemical reaction initiation, while storing the energy in an energy storage device to minimize power loss. This section reviews the potential active materials of a super capacitor and perovskite solar cell towards the coupling of a photo-super capacitor.

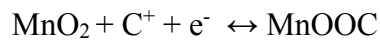
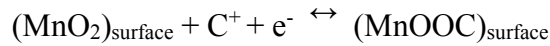
2.2 Supercapacitive Materials

2.2.1 Types of Pseudocapacitive/Active Electrode Materials

A super capacitor has conventionally been composed of carbon-based materials such as activated carbon, single-walled carbon nanotubes (SWCNT), and multi-walled carbon nanotubes (MWCNT) (Chen *et al.*, 2014). Contrary, pseudocapacitive materials such as transition metal oxides and conducting polymers are alternative ways to enhance the specific capacitance of an energy storage system upon their addition by storing an ample capacitance per gram as opposed to EDLC (Ng *et al.*, 2014; Snook *et al.*, 2011). The high specific capacitance and energy density attainability of transition metal oxides such as RuO₂, MnO₂, Co₃O₄, and NiO embedded on a current collector can promote efficient redox reactions due to their ability to exist in various oxidation states (Cai *et al.*, 2014). Theoretically, RuO₂-based materials could reach a specific capacitance in the range of 1300-2200 F/g (Meher *et al.*, 2010). RuO₂ seems to be one of the best options for electrode owing to its high operating stability and has showed a specific capacitance of 1380 F/g (Fang *et al.*, 2007). In addition, the highest specific value reported for an experimental capacitance was 1580 F/g in an acidic electrolyte (Meher *et al.*, 2010). However, its 1 V potential window and high production cost for RuO₂ restrict its application diversity to smaller electronic devices. This has prompted the use of alternative approaches such as the employment of cost-effective metal oxides, conducting polymers, or composite materials as electrode active materials (Fang *et al.*, 2007).

MnO₂ has been widely used in many energy storage systems owing to its low production cost, environmental friendliness, and high specific capacitance (Chen *et al.*, 2010). The availability of MnO₂ for use in various polymorphs in the forms of α -, β -, γ -, and δ - indeed has further widened its application versatility as a catalyst and superior electrode material in Li/MnO₂ and Zn/MnO₂ batteries (Cheng *et al.*, 2011). The proposed faradaic reaction mechanism for MnO₂

involves the process of electrolyte cations such as $C^+ = H^+, Li^+, Na^+, \text{ and } K^+$ adhering to the MnO_2 surface, and subsequently producing various oxidation states (III or IV) of MnO_2 (Wei *et al.*, 2011). The occurrence of a faradaic reaction in the whole system arises from the infusion and de-fusion of electrolyte cations within the MnO_2 matrix. The proposed mechanism is manifested as shown below (Lim *et al.*, 2014; Wei *et al.*, 2011):



Nevertheless, due to MnO_2 possesses poor flexibility and electrochemical performance as a result of its low conductivity of 10^{-6} to 10^{-5} S/cm, it is infrequent to prepare a singly coated pseudo-active material film electrode such as MnO_2 as the only active material electrode (Chen *et al.*, 2013). Evidently, an α - MnO_2 nanorod super capacitor electrode was developed, which delivered a capacitance of 166.2 F/g (Li *et al.*, 2011). Therefore, efforts to composite potential transition metals to MnO_2 or conducting materials have been underway to increase the capacitance, while simultaneously enhancing the storage efficiency and stability of the super capacitor, and subsequently brought forth to an efficient power output delivery system for a photo-super capacitor upon integration with an energy conversion device.

A hybrid polypyrrole/manganese oxide (PPy/ MnO_2) nanocomposite film measured via three-electrode system has achieved a high specific capacitance of 620 F/g owing to the larger surface active area provided by the PPy, while the MnO_2 provided excellent rigidity, which prevented the structure from collapsing (Sharma *et al.*, 2008). The test fixture configuration of a two-electrode system (with only two terminals), which closely mimics the marketed energy storage device, is regarded as more convincing and compatible with real-life applications, as opposed to a three-electrode configuration (Stoller and Ruoff, 2010). The super capacitors such as a polypyrrole/manganese dioxide/polypropylene fibrous film super capacitor and

graphene/MnO₂//activated carbon nanofiber asymmetrical super capacitor measured through two-electrode system have shown the excellent electrochemical stability of a composite super capacitor, with capacitive retention values of 94% over 1500 cycles and 97.3% after 1000 cycles, respectively (Fan *et al.*, 2011; Jin *et al.*, 2011). These works presented high specific capacitances of 110 F/g and 113.5 F/g at a scan rate of 1 mV/s, respectively. Subsequently, a Co₃O₄@MnO₂ nanocomposite was reported with a specific capacitance of 480 F/g (0.7 F/cm²) at 2.67 A/g, along with a cyclic retention of 97.3% after 5000 cycles (Wang *et al.*, 2015). In addition, coupling MnO₂ and Bi₂O₃ exhibited specific capacitance of 312.8 F/g at current density of 0.2 A/g and excellent stability performance where the Bi₂O₃@MnO₂ super capacitor retained 112% of its original capacitance after 1000 long-term cyclic system. The remarkable cycling performance could be attributed to the unique mesoporous structures of the nanocomposite, thereby enhance the contact of electrodes and electrolyte (Ma *et al.*, 2015). Theoretically, Bi₂O₃ has a long durability cyclic performance, depending on its polymorphic form. Bi₂O₃ can exist in five polymorphs, where low-temperature α -Bi₂O₃ (monoclinic) and high-temperature δ -Bi₂O₃ (cubic) are highly stable (Latha *et al.*, 2010). Because of its direct band gap and photoluminescence properties, Bi₂O₃ has been widely applied in gas sensors and solid oxide fuel cells, and has been used as a photocatalyst for water splitting and pollutant decomposing.

ZnO (3.37 eV) is a photo-active material with wide band gap, which can be integrated with other potential active materials as a supercapacitive electrode because it possesses high chemical and thermal stabilities, in addition to exhibiting an excellent electrical conductivity (Cai *et al.*, 2014). ZnO possesses an energy density as high as 650 A/g. Therefore, it is used as an active material for a battery (Wang *et al.*, 2011). In 2014, a binder-free super capacitor composed of ZnO@Co₃O₄ core/shell heterostructures exhibited high specific capacitance of

857.7 F/g at current density of 2 mA/cm² and the ZnO/Co₃O₄ core/shell heterostructures super capacitor retained 63.4% of its initial capacitance, indicative of good rate capability (Cai *et al.*, 2014). A recent two-electrode configuration study reported in 2015 proved the workability and suitability of using ZnO as an active electrode material for a super capacitor. A state-of-the-art device composed of electro-deposited PPy/GO/ZnO on Ni foam as the current collectors and PVA/KOH hydrogel as an electrolyte and a separator, as depicted in Figure 2.4 exhibits a specific capacitance of 123.8 F/g at current density of 1 A/g, implying that the synergism and compatibility of each active component brought forth the catalytic-activity enhancement. A pseudo-triangular galvanostatic charge/discharge profile (blue triangular plot) for the ZnO-based super capacitor is shown in Figure 2.5a. The discharge time taken by the ternary nanocomposite cell is the longest, as opposed to binary and singly coated electrode materials, which is indicative of an almost ideal capacitive behavior. Additionally, the incorporation of ZnO prevents the π -restacking phenomenon of GO due to the strong Van der Waals attraction. Figure 2.5b shows the decreasing trend of specific capacitance, which is due to an insufficient response time for the intercalation and de-intercalation of electrolyte ions to the active surface. In a nutshell, it was proven that the performances of the fabricated flexible ZnO-based state-of-the-art device, such as its reversibility and storage capacity, were still present, regardless of its curvature. In addition, the lighting of an LED verified the concept of the energy storage device even though it was bent at 90°C (Chee *et al.*, 2015).

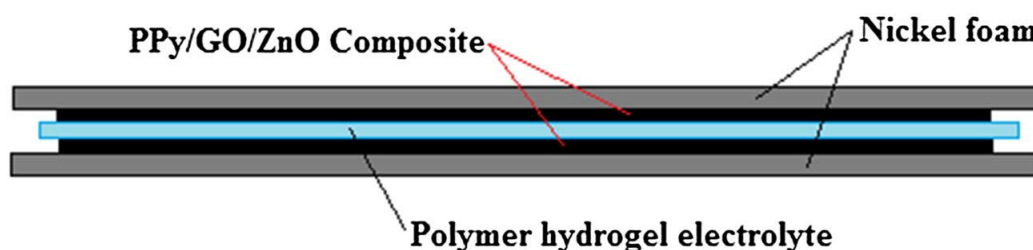


Figure 2.4 A two-electrode configuration of the PPy/GO/ZnO super capacitor. Polypyrrole is denoted as PPy, graphene oxide as GO, and zinc oxide as ZnO. Adapted from (Chee *et al.*, 2015).

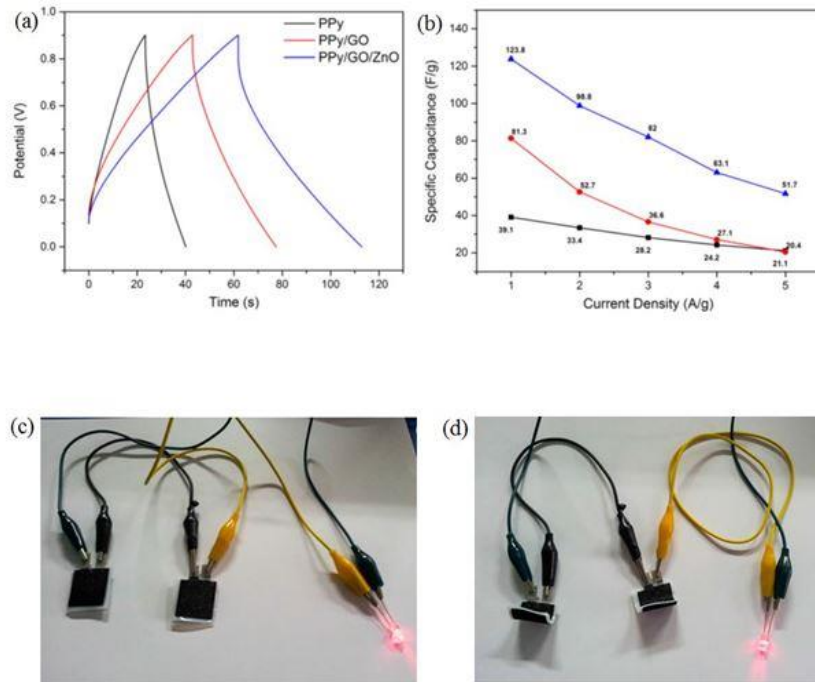


Figure 2.5 (a) Galvanostatic charge/discharge cycles of PPy, PPy/GO, and PPy/GO/ZnO at a current density of 1 A/g. (b) Specific capacitance of PPy, PPy/GO, and PPy/GO/ZnO at various current densities. (c) Prepared super capacitor connected in series lighting up an LED circuit, and (d) super capacitor bent at 90° lighting up an LED circuit. Polypyrrole is denoted as PPy, graphene oxide as GO, and zinc oxide as ZnO. Adapted from (Chee *et al.*, 2015).

In addition to the discussion on commonly used transition metals, some other works on nickel- and cobalt-based electrode materials were explored and investigated. The utilization of nickel oxide (NiO) as an active material for an asymmetrical super capacitor composed of MWCNT-NiO/H₂SO₄/MWCNT presented a specific capacitance of 925.9 mF/cm² or 53.9 F/g (Adekunle *et al.*, 2011). Moreover, an 80.3% Co₃O₄-19.7% rGO/activated carbon asymmetrical super capacitor with a wide potential window of 1.5 V has been reported to have a specific capacitance of 114.1 F/g. It performed under a current density of 0.375 A/g and retained 95% of its specific capacitance over 1000 cycles (Xie *et al.*, 2013). Table 2.1 summarizes the potential active materials used for super capacitor applications reported in literature.

Table 2.1 Potential active materials applied for super capacitor applications.

Active materials	Electrolyte	Capacitance	Comments	Ref.
Bi ₂ O ₃ /Cu	1M NaOH	22 mF/cm ² at 20 mV/s (3-electrode system)	Measured at room temperature.	(Gujar <i>et al.</i> , 2006)
PPy/MnO ₂	0.5M Na ₂ SO ₄	620 F/g at 50 mV/s (3-electrode system)	Measured at room temperature.	(Sharma <i>et al.</i> , 2008)
MnO ₂	0.1M Na ₂ SO ₄	166.2 F/g at 0.2 A/g (3-electrode system)	Measured at room temperature.	(Li <i>et al.</i> , 2011)
MnO ₂ @CNF	0.5M Na ₂ SO ₄	546 F/g at 1 A/g (3-electrode system)	Exhibited good cycling stability (95.3%) at 25°C; diminishing at 75°C (82.4%) after 1000 cycles.	(Wang <i>et al.</i> , 2013)
T-NT/Bi ₂ O ₃	1M NaOH	340 mF at 3 mA/cm ² (3-electrode system)	75% capacitance retained at room temperature after 500 cycles.	(Sarma <i>et al.</i> , 2013)
ZnO@Co ₃ O ₄	2M KOH	857.7 F/g at 2 mA/cm ² (3-electrode system)	63.4% capacitance retained.	(Cai <i>et al.</i> , 2014)
Co ₃ O ₄ @MnO ₂	1M LiOH	480 F/g at 2.65 A/g (3-electrode system)	Cyclic retention of 97.3% after 5000 cycles.	(Wang <i>et al.</i> , 2015)
Bi ₂ O ₃ @MnO ₂	1M Na ₂ SO ₄	312.8 F/g at 0.2 A/g (3-electrode system)	112% capacitance retained after 1000 stability cycles.	(Ma <i>et al.</i> , 2015)
Graphene/MnO ₂ // Activated carbon	1M Na ₂ SO ₄	113.5 F/g at 1 mV/s (2- electrode system)	Retained 97.3% of capacitance after 1000 cycles.	(Fan <i>et al.</i> , 2011)
Co ₃ O ₄ /rGO//Activated carbon	6M KOH	114.1 F/g at 0.375 A/g (2-electrode system)	95% capacitance retained after 1000 cycles.	(Xie <i>et al.</i> , 2013)
PPy/GO/ZnO	PVA/KOH Hydrogel	123.8 F/g at 1A/g (2- electrode system)	Measured at room temperature and able to light up an LED circuit.	(Chee <i>et al.</i> , 2015)

2.2.2 Conducting Polymers

In addition, conducting polymers render good intrinsic conductivity through the conjugated system along the polymer backbone. Thus, the incorporation of conducting polymers such as polypyrrole (PPy), polyaniline (PANI), and PEDOT are able to improve the performances of the super capacitor by increasing the energy storage capability in bulk materials while minimizing self-discharge. Considerable attention has been allocated on conducting polymers because of their fast charging/discharging and doping/de-doping process, cost effectiveness compared to certain expensive metal oxides, and high charge density. The conductivities of various conducting polymers are listed in Table 2.2.

Table 2.2 Typical conductivities of various conducting polymers. Adapted from (Snook *et al.*, 2011).

Polymer	Conductivity (S/m)
Polyaniline	0.1-5
Polypyrrole	10-50
PEDOT	300-500
Polythiophene	300-400

Table 2.2 shows that PEDOT had the best conductivity performance, in the range of 300–500 S/cm. A comparison between poly(3,4-ethylenedioxythiophene), PEDOT-based and poly(3,3-diethyl-3,4-dihydro-2H-thieno-[3,4-b][1,4]dioxepine), PProDOT-Et₂-based super capacitor electrode materials was made to study the superior electrochemical performances of both photo-super capacitors. CV and EIS were employed, and the distorted voltammograms of both active materials at a scan rate of 2 mV/s, as depicted in Figure 2.6, reflect the effect of induced ohmic resistance during electron transfer and ionic movement within the polymer film. Adversely, a more obvious distorted PProDOT-Et₂ voltammogram at a scan rate of 2 mV/s can be ascribed to the ohmic resistance or film thickness, which gives rise to C_E (specific

capacitance per unit electrode active area) values for PEDOT and PProDOT-Et₂ of approximately 5.24 and 6.52 F/cm², respectively, which infer that PProDOT-Et₂ has more electroactive materials on the electrode. In contrast, as seen in the EIS plot, the complex plane plots deviated from a vertical line at a higher frequency, namely the knee frequency, suggesting the occurrence of a faster charge/discharge for the film. Obviously, the PEDOT with a knee frequency of 0.07 Hz, which is greater than that of PProDOT-Et₂, has a larger k_s , and thus induces a faster charge/discharge rate than PProDOT-Et₂. Therefore, the PEDOT-based device presented a weaker or resistance-free environment that prompted a faster charge transfer rate (Hsu *et al.*, 2010). Thus, the above discussion has further proven the necessity and versatility of using pseudocapacitive materials for a super capacitor electrode in an effort to improve the electrochemical performances of a super capacitor.

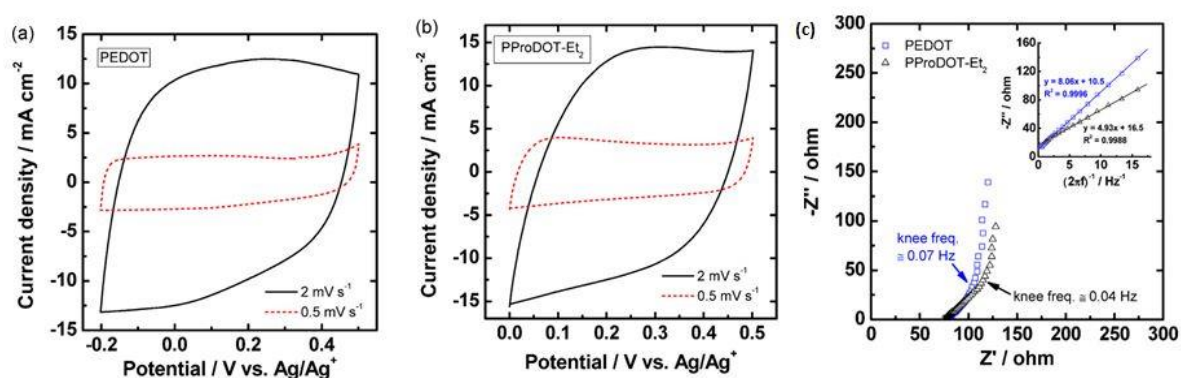


Figure 2.6 Cyclic voltammograms of (a) PEDOT and (b) PProDOT-Et₂ thick films (60C/cm²) on Pt disc (0.1cm diameter) in 0.5M LiClO₄/MPN solution at the scan rate of 2 and 0.5mV/s. (c) Complex plane impedance plots of PEDOT and PProDOT-Et₂ thick films (60C/cm²) on Pt disc (0.1cm diameter) measured at 0.4V vs. Ag/Ag⁺ in 0.5M LiClO₄/MPN solution. Inset: the corresponding linear relations between Z'' and $1/(2\pi f)$ for the two films. Adapted from (Hsu *et al.*, 2010).

2.2.3 Types of Carbon-Based Materials

Carbon-based materials such as CNT and graphene-based materials have been widely employed as active materials because they have larger surface areas, high chemical stability, and exhibit excellent mechanical, electrical, and electrochemical properties (Chen and Dai,

2014; Wang *et al.*, 2012). Graphene is a monolayer sp^2 carbon bonded in a hexagonal sheet that renders superior mechanical and electrochemical properties (Cong *et al.*, 2013; Ray *et al.*, 2011), along with high flexibility and a wide potential window (He *et al.*, 2012). Graphene possesses a large surface area with a theoretical serving surface area of $2630 \text{ m}^2/\text{g}$ (Brownson and Banks, 2010; Zhu *et al.*, 2011), which is larger than that of graphite ($\sim 10 \text{ m}^2/\text{g}$) and double that of CNT ($1315 \text{ m}^2/\text{g}$). Its excellent conductivity with $\sim 64 \text{ mS}/\text{cm}$, which is about 60 times better than SWCNT, favors the inclusion of graphene in energy storage applications as an EDLC contribution (Brownson and Banks, 2010). In addition, activated carbon has a large surface area, where the reported surface area reaches $3000 \text{ m}^2/\text{g}$, as well as good electrical properties. Though activated carbon possesses a surface area of up to $3000 \text{ m}^2/\text{g}$, it only has a small capacitance of $<10 \text{ }\mu\text{F}/\text{cm}^2$, which is comparable to the theoretical EDL capacitance ($15\text{--}25 \text{ }\mu\text{F}/\text{cm}^2$). Therefore, the pore size distribution, shape, and structure, as well as the electrical conductivity and surface functionality, are important aspects to be taken into account to enhance the electrochemical performances. Generally, the additional pseudo-capacitance is also dependent on the surface functionalities, where the capacitance enhancement arises from the wettability of the carbon surface by the electrolyte ions, which increases the affinity and preference of activated carbon in the super capacitor fabrication (Zhang and Zhao, 2009). A combination of an asymmetrical super capacitor using activated carbon and $\text{Ni}(\text{Co})\text{O}_x$ as working electrodes and a DSSC had the capacitive behavior of a pure double layer when analyzed using CV under a potential window in an alkaline medium ranging from -1.0 to 0.2 V (vs. SCE), as illustrated in Figure 2.7. It presented a nearly rectangular CV voltammogram in the negative potential region, indicative of the EDL capacitive behavior of activated carbon when employed as a super capacitor (Bagheri *et al.*, 2014).

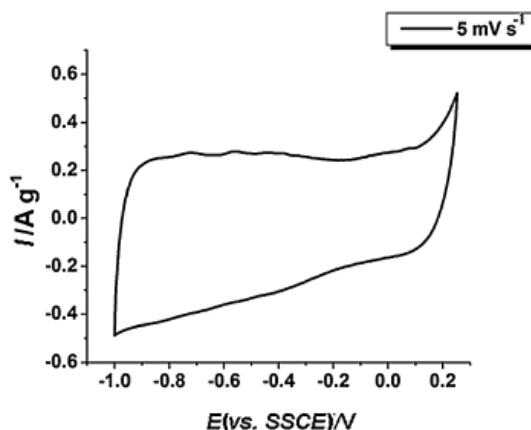


Figure 2.7 Cyclic voltammetric characteristics of activated carbon recorded in three-electrode cell at 5 mV/s. Adapted from (Bagheri *et al.*, 2014).

The success lighting of an LED using a PPy/GO/MnO_x flexible super capacitor reported in 2015 reflects the workability of hybrid electrode active materials as a capacitance contribution that is sufficient for LED illumination (Ng *et al.*, 2014). In a nutshell, carbon-based materials have the properties of a longer life cycle, stability, and high power density, yet still possess a smaller double-layer capacitance. In contrast, transition metal oxides and conducting polymers recorded greater capacitance values per gram with rapid reversible redox kinetics but poor cycling endurance and stability. Hence, compositing EDLC and pseudo-capacitive materials has been proven to work best as complementary materials in surging and enhancing the capacitive performance of electrode materials (Wang *et al.*, 2011).

2.3 Evolution of Third Generation Solar Cell

The continuous supply of solar energy from the sun is estimated to be 3×10^{24} J/year, which is 10^4 times more than the consumption rate of mankind (Gong *et al.*, 2012). This has impelled the development of PV devices, typically solar cells, as prime energy production devices, in conjunction with the depletion of fossil fuels and mineral energy sources (Zhang and Cao, 2011). An arms-race evolution and development of solar cells (Figure 2.8) has arisen from the first generation of conventional single silicon solar cells to the second generation of

semiconductor thin film-based solar cells ascribed to the employment of a thinner film as the working electrode compared to the first generation PV. Now, a third generation PV is emerging, namely molecular absorber solar cells, which comprise polymer solar cells, DSSCs, quantum dot solar cells, and the recently developed perovskite solar cells. A DSSC is a photo-electrochemical device in which sensitizers generate electrons upon light absorption between a dye-adhered metal oxide surface compartment and hole-conducting electrolyte (Fakharuddin *et al.*, 2014). The third generation of solar cells are said to be compatible with any flexible substrates, with lower material and manufacturing costs, even though the first and second solar cells have attained conversion efficiencies of ~15%–25%, as reported in 2010 (Fakharuddin *et al.*, 2014; Saga, 2010). The emerging trend of using third-generation solar cells over well-established first- and second-generation solar cells is ascribed to properties such as the best performance under low-light or indoor conditions, transparency, cost effectiveness, and easy integration in buildings as solar windows (Fakharuddin *et al.*, 2014). A DSSC was first constructed by Oregan and Grätzel in 1991, with a photoelectric energy conversion rate of 7.1% and incident photon-to-electrical current conversion efficiency (IPCE) of ~80% (O'regan and Grätzel, 1991). The advantages of a DSSC over a silicon solar cell are better stability, higher efficiency, low production cost, and easy fabrication (Bessho *et al.*, 2010; Freitas *et al.*, 2008; Gong *et al.*, 2012).

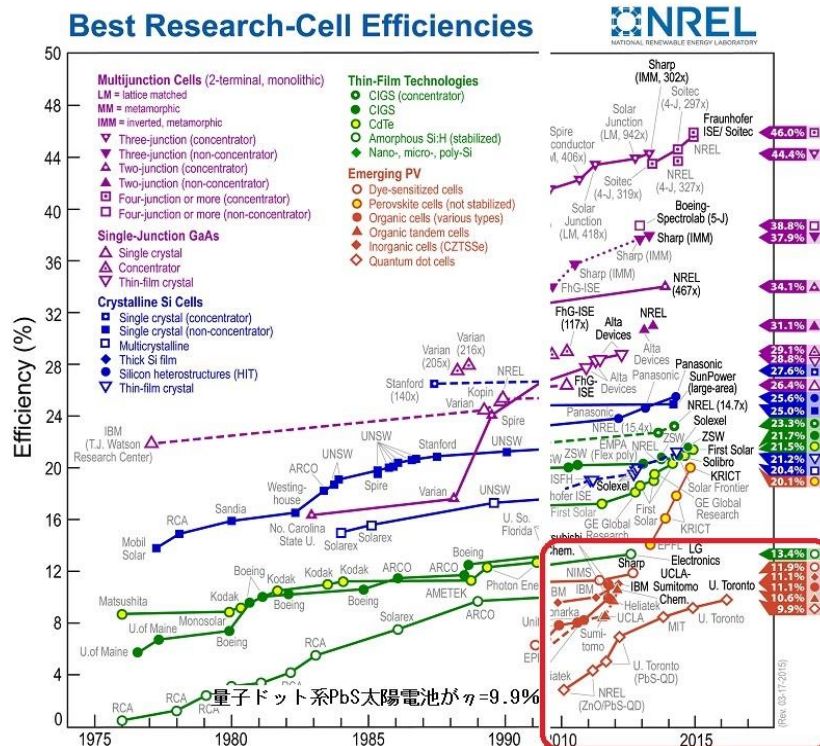


Figure 2.8 Progression of photovoltaic devices. Adapted from <https://phys.org/news/2016-02-solar-cell-efficiency-nrel.html>.

In 2011, another improvement leap occurred for a DSSC, with an improvement in its efficiency up to 11% or 12.3% for certain prototypes (Skunik-Nuckowska *et al.*, 2013) relative to the 7.1% conversion rate of the first DSSC (O'regan and Grätzel, 1991). An improved efficiency DSSC composed of co-sensitizers of donor- π -bridge-acceptor zinc porphyrin dye (YD2-o-C8) and donor- π -bridge-acceptor (D- π -A) with Co^(II/III)tris(bipyridyl)-based redox electrolyte had an efficiency of 12.3% due to its light absorbing ability over the whole visible range, in addition to the presence of long alkoxy group chains, which retarded the electron recombination process (Yella *et al.*, 2011). The most common DSSC prototype was composed of ruthenium (Ru)-based dye adhering to anatase (TiO₂) films with iodide/triiodide (I⁻/I₃⁻) couple liquid, semi-liquid, or redox conducting electrolytes (Skunik-Nuckowska *et al.*, 2013). Its high conversion efficiency could be attributed to the large surface active area of porous titania film, which increases the amount of dye adsorption (Xiao *et al.*, 2010). The application of perovskite light harvester in DSSC provided an efficiency of 3.8% (Kojima *et al.*, 2009) owing to its high

solubility of the ionic crystal of organolead halide perovskite in a polar solvent. Relentless efforts to improve the PCE and stability of the perovskite solar cell were done till an astonishing efficiency up to 20.1% (certified by NREL) was achieved. The further PCE leap for perovskite solar cell is envisaged to be on-par against the Si solar cell in the next decades. Herein, the compatibility of the light harvesting active materials for a high performing perovskite solar cell is tremendously important and is included in the coming discussion.

2.4 Potential Light Responsive Materials for Perovskite Solar Cell

2.4.1 Working Principle of Perovskite Solar Cell

The working principle of a perovskite solar cell is its ability to mimic a DSSC. The distinctively distinguishable feature of both a perovskite solar cell and DSSC is the use of the perovskite material as a sensitizer such as $\text{CH}_3\text{NH}_3\text{PbI}_3$ or MAPbI_3 instead of a liquid-based Ru dye sensitizer, in addition to the bi-functional perovskite harvester, which can function as a light harvester and hole transporting material (Dualet *et al.*, 2014; Gonzalez-Pedro *et al.*, 2014). Upon light absorption, the segregated electrons and hole carriers are injected into the respective electron transporting layer (ETL) and hole transporting material (HTM), typically the mesoporous TiO_2 layer and *Spiro*-OMeTAD from the perovskite material, and subsequently transported externally to the counter electrode to complete the circuit (Zhou *et al.*, 2014). Interestingly, Al_2O_3 -based cells have a unique electron transporting system, where the electrons will remain in the perovskite phase and are collected at the planar TiO_2 -coated FTO electrode, where they are subsequently transported throughout the film thickness in the perovskite, as depicted in Figure 2.9 (Lee *et al.*, 2012; Snaith, 2013). Notably, the segregation of the carriers can only occur in accordance with the suitability of the energy level. Based on the energy band gap diagram shown in Figure 2.10, the $\text{CH}_3\text{NH}_3\text{PbI}_3$ perovskite material has conduction band minimum (CB) and valence band maximum (VB) values of -5.43 eV and -3.93 eV, respectively,

demonstrating the suitability of using the perovskite and hole transporting material for carrier conduction, where VB is suitable for hole separation and CB is suitable for electron separation (Park, 2015a). The anodic work function of an appropriate HTM could be adjusted to form a respective selective contact, to perform as a contact material with a light absorbing layer (Frohne *et al.*, 2002; Yan *et al.*, 2015). The energy band gap diagram depicted in Figure 2.10 shows that the homo level of *Spiro*-OMeTAD is higher than the VB of $\text{CH}_3\text{NH}_3\text{PbI}_3$, whereas the CB of TiO_2 is lower than the CB of $\text{CH}_3\text{NH}_3\text{PbI}_3$, which enables the transportation of electrons and hole carriers into their respective transporting levels. In brief, the generation of free charges could be induced in two ways, as follows (Marchioro *et al.*, 2014; Wang *et al.*, 2014):

- Splitting of bound electron and hole pairs by thermal energy,
- Separation of free charges from the bound electron/hole pairs at the TiO_2 -perovskite interface and perovskite-HTM interface.

The properties of each light harvesting materials, electron, and hole transporting materials will be discussed in the next sections.

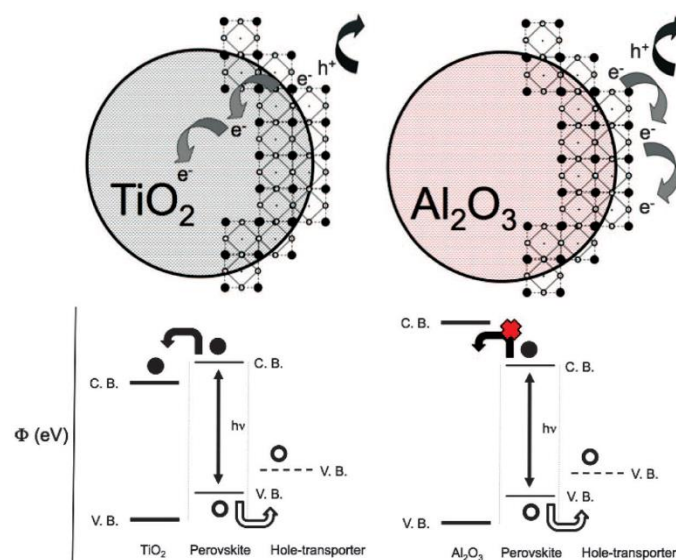


Figure 2.9 Schematic of perovskite-coated TiO_2 and Al_2O_3 , illustrating electron and hole transfer. Adapted from ref. (Snaith, 2013).

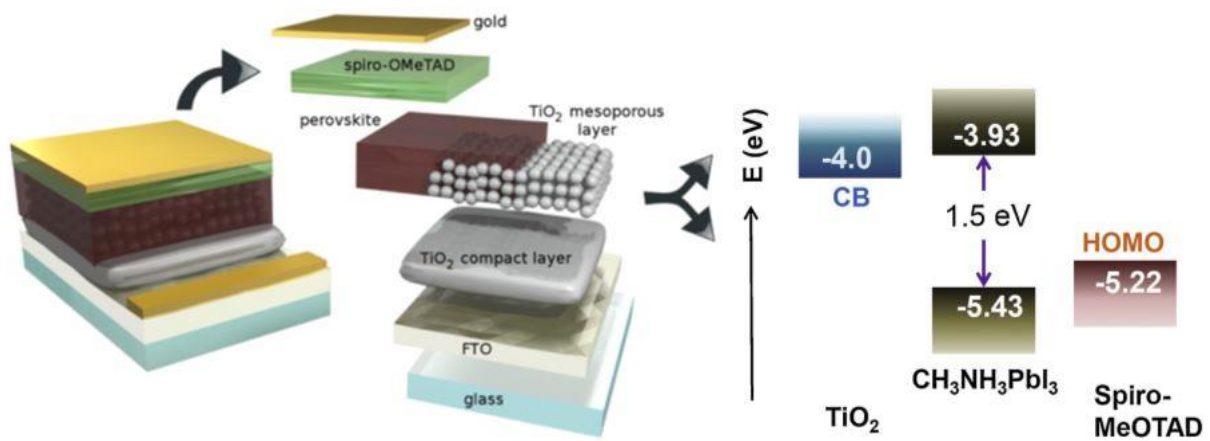


Figure 2.10 Schematic diagram and energy band gap diagram of architecture perovskite solar cell. Adapted from ref. (Juarez-Perez *et al.*, 2014) and (Park, 2015a).

2.4.2 Electron Transporting Material (ETM)

The conventional organic-inorganic lead halide perovskite solar cell is typically composed of compact TiO₂ and mesoporous TiO₂ or Al₂O₃ as the electron transporting layers. The compact TiO₂ acts as a blocking layer to suppress charge recombination at the interface by preventing direct electrical contact between the transparent conductive oxide (TCO) and hole transporting material (Sun *et al.*, 2015). The common mesoporous underlying could be TiO₂ or Al₂O₃. A bulk heterojunction perovskite solar cell with n-type transparent mesoporous-TiO₂ and *Spiro*-OMeTAD as the p-type hole conductor thus exhibited a PCE of nearly 8%. Surprisingly, replacing the insulating Al₂O₃ over the titania as the mesoporous layer could further improve the PCE of the device. This was ascribed to the insulating property of Al₂O₃, with a wide band gap of about 7 to 9 eV, which could act as a scaffold upon perovskite deposition. The alumina meso-superstructured perovskite solar cell had a higher PCE of 10.9% under simulated AM 1.5 full solar illumination compared to a titania meso-superstructured perovskite solar cell (Lee *et al.*, 2012). This phenomenon was most likely due to the electronically inert alumina scaffold for the several nanometer thick perovskite layer, where photogenerated electrons flowed to the front electrode via the perovskite absorber, bypassing the nanoporous oxide layer, while the

holes were collected in the HTM and subsequently transferred to the back electrode (Edri *et al.*, 2013).

2.4.3 Light-Harvesting Materials

Photovoltaic studies by using various types of light harvesting materials, either organic, inorganic or mixture of both materials have been reported such as the $\text{CH}_3\text{NH}_3\text{PbI}_3$, FAPbX_3 , and CsPbX_3 . Although these pure perovskite compounds are highly suitable for photovoltaic applications, however, each perovskite material inherited its disadvantages. The boons and banes of the perovskite materials are listed in Table 2.3. Taking a common example, the CH_3NH_3^+ organic cation is responsible for structural stability of the perovskite structure, while the metal and halide hybridized orbitals are responsible for its electronic properties (Almora *et al.*, 2015). The methylammonium based nanocrystals, $\text{CH}_3\text{NH}_3\text{PbI}_3$ ($X=\text{Cl, Br, I}$) have recorded photoluminescence quantum yield (PLQY) up to 70% with narrow size distributions, and wide color spectrum, depending on the halide composition of the nanocrystals. The halides perovskites are of high ionic conductivities ascribed to anion migration (Akkerman *et al.*, 2015). The ambipolar perovskite material behaves as a p-type material in depleted hole conductor-free heterojunction solar cells and an n-type light harvesting and charge transporting materials (Roiati *et al.*, 2014). Despite the PCE of perovskite solar cell has achieved high efficiency of 22.1% within few years, however, its long-term stability performance of the perovskite solar cell is still left behind (Tu *et al.*, 2017). Engineering mixed halide perovskite materials and replacing an organic methylammonium cation to an inorganic cesium cation, for instance, $\text{CH}_3\text{NH}_3\text{PbI}_{3-x}\text{Cl}_x$, $\text{CH}_3\text{NH}_3\text{PbI}_{3-x}\text{Br}_x$, and CsPbI_2Br are not merely improving the PCE, but also to enhance the stability of the perovskite, to improve its carrier transport, and to tune the band gap of the perovskite materials by adjusting the iodide/bromide ratio.

Table 2.3 The advantages and disadvantages of perovskite materials employed in most reported works.

Perovskite materials	Advantages	Disadvantages	Ref
CH ₃ NH ₃ PbI ₃	* High carrier mobility ranges from 7.5 cm ² /Vs for electrons to 12.5 cm ² /Vs – 66 cm ² /Vs for holes.	* Structural phase transition at 55 °C. * Moisture sensitive. * Light induced trap-state formation.	(Grätzel, 2014; Saliba <i>et al.</i> , 2016)
FAPbI ₃	* Narrower band gap which is closer to the single-junction optimum.	* Lacks structural stability at room temperature. * Sensitive to solvents and humidity.	(Saliba <i>et al.</i> , 2016)
CsPbI ₃	* Exhibited excellent thermal stability with suitable band gap of 1.73 eV.	* High temperature operation where photoactive perovskite phase is only stable above 300 °C. * Crystallizes in a photo-inactive phase at room temperature.	(Saliba <i>et al.</i> , 2016)

Alloyed halides are tailored to produce astonishing photovoltaic performances such as a high V_{oc} by increasing the energy band gap of the hybridized halides, subsequently improving the PCE of the solar cell. Generally, a higher V_{oc} is obtainable in conjunction with a lower electron recombination rate. A high V_{oc} value of up to 1.3 V could be achieved upon the inclusion of Br (Kulbak *et al.*, 2015). Figure 2.11a illustrates a comparison of the photovoltaic performances between alloyed halide and single halide-based solar cells, where the alloyed halide solar cell possesses better photovoltaic performance than a single halide solar cell with a high J_{sc} of 17.9 mA/cm², V_{oc} of 0.97 V, and FF of 0.70. Figure 2.11b depicts the diffusion lengths of CH₃NH₃PbI_{3-x}Cl_x and CH₃NH₃PbI₃ to further investigate the performance of the alloyed halide perovskite material, where the longer diffusion length of mixed halides (CH₃NH₃PbI_{3-x}Cl_x), which is greater than 1 μ m for both electrons and holes, indicates a longer recombination lifetime (slower recombination rate). This enhances the efficiency of the mixed halide planar heterojunction solar cell by giving an efficiency of 12.2%, as shown in Figure 2.11, as opposed

to lead triiodides, which only have an efficiency of 4.2% (Stranks *et al.*, 2013). Hence, it emphasizes the effectiveness of engineered alloyed halides in improving the performances of a perovskite solar cell. Another study on a mixed halide perovskite solar cell based on I⁻/Cl⁻ was reported in 2014, and showed the enhanced efficiency of the alloyed perovskite solar cell relative to a non-alloyed perovskite solar cell. Figure 2.12a depicts the solar cell configuration of the CH₃NH₃PbI_{3-x}Cl_x thin film (TF) on the left and CH₃NH₃PbI₃ nanostructure (NS) on the right. Likewise, the photovoltaic performances of CH₃NH₃PbI_{3-x}Cl_x TF surpassed those of the mono-halide-based perovskite solar cell by rendering a higher V_{oc}, J_{sc}, and an approximately 1.7-fold higher efficiency, as presented in Figure 2.12b. The performance enhancement of the solar cell upon the halide hybridization (CH₃NH₃PbI_{3-x}Cl_x TF) could be further explained in terms of its recombination rate, as shown in Figure 2.13. CH₃NH₃PbI_{3-x}Cl_x TF has a greater recombination resistance, which in turn decreases its recombination rate. Hence, CH₃NH₃PbI_{3-x}Cl_x TF had a longer electron diffusion lifetime compared to a single halide solar cell, in great agreement with Figure 2.11b (Gonzalez-Pedro *et al.*, 2014). In addition, the signs of V_{oc} and J_{sc} were greater for CH₃NH₃PbI_{3-x}Cl_x TF compared to CH₃NH₃PbI₃ NS, thus evidencing the photovoltaic enhancement upon the incorporation of mixed halides. Importantly, the final results for both I⁻/Cl⁻ mixed halide perovskite solar cells could not be compared because of their different fabrication methods and methods for using precursors.

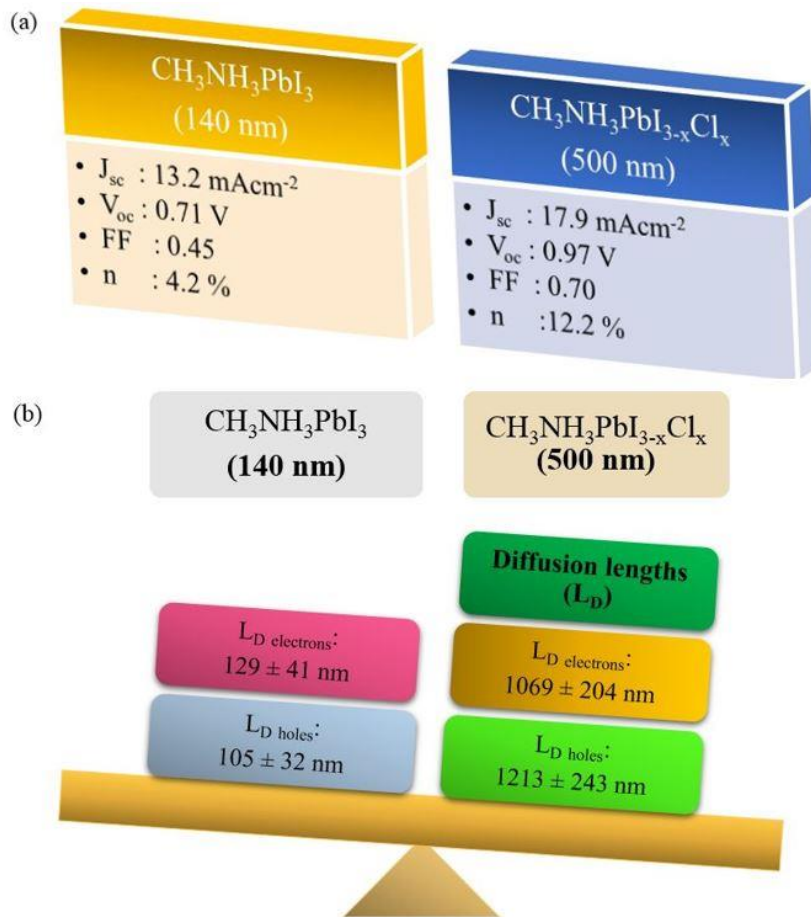


Figure 2.11 (a) Photovoltaic performance of optimized planar heterojunction perovskite solar cells where $CH_3NH_3PbI_{3-x}Cl_x$ (blue box) and $CH_3NH_3PbI_3$ (yellow box) cells were both measured under 100 mW/cm² AM1.5 simulated sunlight. (b) Diffusion lengths (L_D) of optimized planar heterojunction perovskite solar cells where the errors quoted predominantly arise from perovskite film thickness variations, which are ±35 nm for the triiodide perovskite films and ±40 nm for the mixed halide perovskite films. Adapted from ref. (Stranks *et al.*, 2013).

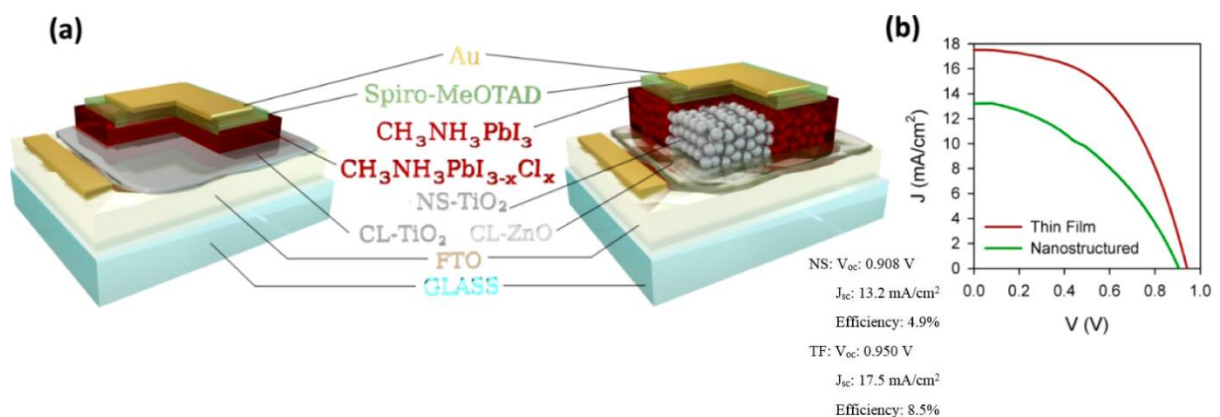


Figure 2.12 Solar cell configuration and performance. (a) Scheme and (b) J–V curves of the two different cell configurations analyzed: Thin film (TF), left, and nanostructured (NS), right. Adapted from ref. (Gonzalez-Pedro *et al.*, 2014).

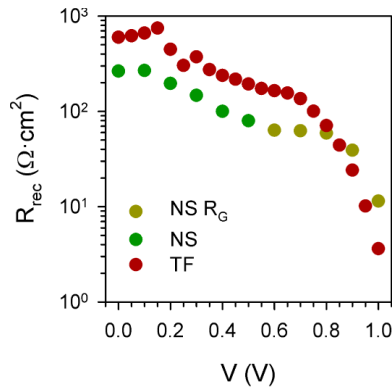


Figure 2.13 Transport and recombination parameters vs voltage: recombination resistance, R_{rec} . Adapted from ref. (Gonzalez-Pedro *et al.*, 2014).

In 2014, there was another attempt to fabricate a mixed halide solar cell through the employment of $\text{CH}_3\text{NH}_3\text{PbI}_2\text{Cl}$ as the perovskite absorber material, and TiO_2 and P3HT as the electron and hole transporting materials, respectively. The photovoltaic performance of $\text{CH}_3\text{NH}_3\text{PbI}_2\text{Cl}$ reached an efficiency of 10.8% (Conings *et al.*, 2014), which was about a 3-fold efficiency increase relative to that of the single $\text{CH}_3\text{NH}_3\text{PbI}_3$ that was reported earlier, which had an efficiency of only 4.2% (Stranks *et al.*, 2013), when the concentration of the precursors was increased to 60 wt%. The ultrahigh J_{sc} value (21.3 mA/cm^2), V_{oc} of 0.932 V, and 0.544 FF thus realized a high efficiency of 10.8% for a bi-halide solar cell. The augmented magnitude absorption of the 60 wt% precursor concentration observed in the UV-Vis spectra shown in Figure 2.14 was also ascribed to the ultra-high J_{sc} (Conings *et al.*, 2014). In 2013, another leap in photovoltaic performance was presented by a vapor deposited $\text{CH}_3\text{NH}_3\text{PbI}_{3-x}\text{Cl}_x$ perovskite solar cell, with J_{sc} , V_{oc} , FF, and efficiency values of 21.5 mA/cm^2 , 1.07 V, 0.68, and 15.4%, respectively (Liu *et al.*, 2013). Comparable to $\text{CH}_3\text{NH}_3\text{PbI}_3$, this device had a stroke PCE of 12.9%, with a slightly lower J_{sc} value of 17.1 mA/cm^2 measured under a light intensity of 95.6 mW/cm^2 . Nevertheless, a slight modification in the $\text{CH}_3\text{NH}_3\text{PbI}_3$ solar cell fabrication by adding a pre-wetting step to reduce the methylammonium iodide concentration led to the growth of larger crystals, which gave rise to a J_{sc} of 20 mA/cm^2 , a V_{oc} of 0.993 V, an FF of

0.73, and a PCE of 15% at a light intensity of 96.4 mW/cm² (Burschka *et al.*, 2013). However, the J_{sc} and V_{oc} values of a single halide solar cell device were still considerably lower than those of the alloyed device.

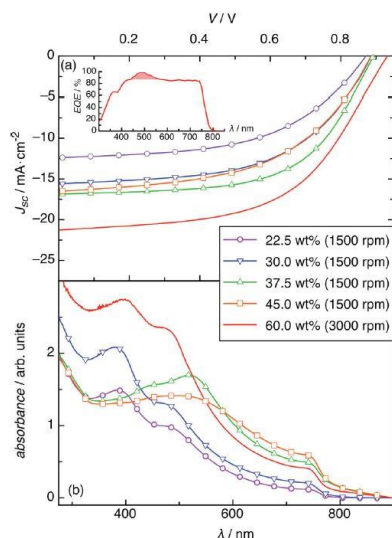


Figure 2.14 (a) J-V curves under AM1.5 illumination of devices made with different concentrations of perovskite precursor. Inset/EQE spectrum of the best device, with the shaded area representing the part of the EQE most likely originating from P3HT. (b) UV-Vis spectra of the perovskite layers used in the devices of (a), deposited on a dense layer of TiO₂. Adapted from ref. (Conings *et al.*, 2014).

When the methylammonium cation is replaced by a cesium cation, a mesoporous titania/CsPbBr₃/*Spiro*-OMeTAD/Au solar cell reported a considerable efficiency of 4.77% with high V_{oc} of 0.96 V. Whereas by substituting the *Spiro*-OMeTAD HTM to PTAA, the mesoporous titania/CsPbBr₃/PTAA/Au solar cell achieved higher PCE of 5.95% with high V_{oc} of 1.28 V. The higher V_{oc} value of PTAA solar cell is ascribed to deeper HOMO level of PTAA than *Spiro*-OMeTAD HTM (Kulbak *et al.*, 2015). It shows that the non-encapsulated CsPbBr₃/PTAA solar cell illustrated smaller and slower decay of 13% loss in photocurrent density after 5 hours illumination period; whereas MAPbBr₃/PTAA device showed strong decay of 55% photocurrent density loss (Kulbak *et al.*, 2016). By engineering a mixed halide perovskite composition, the ambient stability of the device has been significantly improved. It is observable that a black phase CsPbI₃ once exposed to air, the CsPbI₃ film rapidly reverts to

yellow phase, as depicted in Figure 2.15a. Contrary, the CsPbI₂Br is stable under the same conditions with PCE of 9.8%. To further investigate the stability of perovskite materials, XRD profiles of the CsPbI₂Br and MAPbI₂Br before and after heating are depicted in Figure 2.15b and c. It shows that the XRD peaks of CsPbI₂Br (Figure 2.15b) before and after heating remains the same (without presence of additional peaks), indicative of no degradation happen. Whereas, the XRD spectra (Figure 2.15c) of MAPbI₂Br reflected the presence of a new peak (PbI_{2-x}Br_x) near 13° after heating, indicates that MABr and MAI have been removed. In summary, CsPbI₂Br possesses both phase and compositional stability, while MAPbI₂Br is compositionally unstable when heated at 85 °C in 20-25% RH (Sutton *et al.*, 2016). The enhanced PV performances upon alloyed halides is illustrated in Table 2.4.

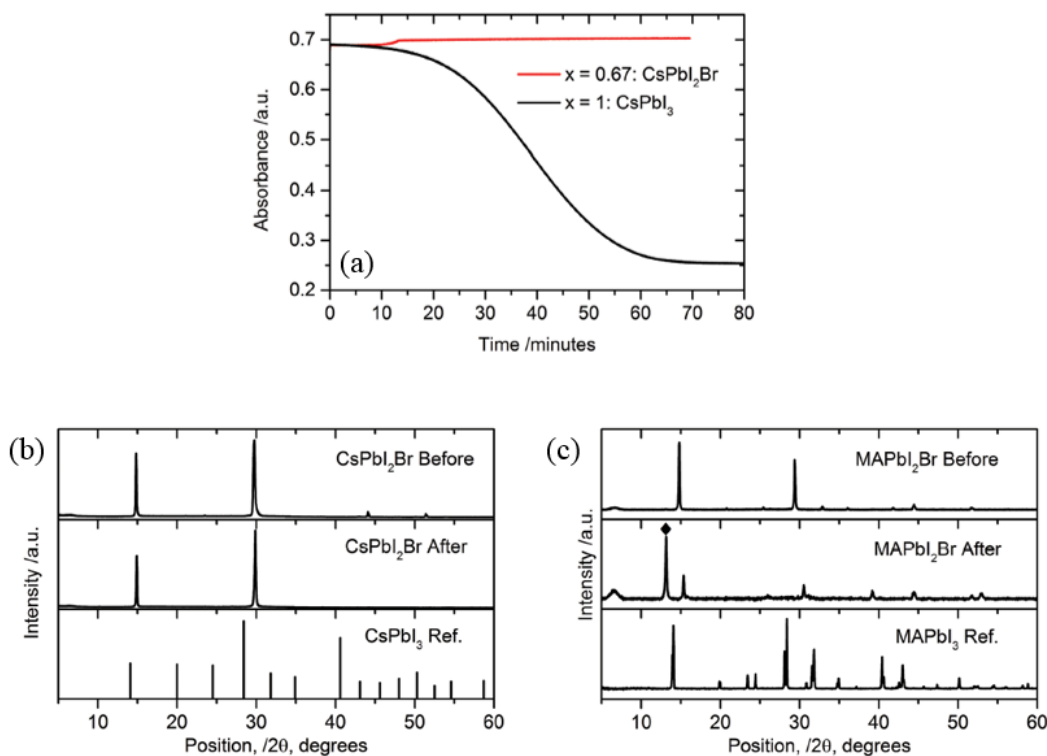


Figure 2.15 (a) Absorbance over time of thin films of CsPbI₃ and CsPbI₂Br, measured at 675 and 625 nm respectively, when exposed to a slow flow of air at 50% RH. The slight increase in the absorbance of the CsPbI₂Br film is not yet fully understood. XRD spectra before and after 270 min of heating at 85 C in 20-25% RH for (b) CsPbI₂Br and (c) MAPbI₂Br. The reference powder pattern for CsPbI₃ (cubic phase) is from Trots and Myagkota; the MAPbI₃ (tetragonal phase) powder pattern is from a crushed single crystal. X-ray absorbance due to the Kapton film is seen below $2\theta = 10^\circ$; the PbI_{2-x}Br_x peak position is indicated by a diamond. Adapted from ref. (Sutton *et al.*, 2016).

Table 2.4 Summary of mono- and alloyed-halide perovskite solar cells.

Perovskite materials	Energy band gap (eV)	J _{sc} (mA/cm ²)	V _{oc} (V)	FF	n (%)	Hysteresis index, HI	Limitations /advantages	Ref
CH ₃ NH ₃ PbI ₃	1.55	20.57	1.0	68.6	15.28	-	-	(Pascoe <i>et al.</i> , 2015)
CH ₃ NH ₃ PbI _{1-x} Br _x	1.58 - 2.28	-	0.87 - 1.13	0.66 - 0.74	12.3 when x=0.2	-	Inclusion of Br ⁻ resulted in widening band gap energy.	(Noh <i>et al.</i> , 2013)
FAPbI ₃	1.47	6.45	0.97	68.7	4.3	-	Reversibility effect of black to yellow FAPbI ₃ non-perovskite materials.	(Koh <i>et al.</i> , 2014; Stoumpos <i>et al.</i> , 2013)
FAPbI _y Br _{3-y}	1.48 - 2.23	-	-	-	-	-	Addition of I ⁻ led to longer wavelength absorption.	(Eperon <i>et al.</i> , 2014)
CH ₃ NH ₃ PbI _{3-x} Cl _x	-	17.9	0.97	0.7	12.2	-	Rendered longer diffusion length (greater than 1 μm) for both electrons and holes.	(Stranks <i>et al.</i> , 2013)
CH ₃ NH ₃ PbI ₃ (440 nm)	-	18.1	0.94	0.66	11.3	0.087	Larger perovskite crystal size alleviates HI effect.	(Kim and Park, 2014)
CH ₃ NH ₃ PbI ₃ (130 nm)	-	18.2	1.06	0.58	11.2	0.212		(Kim and Park, 2014)
CH ₃ NH ₃ PbI ₃ (mp-TiO ₂)	-	18.4	0.93	0.67	11.5	0.059	The inclusion of mp-TiO ₂ mitigate HI effect.	(Kim and Park, 2014)
CH ₃ NH ₃ PbI ₃ (planar)	-	17.1	0.89	0.41	6.3	0.362		(Kim and Park, 2014)
CsPbI ₃	-	8.25	0.72	0.55	3.24	0.106	HI mitigated upon insertion of 8 nm MoO ₃ .	(Ripolles <i>et al.</i> , 2016)
CsPbBr ₃	2.34	7.34	1.25	0.63	5.82	-	-	(Liang <i>et al.</i> , 2017)
CsPbIBr ₂	1.90	12.32	1.08	0.62	8.25	-	Mixed halide perovskite material enhances PCE.	(Liang <i>et al.</i> , 2017)
CsPb _{0.9} Sn _{0.1} IBr ₂	1.79	14.30	1.26	0.63	11.33	-	Encapsulated cell exhibited no degradation after 3 months storing at room temperature.	(Liang <i>et al.</i> , 2017)

2.4.4 Hole-Transporting Materials (HTM)

An efficient hole transport mobility is important for high performance perovskite solar cell. The solid state HTM *Spiro*-OMeTAD has replaced the liquid electrolyte of DSSC, which promotes the efficiency up to 10.9% in 2012. Worth to mention, the *Spiro*-OMeTAD based perovskite solar cell has achieved an efficiency of 20% (Cao *et al.*, 2015). In addition, the poly(3-hexylthiophene), in short P3HT has also been used in CH₃NH₃PbI₃ perovskite solar cell with efficiency of 4.5%. Albeit P3HT possesses lower hole mobility with conductivity of 10⁻⁵ S/cm with high series resistance, its viable solubility in various solvents is beneficial for facile P3HT deposition (Cai *et al.*, 2015). In 2013, a pyrene arylamine derivatives HTM was developed in fabrication mesoporous TiO₂/CH₃NH₃PbI₃/HTM/Au solar cell has thus resulted in PCE of 12.4% (Jeon *et al.*, 2013). In the process of exploring more cost-effective, higher carrier mobility, and energy level compatible HTM, a diketopyrrolopyrrole (DDP)-based polymer, namely (poly[[2,5-bis(2-octyldodecyl)-2,3,5,6-tetrahydro-3,6-dioxopyrrolo[3,4-c]pyrrole-1,4-diyl]-alt-[[2,2'-(2,5-thiophene)bis-thieno[3,2-b]thiophen]-5,5'-diyl]]) or abbreviated as P was investigated and has achieved higher PCE of 10.8%, as opposed of P3HT (6.62%). As reported, the incorporation of P as ITO/perovskite/P/MoO₃/Ag solar cell yielded high PCE ascribed to suitable energy level of P over perovskite material (Zhu *et al.*, 2016). In the nutshell, the perfect matches of HTM's energy level enhances hole transportation and prompts for high PCE.

2.5 The Integrated Photo-Super Capacitor

Though a perovskite solar cell has a high energy conversion efficiency, it is unable to store the converted energy. Therefore, it requires an additional energy storage device such as a super capacitor for a storage system, as well as to serve as the main power delivery output in most applications such as optoelectronic devices (Bagheri *et al.*, 2014). Therefore, a photo-super

capacitor, which is a device that couples a solar cell, typically a DSSC or a perovskite solar cell, and an energy storage device such as a set of batteries, capacitor, or lately a super capacitor, has generated considerable interest because of its superior photon-to-electricity conversion and in-situ energy storage abilities for future energy storage development (Hsu *et al.*, 2010). The hybridization of an energy conversion device and super capacitor is able to provide a 43% internal resistance reduction (Xu *et al.*, 2014), which enhances and smoothes the power delivery system.

2.6 Working Principle of Photo-Super Capacitor

A photo-super capacitor is an integrated energy storage device that comprises a perovskite solar cell, which is the primary charges carrier contributor to their respective contacts upon light absorption, and a super capacitor as the electron storage reservoir, in addition to being an electrical energy delivery output source for various applications. The perovskite solar cell device comprises the electron transporting materials, light harvesting materials, and hole transporting materials. The most commonly used active electron and hole transporting materials are TiO₂ and *Spiro-OMeTAD*. On the other hand, a sandwich-type super capacitor is likely made of stacked current collectors with electrolyte as a separator. Interestingly, both devices share a common counter electrode in completing the circuit. A photo-super capacitor is designed to utilize the excessive and renewable solar energy resource to spike the light-to-electrical energy conversion.

Being a photo-super capacitor, the irradiated electrons are transferred from the perovskite solar cell via the external circuit and stored in the reservoir of the super capacitor. The charging and discharging processes for the photo-super capacitor mimic the working principles of an individual super capacitor, where in this case, the utilization of solar energy to initiate the

generation of photoelectrons instead of electrical energy by any power source is the only distinctive feature differentiating the photo-super capacitor concept from an ordinary super capacitor. Photogenerated electrons are stored in the shared counter electrode, and then, in the absence of light, a discharging process takes place, where the highly efficient conversion of solar energy to electrical energy further enables the production of a surge of electricity that fits energy demanding applications. However, the recombination of electrons with the redox species or dye molecules at the sensitizer-electrolyte interface is inevitable (Park *et al.*, 2003), which reduces its light-to-electrical energy conversion efficiency.

2.7 Emerging Field of Photo-Super Capacitor

An integrated photo-super capacitor device is synchronized with a three-electrode device, which comprises an energy conversion device's photoanode, shared counter electrode, and current collector of the super capacitor in conjunction with two electrolytes. In 2010, work on a photo-super capacitor that utilized PEDOT as the conducting polymer electrode in a super capacitor showed a lower internal resistance estimated to be 160 Ω , which is half that of a carbon-based photo-super capacitor (Murakami *et al.*, 2005). This merit could be credited to the PEDOT, which provided a higher surface area and higher conductivity than other conducting polymers. The specific capacitance of the photo-super capacitor was recorded to be 0.52 F/cm², and the plastic-based DSSC had an efficiency of 4.37% (Chen *et al.*, 2010). Within the same year, another conducting polymer film-based photo-super capacitor was fabricated with the integration of a PProDOT-Et₂ conducting polymer thick film as an energy storage material and an N3 dye-TiO₂ DSSC as an energy conversion device, which showed an energy storage efficiency of 0.6% (Hsu *et al.*, 2010).

In 2013, a hydrogenated single crystal ZnO@amorphous ZnO-doped MnO₂ core shell nanocable (HZM) flexible super capacitor showed a specific capacitance of 1260.9 F/g under inductively coupled plasma atomic emission spectroscopy when the loading of MnO₂ reached 0.11 mg/cm. A stand-alone self-powered system comprised of their newly fabricated all solid-state super capacitor, DSSC, and LED is shown in Figure 2.16a. This novel, self-powered system successfully lit up a blue LED using three series-wound super capacitors and a red LED was lighted for more than 30 min by a super capacitor after being charged for 2 min using four series-wound DSSCs (Yang *et al.*, 2013). The inset of Figure 2.16b shows that the three series-wound super capacitors attained ~2.3 V after 120 s of charging.

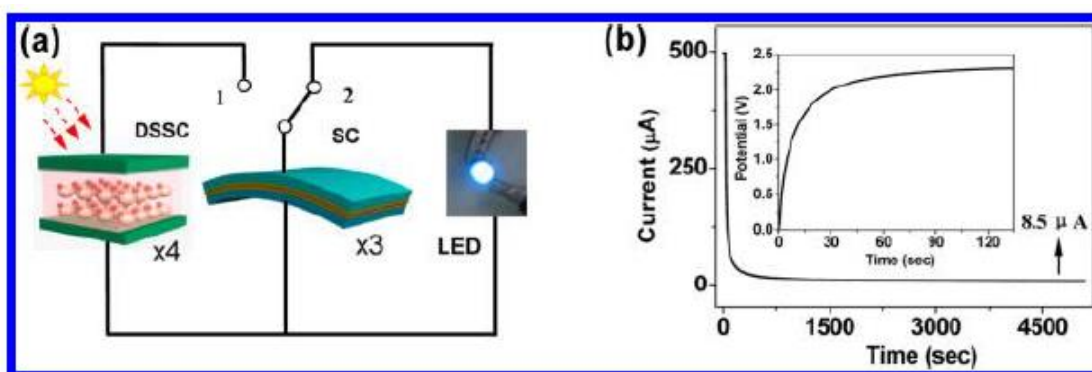


Figure 2.16 (a) Schematic of stand-alone self-powered system consisting of four series-wound DSSCs, three series-wound flexible SCs, and one LED. (b) Leakage current curve of three series-wound SCs charged at 0.5 mA to a potential of 2.4 V and kept at 2.4 V for 5000 s, indicating a small leakage current. Inset is the voltage profile for three SCs in series when being charged by four DSSCs in series. Adapted from ref. (Yang *et al.*, 2013).

In 2014, a maximum overall photon-to-electrical conversion and storage efficiency value of 1.64% had been attained by an integrated photo-super capacitor based on bi-polar anodic titanium oxide (ATO) nanotube arrays with selectively hydrogen plasma treatment on super capacitor sub-device. This device rendered maximum energy storage efficiency of 51.06% and superior retention stability with discharge areal capacitance (1.289 mF/cm²) of 96.5% after 100 cycles at a discharge current density of 0.1 mA/cm (Xu *et al.*, 2014).

Recently, an integrated DSSC-asymmetrical Ni(Co)O_x/AC super capacitor (photo-super capacitor) reported a specific capacitance of 46 F/g for a single super capacitor device. By studying the individual electrodes, redox peaks were observed in the voltammogram of the Ni(Co)O_x electrode, ensuring the effective energy storage within the electrode/electrolyte interface ascribed to the redox transition. Nevertheless, a 14 F/g capacitive reduction of the asymmetrical super capacitor was observed upon the integration with the DSSC, giving a capacitance of 32 F/g and an efficiency of 0.6 % (Bagheri *et al.*, 2014). The integration of photo-lithium ion batteries and photo-super capacitors as a single cell device has been explored extensively. However, the low efficiencies of the solar cell (DSSC and organic hybrid solar cell) and low capacity of the energy storage part turns down the overall integrated performance of the power pack device.

The advantages of the mesoscopic cell structure and facile fabrication of printable perovskite solar cell with the alluring efficiency performance hence shifted the DSSC interest to perovskite based solar cell. In 2015, a power pack device combining a CH₃NH₃PbI₃ perovskite solar cell with a PPy super capacitor (as shown in Figure 2.17), connected in series reached an overall output efficiency of 20% with an output voltage of 1.46 V when the voltage of PPy super capacitor was set at 0.6 V (Xu *et al.*, 2015). In addition, a PEDOT-carbon electrode bridge the perovskite solar cell (CH₃NH₃PbI₃) and super capacitor part (Figure 2.18a) was fabricated in 2016, exhibited a maximum overall efficiency of 4.7% and energy storage efficiency of 73.77%, thus proven the suitability of the perovskite material to be used for photo-super capacitor application (Xu *et al.*, 2016). Figure 2.18b illustrates the photo-charging and discharging of the integrated photo-super capacitor device. Under light illumination, the super capacitor was charged to 0.70 V within 7 s and approaches to the open-circuit voltage, indicates a high storage proportion of the PEDOT-carbon electrode of the photo-super capacitor device.

The discharging process was taken place in dark at current densities from 0.25 to 1.5 mA/cm² (Xu *et al.*, 2016).

Thus far, there are merely works reported on fabrication of photo-super capacitor, as shown in Table 2.5. Nevertheless, by further optimizing the materials' structure and effective encapsulation of the integrated device, the effective self-powered electrochemical energy conversion and storage systems of the photo-super capacitor is envisioned to becoming a promising green storage system in the near future.

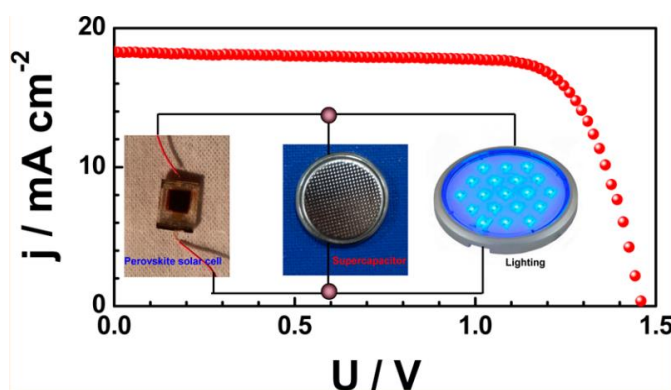


Figure 2.17 The power pack device comprises a perovskite based solar cell and a polypyrrole-based super capacitor. Adapted from ref. (Xu *et al.*, 2015).

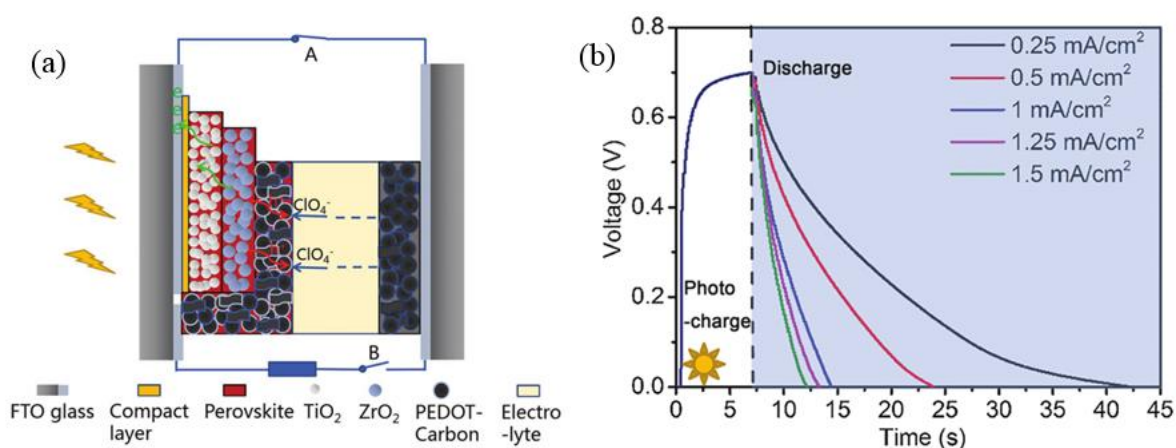


Figure 2.18 (a) Schematic illustration of the printable perovskite solar cell based photo-super capacitor. (b) The voltage response of the perovskite solar cell during photo-charge and galvanostatic discharge of super capacitor at different current densities in dark. Adapted from ref. (Xu *et al.*, 2016).

Table 2.5 A summary on the integration of a photovoltaic device and an energy storage device.

Solar cells				Energy storage devices		PCE (%)	Overall (%)	Cyclic retention	Ref
Photoanode	Light harvesting material	Cathode	Electrolyte/HTM	Types	Electrolyte				
TiO ₂ nanoparticles	N3 dye	Pt sheet	0.5 M LiI, 0.05 M I ₂ /0.5 M TBP in CH ₃ CN	PProDOT-Et ₂ symmetric super capacitor	0.5 M LiClO ₄ in MPN	-	0.6	80% after 10 cycles	(Hsu <i>et al.</i> , 2010)
TiO ₂ particles	N719	Pt sheet	Surlyn	PEDOT-based super capacitor	0.5 M LiClO ₄ in MPN	4.37	-	-	(Chen <i>et al.</i> , 2010)
cTiO ₂ /mTiO ₂	D35	Ag layer	P3HT	RuO _x (OH) _y symmetric super capacitor	Nafion membrane	3.0	0.8	-	(Skunik - Nuckowska <i>et al.</i> , 2013)
TiO ₂ particles	N719	Carbonized porous silicon wafer	50 mM I ₂ , 500 mM LiI, 500 mM TBP in acetonitrile	Carbon-coated porous silicon	PEO:EMIBF ₄ (1:3)	4.8	2.1	-	(Cohn <i>et al.</i> , 2015)
TiO ₂ nanoparticles	CH ₃ NH ₃ PbI ₃	PEDOT-carbon	-	PEDOT-carbon symmetric super capacitor	1 M LiClO ₄ and 10 mg/mL CH ₃ NH ₃ I in isopropanol	6.4	4.7	96.8% after 50 cycles	(Xu <i>et al.</i> , 2016)
TiO ₂ particles	LEG4	PEDOT on Ni foil	Cobalt polypyridyl complex	Ni(Co)O _x positive electrode and activated carbon negative electrode based asymmetric super capacitor	KOH	4.9	0.6	-	(Bagheri <i>et al.</i> , 2014)
TiO ₂ nanotube (bottom cell) and TiO ₂ nanorod (top cell)	N-719 (top cell) and N-749 (bottom cell)	Pt sheet	0.5 M LiI, 50 mM I ₂ , and 0.5 M 4-tertbutylpyridine in 3-methoxypropionitrile	Battery	1 M LiPF ₆ in ethylene carbonate:dimethyl carbonate (1:1)	-	0.82	-	(Guo <i>et al.</i> , 2012)

CHAPTER 3

MATERIALS AND METHODS

In this chapter, the materials, preparation and fabrication methods will be divided into four sections, which involve the materials, fabrication of devices (symmetrical super capacitor, asymmetrical super capacitor, perovskite solar cell, and photo-super capacitor), materials characterizations, and electrochemical measurements.

3.1 Materials

The nickel foam was obtained from Goodfellow Cambridge Ltd. Nylon filter membrane was purchased from Membrane Solutions, LLC, US. Potassium permanganate (KMnO_4 , >99–100.5%) was obtained from R&M Chemicals, Malaysia, while bismuth oxide (Bi_2O_3) with a purity of 99.999% was purchased from Sigma-Aldrich, Malaysia. Graphite powder was obtained from Ashbury Graphite Mills Inc., code no. 3061. Sulphuric acid (H_2SO_4 , 95%–98%), phosphoric acid (H_3PO_4 , 85%), and hydrogen peroxide (H_2O_2 , 30%) were purchased from System, Malaysia. Hydrogen chloride (HCl , 37%), sodium sulphate anhydrous (Na_2SO_4 , 70%), and a toluene-4-sulfonic acid sodium salt (NapTS, 98%) were purchased from Merck. Pyrrole (99%) was purchased from Across Organic, stored at 0°C , and distilled prior using. The graphite sheet (natural graphite >99.5%) was purchased from Latech Singapore. Zinc nitrate hexahydrate, $\text{Zn}(\text{NO}_3)_2 \cdot 6\text{H}_2\text{O}$ and cobalt (II) nitrate hexahydrate, $\text{Co}(\text{NO}_3)_2 \cdot 6\text{H}_2\text{O}$ were purchased from Bendosen and R&M Chemicals, respectively. Nitric acid ACS reagent ($\geq 65\%$) was obtained from Sigma-Aldrich. Urea was purchased from AnalaR, BDH laboratory supplies from England and ammonium chloride (NH_4Cl) was obtained from Merck. The fluorine-doped tin oxide (FTO) glass substrate with a size of $2.5 \times 2.5 \text{ cm}^2$ was purchased from Nippon Sheet

Glass Co. Ltd (10 Ω /sq). Indium tin oxide (ITO) conducting glass slides (7 Ω /sq) were purchased from Xin Yan Technology Limited, China. The mesoporous titanium dioxide (mp-TiO₂) was acquired from JGC Catalysts and Chemicals Ltd (PST-18NR). The lead (II) bromide (PbBr₂, >98%) was purchased from Aldrich, whereas the lead (II) iodide (PbI₂, >98%) was purchased from TCI Tokyo Chemical Industry CO., LTD and Sigma-Aldrich. The cesium bromide (CsBr, 99.9%) was obtained from Alfa Aesar and Sigma-Aldrich. The *Spiro*-OMeTAD was purchased from Sigma-Aldrich. In order to improve its electrical properties, some additives were added as bis (trifluoromethane) sulfonimide lithium salt (Li-TFSI) dissolved in acetonitrile (520 mg/mL, wako) and 4-tert-butylpyridine (TBP) was purchased from Sigma-Aldrich and TCI, respectively. P3HT was acquired from Aldrich and was dissolved in o-dichlorobenzene (Sigma-Aldrich) in a concentration of 17 mg/mL. Titanium (IV) tetraisopropoxide (TTIP >98%), titanium (IV) oxide (P25) powder, and pyrrole (99%) were purchased from Acros Organics. In addition, α -terpineol and methanol were purchased from Wako, whereas dimethylformamide (DMF), chlorobenzene, PEDOT:PSS, and lithium perchlorate (LiClO₄) were obtained from Sigma Aldrich.

3.2 The Bi₂O₃/MnO₂ Symmetrical and Asymmetrical Super Capacitor

3.2.1 Fabrication of Bi₂O₃/MnO₂ Electrode

First, 1 mM of Bi₂O₃ and 10 mM of KMnO₄ powder were dispersed in 40 ml of deionized water. A 2 × 3 cm² piece of nickel foam was immersed in the prepared solution and subjected to hydrothermal treatment at 140 °C for 24 hours. The deposited nickel foam was then dried at 60 °C for 6 hours and calcined at 350 °C for 2 hours.

3.2.2 Fabrication of Bi₂O₃/MnO₂ Symmetrical Super Capacitor

A two-electrode-configuration symmetrical super capacitor was prepared by stacking the Bi₂O₃/MnO₂ electrodes separated by a piece of 1 M Na₂SO₄ soaked filter paper. The super capacitor was fitted into a Swagelok for electrochemical measurements. For temperature tests, the super capacitor was either cooled at 0 °C or heated at 60 °C for 1 hour prior to the electrochemical measurements and was constantly cooled in an ice box or heated on a hot plate throughout the test. For measurement at 30 °C, the super capacitor was left in an ambient condition.

3.2.3 Fabrication of Bi₂O₃/MnO₂//PyR Asymmetrical Super Capacitor

The fabricated Bi₂O₃/MnO₂ positive electrode was stacked with the polypyrrole/reduced graphene oxide (PyR) negative electrode, forming a sandwiched system separated by the membrane filter where 1 M Na₂SO₄ aqueous solution was employed as the redox electrolyte. The sandwich-like asymmetrical super capacitor was fit into a Swagelok for the electrochemical measurements.

3.3 The rGO/ZnO/Co₃O₄//PyR (RZCo//PyR) Asymmetrical Super Capacitor

3.3.1 Preparation of Graphene Oxide (GO)

GO was prepared through the simplified Hummer's method, where the oxidation reaction was carried out by mixing H₂SO₄:H₃PO₄ (360 ml: 40 ml), graphite flakes, and KMnO₄ using a magnetic stirrer at room temperature. The mixture was then left stirring for three days to allow the complete oxidation of the graphite. Subsequently, the H₂O₂ solution was added to the mixture to stop the oxidation process, and the color of the mixture turned bright yellow. Next, graphite oxide was washed with a 1 M HCl aqueous solution three times and with deionized

water ten times by the centrifugation technique until the pH reached a value of approximately 4–5 and GO was formed. The concentration of GO was 6.3 mg/ml.

3.3.2 Preparation of rGO/ZnO/Co₃O₄ (RZCo) Positive Electrode

2 mmol Co(NO₃)₂·6H₂O, 1 mmol Zn(NO₃)₂·6H₂O, 4 mmol NH₄Cl, and 0.02 mg/ml GO precursors were dissolved in 30 ml deionized water and stirred until homogenous. 8 mmol urea was then added into the purplish homogenous solution and sonicated for 15 min, followed by the immersion of nitric acid treated graphite sheet into autoclave for 5 hours of hydrothermal reaction at 120°C. The deposited graphite sheet was calcined at 400°C for 2 hours after the hydrothermal process. The same process was done for Co₃O₄/ZnO (without the inclusion of GO) as a standard comparison, denotes as ZCo in short.

3.3.3 Preparation of PPy/rGO (PyR) Negative Electrode

PyR nanocomposite films were synthesized using a potentiostat–galvanostat at room temperature, where a platinum electrode was used as a counter-electrode, graphite sheet as a working electrode, and a saturated calomel electrode as a reference electrode. The films were electrodeposited onto the graphite sheet at a constant potential of +0.8 V for 15 min where the deposition solution contained 0.1 M of pyrrole, 1 mg/ml of GO, and 0.1 M of toluene-4-sulfonic acid sodium salt (NapTS).

3.3.4 Fabrication of RZCo//PyR Asymmetrical Super Capacitor

The fabricated positive electrode was stacked with the negative electrode, forming a sandwiched system separated by the membrane filter where 1 M Na₂SO₄ aqueous solution was employed as the redox electrolyte. The sandwich-like asymmetrical super capacitor was fit into a Swagelok for the electrochemical measurements.

3.4 The Perovskite Solar Cell

3.4.1 Perovskite Solar Cell Fabrication

The FTO-coated glass was patterned using HCl (6 M)-etching with Zn powder and cleaned by first, ultrasonification in a basic bath of neutral water, acetone, isopropanol, and deionized water and second, plasma system for several minutes. A 20 nm compact titania (c-TiO₂) prepared from titanium diisopropoxide bis (acetylacetonate) was deposited through atomic layer deposition method at 300 °C. The mesoporous-TiO₂ (mp-TiO₂) was spin coated onto the c-TiO₂ surface at the spinning conditions of 500 rpm for 3 seconds and 6000 rpm for 30 seconds, followed by an immediate heating at 80 °C for 10 minutes. Subsequently, the substrates were calcined at 470 °C for 30 minutes. The synthesis of perovskite film was conducted via two-steps sequential method. Firstly, an aliquot of 90 μL PbBr₂:PbI₂, with a molar ratio of 1:0, 1:0.1, 1:0.2, and 1:0.3, was initially spin coated onto the mp-TiO₂ surface at 2500 rpm for 1 minutes. These films were heated at 75 °C for 30 minutes on a hot plate. Subsequently, the films were dipped into CsBr solution for 10 minutes at 50 °C, and washed with 2-propanol solution for 1 minutes at 50 °C as well. The CsPbBr_{3-x}I_x films were formed after annealing at 350 °C for 10 minutes. *Spiro*-OMeTAD was spin coated on the surface of the perovskite film at 500 rpm for 3 seconds, subsequently 4000 rpm for 30 seconds. The films were left to dry inside a petri dish about 15 hours in dark. For comparison, the P3HT samples were prepared through spin coating process at 1000 rpm for 10 minutes and were stored in a petri dish in dark for 16 hours before annealing treatment at 130 °C for 10 minutes was carried out. Finally, an 8 nm of MoO₃ film was evaporated for the P3HT-based solar cells, and 60 nm of Au was vapour deposited for all devices.

3.5 The Photo-Super Capacitor

3.5.1 Fabrication of Perovskite Solar Cell

The ITO glass was cleaned by sonication process using acetone, ethanol, and deionized water for 20 minutes each. The compact titania layer was prepared through aerosol assisted chemical vapour deposition (AACVD) process. The production of aerosol from 0.1 M TTIP in 50 ml toluene solution with the aid of an air humidifier and the flow of argon gas at flow rate of 300 mL/min enable the deposition of compact titania on ITO conductive glass at 450 °C for 30 minutes. After cooled down to room temperature, the mp-TiO₂ was doctor bladed on the c-TiO₂ layer, subsequently sintered at 500 °C for 30 minutes. The TiO₂ paste was prepared through dissolving 1.6 g P25 in 8 ml ethanol with stirring of 5 minutes. 0.01 M TTIP was then added with continual stirring and was horn-sonicated for 30 minutes to obtain a well-disperse paste. Subsequently, the CsPbBr_{3-x}I_x (x = 0 - 0.3) solar cells were prepared through two-steps sequential spin coating process. Firstly, the PbBr₂:PbI₂ (in the ratios of 1:0, 1:0.1, 1:0.2, 1:0.3) were spin coated on the ITO substrate at 2500 rpm (60 seconds), subsequently dried on the hot plate at 75 °C for 30 minutes. Next, the PbBr₂:PbI₂ coated substrate was immersed in CsBr solution for 10 minutes and was washed in isopropanol solution, followed by annealing process at 350 °C for 10 minutes for perovskite crystal growth. The HTM, *Spiro*-OMeTAD was spin coated on the perovskite layer at 500 rpm for 3 seconds, followed by 4000 rpm for 30 seconds. The HTM coated substrates was left to dry in a petri dish in dark prior to be used. A thin layer of PEDOT:PSS was drop casted on an ITO glass as the counter electrode in order to mimic the testing procedure for photo-super capacitor. The whole fabrication process was carried out in ambient condition with RH>80%.

3.5.2 Fabrication of An Asymmetrical Super Capacitor

The super capacitor electrodes are composed of RZCo as the positive electrode and PyR as the negative electrode. Both electrodes were stacked with 1 M LiClO₄/acetonitrile soaked filter paper performing as the separator. The RZCo positive electrode was prepared via hydrothermal process at 120 °C for 5 hours; whereas the PyR negative electrode was prepared through electrodeposition (Ng *et al.*, 2017).

3.5.3 Fabrication of Cesium Perovskite Based Photo-Super Capacitor

The fabrication of photo-super capacitor was carried out by integrating the champion solar cell, CsPbBr_{2.9}I_{0.1} perovskite solar cell and the asymmetrical super capacitor without the connection of external wires. In details, the photoanode, which composed of compact and mesoporous titania, perovskite light harvesting material, and *Spiro*-OMeTAD as the HTM was coupled to a PEDOT:PSS coated RZCo layer positive electrode and PyR negative electrode asymmetrical super capacitor, likewise appointing 1 M LiClO₄/acetonitrile as the redox electrolyte. Clearly, the PEDOT:PSS coated RZCo electrode serves as the sharing electrode for the solar cell and super capacitor. The champion perovskite solar cell (CsPbBr_{2.9}I_{0.1}) was sparked with minute amount of *Spiro*-OMeTAD electrolyte to improve the charge diffusivity before measurement took place.

3.6 Materials Characterizations

3.6.1 Super Capacitors

The chemical states and compositions of the products were analyzed using X-ray photoelectron spectroscopy (XPS) by a PHI Quantera II with Spherical Capacitor Analyzer (SCA) and DZU Shima (Kratos Analytical Ltd.), whereas the crystalline structures of the samples were analyzed using a D8 Advance, Bruker AXS Germany (Cu, K α one radiation) X-ray diffraction (XRD)

technique. The surface morphologies of the samples were investigated using a Quanta 400F FESEM equipped with an EDX feature. Fourier transform infrared (FTIR) spectroscopy was performed using the attenuated total reflectance of a Perkin Elmer 1650, FTIR spectrophotometer. RAMAN spectroscopy was conducted using a WITec Raman Microscope. Transmission electron microscopy (TEM) was conducted using a Hitachi, HT-7700. The electrical conductivity test was performed by Mitsubishi Loresta-GP (MCP-T610).

3.6.2 Perovskite Solar Cells

The glass/FTO/CsPbBr_{3-x}I_x substrates (where x varies between 0, 0.1, 0.2, and 0.3 in molar ratio) were characterized by several techniques. The XRD was conducted through RINT-Ultima III, Rigaku in 2θ range of 10 to 80 degrees using monochromatic Cu, Kα radiation. The UV-Visible spectra was performed via JASCO V-670 spectrophotometer from 200–900 nm. The emission spectra were obtained from JASCO FP- 6600 spectrofluorometer from 450–600 nm. The valence band of perovskite was measured through Ultraviolet Photo-Electron Spectroscopy (UPS) (BUNKOUKEIKI). The band gap of each perovskite material was obtained through Equation 3.1.

$$E_g = \frac{1240}{\lambda} \quad \text{Equation (3.1)}$$

where E_g refers to the band gap and λ is the intersected wavelength of the UV-Vis and photoluminescence.

3.6.3 Photo-Super Capacitor

The crystalline structures of the samples were analysed by using D8 Advance, Bruker AXS Germany (Cu, Kα one radiation) XRD technique. The surface morphologies of the samples were investigated using a Quanta 400F FESEM equipped with an EDX feature. The RAMAN spectroscopy was measured through the WITec Raman Microscope.

3.7 Electrochemical Measurements

The super capacitors were fabricated by employing 1 M Na₂SO₄ aqueous electrolyte soaked membrane filter as the separator and was fitted into a Swagelok. The as-fabricated super capacitors were subjected to cyclic voltammetry, galvanostatic charge/discharge, and electrochemical impedance spectroscopy measurements. The applied working potential for the cyclic voltammetry measurements was in the range of 0–1 V for a symmetrical super capacitor and 0-1.6 V for an asymmetrical super capacitor, measured from scan rates of 100 to 2 mV/s. The specific capacitance of the super capacitors were calculated from the charge/discharge profile using Equation (3.2), where C_m refers to the specific capacitance in farads per gram, I is the current of charge/discharge, Δt is the discharging time, ΔV is the potential window, and m is the electrode mass in grams (Jin *et al.*, 2011):

$$C_m = I\Delta t / \Delta V m \quad \text{Equation (3.2)}$$

The energy density and power density of the super capacitors were calculated using Equations (3.3) and (3.4), respectively (Kang *et al.*, 2012).

$$E_{cell} = 1/2 C_{cell} V^2 \quad \text{Equation (3.3)}$$

$$P_{cell} = E_{cell} / t \quad \text{Equation (3.4)}$$

where E_{cell} is the energy density in Wh/kg, C_{cell} is the specific capacitance of an electrode obtained from cyclic voltammetry, V is the potential window obtained from discharge curve, P_{cell} is the power density in W/kg, and t refers to the discharge time.

For the perovskite solar cell, the current density-voltage (J-V) measurement was measured by a solar simulator (CEP- 2000SRR, Bunkoukeiki Inc) with light source intensity of AM1.5G 100 mW/cm², which was calibrated with a reference silicon cell. All solar cells were measured

using a mask with an active area of 0.12 cm^2 under 1 sun. The photovoltaic measurements were carried out at scan rate of 0.1 V/s , 100 ms delay time and 10 mV voltage step. The measurement of external quantum efficiency (EQE) was performed through CEP-2000SRR, Bunko Keiki with 300 W Xe lamp. The monochromator was adjusted to $1 \times 10^{16} \text{ mW/cm}^2$ and was monitored by Si photodiode. Similar electrochemical measurements were performed for the photo-super capacitor. The galvanostatic charge discharge was performed from the current densities of 0.1 mA/cm^2 to 1 mA/cm^2 and was calculated according to Equation (3.2). Whilst, the electron lifetime of the perovskite solar cell was calculated according to equation (3.5):

$$\tau = 1/2\pi f \quad \text{Equation (3.5)}$$

where f is the highest frequency obtained through Bode plot and π is a constant.

CHAPTER 4

ELECTROCHEMICAL PERFORMANCES OF SUPER CAPACITORS FOR PHOTO-SUPER CAPACITOR APPLICATION

Generally, a high energy and power densities super capacitor is highly desirable for various optoelectronic applications and to fulfil the skyrocketing energy demands. Apparently, a super capacitor which is composing of two similar electrodes, which is a symmetrical super capacitor is unable to fulfil the crave of energies, owing to the narrower potential window, as opposed to an asymmetrical super capacitor. The energy performance is proportional to the cell voltage of the super capacitor. Hence, with the coupling of two different super capacitor electrode materials, which forms an asymmetrical super capacitor, the potential window of the super capacitor was extended, also the capacitive performances of the super capacitor were improved. In this chapter, the performances of a symmetrical and an asymmetrical super capacitors were investigated through a series of electrochemical performances. Additionally, temperature studies were also included to gauge the versatility of the super capacitor electrode under the temperatures influence. The super capacitor with high performance will therefore employed as the energy storage device for the photo-super capacitor.

4.1 Introduction

A green energy device does not solely rely on high electrochemical performance, but must also possess temperature durability to meet and fulfil the various application needs. A super capacitor should be able to operate under mild to severe weather conditions in electric vehicles. It is common for car batteries to malfunction in winter (below $-1.1\text{ }^{\circ}\text{C}$). Hence, a device that is weather resistant, in addition to having a high capacitive performance, is preferable, in order to replace the conventional battery application. A super capacitor offers high power density

and fast charging properties, which can increase the acceleration rate and decrease the charging time (in just a few minutes) of a vehicle relative to a standard electric car battery. Only a few temperature investigations have been reported, with most super capacitor studies focusing on applications at room temperature. A single-wall carbon nanotube coin cell super capacitor employing tetraethylammonium tetrafluoroborate-polypropylene carbonate as the electrolyte was measured at 25–100 °C in 2009. This super capacitor exhibited a high power density of approximately 55 kW/kg at a current density of 100 A/g. The insignificant cell damage to the super capacitor upon operation at a current density of 100 mA/g to 100 A/g at temperature of 25–100 °C showed the superiority of its electrodes (Masarapu *et al.*, 2009). In 2013, a three-electrode manganese oxide-electrospun carbon nanotube-embedded carbon nanofiber electrode was reported with a high capacitance of 546 F/g at 75 °C, which showed a 120 F/g increment compared to that at 25 °C (Wang *et al.*, 2013).

Looking into the capacitive performances, generally, energy density performance is closely relating to the capacity and square of its operating potential window. Composing an asymmetrical super capacitor by utilizing different active materials as the positive and negative electrodes is desirable to widen the potential window of the super capacitor owing to the potential windows of the positive and negative are different (Chae and Chen, 2012). An asymmetrical super capacitor composed of a non-polarized Faradaic electrode as the energy source and a polarized electrode as the power source contributes in high energy density performance, which approaches that of a battery (Tang *et al.*, 2013). The negative electrodes or anodic materials of an asymmetrical super capacitor are mainly composed of carbonaceous materials such as carbon nanotubes, graphene, activated carbons and oxides materials. Despite the monolayer graphene possesses a large specific surface area with excellent conductivity, mechanical, and electrical properties, graphene is inherently hydrophobic in nature, which led

to the non-disperse of graphene in most aqueous solvents (Basu *et al.*, 2010; Chee *et al.*, 2015; Dreyer *et al.*, 2010; Lim *et al.*, 2013; Ou *et al.*, 2014; Zhu *et al.*, 2011). The agglomeration of graphene inferior the ionic accessibility of an asymmetrical super capacitor (Wang *et al.*, 2013) and hence could be solved through the partially reduced graphene oxide to reduce graphene oxide (rGO). The rGO is profound in its electrical conductivity up to 1.28 S/m at 6 wt% (Wang *et al.*, 2010) and the remnant oxygen groups of rGO could prevent the restacking of graphitic sheet owing to the strong Van de Waals forces. Occasionally, compositing rGO with any electrochemically active materials is necessary to leverage the super capacitor performances. Conducting polymers are capable of storing more capacitance per gram, thereby contribute to the higher energy density and faradaic capacitance (Dubal and Holze, 2013; Ng *et al.*, 2015; Yu *et al.*, 2013). One of the most-sought after conducting polymers, polypyrrole (PPy), is highly conductive, has ultrahigh-flexibility, and been reported to display a high capacitance value (Eeu *et al.*, 2013). A hybrid of PPy and rGO significantly improve the capacitive performance of super capacitors (Lim *et al.*, 2014; Ng *et al.*, 2015; Snook *et al.*, 2011).

Meanwhile, the positive electrode or cathodic materials of the asymmetrical super capacitor include oxides such as the cobalt oxides (Co_3O_4), nickel hydroxide ($\text{Ni}(\text{OH})_2$), manganese dioxide (MnO_2), and ruthenium oxide (RuO_2). In 2011, an α - MnO_2 nanorod super capacitor electrode has reported a capacitance of 166.2 F/g (Li *et al.*, 2011). However, the dense morphologies and aggregation of MnO_2 nanosheets could impede the penetration of electrolyte ions within the nanocomposite matrix (Unnikrishnan *et al.*, 2016), which requires the incorporation or doping of another pseudocapacitive material to serve as a scaffold to anchor the MnO_2 , to improve the conductivity of the electrode materials, and to enhance the capacitance performance. Evidently, a $\text{Co}_3\text{O}_4@\text{MnO}_2$ nanocomposite achieved a specific capacitance of 480 F/g at 2.67 A/g with a cyclic retention of 97.3% after 5000 cycles (Wang *et*

al., 2015). In addition, coupling MnO₂ and Bi₂O₃ exhibited specific capacitance of 312.8 F/g at current density of 0.2 A/g and excellent stability performance (112% capacitance retained) after 1000 long-term cyclic system.

In addition, Co₃O₄ is a pseudo-capacitive material with high electro-activity and multi-capacitance storage ability, where Co₃O₄ nanostructures are able to store a charge via the double layer and pseudo-capacitive reaction. Co₃O₄ could theoretically deliver a specific capacitance of ~3650 F/g (Vidyadharan *et al.*, 2014). On the other hand, zinc oxide (ZnO) has a good carrier mobility and provides a high energy density (Chang *et al.*, 2015; Wang *et al.*, 2011). A one-dimensional ZnO nanostructure possesses excellent electron transport properties (Yu *et al.*, 2013) which can enhance the capacitive performances. A composite of Co₃O₄@graphene nanosheet prepared using a microwave-assisted method could homogeneously distribute Co₃O₄ nanoparticles (3-5 nm in size) on a graphene sheet (Wang *et al.*, 2013). Thereby, the inclusion of conductive graphene sheets provided an opened pathway for rapid charge storage and delivery, which resulted in a high electronic conductivity and capacitance performance, and an improved life for the device (Salunkhe *et al.*, 2014; Tang and Yamauchi, 2016). Hence, when transition metal oxides are included, which in our work refer to the ZnO/Co₃O₄ nanostructures, they behave as intercalating agents and intercalate the rGO to prevent the restacking of rGO sheets. This phenomenon is expected to be able to enhance the inflow and outflow of electrolyte ions, resulted in the excellent electrochemical performances, in addition to increasing the porosity of the graphite sheet. The inclusion of rGO could produce better wettability and thus induce the good dispersion in water ascribed to the presence of remaining oxygen groups, in line with the aromatic rings, which offer active sites for the π - π interaction (Qiu *et al.*, 2010). The synergetic effects of the ternary materials (ZnO/Co₃O₄/rGO) hence produce excellent electrical conductivity and better porosity.

In this chapter, first of all, a two-electrode-configured Bi₂O₃/MnO₂ device was fabricated as a symmetrical super capacitor via a one-step facile hydrothermal process, employing nickel foam as the current collector. This work focused on the performances of this super capacitor, specifically the shelf-life of the super capacitor at various temperatures of 0 °C, 30 °C, and 60 °C. A super capacitor with a prolonged lifespan and weather sustainability are the key performances requirements for multi-application viabilities to replace the battery in the automotive sector. However, despite the Bi₂O₃/MnO₂ symmetrical super capacitor possessed remarkable stability (>75%) after 1000 continuous charge/discharge cycles from 0 °C to 60 °C, however, the dissatisfactory capacitive performances of the Bi₂O₃/MnO₂ symmetrical super capacitor, thus urged for the fabrication of an asymmetrical super capacitor.

A Bi₂O₃/MnO₂//PyR asymmetrical super capacitor was fabricated using the same measuring parameters. In this case, a graphite sheet was chosen as the current collector due to its cost effectiveness over the nickel foam. The specifications and prices of the nickel foam and graphite sheet are included in Appendix A (Table A.1). The dissatisfactory capacitive performances of the bismuth-based asymmetrical supercapcitor has lured the search of alternative pseudocapacitive materials. Sequentially, we presented our work on the fabrication of RZCo//PyR asymmetrical super capacitor on graphite sheet via one-step facile hydrothermal and electro-deposition process. RZCo represents reduced GO/ZnO/Co₃O₄, while PyR represents polypyrrole/reduced graphene oxide. The graphite sheet was treated with nitric acid prior to the deposition of active materials. This effort is expected to improve the functionalization between the functional groups of the active materials and carbon surface, consequently responsible for the excellent electro-catalytic activity performance (Collins *et al.*, 2013; Wang and Hu, 2012). To date, there are merely few temperature dependent studies have

been reported and most of the super capacitor application studies focused on the performances at room temperature. The supercapacitive performances of the RZCo//PyR asymmetrical super capacitor at different temperatures were investigated and were also compared against the KEMET commercial super capacitor in this section.

4.2 Bi₂O₃/MnO₂ Symmetrical Super capacitor

4.2.1 Material Characterizations of Bi₂O₃/MnO₂ Pseudocapacitive Materials

FESEM images demonstrated that the spherical Bi₂O₃ particles (Figure 4.1a) were enveloped by 2D sheet-like MnO₂ (Figure 4.1b) after 24 hours of the hydrothermal process, as depicted in Figure 4.1c, which is in great agreement with the TEM image. Bi₂O₃ was featureless before undergoing the hydrothermal process (Figure A.1 in Appendix A). The elemental mapping confirmed the existence of Bi₂O₃ and MnO₂ over the nickel foam (Figure A.2 in Appendix A). The TEM image (Figure 4.1d) indicated the contrast between Bi₂O₃ and MnO₂ in the hybrid. The light color in the TEM image represents the ultrathin MnO₂ nanosheet, while the darker region indicates the Bi₂O₃ nanosphere (white arrows). The formation of MnO₂ sheets and stacked MnO₂ sheets is depicted in the TEM image. The HRTEM (Figure 4.1e) image reveals visible lattice fringes with equal interplanar distances of 0.37 and 0.27 nm, which correspond to MnO₂ (Wang *et al.*, 2010), indicating the wrapping of MnO₂ over the Bi₂O₃ material. In addition, the diffraction rings displayed in the SAED pattern indicate that Bi₂O₃/MnO₂ co-exist in the polycrystalline structure.

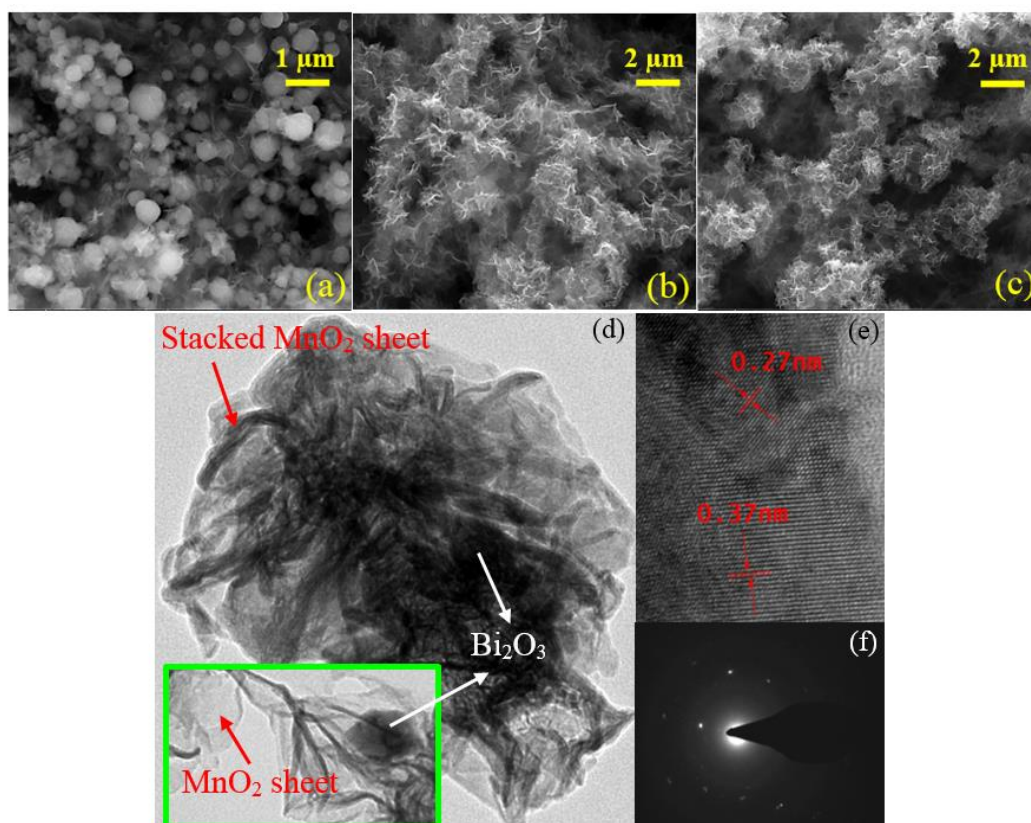


Figure 4.1 FESEM images of (a) Bi_2O_3 after hydrothermal process, (b) MnO_2 , and (c) $\text{Bi}_2\text{O}_3/\text{MnO}_2$ nanocomposite, along with (d) TEM image, (e) HRTEM, and (f) SAED of $\text{Bi}_2\text{O}_3/\text{MnO}_2$ nanocomposite. Inset of Figure 4.1d shows the encapsulation of 2D MnO_2 ultrathin sheet over Bi_2O_3 particles.

The XRD profile (Figure 4.2a) shows the good embedment of the highly crystalline $\text{Bi}_2\text{O}_3/\text{MnO}_2$ composite over the entire surface of the blank Ni foam, which agrees with the FESEM and TEM images. The good adhesion of the $\text{Bi}_2\text{O}_3/\text{MnO}_2$ over the nickel foam scaffold was confirmed through the tremendous decrease in the intensity peak of the nickel foam upon the introduction of active materials. The diffraction peaks detected at 43° , 52° , and 77° correspond to the lattice planes of (111), (200), and (220), which indicate the crystallographic planes of nickel (Cai *et al.*, 2014; Cao *et al.*, 2012; Hou and Gao, 2003; Ng *et al.*, 2015). The major detection point for the nickel foam is ascribed to the low concentration of precursors used. In addition, the XRD profile shows the absence of additional crystalline peaks, which is evidence that an impurity free nanocomposite was successfully synthesized. Figure 4.2b has

further evidence the deposition of the $\text{Bi}_2\text{O}_3/\text{MnO}_2$ hybrid composite on the nickel foam substrate. The FTIR peaks were slightly blue shifted and the intensity of the peaks diminished upon the deposition of Bi_2O_3 and MnO_2 pseudocapacitive materials. The presence of Mn-O bending vibrations for the $[\text{MnO}_6]$ octahedron was found at the peak of $\sim 452\text{ cm}^{-1}$, suggesting that MnO_2 was present within the $\text{Bi}_2\text{O}_3/\text{MnO}_2$ hybrid composite (Gan *et al.*, 2015). The blue shift in wavelength could be due to the strong bond energy between the Bi_2O_3 and MnO_2 in the composite (Liang *et al.*, 2015). The existence of $\text{Bi}_2\text{O}_3/\text{MnO}_2$ is further reflected by the Raman spectroscopies (Figure 4.2c). The prominent peak at 634 cm^{-1} corresponds to the symmetric stretching vibration of the Mn-O lattice, which is perpendicular to the MnO_6 octahedron double chains of MnO_2 (Gan *et al.*, 2015; Gnana *et al.*, 2014). In addition, the peak at 560 cm^{-1} represents the Mn-O stretching vibration in the basal plane of the MnO_6 sheet (Kim *et al.*, 2016). Meanwhile, the Bi_2O_3 nanostructure exists in the $\alpha\text{-Bi}_2\text{O}_3$ (monoclinic) phase (Salazar-Pérez *et al.*, 2005).

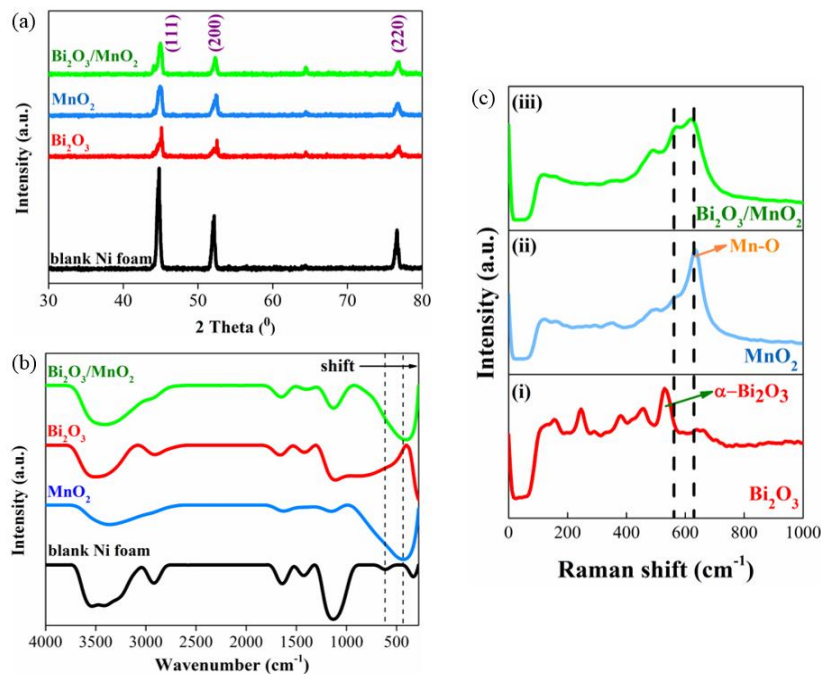
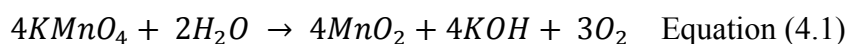


Figure 4.2 (a) XRD profile and (b) FTIR spectrum of blank Ni foam, Bi_2O_3 , MnO_2 , and $\text{Bi}_2\text{O}_3/\text{MnO}_2$, and (c) Raman spectroscopies of Bi_2O_3 , MnO_2 , and $\text{Bi}_2\text{O}_3/\text{MnO}_2$.

The XPS analysis was conducted to study the chemical composition and surface electronic state of the Bi₂O₃/MnO₂ electrode. The wide scan of Bi₂O₃/MnO₂ explicitly revealed the presence of the Bi, Mn, and O elements, as reflected in Figure 4.3a. The narrow scan of the Bi4f spectrum showed two deconvoluted peaks (164 eV and 158 eV) of Bi4f_{5/2} and Bi4f_{7/2}, respectively (Figure 4.3b). The peak separation of 5.3 eV thus clarified the existence of the Bi element in an oxidation state of +3 (Sarma *et al.*, 2013; Zuo *et al.*, 2016). In addition, the Mn2p spectrum shows two deconvoluted peaks at 654 eV and 642.2 eV, which correspond to the Mn2p_{1/2} and Mn2p_{3/2} spin-orbit peaks, respectively (Figure 4.3c) (Qiu *et al.*, 2015). It thus shows the domination of Mn⁴⁺ within the binary system (Yuan *et al.*, 2011). Figure A.3 (Appendix A) additionally proves the formation of MnO₂ with a peak separation of 4.6 eV, as expected from the Mn3s spectrum (Subramanian *et al.*, 2005). The Mn-O-Mn and Mn-O-H peaks are positioned at 529 eV and 532 eV, respectively, as depicted in Figure 4.3d (Yuan *et al.*, 2011). The deconvoluted peak at 530 eV represents the oxide group of Bi₂O₃. The obvious peak at 531 eV is linked to the Ni2p_{3/2} spin-orbit, which is attributed to the nickel foam current collector, and the peak situated at 532.9 eV represents the C=O functional group.

4.2.2 Formation Mechanism of Bi₂O₃/MnO₂ Materials

The formation of 2D MnO₂ occurred through the decomposition of KMnO₄, as depicted in Equation (4.1), as the Bi^{3+/2}/Bi couple theoretically recorded a lower redox potential (+0.308 V vs. SHE) than the MnO₄⁻/MnO₂ couple (+1.679 V vs. SHE), which promotes the spontaneous reduction process of MnO₄⁻ to MnO₂. The MnO₄⁻ ions oxidized water with concurrent oxygen evolution, which resulted in the precipitation of MnO₂ (Ashoka *et al.*, 2010; Liu *et al.*, 2011; Miao *et al.*, 2015; Ray *et al.*, 2016; Wang *et al.*, 2011; Wu *et al.*, 2011; Xia *et al.*, 2012):



The transformation of MnO_2 and Bi_2O_3 into $MnOOH$ and $BiOOH$, respectively, is hypothesized to have occurred during the hydrothermal process (a) in an enclosed self-generated pressurized autoclave system (Equations (4.2) and (4.3)). The formation of $BiOOH$ occurred through the destruction of Bi_2O_3 particles upon contact with water (Liu *et al.*, 2011).

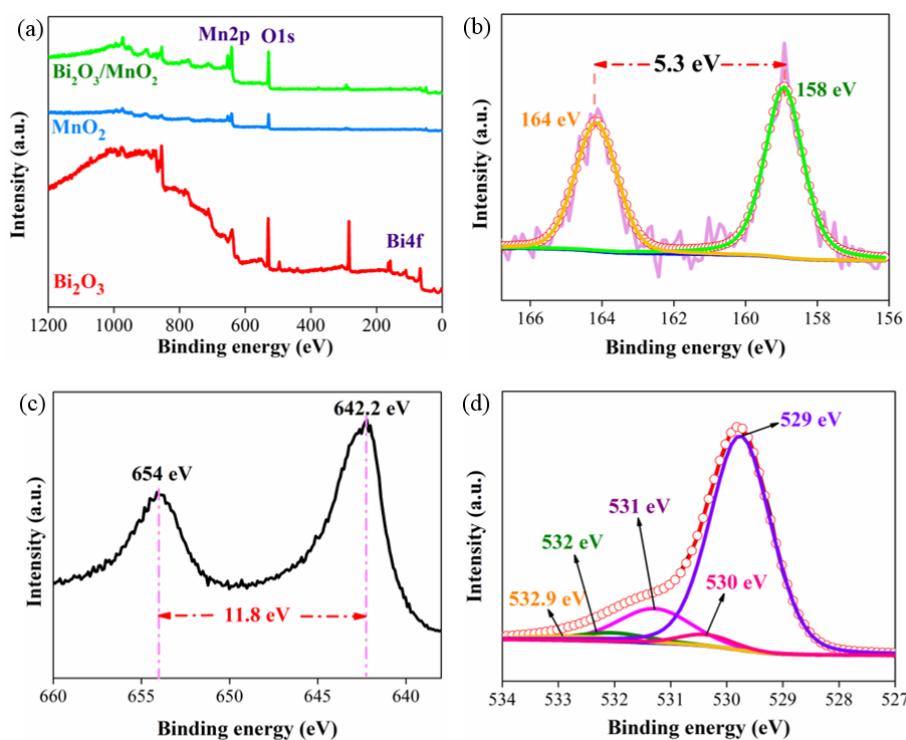
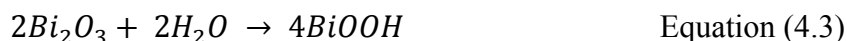
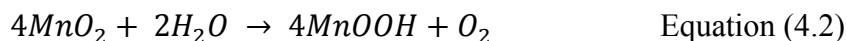


Figure 4.3 XPS analysis of (a) wide scan of Bi_2O_3 , MnO_2 , and Bi_2O_3/MnO_2 , and narrow scan of (b) $Bi4f$, (c) $Mn2p$, and (d) $O1s$. The MnO_2 is postulated to be Mn^{4+} because it has a different binding energy of 4.6 eV, which is the closest to the theoretical value of 4.8 eV, as determined from the $Mn3s$ plot, as shown in Figure A.3.

A schematic diagram that represents the plausible growth mechanism for the Bi_2O_3/MnO_2 precursors is presented in Figure 4.4. The decomposed MnO_4^- nanoparticles resulted in the formation of ultrathin $MnOOH$ nanosheets, which enveloped the $BiOOH$, as evidenced through the FESEM and TEM images. The immediately formed intermediate species $MnOOH$ and $BiOOH$ were subsequently transformed into a pure oxide lattice structure, which was more compact, and an impurity free Bi_2O_3/MnO_2 electrode upon calcination (b).

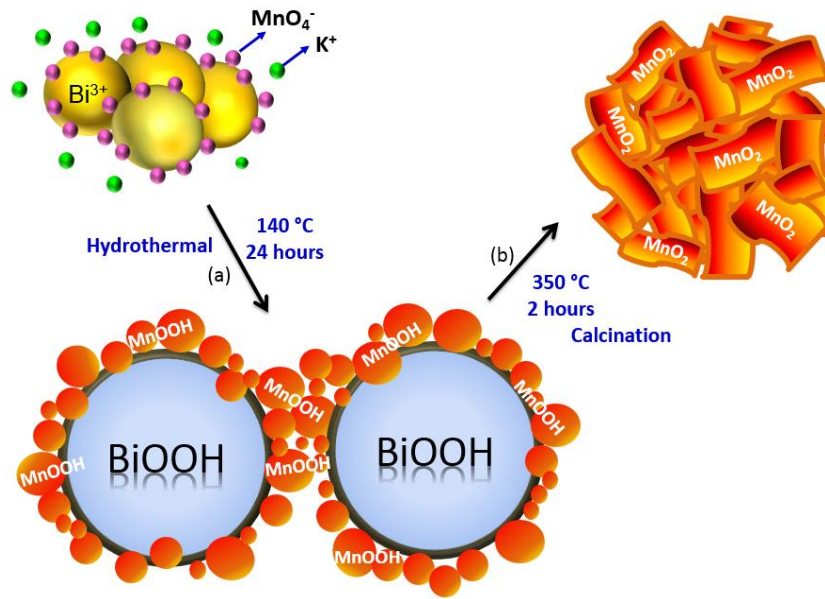
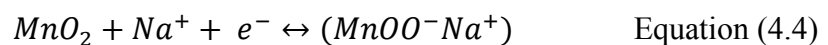


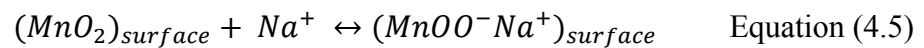
Figure 4.4 Plausible growth of $\text{Bi}_2\text{O}_3/\text{MnO}_2$ on nickel foam substrate during hydrothermal process. It shows that the MnO_2 nanosheet is compactly covering the Bi_2O_3 sphere after calcination.

4.2.3 The Charging and Discharging Mechanism of $\text{Bi}_2\text{O}_3/\text{MnO}_2$ Electrode

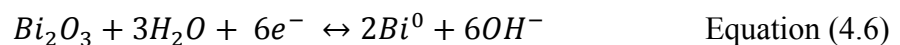
During the charging and discharging processes, two plausible reversible redox reactions of the 2D MnO_2 have been proposed based on its intercalation and de-intercalation process of Na^+ , as shown in Equation (4.4) (Iamprasertkun *et al.*, 2016; Lim *et al.*, 2014):



In addition, the adsorption of cations on the electrode surface from the electrolyte is proposed in Equation (4.5):



The charge storage of the Bi_2O_3 material in the aqueous electrolyte undergoes a quasi-conversion reaction, instead of the conventional intercalation mechanism, which indicates a change in the valence state of bismuth ($\text{Bi}^{3+} \leftrightarrow \text{Bi}^0$) during the repeatable charge/discharge process (Equation (4.6)).



4.2.4 Electrochemical Performances of Pseudocapacitor Under The Influence of Temperatures

The performances of the fabricated pseudocapacitor at various temperatures were investigated with the goal of determining the kinetics and ion diffusion mechanism of the super capacitor, which will govern the rate capability and specific capacitance of the super capacitor in future commercial applications. The voltammogram areas (Figure 4.5a) are precisely parallel to the capacitive performances of the super capacitor. The large cyclic voltammogram area of the super capacitor measured at 60 °C compared to those at 30 °C and 0 °C corresponded to a high specific capacitance of 150.2 F/g at a scan rate of 2 mV/s. The increase in capacitance was caused by enhanced ion mobility at a high temperature, which promoted greater charge transfer and storage capability. Additionally, the evaporation of electrolyte at a high temperature could induce the physisorption of electrolyte ions and give rise to Faradaic currents, which enhanced the capacitance performance (Masarapu *et al.*, 2009). However, the current response deviated slightly from the equilibrium state in the high potential region at a higher temperature, which implied the occurrence of electrochemical polarization (Wang *et al.*, 2013). Likewise, the sequential increase in specific capacitance from the galvanostatic charge/discharge, as shown in Figure 4.5b and Table 4.1, gave evidence that the application of temperature promoted electrochemical activation, which consequently resulted in a high capacitance performance compared to that at 0 °C. The good linear voltage-time profiles at 60 °C compared to those at 30 °C and 0 °C from the prolonged discharge time implied a good capacitive behavior and better charge storage capability at a higher temperature. This phenomenon suggested that the application of heat provided extra energy to trigger the chemical reaction.

The electrochemical impedance spectroscopy (EIS) measurement was conducted to investigate the resistivity performances such as equivalent series resistance (ESR) and charge transfer

resistance (R_{ct}) of the electrodes from the starting frequency of 100 kHz to an ending frequency of 0.01 Hz. The ESR values are obtainable at the first intercepting point on the x-axis, whereas the R_{ct} values could be obtained from the diameter of the semicircle formed (Stoller and Ruoff, 2010). ESR comprises the electrolyte and electrode resistance and R_{ct} is the rate of charge transfer at the electrode and electrolyte interface. Figure 4.5c shows that the super capacitor had a slightly greater resistance performance at 0 °C than at 30 °C and 60 °C. The super capacitor was highly resistive at 0 °C, giving an ESR of 2.76 Ω and R_{ct} of 5.65 Ω , as a result of the crystallization of the Na_2SO_4 electrolyte under a cold influence. Meanwhile, the low ESR of 0.42 Ω and R_{ct} of 0.6 Ω found for the super capacitor at 60 °C could be ascribed to the expansion of the nanocomposite matrix, which facilitated the diffusion of electrolyte ions. In addition, the more vertical line of the 60 °C super capacitor at the lower frequency region was indicative of the ideal capacitive behavior of the electrodes and lower diffusion resistance at a high temperature (Wang *et al.*, 2013).

The cyclic retentive performance of the electrode under the influence of the various temperatures was also investigated, as depicted in Figure 4.5d. The 60 °C super capacitor could still retain 75% of its original capacitance after extensive expansion and contraction processes, even under prolonged heating. The degradation and deterioration of the nanocomposite matrix upon continuous expansion and contraction processes, especially under prolonged high-temperature measurements, stimulated the dissolution of the MnO_2 (Ng *et al.*, 2017; Wang *et al.*, 2013). The influence of heating is hypothesized to exaggerate the mechanical and electrical faults between the MnO_2 and Bi_2O_3 and the framework destruction, thereby leading to a disabled charge storage process. Moreover, the morphological change and phase transition inevitably hastened the material's degradation. Comparably, the super capacitor measured at 30 °C showed a 5% capacitive fade, with negligible capacitance loss for the 0 °C super

capacitor, proving the good electrochemical reversibility of the $\text{Bi}_2\text{O}_3/\text{MnO}_2$ electrodes. In addition, the excellent capacitance retention was ascribed to the milder resistive performance, which facilitated the movement of the electrolyte ions into the inner pores of the nanomaterial. Interestingly, the increase in the capacitance from 0 to 30 °C could be the result of the defrosting of the Na_2SO_4 electrolyte, which hastened the diffusivity of the electrolyte ions. In contrast, the abrupt decrease in the capacitance from 78.8 F/g to 39.3 F/g (60 °C to 30 °C) could be attributed to the partial degradation of the active materials upon heating. Nevertheless, it still possessed high cyclic stability (more than 100% capacitance retention) after 1000 charging/discharging cycles. Overall, the electrochemical performances of the super capacitor at 60 °C were better than those of the super capacitors tested at 0 and 30 °C, which is consistent with the results of other reported works (Table 4.2).

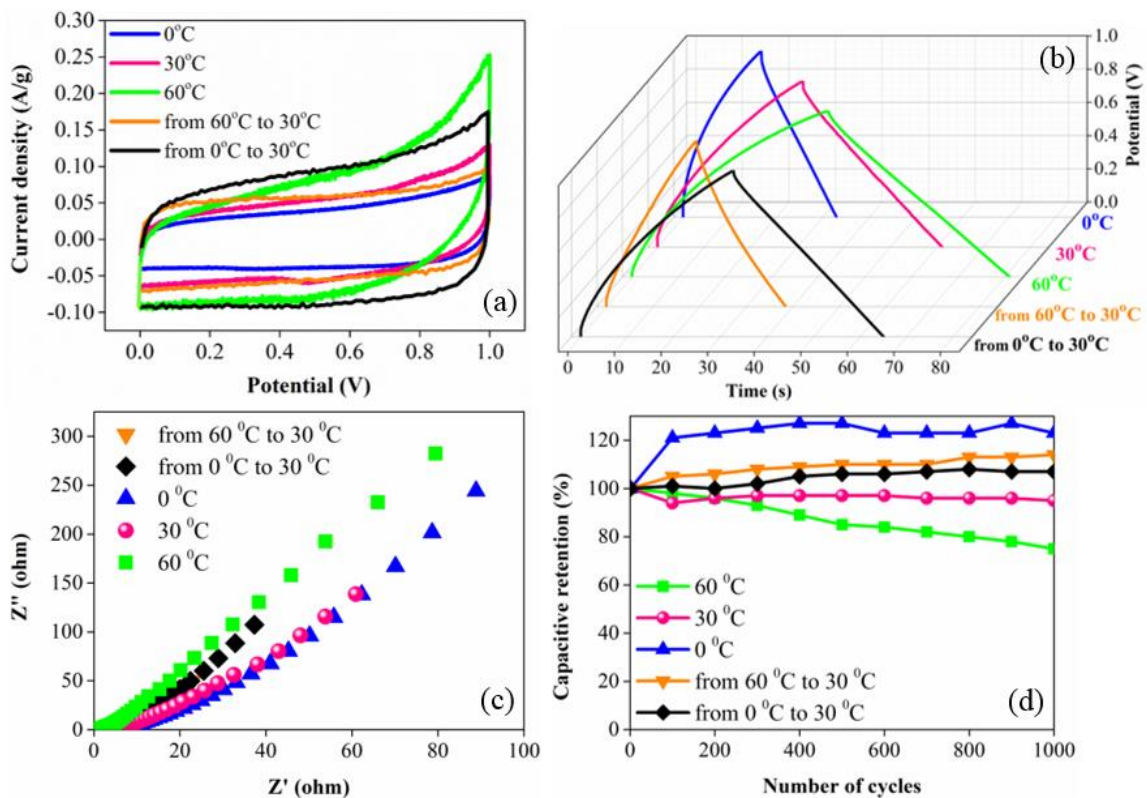


Figure 4.5 (a) Cyclic voltammogram, (b) galvanostatic charge/discharge, (c) Nyquist plot, and (d) life cycle of $\text{Bi}_2\text{O}_3/\text{MnO}_2$ super capacitors at different temperatures.

The milder resistance performance of the $\text{Bi}_2\text{O}_3/\text{MnO}_2$ super capacitor at $60\text{ }^\circ\text{C}$ enhanced the energy storage ability and power delivery efficiency, with energy and power densities of 10.4 Wh/kg and 75.1 W/kg , respectively (Figure 4.6a and Table 4.1). Comparatively, the super capacitor exhibited twofold decreases in its energy (5.3 Wh/kg) and power densities (38.2 W/kg) when it was tested at $0\text{ }^\circ\text{C}$. Figure 4.6b and 4.6c delineate the indistinguishable resistive performances of the cooled super capacitor for various defrosting times. The high capacitance retention ability implies an efficient charge diffusion, transportation, and excellent storage capability of the super capacitor even under cold conditions. As observed, the surface scaffold of the $0\text{ }^\circ\text{C}$ $\text{Bi}_2\text{O}_3/\text{MnO}_2$ electrode (Figure 4.7a) was coarser than those at $30\text{ }^\circ\text{C}$ (Figure 4.7b) and $60\text{ }^\circ\text{C}$ (Figure 4.7c) after being exposed to retention measurement under cold conditions. The rough surface could have resulted from the crystallization of the electrolyte and active materials, which would impede the facilitation of electrolyte ions, and consequently lead to a lower capacitance performance. Cracks were observed on the $60\text{ }^\circ\text{C}$ coated surface and a smoother surface ($30\text{ }^\circ\text{C}$) was presented upon contact with the electrolyte during the continuous cycling measurement.

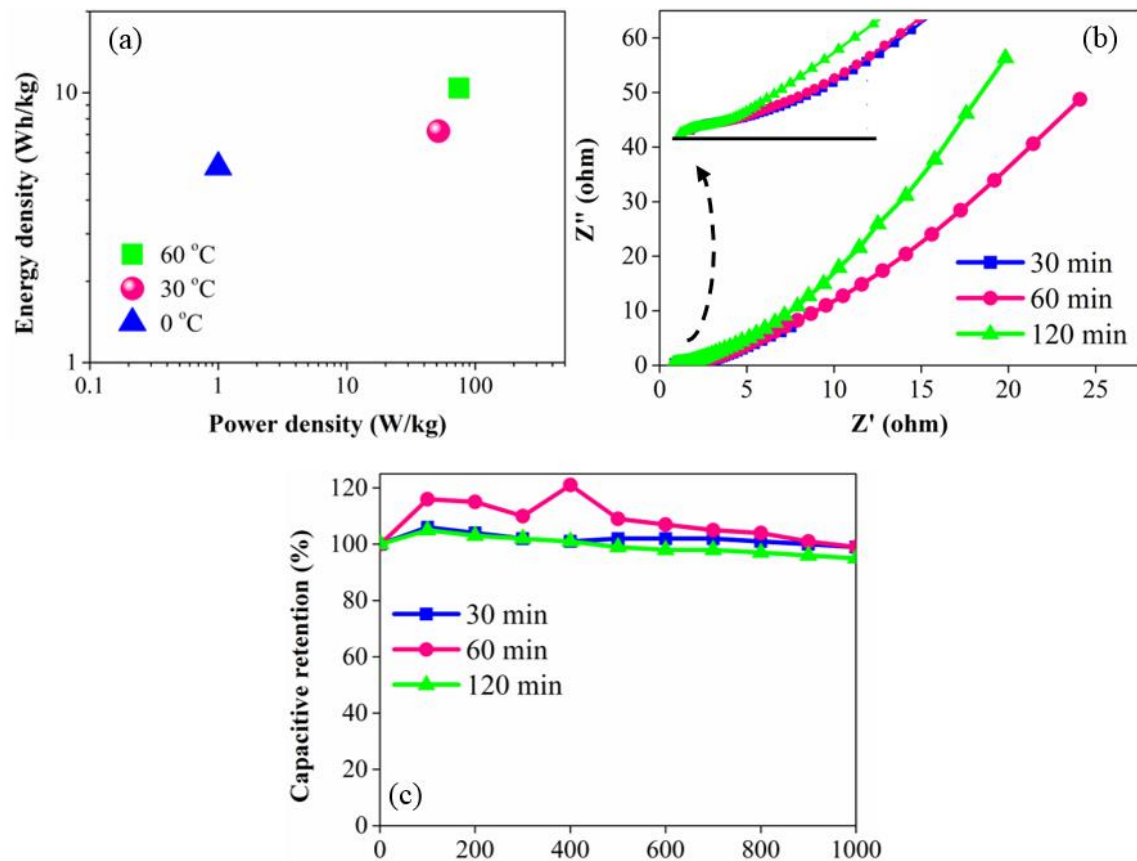


Figure 4.6 (a) Ragone plot of $\text{Bi}_2\text{O}_3/\text{MnO}_2$ super capacitor at temperatures of 0, 30, and 60 °C, while (b) EIS and (c) life cycle of $\text{Bi}_2\text{O}_3/\text{MnO}_2$ super capacitor at various defrosting periods (30, 60, and 120 min) after being cooled at 0 °C for 1 hour. The EIS of $\text{Bi}_2\text{O}_3/\text{MnO}_2$ super capacitor was measured from starting frequency of 100 kHz to ending frequency of 0.01 Hz.

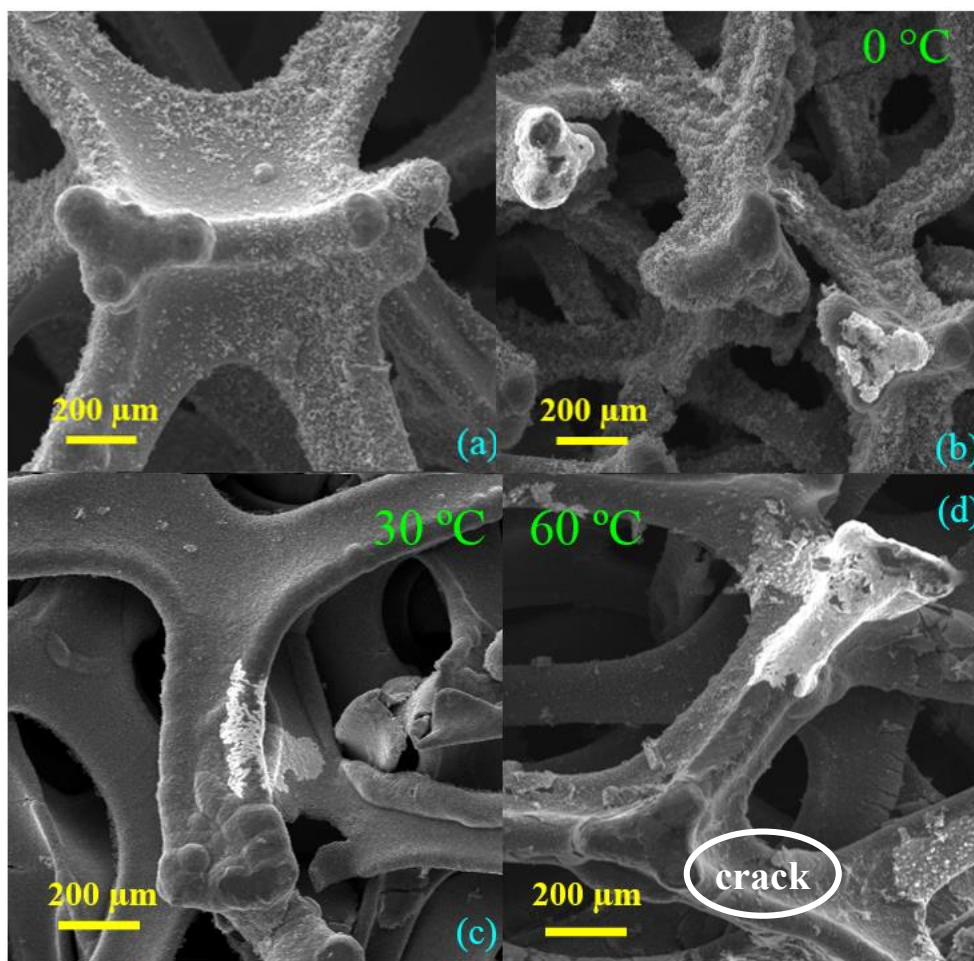


Figure 4.7 FESEM images of $\text{Bi}_2\text{O}_3/\text{MnO}_2$ (a) before life cycle at 30 °C and (b)–(d) after life cycle measurements at 0 °C, 30 °C, and 60 °C, respectively.

Table 4.1 Tabulated energy and power density, and specific capacitance of $\text{Bi}_2\text{O}_3/\text{MnO}_2$ super capacitors, extracted from galvanostatic charge/discharge (CD) at 2 mA/cm².

	0 °C	30 °C	60 °C
Specific capacitance (F/g)	23.9	62.3	78.8
Energy density (Wh/kg)	5.3	7.1	10.4
Power density (W/kg)	38.2	51.8	75.1

Table 4.2 Electrochemical performances of present and reported super capacitor studies under temperature influences or at room temperature.

Active materials	Electrolyte	Capacitance	Comments	Ref.
NiO//AC	PVA-5M KOH-H ₂ O	73.4 F/g at 0.1 A/g (2-electrode system)	Life cycle profile attenuated 7% after 800 cycles at 40°C	(Yuan <i>et al.</i> , 2006)
MnO ₂ @CNF	0.5M Na ₂ SO ₄	546 F/g at 1A/g (3-electrode system)	Exhibited good cycling stability (95.3%) at 25°C; diminishing at 75°C (82.4%) after 1000 cycles.	(Wang <i>et al.</i> , 2013)
T-NT/Bi ₂ O ₃	1M NaOH	340 mF at 3 mA/cm ² (3-electrode system)	75% at room temperature after 500 cycles	(Sarma <i>et al.</i> , 2013)
Bi ₂ O ₃ /Cu	1M NaOH	22 mF/cm ² at 20 mV/s (3-electrode system)	Measured at room temperature	(Gujar <i>et al.</i> , 2006)
Bi ₂ O ₃ /MnO ₂	1M Na ₂ SO ₄	62.3 F/g at 2 mA/cm ² (2-electrode system)	~ 95 % capacitance retained at room temperature, opposed to 63% at 60°C upon 1000 cycles. ~16.5 F/g capacitance increment upon heated.	This work

All in all, the ultra-high durability, stability, and reversibility of the Bi₂O₃/MnO₂ super capacitor, regardless of the temperature, are accredited to the inclusion of Bi₂O₃ within the MnO₂ matrix. The cyclic retentive profile (Figure 4.8a) shows a highly stable and durable Bi₂O₃ electrode material, which could retain 90% of its original capacitance after 1000 galvanostatic cycles, compared to the MnO₂ electrode material (62%). The addition of Bi₂O₃

in the MnO_2 matrix made a major contribution to the sustainability and reversibility of the hybrid super capacitor. Evidently, the stability and durability performances were dramatically improved from 62% (solely MnO_2) to 95% upon the insertion of Bi_2O_3 . The Nyquist plots (Figure 4.8b) before the cyclic tests and after 100, 500, and 1000 cyclic tests show no obvious distinctions, which suggest a negligible or minor degradation of the electrode, demonstrating the properties of a highly sustainable and reversible energy storage device, which is highly suitable for automotive applications (Cheng *et al.*, 2013).

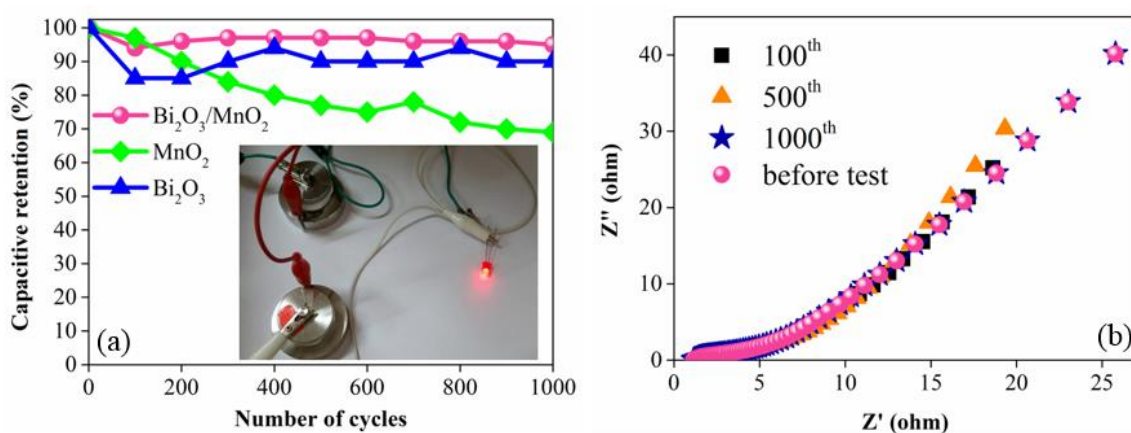


Figure 4.8 (a) Cyclic retention comparison between $\text{Bi}_2\text{O}_3/\text{MnO}_2$, MnO_2 , and Bi_2O_3 super capacitors. (b) Nyquist plots of $\text{Bi}_2\text{O}_3/\text{MnO}_2$ super capacitor after life cycle performances at room temperature. Figure 4.8(a) shows an image of a light emitting diode (LED) lighted by the $\text{Bi}_2\text{O}_3/\text{MnO}_2$ super capacitor. The active electrode possesses an active surface area of 1 cm^2 .

Despite the symmetrical super capacitor renders high stability, which is an alluring trait that suits various applications, however, there is a need for greater energy densities performance for a super capacitor that is viable for large scale commercial applications. To achieve high energy density performance, utilizing a high capacitance electrode and latter through the use of non-aqueous electrolyte with larger electrochemical stability window is much preferable to strike for high energy density. While, a more prominent effort in extending the potential window of a super capacitor for high capacitance value is through the assemble of an

asymmetrical cell; using a capacitor type electrode in conjunction with a battery type electrode (Jampani *et al.*, 2010).

4.3 Bi₂O₃/MnO₂//PyR Asymmetrical Super Capacitor

4.3.1 Electrochemical Measurement of Bi₂O₃/MnO₂//PyR Asymmetrical Super Capacitor

CV (Figure 4.9) was first conducted to determine the positive and negative electrodes of the super capacitor and to estimate the potential window of the super capacitor in a three-electrode system with a platinum and saturated calomel electrode as the counter and reference electrodes, respectively. Figures 4.9a and 4.9b show the CV profiles of Bi₂O₃/MnO₂ and PyR electrodes respectively. Figures 4.9a and 4.9b show the CV profiles of Bi₂O₃/MnO₂ and PyR electrodes at various potential window ranges. It shows that Bi₂O₃/MnO₂ electrode exhibited a quasi-rectangular voltammogram at the positive window ranges from 0-1 V, while PyR has a relatively rectangular voltammogram at the negative region (potential window ranges from -0.2-0.4 V).

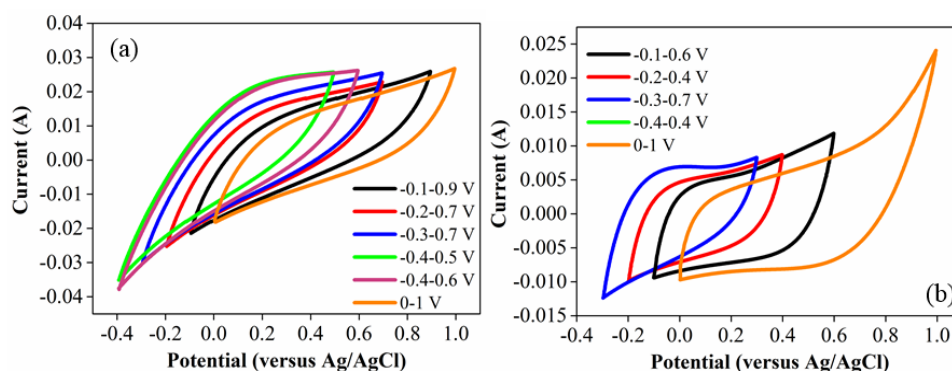


Figure 4.9 Assignment of positive and negative electrodes determine through three-electrodes cyclic voltammetry system. The CV curves of (a) Bi₂O₃/MnO₂ positive and (b) PyR negative electrodes at different potential ranges. The pseudo-rectangular Bi₂O₃/MnO₂ and PyR voltammograms are prominent at 0-1 V and -0.2-0.4 V potential range, respectively, giving an overall potential window of 1.6 V. PyR refers to polypyrrole and reduced graphene oxide.

Subsequently, a Bi₂O₃/MnO₂ positive electrode was integrated towards a PyR negative electrode for an asymmetrical super capacitor. The potential window is the sum of the potential

range of $\text{Bi}_2\text{O}_3/\text{MnO}_2$ and PyR, which was successfully being widened to 1.6 V, which gave a specific capacitance of 144.1 F/g, obtained at a scan rate of 2 mV/s. The asymmetrical super capacitor exhibited 3.6-fold increment in its energy and 2.2-fold power densities performances relative to the $\text{Bi}_2\text{O}_3/\text{MnO}_2$ symmetrical super capacitor (Figure 4.10). The improved supercapacitive performances, in terms of its specific capacitance and energy density confirm the suitability of the asymmetrical super capacitor to be integrated as part of the photo-super capacitor. However, the dissatisfying stability performance of $\text{Bi}_2\text{O}_3/\text{MnO}_2//\text{PyR}$ asymmetrical super capacitor implies the non-synergism of nanocomposite materials between the positive and negative electrode, which hence urge for the discovery of new super capacitor materials. Table 4.3 tabulated the performances of symmetrical $\text{Bi}_2\text{O}_3/\text{MnO}_2$ super capacitor and $\text{Bi}_2\text{O}_3/\text{MnO}_2//\text{PyR}$ asymmetrical super capacitor. In the next section, an RZCo/PyR asymmetrical super capacitor was fabricated for further electrochemical assessments.

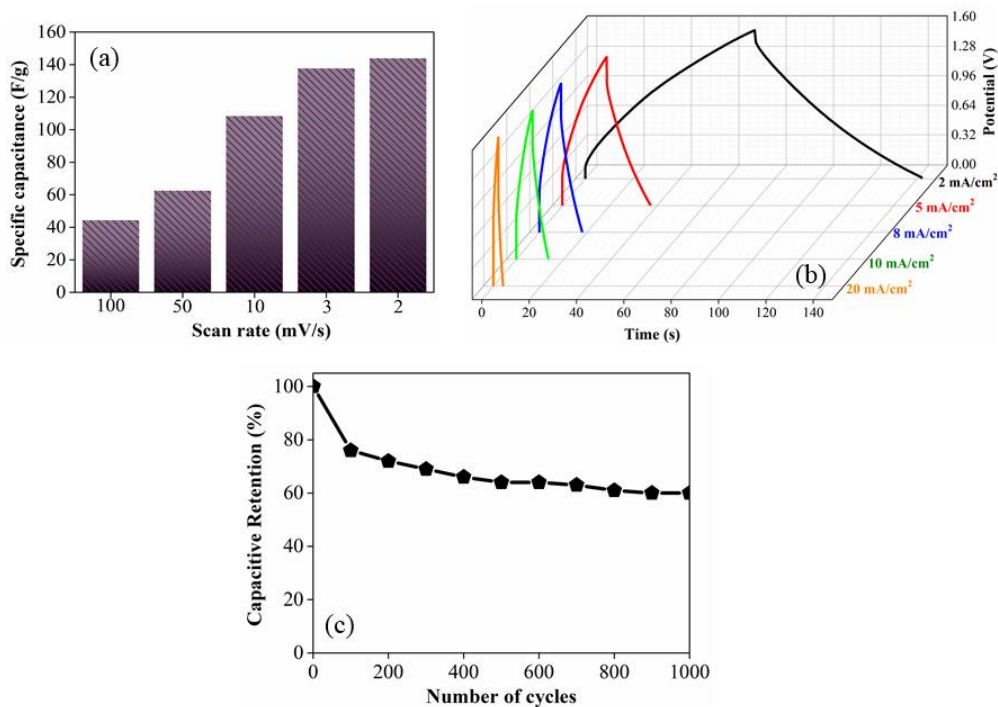


Figure 4.10 (a) Specific capacitance obtained through cyclic voltammogram at the scan rate of 100 to 2 mV/s, (b) galvanostatic charge/discharge from current density of 2 mA/cm² to 20 mA/cm², and (c) capacitive retention of $\text{Bi}_2\text{O}_3/\text{MnO}_2//\text{PyR}$ asymmetrical super capacitor.

Table 4.3 Electrochemical performances of Bi₂O₃/MnO₂ symmetrical super capacitor and Bi₂O₃/MnO₂//PyR asymmetrical super capacitor. The Bi₂O₃/MnO₂ is assigned as the positive electrode, while the PyR is the negative electrode for the asymmetric configured super capacitor. The specific capacitance is obtained from galvanostatic charge/discharge.

Super Capacitors	Potential Window (V)	Specific Capacitance (F/g)	Energy Density (Wh/kg)	Power Density (W/kg)	Capacitive Retention (%)
Bi ₂ O ₃ /MnO ₂ (Symmetrical)	1.0	62.3	7.1	51.8	95 after 1000 cycles
Bi ₂ O ₃ /MnO ₂ //PyR (Asymmetrical)	1.6	89.4	25.6	115.3	60 after 1000 cycles

4.4 RZCo//PyR Asymmetrical Super Capacitor

In searching of high performing asymmetrical super capacitor for photo-super capacitor application, the synergistic effect and compatibility of the active materials used for positive and negative super capacitor are highly important. In this section, we study the performances of an asymmetrical super capacitor composed of reduced graphene oxide (rGO), zinc oxide (ZnO), and cobalt oxide (Co₃O₄), in short denoted as RZCo as the positive electrode; whilst rGO and polypyrrole (abbreviated as PyR) performs as the negative electrode of the asymmetrical super capacitor. The sandwiched system between RZCo positive electrode and PyR negative electrode brought to RZCo//PyR asymmetrical super capacitor. The performance of RZCo//PyR asymmetrical super capacitor was evaluated and was compared against ZCo//PyR asymmetrical super capacitor and KEMET commercial super capacitor.

4.4.1 Material Characterizations of RZCo Cathodic Materials

Figure 4.11a shows the highly crystalline zinc oxide/cobalt oxide (ZCo) flower-like structures on the surface of a graphite sheet that acted as the current collector for the as-assembled super capacitor. Meanwhile, Figure 4.11b reveals similar flower-like structures adhering on both surfaces of the translucent rGO sheets, in which the composite formed a layer on a graphite

sheet. The size of ZCo on rGO was fourfold smaller than that of the neat ZCo because the growth of the flower-like structures was impeded by the presence of rGO that acted as a support. Figure 4.12 depicts the postulated formation of ZCo and RZCo. In the case of ZCo, the precursors freely dispersed and adhered on the graphite sheet during the hydrothermal process, which subsequently grew and formed flower-like structures. Meanwhile, for RZCo, the growth of the ZCo structures was hindered by the overcrowded nucleation sites on the graphene oxide (GO). As GO had a stronger affinity towards the graphite sheet compared to the metal ions due to the hydrophobic interaction, therefore, the GO would adhere onto the surface of the graphite sheet first, followed by the metal ions. This overcrowding phenomenon restricted the growth of ZCo, resulting in smaller particle size of ZCo on rGO.

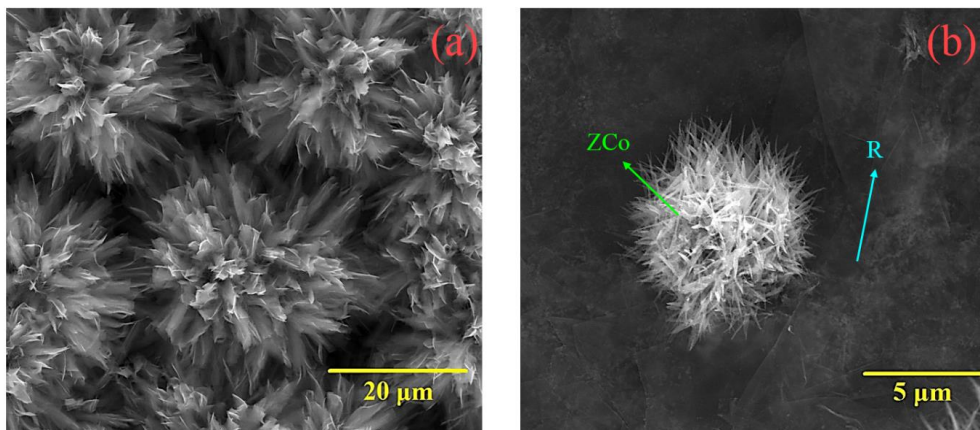


Figure 4.11 FESEM images of (a) ZCo positive electrode and (b) RZCo positive electrode.

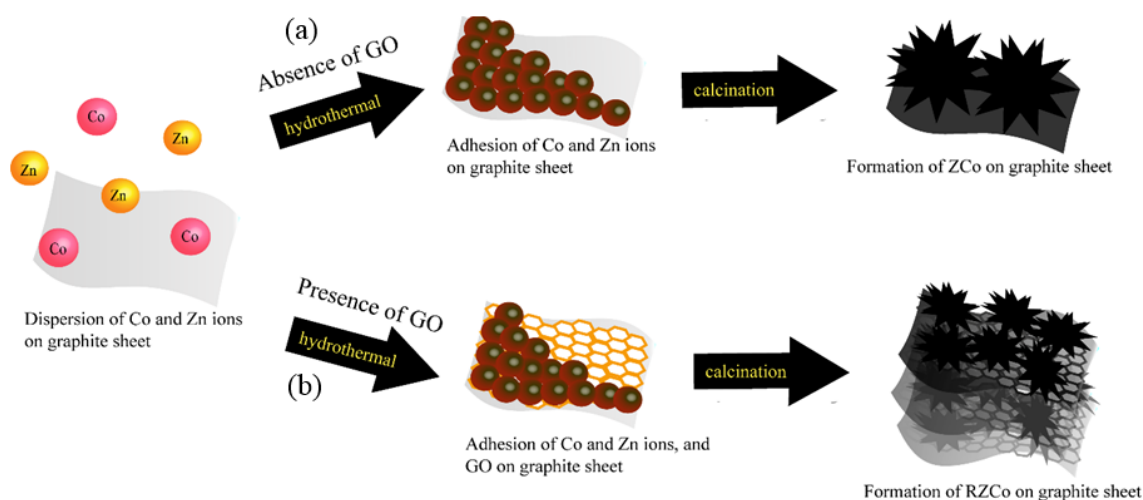


Figure 4.12 The growth of (a) ZCo and (b) RZCo on graphite sheet. The eventual particle size of ZCo was dependent on the presence of GO. The graphite sheet acted as a current collector for the as-assembled super capacitor.

The XRD profile (Figure 4.13a) provides evidence for the embedment of ZnO, Co₃O₄, and rGO on the current collector (graphite sheet). The high-intensity graphite peak shown at $\sim 26^\circ$ is ascribed to the major detection from the current collector itself due to the low concentration of the active materials used. The absence of GO peak was at $\sim 10^\circ$ and appearance of the weak intensity peak was at $\sim 24^\circ$, hence manifests the graphitic carbon has been successfully reduced to rGO (Pei *et al.*, 2010). The non-prominent rGO peak is due to the only small amount (0.02 mg/ml) of GO used in this reaction. On the contrary, the ZnO crystalline peaks were observed at 31.35° , 37.02° , 54.73° , and 77.51° whilst Co₃O₄ denotes peaks residing at 31.35° , 37.02° , 44.87° , 59.42° , and 65.22° . The Co₃O₄ nanoparticles were present in the cubic phase structure with Fd-3m (227) space group. The peak of ZnO at high intensity 54.73° was assigned to hkl indices of 110 (Rahman *et al.*, 2013; Subhan and Ahmed, 2014). It thus conclusively evidenced the complete transformation of active precursors into the oxides form. The FTIR spectrum could further prove the presence of Co₃O₄ and ZnO within the ternary system, where the peaks of Co₃O₄ and ZnO are indistinguishable in the region below 700 cm^{-1} . The ZnO peaks split into two (521.94 and 643.55 cm^{-1}) upon 400°C calcination, as observed in Figure 4.13b (Sowri *et*

al., 2013). Simultaneously, the fully transformed spinel phase of Co_3O_4 at 521.94 and 643.55 cm^{-1} indicates the OB3 vibration in spinel lattice (B is Co^{3+} in octahedral hole) at 521.94 cm^{-1} , while the IR absorption at 643 cm^{-1} denotes Co^{2+} resided in tetrahedral hole. It thus evidenced the complete formation of Co_3O_4 spinel phase after heat treatment (Xu *et al.*, 2012). The medium intensity of C-O peak (1069.19 cm^{-1}) implies the remaining oxygen groups ascribed to the partial reduction of GO. On the contrary, the absorption band at 1616.59 cm^{-1} indicates C=C sp^2 carbon (Wang *et al.*, 2013).

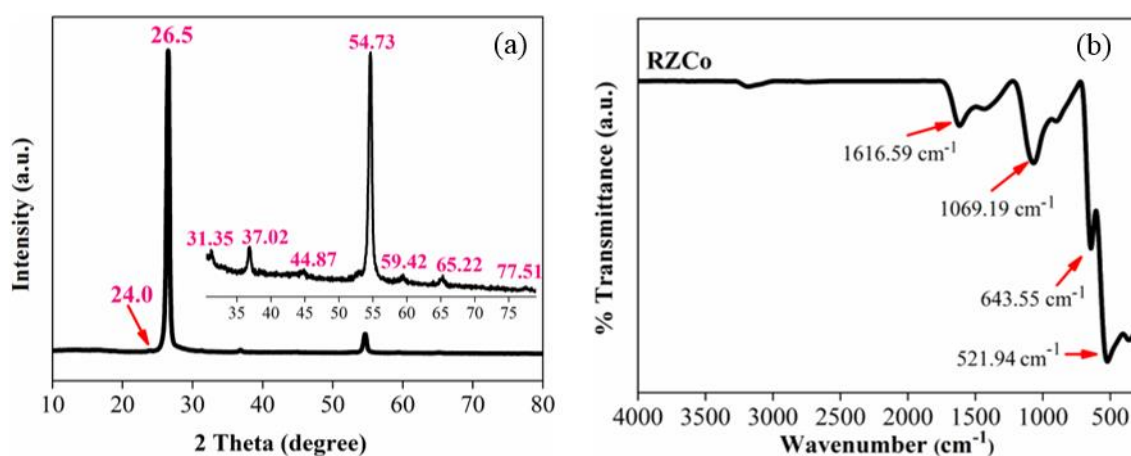


Figure 4.13 (a) XRD profile and (b) FTIR spectrum of RZCo positive electrode. Inset shows the magnified XRD peaks of RZCo positive electrode.

The wide scan of RZCo (Figure 4.14a) has evidenced the embedment of GO, Zn and Co elements in the form of oxide within the matrix with binding energy in the range of ~ 1022 eV to ~ 282 eV. Generally, C1s has the binding energy of ~ 284 eV and O1s at the peak of 531 eV, whereas Co2p and Zn2p are located at the binding energy of 743 eV and 1020 eV, respectively. The weak intensities of wide scan analysis could be due to the employment of low concentration of precursors and active materials. The succession in depositing Zn- and Co-based active materials on the graphite sheet were proven from the Zn2p and Co2p regions, as depicted in Figures 4.14b and 4.14c. Two strong intensities of the Zn2p peaks, which are the Zn2p_{1/2} and Zn2p_{3/2} peaks resided at 1043.7 eV and 1020.7 eV, respectively recorded a

difference in the binding energy of 23 eV, and proved the formation of ZnO. On the contrary, Figure 4.14c shows two strong deconvoluted $\text{Co}2p_{1/2}$ and $\text{Co}2p_{3/2}$ peaks located at ~ 795 eV and ~ 780 eV, respectively. Co possesses a huge spin-orbit splitting constant of 15 eV and the deconvoluted $\text{Co}2p_{3/2}$ peak was assigned to the oxidation state of Co^{3+} (Baek *et al.*, 2012). Figure 4.14d reflects four deconvoluted peaks from the O1s region where C=O bonding is located at 532.6 eV, which could be either the remnant oxygen groups of rGO. The weak intensities of GO oxygen groups were observed in the C1s region (Figure 4.14e) thus deduced the succession in reducing GO into rGO, which was in good agreement with the XRD profile. In addition, the peak of 531.5 eV represented the OH groups adsorbed on the surface of metal oxides and a weak intensity Zn-O peak resided at 530.3 eV, which implies the presence of ZnO materials (Al-Gaashani *et al.*, 2013). The high-intensity C1s (Figure 4.14e) peak at 284.2 eV represented the sp^2 hybridized carbon (Ray *et al.*, 2011), which was expected to be attributed from GO. Thus, we deduced the accomplishment of forming ZnO and Co_3O_4 within the nanocomposite upon calcination for 2 hours at 400°C .

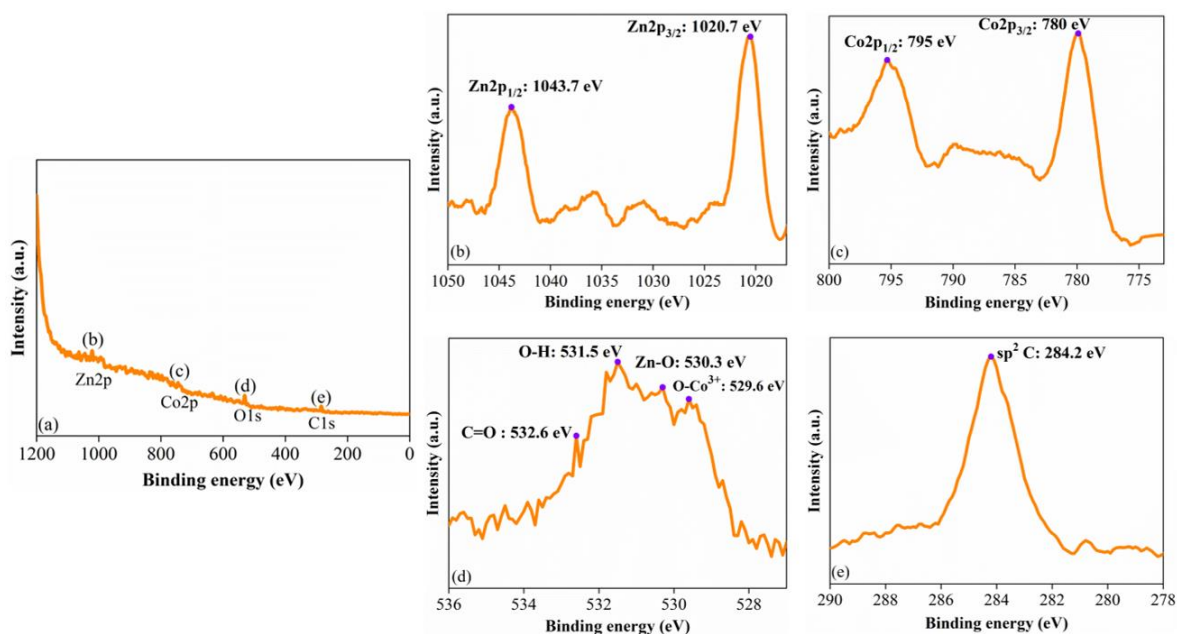


Figure 4.14 XPS analysis of (a) wide scan, (b) Zn2p, (c) Co2p, (d) O1s, and (e) C1s of RZCo positive electrode.

4.4.2 Electrical Conductivity

The electrical conductivity of the super capacitor positive electrode was investigated to study the electrical charge flow efficiency, as depicted in Table 4.4. It shows that the ternary nanocomposites (83.542 S/m) render better conductivity as opposed to the binary nanocomposites (72.254 S/m), which implies an ease of charges flow within the composite vicinity which could be ascribed to the low resistivity of $1.197 \times 10^{-2} \Omega$. It hence significantly shows the contribution of rGO in framing a highly porous, intercalated, and resistive-less pathway, consequently eases the diffusivity of electrolyte ions, which is consistent with the FESEM image as discussed in Figure 4.11 (Kim *et al.*, 2014).

Table 4.4 Electrical conductivity measurements performed on (a) ZCo, and (b) RZCo graphite sheets positive electrode.

	Positive Electrode	Resistivity, $\times 10^{-2} (\Omega)$	Electrical conductivity (S/m)
(a)	ZCo	1.384	72.254
(b)	RZCo	1.197	83.542

4.4.3 Electrochemical Performances of RZCo//PyR Asymmetrical Super Capacitor

Before electrochemical performances of the RZCo//PyR asymmetrical super capacitor were conducted, three-electrode cyclic voltammetry was prior to be conducted:

- (i) To determine the positive and negative electrodes of an asymmetrical super capacitor
- (ii) To determine the overall potential window of the asymmetrical super capacitor

Figure 4.15a shows the PyR electrode is suitable to be assigned as the negative electrode as it displays a pseudo-rectangular cyclic voltammogram in the negative region. At the potential range of 0-1 V, the voltammogram of PyR is distorted, which is an indication of limited energy storage ability. Among the pseudo-voltammograms, the best capacitance of PyR electrode recorded at the potential from -0.2-0.4 V. Meanwhile, the RZCo electrode is suitable as the

positive electrode. The RZCo electrode (Figure 4.15b) exhibited the highest capacitance at the potential range of 0-1 V, as opposed to other potential ranges. Additionally, a more pseudo-rectangular voltammogram is illustrated at 0-1 V, which implies an ideal capacitive behavior with fast charge/discharge process.

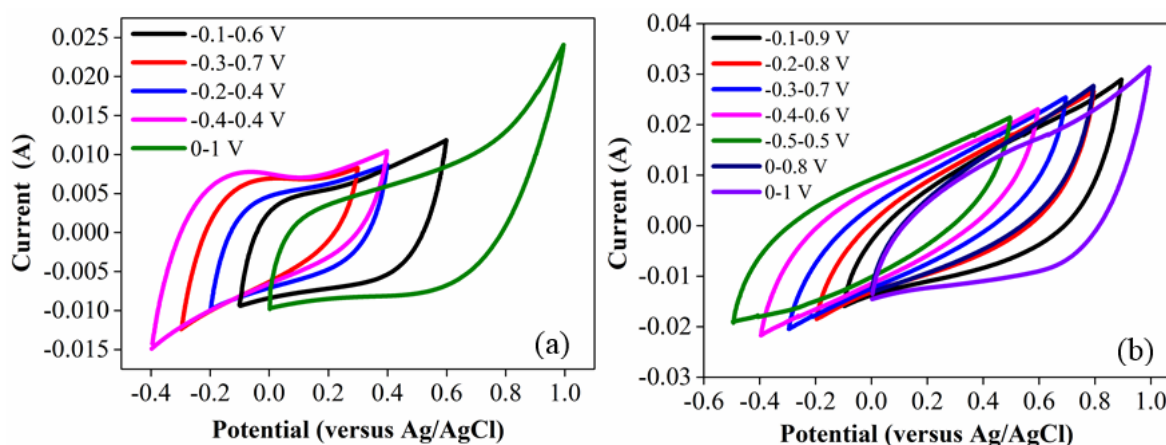


Figure 4.15 Cyclic voltammograms of (a) PyR and (b) RZCo electrodes at various potentials range.

Subsequently, the electrochemical performances were measured via two-electrode system to mimic the real application of a super capacitor. The EIS measurement was conducted to investigate the resistivity performances such as ESR and R_{ct} of the electrodes from the starting frequency of 100 kHz to an ending frequency of 0.01 Hz as shown in Figure 4.16a. The inset shows that the magnified semicircle (R_{ct}) of RZCo//PyR asymmetrical super capacitor is larger than ZCo//PyR, denoted the values of 16.519 Ω and 9.395 Ω , respectively. The high resistivity of RZCo//PyR asymmetrical super capacitor could be attributed to the diffusion of Na^+ between the electrolyte and bulky electrode interface, which brought to the high series interfacial resistance and Faradaic reaction (Meher *et al.*, 2010). Nevertheless, the limitation of rGO could be mitigated with the incorporation of pseudo-capacitive materials where the synergistic effect between rGO and transition metal oxides rendered low ESR of 0.9254 Ω , which is approximately 2-fold lower than ZCo//PyR asymmetrical super capacitor (1.9331 Ω). This

phenomenon could be ascribed to the inclusion of rGO and binder-less feature, consequently, enhances the charge transport ability thus reduces the total resistance of the wholly asymmetrical super capacitor.

The Ragone plot (Figure 4.16b) reflects the efficiencies of storing and delivering energy from the fabricated asymmetrical super capacitor device. The inclusion of rGO and the symbiosis effect between the positive and negative electrodes of the RZCo//PyR asymmetrical super capacitor contributed to an energy density of 15.8 Wh/kg and power density of 3575.3 W/kg at a scan rate of 100 mV/s. Meanwhile, the amount of energy stored increased to 41.8 Wh/kg, with an attainable power density value of 188.33 W/kg at a scan rate of 2 mV/s, as opposed to the energy (14.6 Wh/kg) and power density (65.9 W/kg) of ZCo//PyR. The RZCo//PyR asymmetrical super capacitor possessed twice the energy density and eight times the power density of the KEMET commercial super capacitor at a scan rate of 2mV/s (Figure 4.16b and Table 4.5). In addition, the electrochemical performances of the RZCo//PyR asymmetrical super capacitor were comparable to those of others, as depicted in Table 4.6. The higher energy density was achievable at the lower scan rate ascribed to the highly efficient intercalation and de-intercalation of electrolyte ions within the open pore system of the asymmetrical super capacitor matrix (Dubal and Holze, 2013; Lu *et al.*, 2011). The lower energy density and inefficient energy transfer rate of ZCo//PyR could be attributed to the highly resistive environment and undesirable pore size distribution within the matrix with the absence of rGO on the positive electrode (Fan *et al.*, 2011). In addition, the rigid and open structure of the nanocomposite matrix served as an electrolyte ion diffusivity valley. This enhanced the energy transfer rate, which is in great agreement with the low ESR value reported in Figure 4.16a.

The cyclic retention and stability were performed under a current density of 2mA/cm², as depicted in Figure 4.16c. The cyclic retention, which was effectively improved upon the

incorporation of rGO, gave rise to a specific capacitive retention of 87% relative to an asymmetrical super capacitor without rGO, which had a retentive specific capacitance of only 60%. A minor degradation occurred upon the inclusion of rGO because of the EDLC nature of the graphitic materials, which could provide cyclic stability (Ng *et al.*, 2015) without compromising the highly conductive and large surface active area properties of rGO. The pseudo-capacitive materials (Co_3O_4 and ZnO), which acted as spacers in preventing the restacking of rGO layers, were also essential contributors to the capacitive enhancement, because of the resistive-less electrolyte ion flow, which enhanced the charge storage reactions (Chen *et al.*, 2014). Nevertheless, the gradual declines in the cyclic retention observed in both plots were due to the deterioration of the active materials and polymer chain degradation after an excessive swelling and shrinking process (Eeu *et al.*, 2013). As a comparison, the ZCo//PyR asymmetrical super capacitor lost its capacitive retention ability of ~ 7.35 F/g after 100 cycles of charging/discharging process, which implies an unsustainable electrocatalytic activity performance for the asymmetrical super capacitor without the inclusion of rGO.

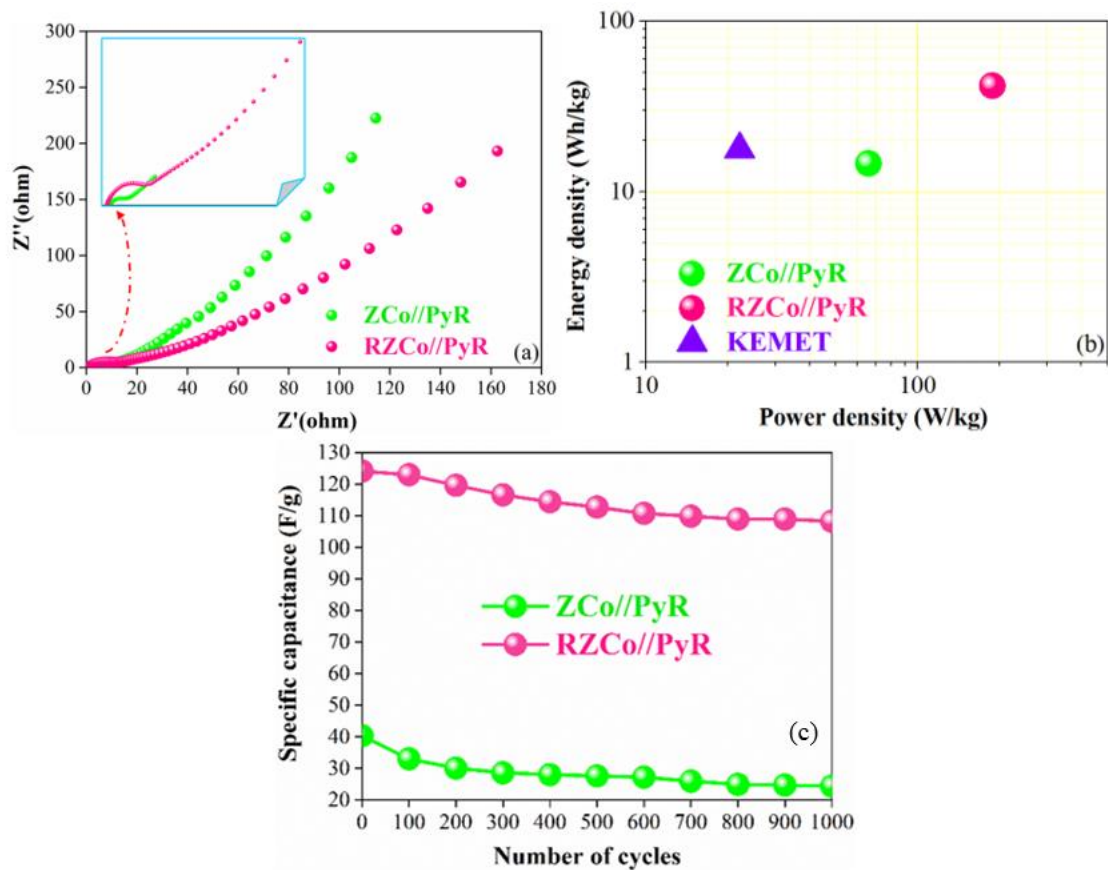


Figure 4.16 (a) Nyquist plot, (b) ragone plot, and (c) life retention of ZCo//PyR and RZCo//PyR asymmetrical super capacitor. Inset shows the magnified high frequency region and the life cycle was measured at current density of 2 mA/cm². The energy and power density of as-fabricated asymmetrical super capacitors were compared against the KEMET commercial super capacitor.

Table 4.5 Tabulated results of energy and power density of as-fabricated asymmetrical super capacitor against KEMET commercial super capacitor at scan rate of 2mV/s.

Asymmetric super capacitor	Energy density (Wh/kg)	Power density (W/kg)
ZCo//PyR	14.6	65.9
RZCo//PyR	41.8	188.3
KEMET	17.7	22.1

Table 4.6 Comparison of electrochemical performances of RZCo//PyR asymmetrical super capacitor against the reported zinc cobalt based super capacitor in the literatures.

Active materials	Potential window (V)	Electrolyte	Energy density (Wh/kg)	Power density (W/kg)	Ref
Co ₃ O ₄ //carbon	0 – 1.6	6M KOH	36	1600	(Salunkhe <i>et al.</i> , 2015)
Co ₃ O ₄ -rGO//carbon	0 – 1.5	6M KOH	35.7	255	(Xie <i>et al.</i> , 2013)
Ni _x Co _{1-x} LDH-ZTO//Activated carbon	0 – 1.2	2M KOH	23.7	284.2	(Wang <i>et al.</i> , 2012)
Co ₃ O ₄ //Activated carbon	0 – 1.5	6M KOH	24.9	225	(Zhang <i>et al.</i> , 2013)
NiCo ₂ O ₄ @MnO ₂ //Activated carbon	0 – 1.5	1M NaOH	35	163	(Xu <i>et al.</i> , 2014)
Co ₃ O ₄ @Ni(OH) ₂ //Activated carbon	0 – 1.7	6M KOH	41.8	33.5	(Tang <i>et al.</i> , 2013)
Co ₃ O ₄ @Ni(OH) ₂ //RGO	0 – 1.7	6M KOH	41.9	36.1	(Tang <i>et al.</i> , 2013)
CoMoO ₄ /MnO ₂ NFs//Activated carbon	0 – 1.6	2M KOH	54	800	(Wang <i>et al.</i> , 2016)
RZCo//PyR	0 – 1.6	1M Na ₂ SO ₄	41.9	188.3	This work

4.4.4 Influence of Graphene Oxide Concentration on Supercapacitive Performances

A comparison was made between the specific capacitance values of the RZCo//PyR and ZCo//PyR asymmetrical super capacitor under the influence of GO concentration. The concentration of GO played a major role in rendering a greater capacitance per gram because a higher concentration of GO could lead to the aggregation of graphitic sheets, which could impede the penetration of electrolyte ions and thereby reduce the redox-active area (Figure 4.17).

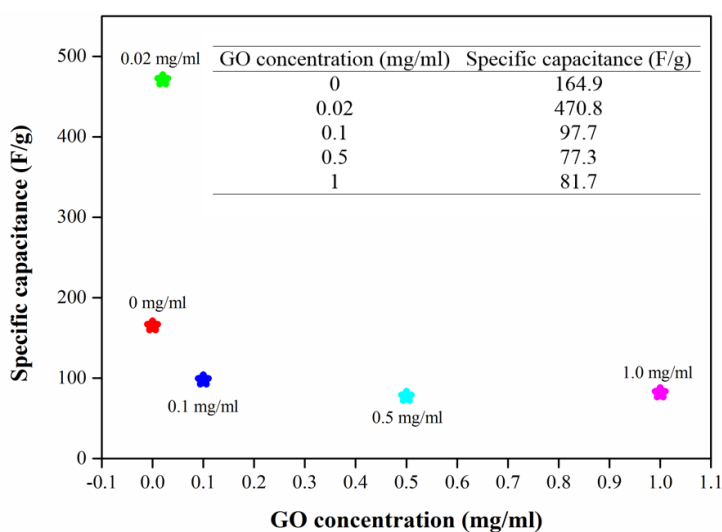


Figure 4.17 Plot of specific capacitance of asymmetrical super capacitor versus GO concentrations. The specific capacitance results were extracted from cyclic voltammetric. Inset is the tabulated results of asymmetrical super capacitor with various GO concentrations.

The specific capacitance of ZCo//PyR asymmetrical super capacitor (Figure 4.18) was merely 51.9 F/g at the current density of 2 mA/cm² relative to 139.8 F/g capacitive performance of the RZCo//PyR asymmetrical super capacitor. This phenomenon could be due to the slightly bulky matrix of the asymmetrical super capacitor without rGO which impeded the facilitation of the electrolyte ions in and out of the matrix. In addition, it was suspected that the lower specific capacitance of ZCo//PyR asymmetrical super capacitor could be ascribed to the solely pseudo-capacitive behavior on the positive electrode, which rapidly deteriorated the stability performance of the asymmetrical super capacitor.

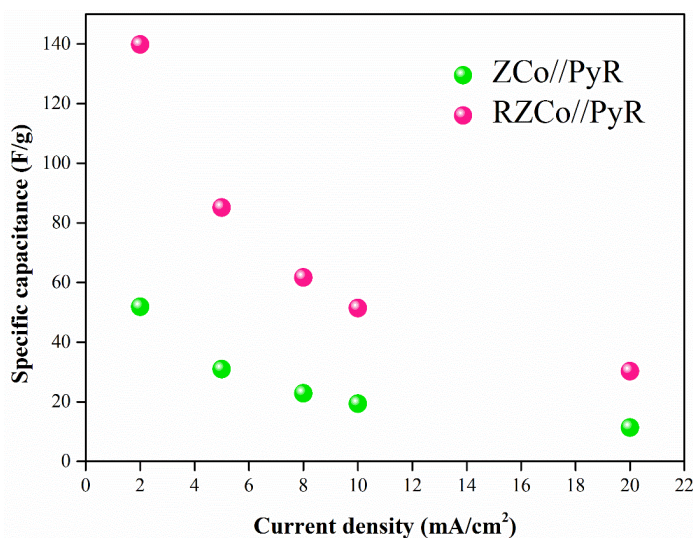


Figure 4.18 Plot of specific capacitance of asymmetrical super capacitor with rGO and asymmetrical super capacitor without rGO at different current densities from 2 mA/cm² to 20 mA/cm². The area of each electrode is 1 cm². The specific capacitance results were extracted from galvanostatic charge/discharge profile.

4.4.5 Electrochemical Performances of Asymmetrical Super Capacitor Under Temperature Influence

The performances of the asymmetrical super capacitor at different operating temperature were studied (as shown in Figure 4.19) to investigate the ability, sustainability, and versatility of the as-fabricated energy storage device under any condition, in either cold or hot weather, for future practical applications. The asymmetrical super capacitor was tested under 0 °C, 30 °C (room temperature), and 60 °C. Figure 4.19a shows that under high temperatures (30 °C and 60 °C), the asymmetrical super capacitor had a smaller ESR than under a cold condition (0 °C). The higher ESR under cold condition could have been due to freezing or the recrystallization of Na₂SO₄, which had an adverse effect on the diffusivity of the electrolyte ions. On the other hand, the ESR value of the asymmetrical super capacitor at 60 °C was comparatively higher than that under room temperature. The results are tabulated in Table 4.7. This phenomenon could be attributed to the vibration of the ions and electrons when subjected to a high temperature. Theoretically, the Na₂SO₄ electrolyte might still be stable at room temperature. However, as reported, Na₂SO₄ has a transition temperature at ~ 32 °C, where its transitioned phase

or morphology could hinder the facilitation of electrolyte ions, thereby exaggerate the resistivity of the asymmetrical super capacitor at a higher temperature (Kenisarin and Mahkamov, 2016). In contrast, the electrolyte might start to crystalline below its stable temperature ($\sim 30\text{ }^{\circ}\text{C}$), which would lead to the high ESR and R_{ct} values.

Table 4.7 Tabulated results for EIS and life cycle of RZCo//PyR asymmetrical super capacitor at $0\text{ }^{\circ}\text{C}$, $30\text{ }^{\circ}\text{C}$, and $60\text{ }^{\circ}\text{C}$. EIS was performed from starting frequency of 100 kHz to an ending frequency of 0.01 Hz, while the life cycle was performed at current density of 2 mA/cm^2 .

Temperature ($^{\circ}\text{C}$)	0	30	60
ESR (Ω)	5.6	0.9	1.1
R_{ct} (Ω)	66.2	16.5	4.8
Retention (%)	49	87	83

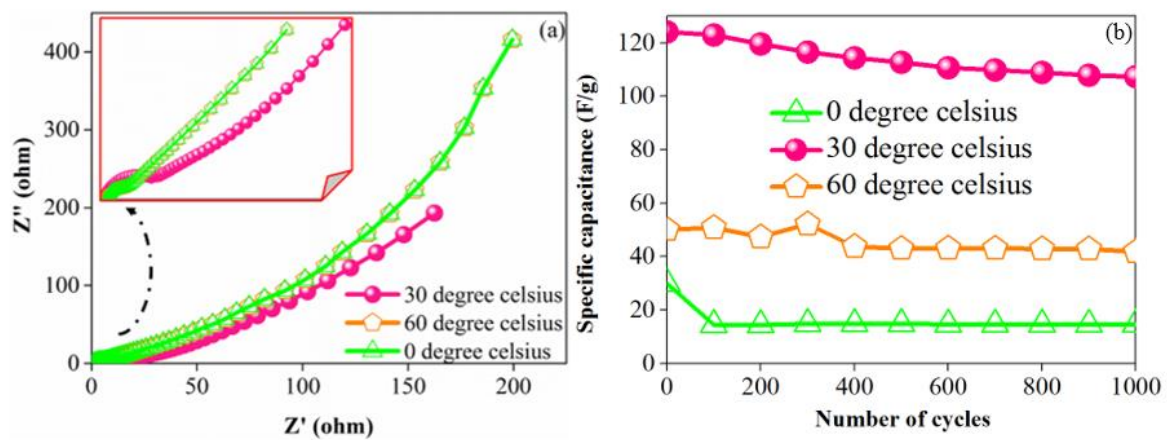


Figure 4.19 (a) Nyquist plot, (b) life cycle of asymmetrical super capacitor at different operating temperatures ($0\text{ }^{\circ}\text{C}$, $30\text{ }^{\circ}\text{C}$, and $60\text{ }^{\circ}\text{C}$).

The life cycle profile (Figure 4.19b) explicitly reflected the best performing asymmetrical super capacitor in terms of its specific capacitance and life retention (87%) at room temperature. The asymmetrical super capacitor at an operating temperature of $60\text{ }^{\circ}\text{C}$ had a comparable life retention of 83% but a lower specific capacitance of $\sim 50\text{ F/g}$, which is about half the specific capacitance of the asymmetrical super capacitor at $30\text{ }^{\circ}\text{C}$. The reversibility of the asymmetrical

super capacitor after being heated and cooled was investigated to study the performance stability of the energy device under the influence of temperature variations. As depicted in Figure 4.20a, when the temperature was increased to 30 °C from 0 °C (0 °C → 30 °C), the specific capacitance of the device increased 1.7-fold compared to that of the device tested at 0 °C. However, the device tested at 30 °C still had the best specific capacitance. Meanwhile, when the temperature was decreased to 30 °C from 60 °C (60 °C → 30 °C), the device could only retain 51% of its initial capacitance, which was worse than the device tested at 30 °C (87%). The performance deterioration could have been due to the partial deformation of the active materials. The charge storage matrix was destroyed by the freezing and heating processes, which was ascribed to the material contraction and expansion, and this compromised the diffusive capability of the electrolyte ions. In addition, the performances of the asymmetrical super capacitor at different defrosting times are depicted in Figure 4.20b. The asymmetrical super capacitor with a longer defrosting time (120 min) possessed a longer discharging time, which implies that the 120 min defrosted asymmetrical super capacitor had a better storage capability and could retain more charge than the 60 min defrosted asymmetrical super capacitor. As observed from the morphology of the RZCo materials (Figure 4.21), the severe cracking and inhomogeneity of the active surface conclusively evidenced the performance deterioration of the asymmetrical super capacitor after the heating and cooling processes.

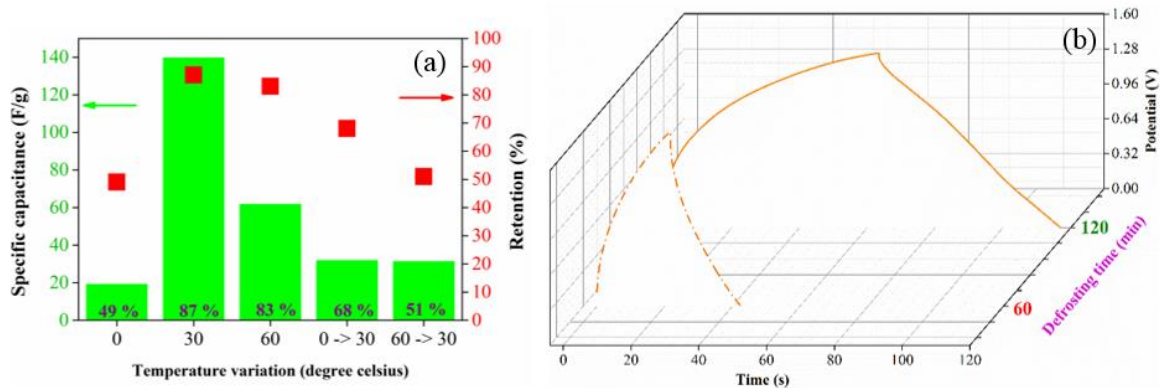


Figure 4.20 Reversibility performance of RZCo//PyR asymmetrical super capacitor (a) at various temperatures and (b) at various defrosting time. The specific capacitance was extracted from galvanostatic charge/discharge profile measured at $2\text{mA}/\text{cm}^2$, whereas the cyclic retention was calculated upon 1000 continuous charge/discharge measurement.

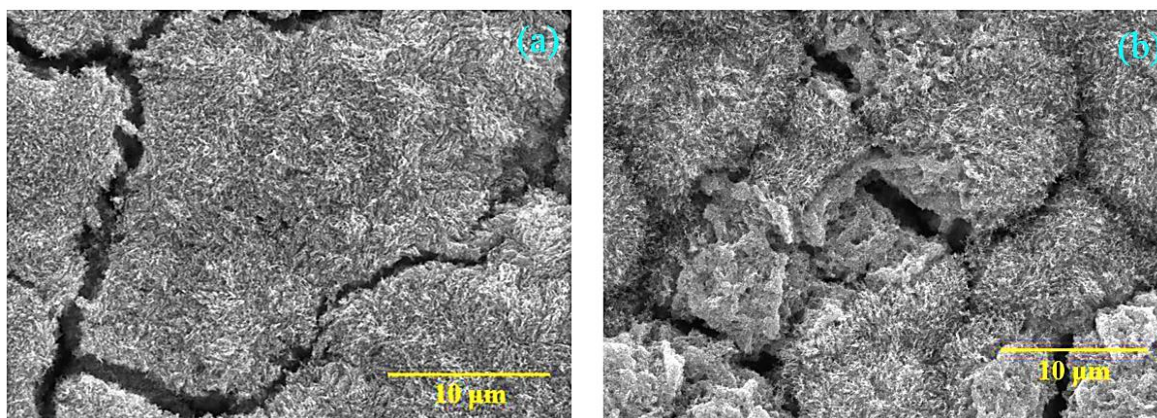


Figure 4.21 FESEM images of RZCo positive electrode under (a) cold ($0\text{ }^{\circ}\text{C}$) and (b) hot condition ($60\text{ }^{\circ}\text{C}$).

4.4.6 Electrochemical Comparison Between As-Fabricated Asymmetrical Super Capacitor and KEMET Commercial Super Capacitor

The supercapacitive properties of the as-fabricated asymmetrical super capacitor were investigated through a series of electrochemical measurements (as shown in Figure 4.22) and were compared to those of a commercial super capacitor to gauge the applicability, compatibility, and potential of our fabricated asymmetrical super capacitor for future commercialization. The general information and specifications of the commercial super capacitor are listed in Table A.3 (Appendix A). As depicted in Figure 4.22a and 4.22b, the

RZCo//PyR as-fabricated super capacitor exhibited a roughly two-fold higher specific capacitance than the KEMET commercial super capacitor, which implies that our fabricated device had a better capacitance performance. The KEMET commercial super capacitor had a more obvious IR drop than the as-fabricated super capacitor, which led to a high ESR, as shown in Figure 4.22c. The ESR is closely correlated to the IR drop and discharge current density (Baek *et al.*, 2012). Figure 4.22c shows that the KEMET commercial super capacitor possesses a high total resistance (ESR) of 34 Ω without any signs of a semicircle detected. The ultra-high ESR could have been due to the lower conductivity of the carbon materials. In comparison, the as-fabricated asymmetrical super capacitor had a lower ESR of merely 0.92 Ω and its straight line at the low-frequency region leaned more towards the Z'' axis, which implied that the device had a better capacitive behavior (Basri and Dolah, 2013). Life retention tests were performed (Figure 4.22d) for both energy storage devices, and the KEMET commercial super capacitor had a better cycling life, with 97% of the capacitance being retained after 1000 continuous charge/discharge cycles, compared to the as-fabricated asymmetrical super capacitor (87%). The excellent reversibility of the commercial super capacitor is ascribed to the absence of the faradaic reaction (as proven by the square voltammogram in Figure A.4) and polymeric materials, which could cause electrode deterioration after the extensive swelling and contraction of the electrodes during cyclic measurement, as evidenced by the performance of the as-fabricated asymmetrical super capacitor. Despite the fact that the as-fabricated asymmetrical super capacitor had a higher power output, its cyclic sustainability would be an issue and limitation for industrial applications. Thus, relentless efforts to improve the as-fabricated device are needed for industrial realization.

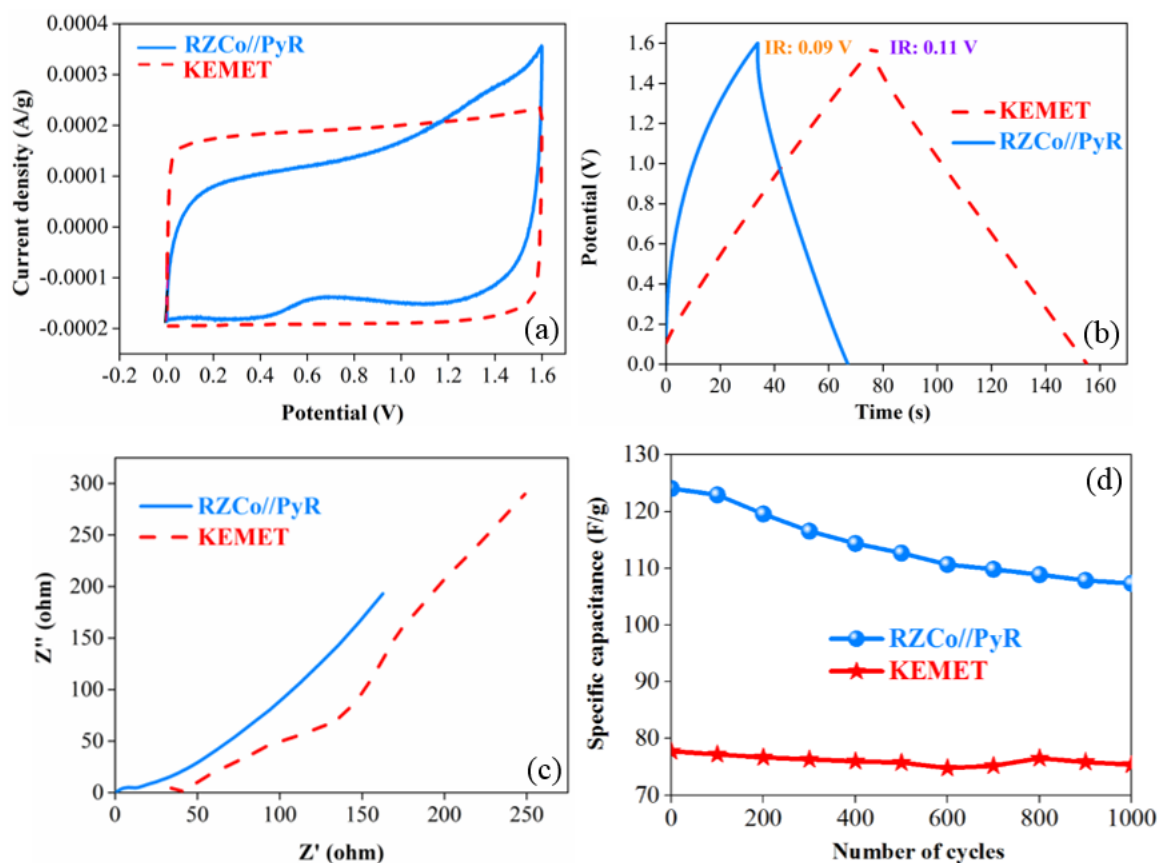


Figure 4.22 Electrochemical measurements of (a) cyclic voltammetry at scan rate of 2 mV/s, (b) galvanostatic charge/discharge at current density of 2 mA/cm², (c) EIS, and (d) life cycle of as-fabricated and KEMET commercial super capacitor.

4.5 Conclusion

A brief summary on the Bi₂O₃/MnO₂ symmetrical super capacitor where the temperature investigation tests unveiled the excellent reversibility and sustainability of the Bi₂O₃/MnO₂ symmetrical super capacitor. The symbiosis effect between the Bi₂O₃ and MnO₂ materials dramatically improved the cyclic reversibility, sustainability, and stability of the Bi₂O₃/MnO₂ super capacitor, regardless of the temperature influence. Excellent electrochemical performances were found for the Bi₂O₃/MnO₂ super capacitor, typically at a high temperature (60 °C) compared to those measured at 0 and 30 °C. This showed that the super capacitor with a longer defrosting period possessed better electrolyte ion diffusivity, which consequently contributed to enhanced capacitive performances. The remarkable stability and reversibility performances of the Bi₂O₃/MnO₂ super capacitor under any conditions (up to >75%) show its

suitable for use in seasonal countries and the automotive sector. Further efforts are still devoting for capacitive surge to meet the target for commercialization.

To realize the energy and power densities performances of the super capacitor, an asymmetrical super capacitor composed of $\text{Bi}_2\text{O}_3/\text{MnO}_2$ as the positive electrode and PyR as the negative electrode was fabricated. The $\text{Bi}_2\text{O}_3/\text{MnO}_2//\text{PyR}$ asymmetrical super capacitor exhibited 3.6-fold higher in energy density (25.6 Wh/kg) and about twice the power density (115.3 W/kg) performance relative to the $\text{Bi}_2\text{O}_3/\text{MnO}_2$ symmetrical super capacitor (7.1 Wh/kg and 51.8 W/kg for energy and power densities, respectively). Nevertheless, the dissatisfying stability performance has disfavoured the use of such device for photo-super capacitor application. Subsequently, an asymmetrical super capacitor composed of RZCo as the positive electrode and PyR as the negative electrode was successfully fabricated via a facile one-step hydrothermal and electro-deposition method. The highly crystalline flower-like RZCo nanostructure positive electrode provided excellent electrochemical performances compared to the ZCo electrode. The high potential window of 1.6 V and symbiosis effects of both positive and negative electrodes contributed to an asymmetrical super capacitor with high energy (41.8 Wh/kg) and power densities (188.3 W/kg). The calculated energy and power densities of the RZCo//PyR asymmetrical super capacitor are comparable to those recently reported in the literature. In addition, the incorporation of 0.02 mg/ml rGO on the positive electrode significantly enhanced the retention ability of the as-fabricated asymmetrical super capacitor, thus rendering a cyclic retention of 87% after being subjected to 1000 charge/discharge cycles, which was 1.4-fold more stable than the ZCo//PyR asymmetrical super capacitor (60%). Despite the ability of the KEMET commercial super capacitor to retain 97% of its capacitance, its power output (77.7 F/g) did not outperform our as-fabricated super capacitor. When operated at the temperature of 30 °C, the asymmetrical super capacitor had better

electrochemical performances than when operated at 0 °C and 60 °C. In summary, the RZCo//PyR binder-less as-fabricated asymmetrical super capacitor device has the potential for wide application in the super capacitor industry and is suitable to be used for photo-super capacitor integration.

CHAPTER 5

INTEGRATION OF CESIUM-BASED PEROVSKITE SOLAR CELL TOWARDS THE FABRICATION OF PHOTO-SUPER CAPACITOR

The previous chapter investigated the performances of the symmetrical and asymmetrical super capacitors and concluded that the RZCo//PyR asymmetric configured super capacitor is suitable for photo-super capacitor integration. In this chapter, a series of mixed-halide perovskite solar cells ($\text{CsPbBr}_{3-x}\text{I}_x$, where $x=0-0.3$) will be fabricated and their J-V performances will be examined, even at high humidity condition. The champion perovskite solar cell will be appointed as the energy conversion device for the photo-super capacitor. Fundamental studies for the photo-super capacitor such as the light responsiveness of the photo-super capacitor will be studied in this chapter.

5.1 Introduction

Perovskite solar cell has attracted great attention as the prime energy conversion device, owing to its reasonable low fabrication cost without compromising its photovoltaic performances. Relentless efforts have been done to improve the performance of perovskite solar cell, typically the hybrid organic-inorganic methylammonium lead halide ($\text{CH}_3\text{NH}_3\text{PbX}_3$ or MAPbX_3 , where X is a halide Cl, Br, I, or mixture of halides) which has accomplished power conversion efficiencies (PCE) over 20% (Green *et al.*, 2016; Hutter *et al.*, 2015; Lee *et al.*, 2012).

Particularly, series of mixed halide perovskite solar cells were envisioned to be able to adjust the absorption spectra which may be an advantageous property for full spectrum energy harvesting and photo-electrochemical applications. By tuning the iodide/bromide ratio of the mixed halide perovskite solar cell such as the increment of iodide concentration led to red-

shifting of the absorption range and thereby, enhances the photovoltaic performance. A PCE of 12.3% has been obtained for the MAPb(I_{1-x}Br_x)₃ perovskite solar cell and manifested the feasibility to obtain excellent photovoltaic performances by manipulating the ratio between halides of I⁻ and Br⁻ (Noh *et al.*, 2013; Bi *et al.*, 2015). Additionally, hybrid iodide/bromide perovskite hole conductor free solar cell shows good stability and efficiencies of 8.54% (Aharon *et al.*, 2014), implies the advantageous of halides mixture. Despite the methylammonium based perovskite material has attained high PCE performance, however, aforementioned perovskite material possesses poor stability, which consequently lured the replacement of organic CH₃NH₃⁺ cation to an inorganic cesium (Cs⁺) cation. Specifically, CH₃NH₃PbI₃ thin film thermally degrades to PbI₂ at > 85 °C, while CsPbBr₃ is compositionally stable up to their melting point (>460 °C). Thermogravimetric analyses confirm that an inorganic CsPbBr₃ perovskite has higher thermal stability over the hybrid organic-inorganic CH₃NH₃PbBr₃ perovskite, (Kulbak *et al.*, 2016). Additionally, CsPbBr₃ exhibits good charge transport properties with an electron mobility of ~1000 cm²/Vs and electron lifetime of 2.5 μs (Kulbak *et al.*, 2015; Stoumpos *et al.*, 2013). While, CsPbI₃ perovskite solar cells possesses excellent optical and electrical properties (Ripolles *et al.*, 2016). Despite CsPbI₃ perovskite solar cell fabricated under vacuum-processed has achieved high efficiency of 10.5 %, subsequently the improved efficiency of mixed halide or mixed halide-mixed Pb/Sn perovskite solar cells up to 11 % has been reported, however, the needs of high technology equipment such as vacuum chamber and glove box during the fabrication process have restrained its outdoor applications competency owing to the unsolved stability issue and high production cost (Beal *et al.*, 2016; Frolova *et al.*, 2017; Niezgoda *et al.*, 2017; Liang *et al.*, 2017). Therefore, engineering halide mixture for cesium perovskite absorber material (CsPbBr_{3-x}I_x) can be a suitable candidate to improve the optical and electrical properties, subsequently to improve cell and stability performance.

Generally, striking for high V_{oc} is one of the photovoltaic parameters to achieve high overall photoconversion efficiencies. It is considered that the factors controlling the V_{oc} are the perfect matching of the LUMO level of the electron transport material with the conduction band of the perovskite layer, and the HOMO level of the hole transport material with the valence band of perovskite layer (Ryu *et al.*, 2014). However, other studies predicted that the V_{oc} is closely related to the charge recombination rate and the work functions of the HTMs (Suarez *et al.*, 2014; Yan *et al.*, 2015; Yan *et al.*, 2016). An example that confirms this theory where a $TiO_2/CH_3NH_3PbI_3$ layer covered by copper iodide, CuI as the p-type semiconductor has reduced the V_{oc} as compared to other devices without this layer. This behavior was attributed to high recombination processes. Other reports also confirm that the V_{oc} is solely determined by the perovskite absorber, regardless of the TiO_2 surface modifications such as TiO_2 -coating with a thin film of MgO in order to change the conduction band (Christians *et al.*, 2013; Gouda *et al.*, 2015; Yan *et al.*, 2015; Yan *et al.*, 2016 ; Carli *et al.*, 2016). Therefore, in-depth study to further improve the V_{oc} and efficiency performance is still continuing.

Though the perovskite solar cell is good in light harvesting, however, it is unable to store the converted energy. Hence, an energy storage device such as a battery, capacitor, or a super capacitor is required for energy storage system, additionally to perform as main power delivery output for most applications (Ng *et al.*, 2015), which gives rise to photo-super capacitor. The photo-super capacitor is the combination of an energy conversion device, regardless of its types (dye-sensitized, silicon, or perovskite solar cell, etc.) and an energy storage device (battery, capacitor, or super capacitor) in building a green and sustainable energy harvesting power back device. The excellence performances of a super capacitor in terms of cyclic stability and charging-discharging at high power density (Ng *et al.*, 2017) compensate fluctuations in power network supply. A high performance super capacitor is always relying on criteria such as large

surface area, controlled pore size, stacking layer, and distribution of electrode materials is desired to maximize the power storage ability and to minimize energy loss, as well as to ensure a smooth power delivery system (Ng *et al.*, 2015).

Generally, the energy conversion and storage devices were operated independently with the connection of external wires and merely a single photo-super capacitor device has been reported. A first $\text{CH}_3\text{NH}_3\text{PbI}_3$ perovskite based solar cell-polypyrrole super capacitor connected in series power back system was successfully presented in 2015 with an overall conversion efficiency of 10% for a combined system (Xu *et al.*, 2015). Nevertheless, the loss of power and energy has further prompted the integration of photovoltaic device and super capacitor into a single device, which targeted to reduce 43% of its internal resistance (Xu *et al.*, 2014). An advancement on photo-super capacitor where a singly integrated $\text{CH}_3\text{NH}_3\text{PbI}_3$ -PEDOT modified printable perovskite solar cell has exhibited a maximum overall efficiency of 4.70% with high energy storage efficiency of 73.77% (Xu *et al.*, 2016). So far, most of the reported photo-super capacitor works were mostly utilizing DSSC as the energy conversion part and few reports on perovskite solar cell have been reported. Generally, the DSSC-based photo-super capacitor exhibited low energy density because most of the liquid based DSSC could only achieved maximum V_{oc} of 0.8 V. Ideally, the maximum charging voltage of the super capacitor for the photo-super capacitor should be equal to the V_{oc} of the solar device. As a result, the low charging voltage of a DSSC thus contributes to low energy density of photo-super capacitor (Sun *et al.*, 2017). Hence, a solar cell equipped with high V_{oc} and efficient solar harvesting ability is highly favourable for photo-super capacitor application.

The first section (section 5.2) in this chapter studies the performances of the perovskite solar cell with varies halide ratios at low humidity condition (<80% RH). Two important parameters

that promote high V_{oc} achievement for a standard solar cell, which are the tunable band gap of the inorganic perovskite absorbers and the usage of HTM with various work functions were studied. The $CsPbBr_{3-x}I_x$ perovskite films were synthesized through two-step deposition technique by varying the amount of x ratio from 0 to 0.3 and were characterized through X-ray diffraction (XRD), UV-Vis spectroscopy, photoluminescence, and ultraviolet photoelectron spectroscopy (UPS). Upon the addition of optimized amount of iodide (0.1 molar ratio) into the $CsPbBr_3$ matrix, drastic improvement in fill factor (FF) and short-circuit current (J_{sc}) thus contributed to enhanced PCE of 3.98%. The V_{oc} of $CsPbBr_{3-x}I_x$ perovskite solar cells using *Spiro*-OMeTAD as the HTM have achieved high V_{oc} of $\sim 1V$ and when P3HT/MoO₃ bilayer was used as the HTM, the V_{oc} performance has further improved up to 1.30 V for the $CsPbBr_3$ solar cell. Finally, the stability issues were also analysed in this work, concluding that the addition of small amount of iodide indeed improve the stability performance of the photovoltaic devices.

The second part (section 5.3) of this thesis provides the performance evaluation of the photo-super capacitor. A cesium based perovskite solar cell was successfully fabricated in ambient condition (RH >80%) without any encapsulation and was first to integrate with an asymmetrical super capacitor. To date, the cesium based perovskite solar cell is the first solar cell to be used for photo-super capacitor application. The performances of the perovskite solar cell and super capacitor were individually being evaluated before proceeding for integration. This work is mainly focus on the fundamental study on the performances of a series of mixed halide cesium based perovskite solar cell ($CsPbBr_{3-x}I_x$) under high humidity influence (>80% RH) and to investigate the possibility to be adopted as photo-super capacitor device. It shows that the $CsPbBr_{3-x}I_x$ solar cell gives the best efficiency and V_{oc} of 0.46% and 0.67 V, respectively when $x=0.1$. The stability evaluation where 70% of its original PCE was retained

after a week storage in dark and humidity controlled desiccator (<80% RH) hence proven the potential of the perovskite solar cell to be coupled as part of photo-super capacitor device. The photo-super capacitor measurements were performed and the photo-super capacitor indeed show positive results on photovoltage and photocurrent responses in the presence and absence of light.

5.2 Performance Evaluation of Perovskite Solar Cells at Low Humidity Condition

5.2.1 Crystallographic Study

Crystallinity was investigated via XRD to study the crystal phase transition of the $\text{CsPbBr}_{3-x}\text{I}_x$ perovskite materials. The temperature dependent CsPbX_3 perovskite material could be existed in three polymorphic structures, either in tetragonal, orthorhombic, or in cubic structure. Interestingly, at high annealing temperature of 350 °C, the transformation of CsPbX_3 material into cubic phase was observed from the XRD profile (Figure 5.1). The experimental peaks are closely matches the theoretical peaks (JCPDS file #00-054-0752) (Chen *et al.*, 2017; Protesescu *et al.*, 2015). The highly crystalline peaks at 15°, 20°, and 30° are indexed to (100), (110), and (200). The XRD profile explicates an unnoticeable blue-shifted trend to lower angles region as the concentration of iodide increases. This is owing to the substitution of larger iodide ions over the bromide lattice, which expanded the d-spacing of the halide matrix and thus inversely brought to lower degree detection (Beal *et al.*, 2016).

5.2.2 Energy Level Diagram

Figure 5.2 shows the UV-visible absorption and emission spectra of the $\text{CsPbBr}_{3-x}\text{I}_x$ perovskite films with different bromide/iodide molar ratio. Both the absorption and emission spectra display red-shifted trend towards longer wavelength as the iodide concentration of the $\text{CsPbBr}_{3-x}\text{I}_x$ perovskite films increases, as illustrated in Figures 5.2a and 5.2b. The lower absorption

coverage of a purely bromide film could be ascribed to the bromide ion, which narrows the vibration mode and band near-IR region (Dimesso *et al.*, 2014). Figure 5.2c shows the band gap (E_g) of the perovskite materials. To be specific, the band gap of each perovskite material was calculated by obtaining the wavelength from the intersection point between UV-Vis and photoluminescence and was then inserted into Equation (3.1). When the amount of PbI_2 in CsPbBr_3 matrix increases, gradual reduction in E_g was observed from 2.39 (CsPbBr_3), 2.38 ($\text{CsPbBr}_{2.9}\text{I}_{0.1}$), 2.35 ($\text{CsPbBr}_{2.8}\text{I}_{0.2}$), to 2.32 eV ($\text{CsPbBr}_{2.7}\text{I}_{0.3}$), which is in great agreement with the previous reports in the literature (Noh *et al.*, 2013; Wang *et al.*, 2014). In order to complete the energy level diagram, the valence band of each $\text{CsPbBr}_{3-x}\text{I}_x$ perovskite material, $x = 0, 0.1, 0.2,$ and 0.3 , respectively, was measured through ultraviolet photoelectron spectroscopy (UPS). The highest occupied molecular orbital (HOMO) levels have recorded the values of $-5.52, -5.35, -5.60,$ and -5.61 eV, corresponding to $\text{CsPbBr}_{3-x}\text{I}_x$, where $x = 0, 0.1, 0.2,$ and 0.3 , respectively, as manifested in Figure 5.3.

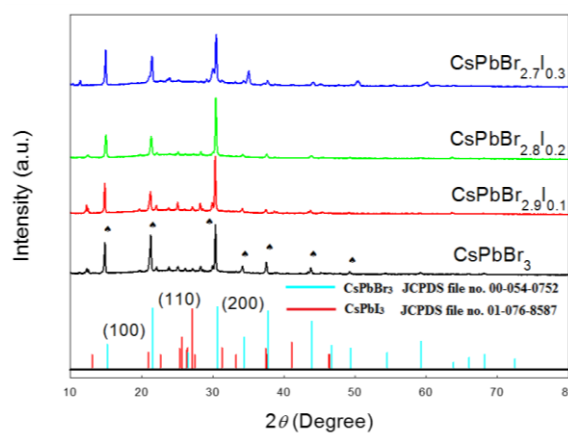


Figure 5.1 XRD patterns of glass/ $\text{CsPbBr}_{3-x}\text{I}_x$, where the amount of iodide varies as $x = 0, 0.1, 0.2,$ and 0.3 in molar ratio.

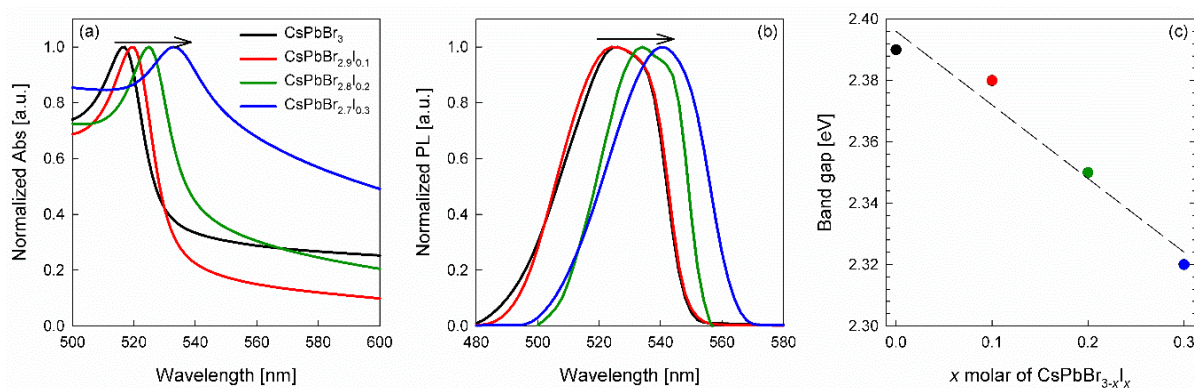


Figure 5.2 Normalized (a) absorption and (b) photoluminescence of CsPbBr_{3-x}I_x, where x is 0, 0.1, 0.2, and 0.3 molar ratio, and (c) band gap energy.

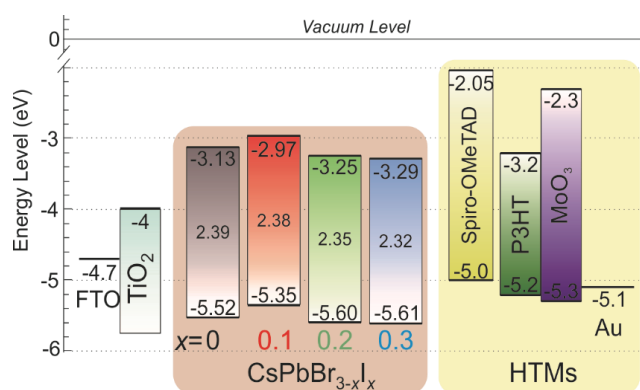


Figure 5.3 Schematic energy level diagram of FTO/TiO₂/CsPbBr_{3-x}I_x/HTM/Au, where x is 0, 0.1, 0.2 or 0.3 perovskite solar cell, employing HTM as either *Spiro*-OMeTAD or P3HT/MoO₃. The band gap of each perovskite is also indicated.

5.2.3 Effect of Iodide Inclusion on The Performance of Perovskite Solar Cells

The photovoltaic performances of CsPbBr_{3-x}I_x (x varies between 0, 0.1, 0.2, and 0.3 in molar ratio) perovskite solar cell, employing *Spiro*-OMeTAD as the HTM were measured under 1 sun (AM1.5 G 100 mW/cm²) illumination and dark conditions, as depicted in Figure 5.4a and 5.4b and the corresponding photovoltaic results were tabulated in Table 5.1. It shows that the addition of minute amount of iodide has dramatically improved the photo-conversion efficiency of CsPbBr₃ from 2.97 % to 3.98 % for CsPbBr_{2.9}I_{0.1} solar cell with high V_{oc} of 1.13 V and FF of 0.64. Similar photovoltaic trends were also observed for CsPbBr_{2.8}I_{0.2} device. Nevertheless, further increasing the iodide amount in CsPbBr_{3-x}I_x does not improve the cell performance. Contrary, the photo-conversion efficiency plunged to 2.73 % when 0.3 molar

ratio of iodide was incorporated to the bromide matrix. The performance differences were dependent on the J_{sc} and FF; while keeping the V_{oc} almost constant (Figure 5.4a). The substantial reduction of FF for $CsPbBr_{2.7}I_{0.3}$ solar cell could be attributed to the occurrence of minor interfacial charge recombination, which resulted from relatively higher series and lower shunt resistances, as manifested in Table 5.1. The J-V curves under dark at -1 V reflected small differences between devices (Figure 5.4b) implies suppressed charge recombination. The J_{sc} and FF parameters were improved when the iodide concentration is either in 0.1 or 0.2 molar ratio ($CsPbBr_{2.9}I_{0.1}$ or $CsPbBr_{2.8}I_{0.2}$) relative to $CsPbBr_3$ and $CsPbBr_{2.7}I_{0.3}$ perovskite solar cells. These results imply that higher amount of iodide disturbs the charge extraction of the cell and thus only an optimized amount of PbI_2 is favourable. Figure 5.4c shows the external quantum efficiency (EQE) spectra of $CsPbBr_{3-x}I_x$ devices and the results are consistent with the J_{sc} performance. The EQE intensity increases from 350 nm to 500 nm upon the addition of iodide into the pure $CsPbBr_3$. The current calculated from the integration of the EQE curves demonstrated the occurrence of some recombination mechanisms that affect these devices, consequently reduce the J_{sc} performance. Figure 5.4d shows the enlarged EQE spectrum of $CsPbBr_{3-x}I_x$ based perovskite devices. It can be seen that there are noticeable shifts of EQE onset to longer wavelengths in conjunction with the iodide increment, which is in great agreement with the absorption spectra in Figure 5.2.

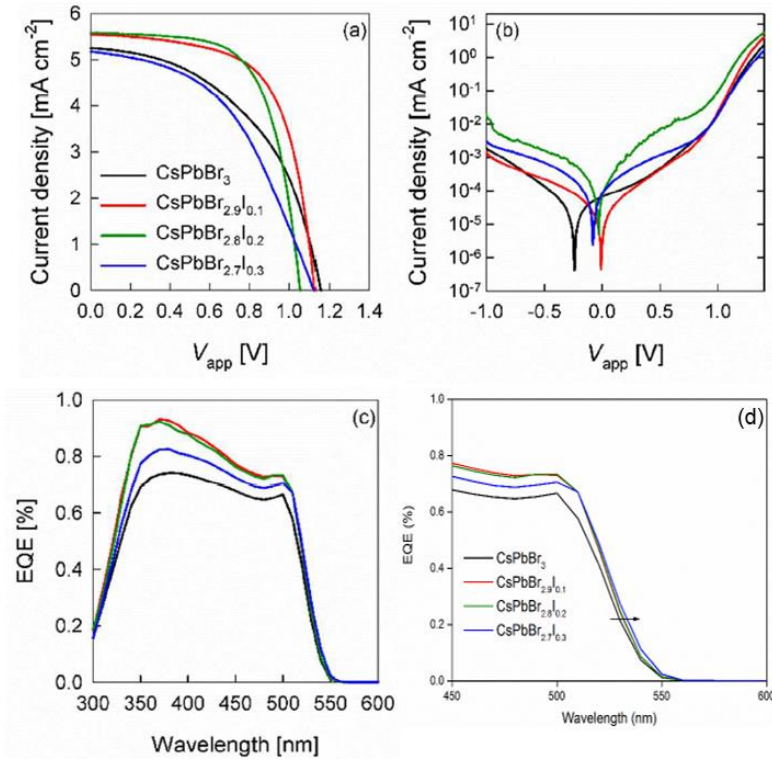


Figure 5.4 J-V measurements (a) under simulated AM 1.5G sun light of 100 mW cm^{-2} irradiance, and (b) under dark. (c) EQE for glass/FTO/c-TiO₂/mp-TiO₂/CsPbBr_{3-x}I_x/Spiro-OMeTAD/Au solar cells, where x varies in 0, 0.1, 0.2, and 0.3 molar ratio. (d) Enlarged EQE spectrum of CsPbbr_{3-x}I_x perovskite solar cells shows the red-shifted EQE onsets.

Table 5.1 Photovoltaic parameters of the CsPbBr_{3-x}I_x solar cells (x varies between 0, 0.1, 0.2, and 0.3 in molar ratio) with Spiro-OMeTAD as the HTM. The photocurrent calculated from the integration of the EQE curves is also added.

Perovskite	V _{oc} (V)	J _{sc} (mA/cm ²)	FF	PCE (%)	J _{sc} [Cal.] (mA/cm ²)	R _{sh} (kΩ/cm ²)	R _s (Ω/cm ²)
CsPbBr ₃	1.16	5.25	0.49	2.97	5.85	220.3	2711
CsPbBr _{2.9} I _{0.1}	1.13	5.54	0.64	3.98	6.83	294.5	1674
CsPbBr _{2.8} I _{0.2}	1.06	5.58	0.65	3.83	6.78	673.0	1724
CsPbBr _{2.7} I _{0.3}	1.12	5.17	0.47	2.73	6.44	158.5	5194

There are two factors that are able to tune the V_{oc} performance of a perovskite solar cell, which are the band gap of the CsPbBr_{3-x}I_x perovskite material and the employment of different work function's HTM, as manifested in Figure 5.5. By analyzing solar cells of different perovskite band gap, the V_{oc} supposing should be improved for the solar cells with larger perovskite band gap rather than narrower band gap. Figure 5.5a and 5.5b illustrated the V_{oc} behavior of a

perovskite solar cell with a narrower and a wider perovskite band gap, respectively. It shows that small V_{oc} increment was observed even when a device with larger perovskite band gap was used; taking the hole and electron transport materials the same, which is due to the addition of minute amount of iodide within the $CsPbBr_{3-x}I_x$ matrix, which resulted in small shift in band gap. Consequently, the V_{oc} changed slightly under these circumstances.

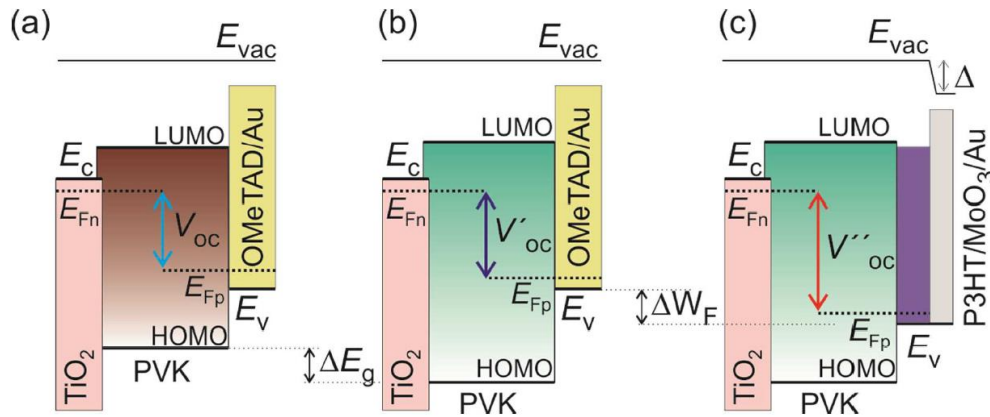


Figure 5.5 The V_{oc} behavior is represented in the energy level diagrams for perovskite solar cells with narrow (a) or wide band gaps (E_g) (b) and (c) of absorber and different HTMs, such as *Spiro*-OMeTAD/Au in (a) and (b) or deeper work function (W_F) as P3HT/MoO₃/Au in (c). The conduction band (E_c), valence band (E_v), Fermi level of electrons (E_{Fn}) and holes (E_{Fp}) were indicated. The MoO₃ layer creates a dipole (Δ) at the interface, reducing the vacuum level energy (E_{vac}).

Despite the photovoltaic devices employed *Spiro*-OMeTAD as the HTM performed high V_{oc} close to 1.1 V, nevertheless, it was expected to achieve even higher V_{oc} values when a wider band gap perovskite material was used. To gain further insight on V_{oc} tuning and the performance of the photovoltaic device, the choice of hole extractor is the second factor to be considered besides the band gap of the perovskite absorbers. When a bilayer polymer/oxide (P3HT/MoO₃) was used as the HTM, the V_{oc} was drastically improved from 1.16 V to 1.3 V, as manifested in Figure 5.6 and Table 5.2 owing to deeper HOMO energy level of P3HT/MoO₃ than *Spiro*-OMeTAD. The offsets of HOMO level between P3HT-perovskite in the range of 0.1-0.4 eV merit the hole extraction process. Moreover, the inclusion of MoO₃ interlayer between P3HT and Au performs as exciton blocking layer, herein retards reverse charge flow

(Wang *et al.*, 2016). Figure 5.5c shows that the P3HT-based solar cells with the same perovskite materials shifted the hole Fermi level (E_{Fp}) to lower energy level, hence enhances the V_{oc} considerably. In all cases, V_{oc} enhancement was observed for the P3HT/MoO₃ perovskite solar cell devices, as compared to the *Spiro*-OMeTAD devices, except for CsPbBr_{2.7}I_{0.3} solar cell. This situation is similar to the large V_{oc} increment obtained in dye-sensitized solar cells when using redox couple with more positive redox potential (Feldt *et al.*, 2010). Figure 5.6c illustrated the EQE spectra of CsPbBr_{3-x}I_x devices using P3HT/MoO₃ as the HTM is well correlating to the J_{sc} performances. All in all, it thus confirms that the origin of the V_{oc} is dependent on both the band gap of the perovskites and the work function of the HTMs.

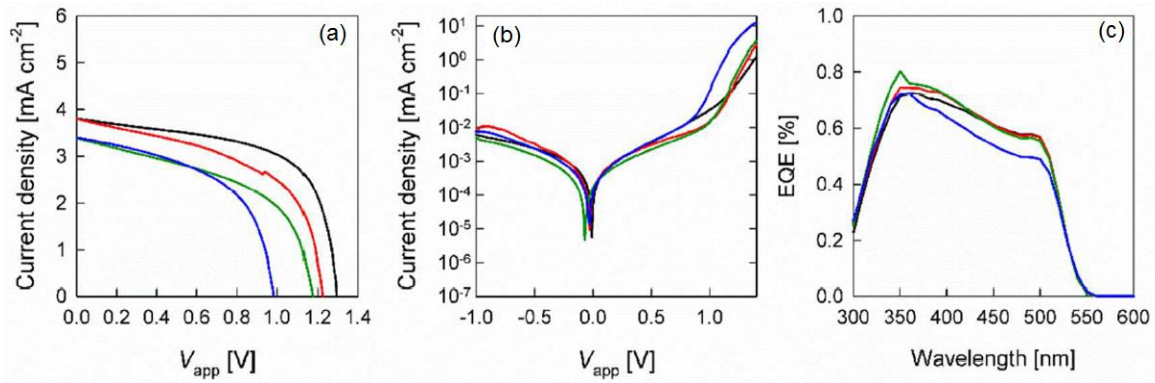


Figure 5.6 J-V measurements (a) under simulated AM 1.5G sun light of 100 mW cm⁻² irradiance, and (b) under dark. (c) EQE for glass/FTO/c-TiO₂/mp-TiO₂/CsPbBr_{3-x}I_x/P3HT/MoO₃/Au solar cells, where x varies in 0, 0.1, 0.2, and 0.3 molar ratio.

Table 5.2 Photovoltaic parameters of the CsPbBr_{3-x}I_x solar cells (x varies between 0, 0.1, 0.2, and 0.3 in molar ratio) with P3HT as the HTM. The photocurrent calculated from the integration of the EQE curves is also added.

Perovskite	V_{oc} (V)	J_{sc} (mA/cm ²)	FF	PCE (%)	J_{sc} [Cal.] (mA/cm ²)
CsPbBr ₃	1.30	3.80	0.62	3.07	5.35
CsPbBr _{2.9} I _{0.1}	1.23	3.80	0.54	2.51	5.41
CsPbBr _{2.8} I _{0.2}	1.17	3.39	0.51	2.01	5.40
CsPbBr _{2.7} I _{0.3}	0.99	3.40	0.53	1.76	4.87

5.2.4 Stability Investigation of Perovskite Solar Cells With Different HTM Contacts Upon Encapsulation

Another important factor to be studied is the stability performance of the $\text{CsPbBr}_{3-x}\text{I}_x$ perovskite solar cell devices. The measurements were carried out in ambient air with a thin film of polymethylmethacrylate, PMMA deposited on the Au surface for encapsulation purpose. Thus, oxygen and water factors were to be omitted in this case. The performance was measured for six days and between measurements, the devices were kept in a glove box under nitrogen ambient and dark conditions. Aging analysis of $\text{CsPbBr}_{3-x}\text{I}_x$ solar cells are summarized in Figure 5.7.

The CsPbBr_3 - and $\text{CsPbBr}_{2.7}\text{I}_{0.3}$ -based devices showed steady decay in FF and more pronounced decay in J_{sc} with constant V_{oc} . The decrement in J_{sc} for $\text{CsPbBr}_{2.9}\text{I}_{0.1}$ and $\text{CsPbBr}_{2.8}\text{I}_{0.2}$ solar cells was less drastic, whilst the FF and V_{oc} remain constant. There are several reasons to explain the reduction of J_{sc} , as observed in all devices. The *Spiro*-OMeTAD solution used as a HTM was composed of 4-*tert*-butylpyridine, which is an additive that may react with the perovskite layer (Zhao & Park, 2015). In addition, the usage of *bis* (trifluoromethane) sulfonimide lithium salt (Li-TFSI) as a dopant although can improve the hole mobility and conductivity, but Li-TFSI is hygroscopic and the cell stability can be affected by the oxidation process (Zhao & Park, 2015). Or even, some studies confirm that the mesoporous- TiO_2 created additional deep traps due to oxygen desorption at the surface caused by the UV-illumination (Leijtens *et al.*, 2013). It is important to highlight that a small addition of iodide into the CsPbBr_3 not merely improved the photo-conversion efficiencies from 0.66 % for CsPbBr_3 to 3.53 % for $\text{CsPbBr}_{2.9}\text{I}_{0.1}$ after 144 hours of evaluation, but also its stabilities. Contrary, the addition of high amount of PbI_2 such as $\text{CsPbBr}_{2.7}\text{I}_{0.3}$ perovskite fasten the degradation process across the absorber composition over time, consequently resulted an

efficiency of 1.16 % after 144 hours. Other important factor to be considered for stability enhancement is the selective HTM used in perovskite solar cells. When the *Spiro*-OMeTAD was substituted by P3HT/MoO₃, the P3HT/MoO₃/Au layer acted as a stabilizer in the solar cells and the inorganic MoO₃ passivates the perovskite surface, thus keeping all photovoltaic parameters constant over time. The large V_{oc} (>1.3 V) achieved for the CsPbBr₃/P3HT/MoO₃-based solar cell highlights that this material is promising for its numerous applications.

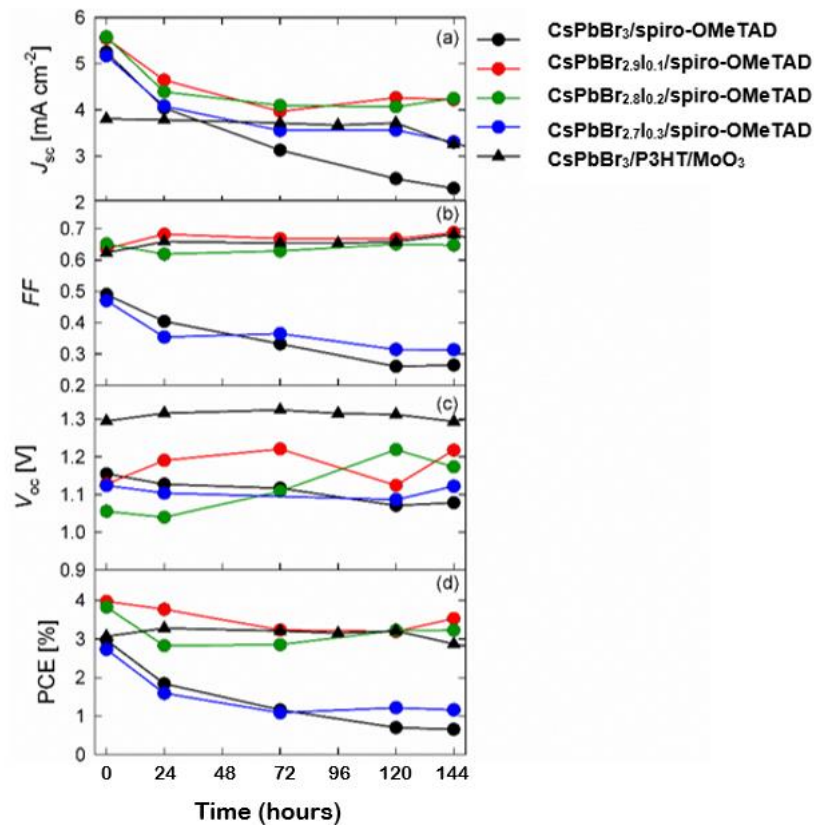


Figure 5.7 Stability test of CsPbBr_{3-x}I_x devices (x = 0, 0.1, 0.2, and 0.3 molar ratios). Figures show the cell parameters of (a) J_{sc}, (b) FF, (c) V_{oc}, and (d) efficiency as a function of time.

5.3 Towards The Integration of Photo-Super Capacitor

In this section, firstly, the performances of a series of halides mixture perovskite solar cells and the asymmetrical super capacitor were individually being evaluated prior to integration takes place.

5.3.1 Materials Characterizations of Perovskite Solar Cells

Figure 5.8 illustrated the images of as-synthesized yellowish cesium based perovskite solar cells fabricated in ambient condition. The complete cell is composed of compact and mesoporous TiO₂, CsPbBr_{3-x}I_x perovskite material, and *Spiro*-OMeTAD as HTM. The surface morphologies and cross section of the perovskite solar cell are shown in Figure 5.9. The cross section of the solar cell (Figure 5.9a) is composed of compact and mesoporous TiO₂ layers, perovskite materials, and *Spiro*-OMeTAD as the HTM. According to Figure 5.9a, the perovskite and mesoporous TiO₂ interfaces are indistinguishable; speculated that the pores of mesoporous TiO₂ are fully filled with CsPbBr_{3-x}I_x perovskite materials. Figure 5.9(b-e) sequentially show the top view morphological surface of the spin coated CsPbBr₃, CsPbBr_{2.9}I_{0.1}, CsPbBr_{2.8}I_{0.2}, and CsPbBr_{2.7}I_{0.3}. The presence of tiny voids (darker pits) as observed in Figure 5.9b could be due to the evaporation of organic solvent during thermal annealing process. The non-pinholes free perovskite film prone to degradation of perovskite solar cell (Atourki *et al.*, 2017; Xiong *et al.*, 2016). Interestingly, the addition of small amount of iodide subtly changes the surface morphology of the solar cell. As the concentration of iodide increase, the compactness of the perovskite film has been improved. Figure 5.9c shows pits were partially covered by the growth of perovskite and the crystallinity of the perovskite grains was improved. At a higher concentration of iodide ($x = 0.2$ and 0.3), a complete coverage and compact perovskite surface was presented, as illustrated in Figure 5.9d and 5.9e. The magnified FESEM images show the coverage of voids by the perovskite grains along with the increment of iodide concentration are included in Figure B.1 (Appendix B) for clarification purpose.

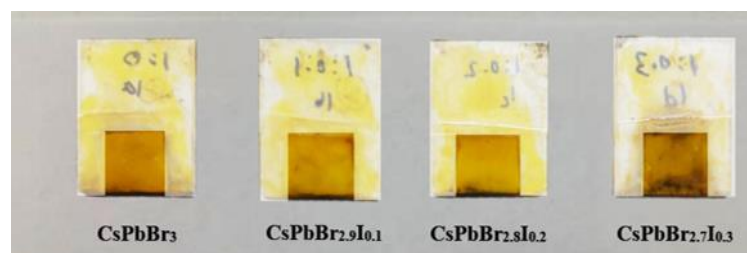


Figure 5.8 Digital photographic image of as-fabricated $\text{CsPbBr}_{3-x}\text{I}_x$ perovskite solar cells where $x=0, 0.1, 0.2,$ and 0.3 .

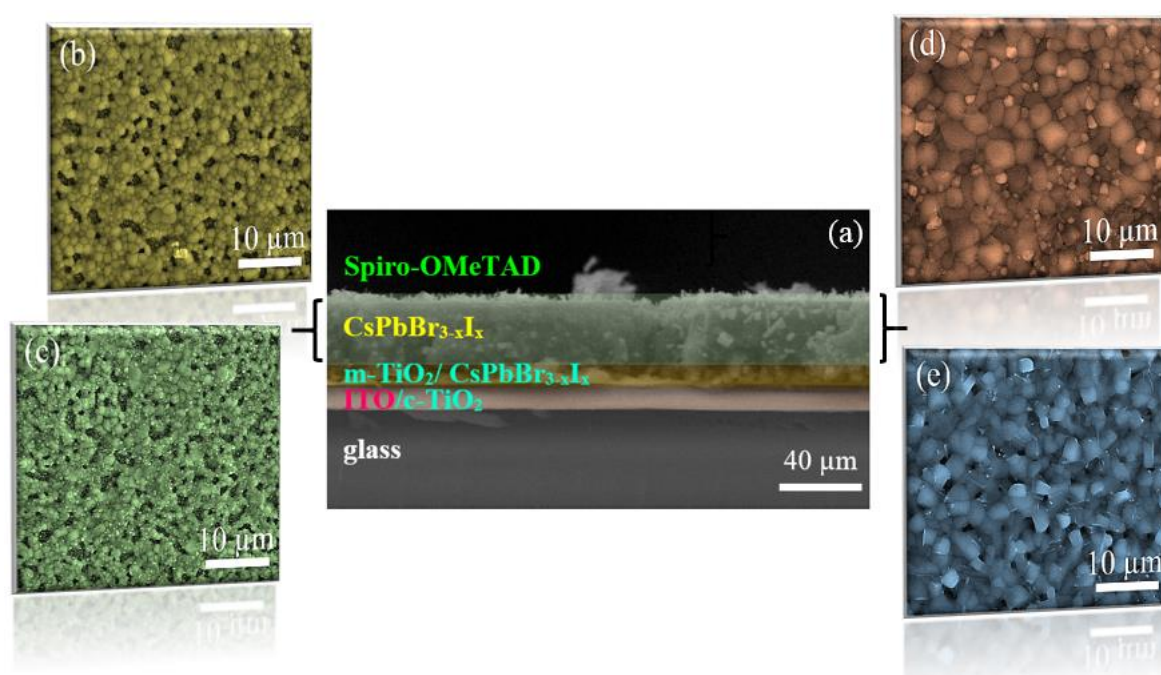


Figure 5.9 (a) Cross section of $\text{ITO}/\text{c-TiO}_2/\text{m-TiO}_2/\text{CsPbBr}_{3-x}\text{I}_x/\text{HTM}$ and (b-e) top view surface morphology of $\text{ITO}/\text{CsPbBr}_{3-x}\text{I}_x$ perovskite solar cells in the molar ratios of (b) 0, (c) 0.1, (d) 0.2, and (e) 0.3.

5.3.2 Photovoltaic Performances of The Fabricated Perovskite Solar Cells

The J-V and stability performances of each perovskite solar cell were carried out to investigate the performances and rate of degradation of the solar cells in an ambient environment. The PCE performances of $\text{CsPbBr}_{3-x}\text{I}_x$ perovskite solar cells incorporated with PEDOT:PSS counter electrode were investigated, in which the system would be employed for photo-super capacitor. The J-V performance of $\text{CsPbBr}_{3-x}\text{I}_x$ solar cell is shown in Figure 5.10a. The V_{oc} and FF of all type of solar cells are constantly maintain at 0.6 V and 30%, respectively, consequently the

PCE is solely depending on J_{sc} . The champion cell of $CsPbBr_{2.9}I_{0.1}$ exhibited high V_{oc} of 0.67 V, FF of 31%, and J_{sc} of 2.2 mA/cm² with PCE of 0.46%. The low efficiency obtained in our work as compared to the reported works could be due to dissimilar fabrication method, non-optimal thickness of the TiO_2 layers, and minor degradation of the precursors or perovskite materials at a highly humid environment. Nevertheless, worth to be mentioned, the succession of a low cost perovskite solar cell fabricated at high humidity condition; without any encapsulating layer over the active materials is highly feasible for the installation or incorporation of perovskite solar cell for multi-applications once the stability issue is solved. Figure 5.10b illustrated the electrochemical impedance of perovskite solar cell. The radius of the semicircle corresponds to the internal resistances of TiO_2 /perovskite interface, TiO_2 layer, and ITO/ TiO_2 interface (Tu *et al.*, 2015). The $CsPbBr_{2.9}I_{0.1}$ device presented the smallest semicircle, indicates the smallest internal resistance, as compared to the other molar ratios' devices. The internal resistance of the devices increases (larger semicircle) as the iodide concentration increases. Bode plot is presented in Figure 5.10c to investigate the electron lifetimes (τ_e) of the $CsPbBr_{3-x}I_x$ perovskite materials where $x= 0, 0.1, 0.2,$ and 0.3 . The frequency peaks of Bode plot is corresponded to the charge transfer of the light harvesting materials. It shows that the frequency peak shifted to lower frequency region upon incorporation of small amount of iodide ($x=0.1$), which implies longer electron lifetime (4842 μ s). As in great agreement with Figure 5.10b, the addition of minute amount of iodide has successfully prolonged its electron lifetime, thereby decelerate its recombination process, which shows the positive effect of iodide inclusion that improved the surface coverage of the perovskite film. As depicted in Table 5.3, the electron lifetimes of $CsPbBr_{2.7}I_{0.3}$ is eightfold shorter than $CsPbBr_{2.9}I_{0.1}$, implying that the inclusion of larger size of iodide ion indeed altered the morphological structure of the perovskite film, which is in agreement with the FESEM images, consequently impede the transportation of charges. In addition, it proofs that the

addition of optimum amount of iodide has enhanced the charge transport and reduce resistivity performance, in turns contribute in longer electron lifetimes (Chen *et al.*, 2016).

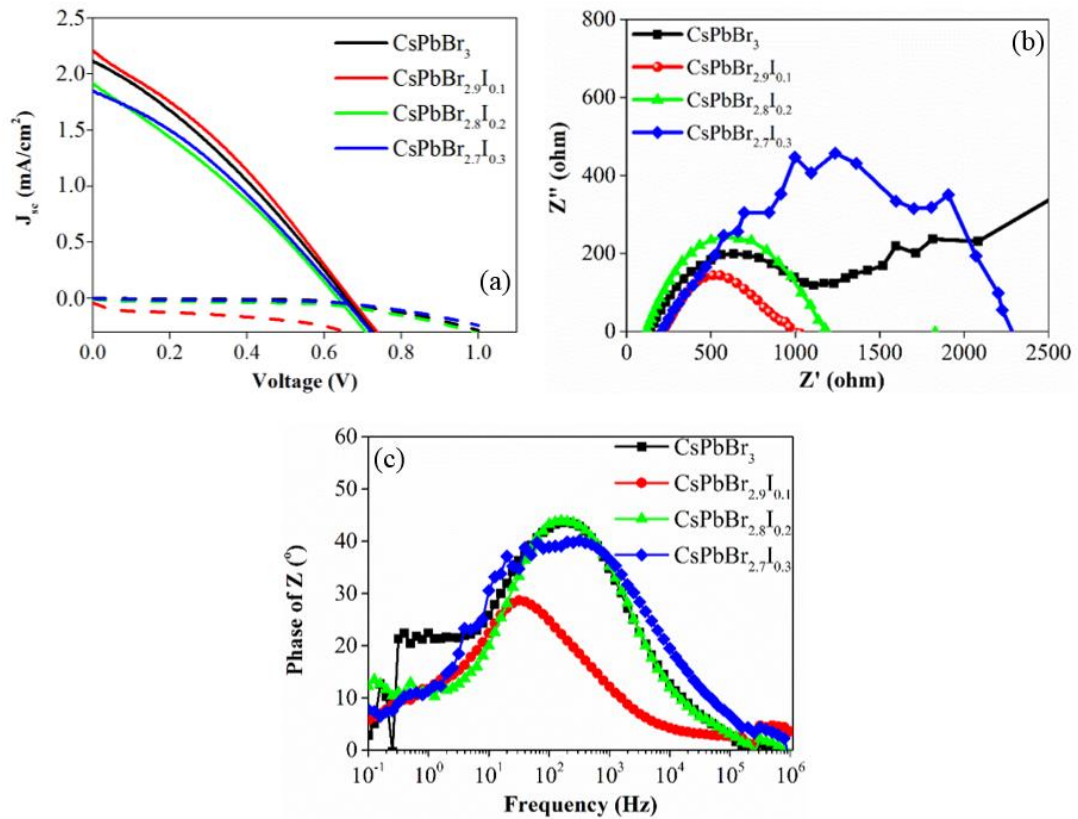


Figure 5.10 (a) J-V performances of $\text{CsPbBr}_{3-x}\text{I}_x$ solar cell under 1sun illumination and in dark, (b) Nyquist plot and (c) Bode phase diagram of $\text{CsPbBr}_{3-x}\text{I}_x$ solar cell under 1sun illumination measured at near open-circuit voltage. The solar cells were measured under 1sun illumination (solid lines) and in dark (dotted lines) for J-V test. The complete set of perovskite solar cell for both measurements is composed of ITO/c-TiO₂/m-TiO₂/ $\text{CsPbBr}_{3-x}\text{I}_x$ /*Spiro*-OMeTAD and PEDOT:PSS as the counter electrode. The electrochemical impedance spectroscopy was measured from a starting frequency of 1 MHz to an ending frequency of 0.1 Hz.

Table 5.3 Electron lifetimes of the mixed halides solar cells under 1sun illumination. The electron lifetimes are calculated based on Equation (3.5).

Solar cells	Electron lifetimes under 1sun illumination (τ_e), μs
CsPbBr_3	931 ± 0.2
$\text{CsPbBr}_{2.9}\text{I}_{0.1}$	4842 ± 0.5
$\text{CsPbBr}_{2.8}\text{I}_{0.2}$	931 ± 0.05
$\text{CsPbBr}_{2.7}\text{I}_{0.3}$	619 ± 0.1

Degradation and decomposition of perovskite upon exposed to UV, air and water are inevitable. To date, the stability of the perovskite solar cell is the utmost important factor to be concerned for further practical applications. In this work, stability performance of the perovskite solar cell was also investigated, as manifested in Figure 5.11a-d. The insertion of optimized amount of iodide not merely contributes in PCE performance, additionally improves the morphological formation with pinholes free perovskite surface, and thus retards the degradation process (>64% efficiency retained after 168 hours). The advantage of cesium based material such as CsPbBr₃ solar cell could retain 81% of its original PCE upon storage of 168 hours, relative to 64%-76% PCE retention for iodide incorporated solar cells. The stability of the perovskite films is highly dependent on the iodide concentration where higher iodide concentration exaggerates the degradation process. The retarded degrading phenomenon could be due to self-degradation of the iodide-based perovskite solar cell, which is when exposed to air, light illumination, and electric field, initial degradation of the perovskite layer induces the generation of I₂ product. Concurrently, the high vapour pressure of I₂ at room temperature is expected to diffuse to the non-degraded perovskite region and exacerbate the perovskite film (Wang *et al.*, 2016). Additionally, degradation of perovskite could be also due to UV factor. Based on the stability profiles, the fluctuation of J_{sc} and PCE performances might be ascribed to the initial UV degradation of perovskite film. The abrupt decrease of J_{sc} during the first 48 hours is due to the presence of trap which prevent electron extraction. In the next few hours, the J_{sc} performance bounce back due to the generation of PbI₂ which then can passivate recombination sites and improve carrier extraction. Subsequently, further degradation resulted in PCE decrement (Lee *et al.*, 2016). Further discussion on the beneficial effect of degradation by the formation of PbI₂ by-product will be discussed next.

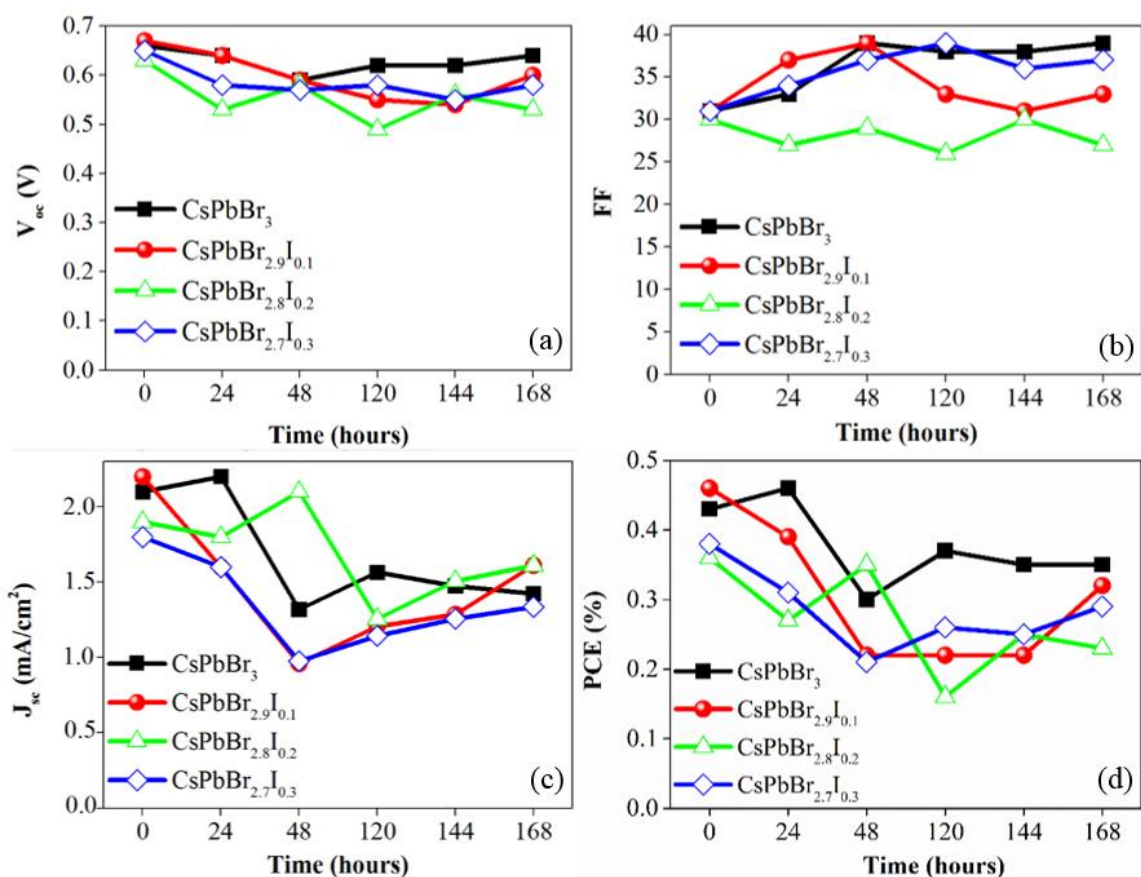


Figure 5.11 Stability performances of CsPbBr_{3-x}I_x perovskite solar cells where (a) corresponds to the V_{oc} , (b) FF, (c) J_{sc} , and (d) PCE. For the stability test, the perovskite solar cells were stored in dark in a humidity control desiccator after 1sun illumination test for 168 hours.

The outperforming CsPbBr_{2.9}I_{0.1} perovskite solar cell is chosen for the photo-super capacitor application after preliminary screening of the performance of mixed halide perovskite films.

The stability investigation of the perovskite solar cell stored in dark and humidity controlled has been discussed in Figure 5.11. Next, an in-depth stability investigation of the CsPbBr_{2.9}I_{0.1} perovskite solar cell under prolong exposure to UV and moisture for 24 hours (>80% RH) is presented in Figure 5.12, which highlights the beneficial effect of addition of an optimized amount of iodide. As a comparison to methylammonium lead halide perovskite material, the cesium lead halide perovskite material possesses much better stability where 33% of its original PCE of CsPbBr_{2.9}I_{0.1} was retained relative to the methylammonium based solar cell stored in air, which retained less than 20% of its PCE after 24 hours (Zhou *et al.*, 2014). The declining

PCE of the CsPbBr_{2.9}I_{0.1} solar cell is mainly attributed to the plunge of J_{sc}. Noticeably, the fluctuation of V_{oc} is less noticeable ascribed to the V_{oc} value is only tuneable by the HOMO and LUMO levels of the HTM and titania, which is not the main target study in this work. After 30 min of UV exposure in air, the abrupt leaping of J_{sc} leads to 1.3-fold PCE increment at the first 30 min, might could be due to the passivation effect of PbI₂ which reduces the defect states and recombination sites at the perovskite grain boundary and the perovskite/TiO₂ interface. The skyrocketed V_{oc} and FF performance are the evident on traps passivation and reduced recombination process, as in great agreement with Figure 5.10c (longer electron lifetime). The PCE degradation process was retarded due to the increasing FF and V_{oc} (Lee *et al.*, 2016). Continuous UV degradation prompts to more PbI₂ is generated and the exposure to moisture thus gradually reduces the cell performance. The degradation phenomenon of the CsPbBr_{2.9}I_{0.1} solar cell is considerably low due to low iodide composition (x = 0.1) within the bromide scaffold.

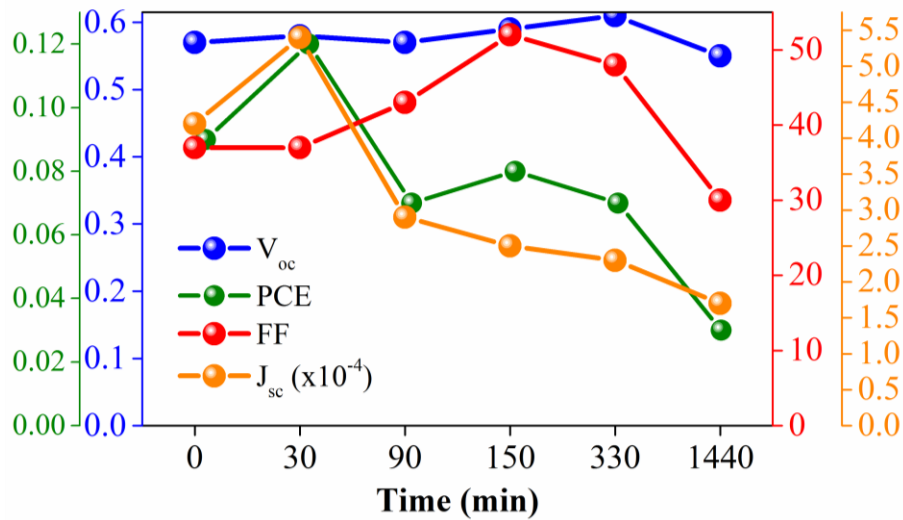


Figure 5.12 Stability performance of CsPbBr_{2.9}I_{0.1} perovskite solar cell under exposure to UV and moisture (>80% RH). The CsPbBr_{2.9}I_{0.1} perovskite solar cell is potential to be employed for photo-super capacitor application.

5.3.3 Materials and Electrochemical Measurements of Asymmetrical Super Capacitor

A PEDOT:PSS-assisted RZCo positive super capacitor electrode was stacked to a PyR negative electrode, utilizing LiClO₄/acetonitrile as the electrolyte was tested before the employment for photo-super capacitor application. RZCo represents reduced graphene oxide, zinc oxide, and cobalt oxide, while PyR represents polypyrrole and reduced graphene oxide. The FESEM image of RZCo shows the growth of ZCo on the graphite sheet (Figure 5.13a). The presence of Co₃O₄, ZnO, and reduced graphene oxide active materials are shown through the RAMAN spectroscopy (Figure 5.13b) and EDX spectrum (Figure 5.13c). Figure 5.14a depicted the galvanostatic charge discharge of PEDOT:PSS-assisted RZCo//PyR super capacitor where the slightly non-linear discharge curve (IR drop) indicates the presence of Faradaic reaction and internal resistance. The prolong discharging time at current density of 0.1 mA/cm² has contributed to a specific capacitance of 191.8 F/g (Ng *et al.*, 2015). Despite the super capacitor exhibited high capacitance, however, it possesses high charge transfer (R_{ct}) resistive performance, which could be attributed to the bulky electrode interface. Additionally, the conductivity of the electrolyte (Liu *et al.*, 2012) where mild conductive LiClO₄/acetonitrile impedes the ease penetration of electrolyte ions across the hybrid matrix. In addition, the large R_{ct} performance might be arises from the activation barrier (kinetic regime) between electrode and electrolyte interface, thereby limits the diffusion of charge-complexes (Lim *et al.*, 2014). The super capacitor (Figure 5.14c) shows 4% capacitance losses upon 1000 continuous charge discharge cycles. The minor capacitance losses is due to deterioration of the active materials and degradation of polymer chain after excessive swelling and shrinking process.

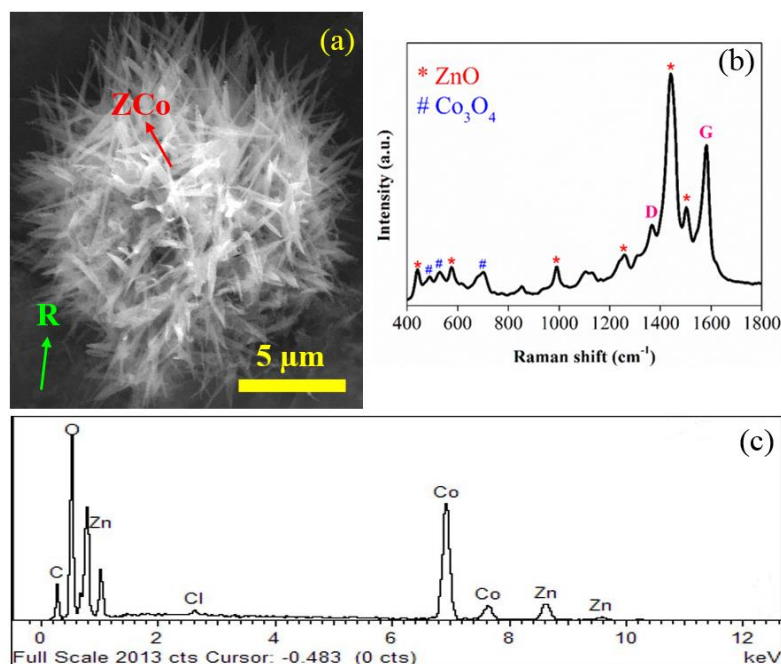


Figure 5.13 (a) FESEM image, (b) RAMAN spectroscopy, and (c) EDX spectrum of RZCo active material deposited on a graphite sheet.

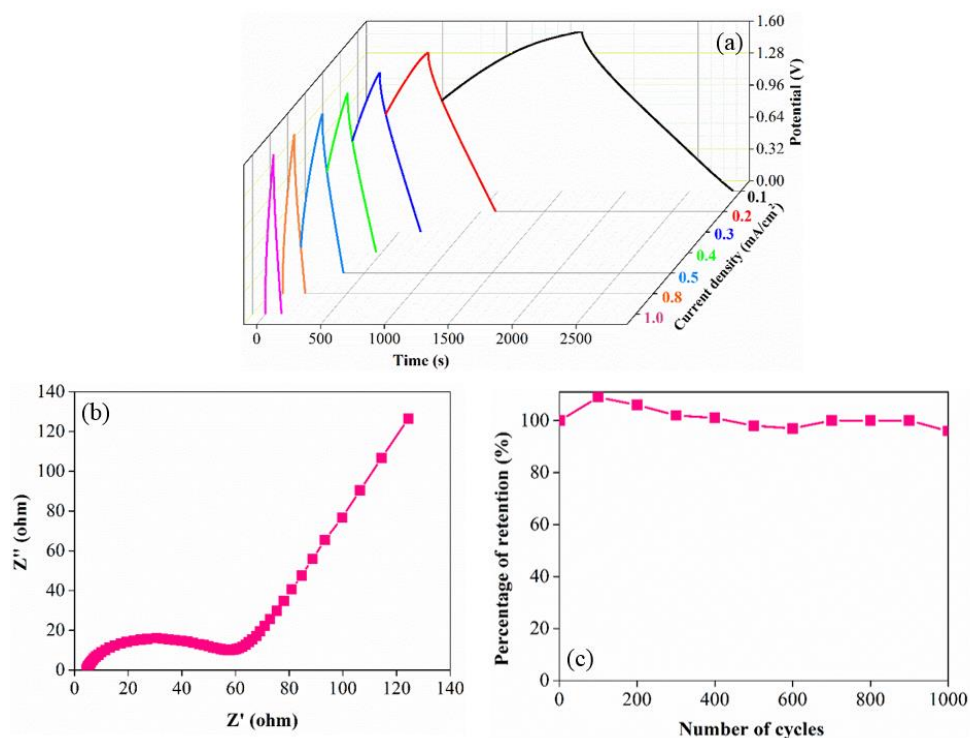


Figure 5.14 (a) Galvanostatic charge discharge, (b) Nyquist plot, and (c) cyclic retention of PEDOT:PSS-assisted RZCo//PyR super capacitor in a swagelok. RZCo is representing reduced graphene oxide/zinc oxide/cobalt oxide, while the PyR is representing the polypyrrole/reduced graphene oxide. The electrochemical impedance spectroscopy was conducted from starting frequency of 100 kHz to an ending frequency of 0.01 Hz.

5.3.4 Electrochemical Performances of Assembled Photo-Super Capacitor

The cesium based perovskite solar cell ($\text{CsPbBr}_{2.9}\text{I}_{0.1}$) was first to be integrated to a PEDOT:PSS-assisted RZCo//PyR asymmetrical super capacitor for a photo-super capacitor device (Figure B.2 in Appendix B). The $\text{CsPbBr}_{2.9}\text{I}_{0.1}$ perovskite solar cell was stacked to a PEDOT:PSS casted shared intermediate cathode for the energy conversion part, whilst the positive electrode of PEDOT:PSS-assisted RZCo was coupled to a PyR negative electrode separated by 1M LiClO_4 /acetonitrile soaked filter paper for the energy storage part. PEDOT can function as an electrode material owing to its fast charge discharge kinetics, low cost, and fast doping dedoping process, and the addition of PSS is expected to be able to improve the conductivity of PEDOT:PSS (Cheng *et al.*, 2016; Xu *et al.*, 2016). Fundamental studies and measurements such as the photovoltage and photocurrent responses were performed, as manifested in Figure 5.15a and 5.15b where both figures featuring positive effect towards light response. Based on Figure 5.15a, zero voltage was presented at the first 50 s without the shine of light. Subsequently, in the presence of light, the photovoltage was abruptly shot up to ~ 80 mV and continue increasing to 90 mV for 100 s, and was then decreases drastically when light was switched off. Likewise, the rapid increment of photocurrent upon light illumination to 0.16 mA/cm^2 , subsequently decreases gradually across time, indicates the projection of photo-generated charges into the super capacitor vicinity (Bagheri *et al.*, 2014). While during the discharging process, the sudden decrement of current shows no current is generated in the absence of solar illumination, which proven the charging of super capacitor is indeed comes from light source. To further proof the energy conversion and storage of the photo-super capacitor, the photocharged integrated device was galvanostatically discharged in dark at the current of 0.1 mA. As the integrated device reaches the cut off potential of 0.07 V, the discharging process took place in dark with the connection of only super capacitor's electrodes (Figure 5.15c).

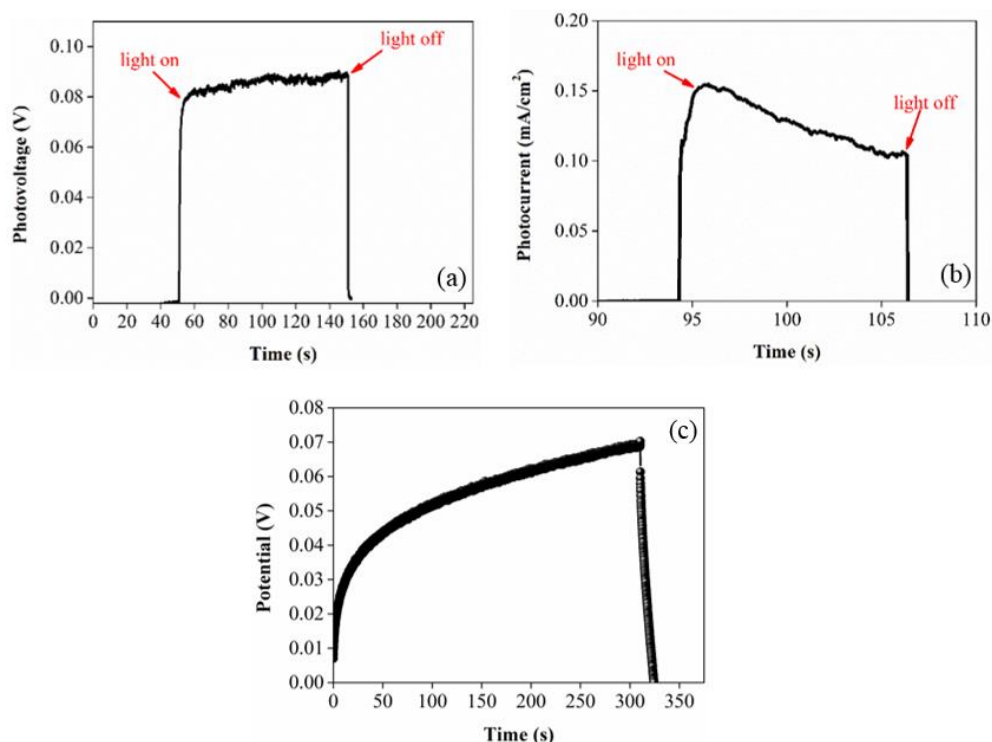


Figure 5.15 (a) Photovoltage response and (b) photocurrent response of CsPbBr_{2.9}I_{0.1} perovskite solar cell in the presence of illumination and in dark condition. (c) galvanostatic charge/discharge of integrated asymmetrical super capacitor in dark condition.

5.3.5 Working Mechanism of Photo-Super Capacitor

In brief, the solar cell composed of glass/ITO/compact and mesoporous TiO₂/CsPbBr_{2.9}I_{0.1} perovskite/*Spiro*-OMeTAD HTM was stacked to an intermediate electrode. The intermediate electrode is composed of PEDOT:PSS-assisted RZCo electrode, which is a sharing bi-functional electrode that performs as the cathode for the solar cell and positive electrode for the super capacitor. Whilst, the super capacitor part is prepared by stacking the positive PEDOT:PSS-assisted RZCo electrode to a PyR negative electrode, and is separated by a 1M LiClO₄/acetonitrile soaked membrane film to prevent short-circuit. RZCo is denoted as reduced graphene oxide, zinc oxide, and cobalt oxide, while PyR stands for polypyrrole and reduced graphene oxide.

To charge the photo-super capacitor, we will need to take note on the circuit connection. Generally, both the super capacitor and perovskite solar cell share an intermediate electrode, which is composed of PEDOT:PSS-assisted RZCo. The bi-functional PEDOT:PSS-assisted RZCo acts as the cathode for the solar cell and positive electrode for the super capacitor. As shown in Figure 5.16, the wire connection should be connected from ITO anode to the negative electrode (PyR) of the super capacitor, thus create the electron alignment along the negative electrode surface, as shown in Figure 5.17a. While the hole will flow to the cathode and to the positive electrode of the super capacitor. It hence created the alignment of positive charge along the positive electrode and electrolyte interface of the super capacitor (Figure 5.17a). Hence, an electric double layer (EDL) property super capacitor is generated. Figure 5.17b shows the magnified alignment of charges along the electrode/electrolyte interface, thus forms an electric double layer capacitor.

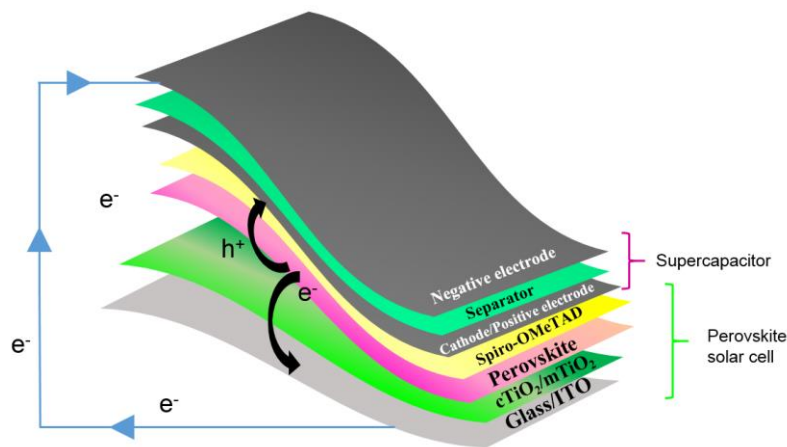


Figure 5.16 Charging mechanism of photo-super capacitor. Positive electrode/cathode represents PEDOT:PSS-assisted RZCo, while negative electrode represents PyR. RZCo is denoted as reduced graphene oxide, zinc oxide, and cobalt oxide, while PyR stands for polypyrrole and reduced graphene oxide.

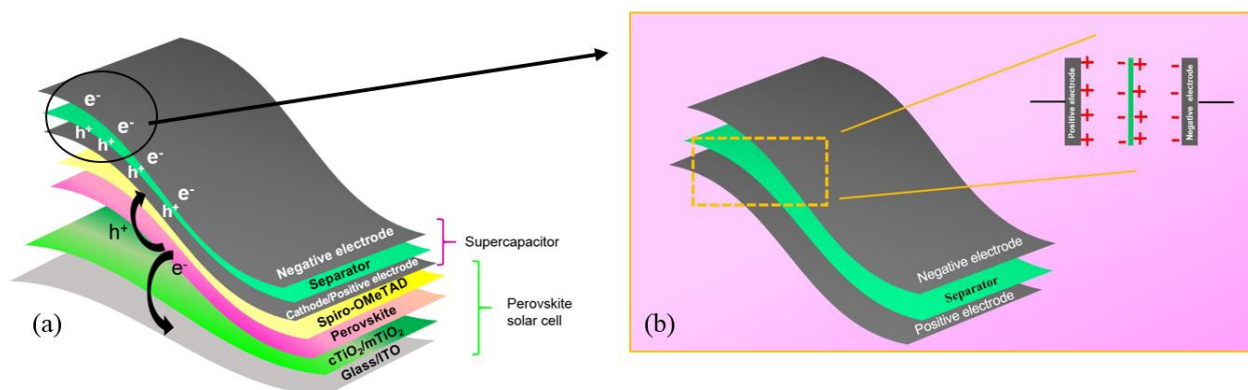


Figure 5.17 (a) Discharging of photo-super capacitor and (b) magnified alignment of charges along the electrode and electrolyte interface of electric double layer capacitor (EDLC).

5.4 Conclusion

In summary, we reported a complete film and device characterization for CsPbBr_{3-x}I_x perovskite solar cells (x varies between 0, 0.1, 0.2, and 0.3 molar ratio), where the absorbers fall in large band gap's category, specifically more than 2.3 eV. The inorganic perovskite solar cell with the inclusion of small amount of iodide, CsPbBr_{2.9}I_{0.1} as the absorber and *Spiro*-OMeTAD as the HTM prepared in ambient condition achieved well-performance of 3.98 % efficiency, as opposed to 2.97 % for pure CsPbBr₃ perovskite. We thus concluded that there are two main factors to explain the origin of the V_{oc} in lead halide perovskite solar cells, which are the large band gap of the perovskite absorber and the deep hole selective transport material that are important for V_{oc} increment. Regarding the perovskite layer, improvement in the V_{oc} was observed when the band gap of the CsPbBr_{3-x}I_x perovskite increases, regardless of the HTM used. Additionally, the V_{oc} was also affected by the selected HTM. When the *Spiro*-OMeTAD was substituted by P3HT/MoO₃, an increment in V_{oc} from 1.16 V to 1.3 V was obtained due to lower work function property of P3HT/MoO₃. However, J_{sc} was compromised due to the charge extraction issues. Stability operation showed that the CsPbBr_{2.9}I_{0.1} and CsPbBr_{2.8}I_{0.2}-based solar cells pose better stability than the pure bromide and CsPbBr_{2.7}I_{0.3} solar cells when *Spiro*-OMeTAD was used as the HTM. Whilst, the perovskite solar cells show no

significant decay for the P3HT/MoO₃ contact. All in all, it shows that the inclusion of optimized amount of iodide not merely improve the stability performance of CsPbBr_{2.9}I_{0.1} solar cell, but also contributed for high PCE performance. The high performing CsPbBr_{2.9}I_{0.1} perovskite solar cell is highly feasible to be integrated for photo-super capacitor application.

For the photo-super capacitor section, the utilization of an inorganic cesium based perovskite material and the beneficial effect of incorporating minute amount of iodide into the bromide framework has improved the film's compactness and has significantly improved its stability performance of a solar cell. A PCE of 70% was successfully retained after a week storage in a humidity controlled desiccator in dark condition for the CsPbBr_{2.9}I_{0.1} perovskite solar cell. The stability of the CsPbBr_{2.9}I_{0.1} device under UV and moisture (> 80% RH) exposure was also investigated. The cesium based lead halide solar cell stored in air could still retain 33% power conversion efficiency, which is 1.6-fold higher than a methylammonium based solar cell (could only retain 20% of its efficiency) after 24 hours. The addition of an optimized amount of iodide has dramatically improved the electron lifetime of the CsPbBr_{2.9}I_{0.1} perovskite solar cell, which is 5-fold longer than a pure bromide perovskite material. The achievement of the inorganic based perovskite solar cell at such high humidity condition (>80% RH) has prompted for integration with an asymmetrical super capacitor for photo-super capacitor application. This integrated device successively shows the photogenerated carriers are being transferred and stored in the super capacitor matrix. The photo-super capacitor shows positive effect towards light illumination. On the contrary, photovoltage and photocurrent abruptly descended to zero when light was switched off. Further optimization of the perovskite and electrode materials of the photo-super capacitor, typically targeting on the stability performance surely promoting this novel device as the new generation green power pack device.

CHAPTER 6

CONCLUDING REMARKS AND RECOMMENDATIONS FOR FUTURE WORKS

6.1 Conclusions

In summary, a photo-super capacitor, which is the combination of a cesium-based perovskite solar cell and a RZCo//PyR asymmetrical super capacitor was successfully fabricated under high relative humidity condition of >80%. In the process of integration, the super capacitor and perovskite solar cell were individually being investigated and studied. For the super capacitor section, the electrochemical performances of symmetrical and asymmetrical super capacitors were studied, followed by the investigation on the performances of a perovskite solar cell before integration process.

In chapter 4, a $\text{Bi}_2\text{O}_3/\text{MnO}_2$ electrode was fabricated via hydrothermal process at high temperature of 140 °C for 24 hours. The synthesized $\text{Bi}_2\text{O}_3/\text{MnO}_2$ electrode was subsequently sandwiched and separated by a Na_2SO_4 soaked filter paper. The symmetrical super capacitor exhibited a specific capacitance of 62.3 F/g (current density of 2 mA/cm²) at 30 °C with energy and power density values of 7.1 Wh/kg and 51.8 W/kg, respectively, where the electrochemical performances of the $\text{Bi}_2\text{O}_3/\text{MnO}_2$ symmetrical super capacitor are dissatisfying for practical use. Notably, the energy density performance of a super capacitor is proportional to the cell voltage of a super capacitor. Thus, a bismuth-based asymmetrical super capacitor was fabricated by stacking the $\text{Bi}_2\text{O}_3/\text{MnO}_2$ positive electrode to a polypyrrole/reduced graphene oxide (rGO) negative electrode. Owing to the different potential window of each electrode, the cell voltage is thereby being widen to 1.6 V, gave rise to higher energy (25.6 Wh/kg) and power (115.3 W/kg) densities performances. Nevertheless, the electrochemical performances of the

Bi₂O₃/MnO₂//PyR asymmetrical super capacitor, typically its stability performances (60% of its capacitance retained after 1000 cycles) are still considerably low and is incompetent for commercialization. Hereafter, a RZCo//PyR asymmetrical super capacitor was fabricated where the RZCo electrode was synthesized through hydrothermal process at lower temperature of 120 °C for 5 hours. The formation of rGO, ZnO, and Co₃O₄ were evidenced through XRD, XPS, etc. The flowerlike structure of RZCo contributed to high specific capacitance of 139.8 F/g, which is about 1.6-fold higher than the Bi₂O₃/MnO₂//PyR asymmetrical super capacitor (89.4 F/g at current density of 2 mA/cm²). The skyrocketed energy and power densities performance of RZCo//PyR asymmetrical super capacitor is about 1.6-fold greater than the bismuth-based asymmetrical super capacitor, and about 6-fold higher in energy density and 3.6-fold higher in power density than the Bi₂O₃/MnO₂ symmetrical super capacitor. In addition, the inclusion of optimum amount of graphene oxide into the ZCo matrix has beneficially improved the cyclic stability of the RZCo//PyR super capacitor (87%) from 60% capacitance retained by the Bi₂O₃/MnO₂//PyR super capacitor. The RZCo//PyR super capacitor exhibited better performances at 30 to 60 °C, which shows its suitability to be employed as the energy storage device for the photo-super capacitor.

In chapter 5, a mixture of halide based cesium perovskite solar cells (CsPbBr_{3-x}I_x) were synthesized via two-step sequential spin-coating process. The addition of an optimum amount of iodide into the bromide matrix (CsPbBr_{2.9}I_{0.1}) has contributed to high power conversion efficiency of 3.9%, higher than a pure bromide perovskite solar cell (CsPbBr₃) with efficiency of 2.9%. In this section, the absorber band gap and the work function of the electron and hole extraction contacts were investigated. It shows that the substitution of P3HT hole extraction contact over the *Spiro*-OMeTAD has improved the V_{oc} from 1.16 to 1.30 V for CsPbBr₃-based solar cell owing to deeper work function of P3HT. In addition, the inclusion of 0.1 molar ratio

of iodide contributed to enhanced stability of perovskite solar cell. Lastly, the CsPbBr_{2.9}I_{0.1} perovskite solar cell was first to be coupled to the RZCo//PyR super capacitor for photo-super capacitor application. The as-fabricated photo-super capacitor showed positive responses towards light illumination and in the absence of light, the photocurrent and voltage dropped to zero abruptly. This arising novel device is envisioned to becoming the next green energy salvor in minimizing the usage of non-renewable energy resources towards sustainable energy production.

6.2 Recommendations for Future Works

So far, this work preliminary shows the accomplishment of perovskite solar cell to be fabricated under a high humidity condition and eventually being integrated for photo-super capacitor application, without emphasizing on its performances. Nevertheless, relentless improvements are essentially needed to further improvise the devices (perovskite solar cell, super capacitor, and photo-super capacitor) so as to meet the outdoor stringent conditions. Further improvizations of all devices are needed such as:

- **Thickness of each active layer.** An optimized thickness of each active layer is duly important to ensure the compactivity without compromising the charge extraction ability. An over-thick layer may impede the charge transfer and increase the series resistance performance, whilst an over-thin layer may create pinholes over the film's surface.
- **Encapsulation of the perovskite materials.** The perovskite material is sensitive to moisture and prone to degradation and decompositon when exposed to high humidified environment. Hence, encapsulation of the perovskite absorber by using hydrophobic hole transporting material or encapsulation of the whole perovkite solar cell device with

a polymeric material such as PMMA could decelerate the degradation process of the solar cell.

- **Encapsulation of the super capacitor and photo-super capacitor devices (to prevent electrolyte loss).** The electrolyte within the super capacitor electrode is highly volatile, especially at high temperature. The loss of electrolyte exaggerate the resistive performances, thus lead to diminish performance of the super capacitor. The super capacitor electrodes should be cased to minimize loss of electrolyte (similar to the battery's casing). Additionally, gel-electrolyte should be employed to replace the liquid electrolyte.

REFERENCES

- Adekunle, A. S., Ozoemena, K. I., Mamba, B. B., Agboola, B. O., and Oluwatobi, O. S. (2011). Supercapacitive properties of symmetry and the asymmetry two electrode coin type supercapacitor cells made from MWCNTS/nickel oxide nanocomposite. URL: <https://researchspace.csir.co.za/dspace/handle/10204/5864>
- Aharon, S., Cohen, B. E., & Etgar, L. (2014). Hybrid lead halide iodide and lead halide bromide in efficient hole conductor free perovskite solar cell. *The Journal of Physical Chemistry C*. **118(30)**: 17160-17165.
- Akkerman, Q. A., D'Innocenzo, V., Accornero, S., Scarpellini, A., Petrozza, A., Prato, M. and Manna, L. (2015). Tuning the optical properties of cesium lead halide perovskite nanocrystals by anion exchange reactions. *Journal of the American Chemical Society*. **137(32)**: 10276-10281.
- Al-Gaashani, R., Radiman, S., Daud, A. R., Tabet, N. and Al-Douri, Y. (2013). XPS and optical studies of different morphologies of ZnO nanostructures prepared by microwave methods. *Ceramics International*. **39(3)**: 2283-2292.
- Almora, O., Zarazua, I., Mas-Marza, E., Mora-Sero, I., Bisquert, J. and Garcia-Belmonte, G. (2015). Capacitive dark currents, hysteresis, and electrode polarization in lead halide perovskite solar cells. *The Journal of Physical Chemistry Letters*. **6(9)**: 1645-1652.
- Ashoka, S., Nagaraju, G. and Chandrappa, G. T. (2010). Reduction of KMnO_4 to Mn_3O_4 via hydrothermal process. *Materials Letters*. **64(22)**: 2538-2540.
- Atourki, L., Vega, E., Mollar, M., Marí, B., Kirou, H., Bouabid, K. and Ihlal, A. (2017). Impact of iodide substitution on the physical properties and stability of cesium lead halide perovskite thin films $\text{CsPbBr}_{3-x}\text{I}_x$ ($0 \leq x \leq 1$). *Journal of Alloys and Compounds*. **702**: 404-409.
- Baek, J., Park, J., Hwang, A. and Kang, Y. (2012). Spectroscopic and morphological investigation of Co_3O_4 microfibers produced by electrospinning process. *Bulletin of the Korean Chemical Society*. **33(4)**: 1242-1246.
- Bagheri, N., Aghaei, A., Ghotbi, M. Y., Marzbanrad, E., Vlachopoulos, N., Häggman, L., Wang, M., Boschloo, Gerrit., Hagfeldt, A., Skunik-Nuckowska, M. and Kulesza, P. J. (2014). Combination of asymmetric supercapacitor utilizing activated carbon and nickel oxide with cobalt polypyridyl-based dye-sensitized solar cell. *Electrochimica Acta*. **143(0)**: 390-397.
- Basri, N. and Dolah, B. (2013). Physical and electrochemical properties of supercapacitor electrodes derived from carbon nanotube and biomass carbon. *Int. J. Electrochem. Sci*. **8**: 257-273.
- Basu, J., Basu, J. K. and Bhattacharyya, T. K. (2010). The evolution of graphene-based electronic devices. *International Journal of Smart and Nano Materials*. **1(3)**: 201-223.

- Beal, R. E., Slotcavage, D. J., Leijtens, T., Bowering, A. R., Belisle, R. A., Nguyen, W. H., Burkhard, G. F., Hoke, E. T. and McGehee, M. D. (2016). Cesium lead halide perovskites with improved stability for tandem solar cells. *The Journal of Physical Chemistry Letters*. **7(5)**: 746-751.
- Bessho, T., Zakeeruddin, S. M., Yeh, C.Y., Diau, E. W.G. and Grätzel, M. (2010). Highly efficient mesoscopic dye-sensitized solar cells based on donor-acceptor-substituted porphyrins. *Angewandte Chemie International Edition*. **49(37)**: 6646-6649.
- Bi, C., Yuan, Y., Fang, Y. and Huang, J. (2015). Low-temperature fabrication of efficient wide - bandgap organolead trihalide perovskite solar cells. *Advanced Energy Materials*, **5(6)**.
- Boix, P. P., Nonomura, K., Mathews, N. and Mhaisalkar, S. G. (2014). Current progress and future perspectives for organic/inorganic perovskite solar cells. *Materials Today*. **17(1)**: 16-23.
- Brownson, D. A. C. and Banks, C. E. (2010). Graphene electrochemistry: An overview of potential applications. *Analyst*. **135(11)**: 2768-2778.
- Brownson, D. A. C., Kampouris, D. K. and Banks, C. E. (2011). An overview of graphene in energy production and storage applications. *Journal of Power Sources*. **196(11)**: 4873-4885.
- Burschka, J., Pellet, N., Moon, S.J., Humphry-Baker, R., Gao, P., Nazeeruddin, M. K. and Gratzel, M. (2013). Sequential deposition as a route to high-performance perovskite-sensitized solar cells. *Nature*. **499(7458)**: 316-319.
- Cai, D., Huang, H., Wang, D., Liu, B., Wang, L., Liu, Y., Li, Q. and Wang, T. (2014). High-performance supercapacitor electrode based on the unique ZnO@Co₃O₄ core/shell heterostructures on nickel foam. *ACS Applied Materials & Interfaces*. **6(18)**: 15905-15912.
- Cai, M., Tiong, V. T., Hreid, T., Bell, J. and Wang, H. (2015). An efficient hole transport material composite based on poly(3-hexylthiophene) and bamboo-structured carbon nanotubes for high performance perovskite solar cells. *Journal of Materials Chemistry A*. **3(6)**: 2784-2793.
- Cai, S., Zhang, D., Shi, L., Xu, J., Zhang, L., Huang, L., Li, H. and Zhang, J. (2014). Porous Ni-Mn oxide nanosheets in situ formed on nickel foam as 3D hierarchical monolith de-NO_x catalysts. *Nanoscale*. **6(13)**: 7346-7353.
- Cao, H., Yang, D., Zhu, S., Dong, L. and Zheng, G. (2012). Preparation, characterization, and electrochemical studies of sulfur-bearing nickel in an ammoniacal electrolyte: the influence of thiourea. *Journal of Solid State Electrochemistry*. **16(9)**: 3115-3122.
- Cao, K., Zuo, Z., Cui, J., Shen, Y., Moehl, T., Zakeeruddin, S. M., Grätzel, M. and Wang, M. (2015). Efficient screen printed perovskite solar cells based on mesoscopic TiO₂/Al₂O₃/NiO/carbon architecture. *Nano Energy*. **17**: 171-179.

- Carli, S., Baena, J. P. C., Marianetti, G., Marchetti, N., Lessi, M., Abate, A., Caramori, S., Grätzel, M., Bellina, F. and Bignozzi, C. A. (2016). A new 1, 3, 4-oxadiazole-based hole-transport material for efficient $\text{CH}_3\text{NH}_3\text{PbBr}_3$ perovskite solar cells. *ChemSusChem*. **9**: 657-661.
- Chae, J. H. and Chen, G. Z. (2012). 1.9 V aqueous carbon-carbon supercapacitors with unequal electrode capacitances. *Electrochimica Acta*. **86**: 248-254.
- Chang, Q., Ma, Z., Wang, J., Yan, Y., Shi, W., Chen, Q., Huang, Y., Yu, Q. and Huang, L. (2015). Graphene nanosheets@ZnO nanorods as three-dimensional high efficient counter electrodes for dye sensitized solar cells. *Electrochimica Acta*. **151(0)**: 459-466.
- Chee, W. K., Lim, H. N., Harrison, I., Chong, K. F., Zainal, Z., Ng, C. H. and Huang, N. M. (2015). Performance of flexible and binderless polypyrrole/graphene oxide/zinc oxide supercapacitor electrode in a symmetrical two-electrode configuration. *Electrochimica Acta*. **157(0)**: 88-94.
- Chee, W. K., Lim, H. N. and Huang, N. M. (2015). Electrochemical properties of free-standing polypyrrole/graphene oxide/zinc oxide flexible supercapacitor. *International Journal of Energy Research*. **39(1)**: 111-119.
- Chen, H.W., Hsu, C.Y., Chen, J.G., Lee, K.M., Wang, C.C., Huang, K.C. and Ho, K.C. (2010). Plastic dye-sensitized photo-supercapacitor using electrophoretic deposition and compression methods. *Journal of Power Sources*. **195(18)**: 6225-6231.
- Chen, H.W., Huang, T.Y., Chang, T.H., Sanehira, Y., Kung, C.W., Chu, C.W., Ikegami, M. and Ho, K.C. (2016). Efficiency enhancement of hybrid perovskite solar cells with MEH-PPV hole-transporting layers. *Scientific Reports*. **6**: 34319.
- Chen, S.M., Ramachandran, R., Mani, V. and Saraswathi, R. (2014). Recent advancements in electrode materials for the high-performance electrochemical supercapacitors: A review. *Int. J. Electrochem. Sc.* **9**: 4072-4085.
- Chen, S., Zhu, J., Wu, X., Han, Q. and Wang, X. (2010). Graphene oxide-MnO₂ nanocomposites for supercapacitors. *ACS Nano*. **4(5)**: 2822-2830.
- Chen, T. and Dai, L. (2014). Flexible supercapacitors based on carbon nanomaterials. *Journal of Materials Chemistry A*. **2(28)**: 10756-10775.
- Chen, W., He, Y., Li, X., Zhou, J., Zhang, Z., Zhao, C., Gong, C., Li, S., P, X. and Xie, E. (2013). Facilitated charge transport in ternary interconnected electrodes for flexible supercapacitors with excellent power characteristics. *Nanoscale*. **5(23)**: 11733-11741.
- Chen, W., Xia, C. and Alshareef, H. N. (2014). One-step electrodeposited nickel cobalt sulfide nanosheet arrays for high-performance asymmetric supercapacitors. *ACS Nano*. **8(9)**: 9531-9541.
- Chen, X., Hu, H., Xia, Z., Gao, W., Gou, W., Qu, Y. and Ma, Y. (2017). CsPbBr₃ perovskite nanocrystals as highly selective and sensitive spectrochemical probes for gaseous HCl detection. *Journal of Materials Chemistry C*. **5(2)**: 309-313.

- Cheng, Q., Tang, J., Ma, J., Zhang, H., Shinya, N. and Qin, L.C. (2011). Graphene and nanostructured MnO₂ composite electrodes for supercapacitors. *Carbon*. **49(9)**: 2917-2925.
- Cheng, T., Zhang, Y.Z., Zhang, J.D., Lai, W.Y. and Huang, W. (2016). High-performance free-standing PEDOT:PSS electrodes for flexible and transparent all-solid-state supercapacitors. *Journal of Materials Chemistry A*. **4(27)**: 10493-10499.
- Cheng, Y., Zhang, H., Lu, S., Varanasi, C. V. and Liu, J. (2013). Flexible asymmetric supercapacitors with high energy and high power density in aqueous electrolytes. *Nanoscale*. **5(3)**: 1067-1073.
- Choi, H., Jeong, J., Kim, H.B., Kim, S., Walker, B., Kim, G.H. and Kim, J. Y. (2014). Cesium-doped methylammonium lead iodide perovskite light absorber for hybrid solar cells. *Nano Energy*. **7**: 80-85.
- Christians, J. A., Fung, R. C. and Kamat, P. V. (2013). An inorganic hole conductor for organolead halide perovskite solar cells. Improved hole conductivity with copper iodide. *Journal of the American Chemical Society*. **136(2)**: 758-764.
- Cohn, A. P., Erwin, W. R., Share, K., Oakes, L., Westover, A. S., Carter, R. E., Bardhan, R. and Pint, C. L. (2015). All silicon electrode photocapacitor for integrated energy storage and conversion. *Nano Letters*. **15(4)**: 2727-2731.
- Collins, J., Ngo, T., Qu, D. and Foster, M. (2013). Spectroscopic investigations of sequential nitric acid treatments on granulated activated carbon: Effects of surface oxygen groups on π density. *Carbon*. **57**: 174-183.
- Cong, H.P., Ren, X.C., Wang, P. and Yu, S.H. (2013). Flexible graphene-polyaniline composite paper for high-performance supercapacitor. *Energy & Environmental Science*. **6(4)**: 1185-1191.
- Conings, B., Baeten, L., De Dobbelaere, C., D'Haen, J., Manca, J. and Boyen, H. G. (2014). Perovskite-based hybrid solar cells exceeding 10% efficiency with high reproducibility using a thin film sandwich approach. *Advanced Materials*. **26(13)**: 2041-2046.
- Dimesso, L., Dimamay, M., Hamburger, M. and Jaegermann, W. (2014). Properties of CH₃NH₃PbX₃ (X = I, Br, Cl) powders as precursors for organic/inorganic solar cells. *Chemistry of Materials*. **26(23)**: 6762-6770.
- Dreyer, D. R., Park, S., Bielawski, C. W. and Ruoff, R. S. (2010). The chemistry of graphene oxide. *Chemical Society Reviews*. **39(1)**: 228-240.
- Dualeh, A., Moehl, T., T etreault, N., Teuscher, J., Gao, P., Nazeeruddin, M. K. and Gr atzel, M. (2014). Impedance spectroscopic analysis of lead iodide perovskite-sensitized solid-state solar cells. *ACS Nano*. **8(1)**: 362-373.
- Dubal, D. P. and Holze, R. (2013). All-solid-state flexible thin film supercapacitor based on Mn₃O₄ stacked nanosheets with gel electrolyte. *Energy*. **51**: 407-412.

- Edri, E., Kirmayer, S., Cahen, D. and Hodes, G. (2013). High open-circuit voltage solar cells based on organic–inorganic lead bromide perovskite. *The Journal of Physical Chemistry Letters*. **4(6)**: 897-902.
- Eeu, Y. C., Lim, H. N., Lim, Y. S., Zakarya, S. A. and Huang, N. M. (2013). Electrodeposition of polypyrrole/reduced graphene oxide/iron oxide nanocomposite as supercapacitor electrode material. *Journal of Nanomaterials*. **2013**: 6.
- Eperon, G. E., Stranks, S. D., Menelaou, C., Johnston, M. B., Herz, L. M. and Snaith, H. J. (2014). Formamidinium lead trihalide: a broadly tunable perovskite for efficient planar heterojunction solar cells. *Energy & Environmental Science*. **7(3)**: 982-988.
- Fakharuddin, A., Jose, R., Brown, T. M., Fabregat-Santiago, F. and Bisquert, J. (2014). A perspective on the production of dye-sensitized solar modules. *Energy & Environmental Science*. **7(12)**: 3952-3981.
- Fan, Z., Yan, J., Wei, T., Zhi, L., Ning, G., Li, T. and Wei, F. (2011). Asymmetric supercapacitors based on graphene/MnO₂ and activated carbon nanofiber electrodes with high power and energy density. *Advanced Functional Materials*. **21(12)**: 2366-2375.
- Fang, W.C., Chyan, O., Sun, C.L., Wu, C.T., Chen, C.P., Chen, K.H., Chen, Li.C. and Huang, J.H. (2007). Arrayed CN_xNT–RuO₂ nanocomposites directly grown on Ti-buffered Si substrate for supercapacitor applications. *Electrochemistry Communications*. **9(2)**: 239-244.
- Feldt, S. M., Gibson, E. A., Gabrielsson, E., Sun, L., Boschloo, G. and Hagfeldt, A. (2010). Design of organic dyes and cobalt polypyridine redox mediators for high-efficiency dye-sensitized solar cells. *Journal of the American Chemical Society*. **132(46)**: 16714-16724.
- Freitas, J. N. d., Gonçalves, A. d. S., De Paoli, M.-A., Durrant, J. R. and Nogueira, A. F. (2008). The role of gel electrolyte composition in the kinetics and performance of dye-sensitized solar cells. *Electrochimica Acta*. **53(24)**: 7166-7172.
- Frohne, H., Shaheen, S. E., Brabec, C. J., Müller, D. C., Sariciftci, N. S. and Meerholz, K. (2002). Influence of the anodic work function on the performance of organic solar cells. *ChemPhysChem*. **3(9)**: 795-799.
- Frolova, L. A., Anokhin, D. V., Piryazev, A. A., Luchkin, S. Y., Dremova, N. N., Stevenson, K. J. and Troshin, P. A. (2017). Highly efficient all-inorganic planar heterojunction perovskite solar cells produced by thermal coevaporation of CsI and PbI₂. *The Journal of Physical Chemistry Letters*. **8(1)**: 67-72.
- Gan, J. K., Lim, Y. S., Huang, N. M. and Lim, H. N. (2015). Effect of pH on morphology and supercapacitive properties of manganese oxide/polypyrrole nanocomposite. *Applied Surface Science*. **357**: 479-486.

- Gnana kumar, G., Awan, Z., Suk Nahm, K. and Stanley Xavier, J. (2014). Nanotubular MnO₂/graphene oxide composites for the application of open air-breathing cathode microbial fuel cells. *Biosensors and Bioelectronics*. **53**: 528-534.
- Gong, J., Liang, J. and Sumathy, K. (2012). Review on dye-sensitized solar cells (DSSCs): Fundamental concepts and novel materials. *Renewable and Sustainable Energy Reviews*. **16(8)**: 5848-5860.
- Gonzalez-Pedro, V., Juarez-Perez, E. J., Arsyad, W.S., Barea, E. M., Fabregat-Santiago, F., Mora-Sero, I. and Bisquert, J. (2014). General working principles of CH₃NH₃PbX₃ perovskite solar cells. *Nano Letters*. **14(2)**: 888-893.
- Gouda, L., Gottesman, R., Ginsburg, A., Keller, D. A., Haltzi, E., Hu, J., Tirosh, S., Anderson, A., Zaban, A. and Boix, P. P. (2015). Open circuit potential build-up in perovskite solar cells from dark conditions to 1 sun. *The Journal of Physical Chemistry Letters*. **6(22)**: 4640-4645.
- Grätzel, M. (2014). The light and shade of perovskite solar cells. *Nature materials*. **13(9)**: 838-842.
- Green, M. A., Emery, K., Hishikawa, Y., Warta, W. and Dunlop, E. D. (2016). Solar cell efficiency tables (version 47). *Progress in Photovoltaics*. **24(1)**: 3-11.
- Gujar, T. P., Shinde, V. R., Lokhande, C. D. and Han, S.H. (2006). Electrosynthesis of Bi₂O₃ thin films and their use in electrochemical supercapacitors. *Journal of Power Sources*. **161(2)**: 1479-1485.
- Guo, W., Xue, X., Wang, S., Lin, C. and Wang, Z. L. (2012). An integrated power pack of dye-sensitized solar cell and Li battery based on double-sided TiO₂ nanotube arrays. *Nano Letters*. **12(5)**: 2520-2523.
- Hall, P. J. and Bain, E. J. (2008). Energy-storage technologies and electricity generation. *Energy Policy*. **36(12)**: 4352-4355.
- He, Y., Chen, W., Li, X., Zhang, Z., Fu, J., Zhao, C. and Xie, E. (2012). Freestanding three-dimensional graphene/MnO₂ composite networks as ultralight and flexible supercapacitor electrodes. *ACS Nano*. **7(1)**: 174-182.
- Hou, Y. and Gao, S. (2003). Monodisperse nickel nanoparticles prepared from a monosurfactant system and their magnetic properties. *Journal of Materials Chemistry*. **13(7)**: 1510-1512.
- Hsu, C.Y., Chen, H.W., Lee, K.M., Hu, C.W. and Ho, K.C. (2010). A dye-sensitized photo-supercapacitor based on PProDOT-Et₂ thick films. *Journal of Power Sources*. **195(18)**: 6232-6238.
- Hutter, E. M., Eperon, G. E., Stranks, S. D. and Savenije, T. J. (2015). Charge carriers in planar and meso-structured organic-inorganic perovskites: mobilities, lifetimes, and concentrations of trap states. *The Journal of Physical Chemistry Letters*. **6(15)**: 3082-3090.

- Iamprasertkun, P., Krittayavathananon, A., Seubsai, A., Chanlek, N., Kidkhunthod, P., Sangthong, W., Maensiri, S., Yimnirun, R., Nilmoung, S., Panopard, P., Ittisanronnachai, S., Kongpatpanich, K., Limtrakul, J. and Sawangphruk, M. (2016). Charge storage mechanisms of manganese oxide nanosheets and N-doped reduced graphene oxide aerogel for high-performance asymmetric supercapacitors. *Scientific Reports*. **6**: 37560.
- Jampani, P. H., Manivannan, A. and Kumta, P. N. (2010). Advancing the supercapacitor materials and technology frontier for improving power quality. *The electrochemical Society interface*. **19(3)**: 57-62.
- Jeon, N. J., Lee, J., Noh, J. H., Nazeeruddin, M. K., Grätzel, M. and Seok, S. I. (2013). Efficient inorganic–organic hybrid perovskite solar cells based on pyrene arylamine derivatives as hole-transporting materials. *Journal of the American Chemical Society*. **135(51)**: 19087-19090.
- Jin, M., Han, G., Chang, Y., Zhao, H. and Zhang, H. (2011). Flexible electrodes based on polypyrrole/manganese dioxide/polypropylene fibrous membrane composite for supercapacitor. *Electrochimica Acta*. **56(27)**: 9838-9845.
- Jost, K., Dion, G. and Gogotsi, Y. (2014). Textile energy storage in perspective. *Journal of Materials Chemistry A*. **2(28)**: 10776-10787.
- Juarez-Perez, E. J., Wußler, M., Fabregat-Santiago, F., Lakus-Wollny, K., Mankel, E., Mayer, T., Jaegermann, W. and Mora-Sero, I. (2014). Role of the selective contacts in the performance of lead halide perovskite solar cells. *The Journal of Physical Chemistry Letters*. **5(4)**: 680-685.
- Kang, Y. J., Chun, S.J., Lee, S.S., Kim, B.Y., Kim, J. H., Chung, H., Lee, S.Y. and Kim, W. (2012). All-solid-state flexible supercapacitors fabricated with bacterial nanocellulose papers, carbon nanotubes, and triblock-copolymer ion gels. *ACS Nano*. **6(7)**: 6400-6406.
- Kenisarin, M. and Mahkamov, K. (2016). Salt hydrates as latent heat storage materials: Thermophysical properties and costs. *Solar Energy Materials and Solar Cells*. **145**: 255-286.
- Kim, H.S. and Park, N.G. (2014). Parameters affecting i–v hysteresis of CH₃NH₃PbI₃ perovskite solar cells: effects of perovskite crystal size and mesoporous TiO₂ layer. *The Journal of Physical Chemistry Letters*. **5(17)**: 2927-2934.
- Kim, H., Watthanaphanit, A. and Saito, N. (2016). Synthesis of colloidal MnO₂ with a sheet-like structure by one-pot plasma discharge in permanganate aqueous solution. *RSC Advances*. **6(4)**: 2826-2834.
- Kim, S. Y., Yang, K. and Kim, B.H. (2014). Enhanced electrical capacitance of heteroatom-decorated nanoporous carbon nanofiber composites containing graphene. *Electrochimica Acta*. **137**: 781-788.

- Kitazawa, N., Watanabe, Y. and Nakamura, Y. (2002). Optical properties of $\text{CH}_3\text{NH}_3\text{PbX}_3$ (X= halogen) and their mixed-halide crystals. *Journal of Materials Science*. **37(17)**: 3585-3587.
- Koh, T. M., Fu, K., Fang, Y., Chen, S., Sum, T. C., Mathews, N., Mhaisalkar, S.G., Boix, P.P. and Baikie, T. (2014). Formamidinium-containing metal-halide: an alternative material for near-IR absorption perovskite solar cells. *The Journal of Physical Chemistry C*. **118(30)**: 16458-16462.
- Kojima, A., Teshima, K., Shirai, Y. and Miyasaka, T. (2009). Organometal halide perovskites as visible-light sensitizers for photovoltaic cells. *Journal of the American Chemical Society*. **131(17)**: 6050-6051.
- Kulbak, M., Cahen, D. and Hodes, G. (2015). How important is the organic part of lead halide perovskite photovoltaic cells? Efficient CsPbBr_3 cells. *The Journal of Physical Chemistry Letters*. **6(13)**: 2452-2456.
- Kulbak, M., Gupta, S., Kedem, N., Levine, I., Bendikov, T., Hodes, G. and Cahen, D. (2016). Cesium enhances long-term stability of lead bromide perovskite-based solar cells. *The Journal of Physical Chemistry Letters*. **7(1)**: 167-172.
- Latha, K., Lin, J.H. and Ma, Y.R. (2007). One-dimensional Bi_2O_3 nanohooks: synthesis, characterization and optical properties. *Journal of Physics: Condensed Matter*. **19(40)**: 406204.
- Lau, S.C., Lim, H.N., Ravooof, T.B.S.A., Yaacob, M.H., Grant, D.M., MacKenzie, R.C.I., Harrison, I. and Huang, N.M. (2017). A three-electrode integrated photo-supercapacitor utilizing graphene-based intermediate bifunctional electrode. *Electrochimica Acta*. **238**: 178-184.
- Lee, M. M., Teuscher, J., Miyasaka, T., Murakami, T. N. and Snaith, H. J. (2012). Efficient hybrid solar cells based on meso-superstructured organometal halide perovskites. *Science*. **338(6107)**: 643-647.
- Lee, S.W., Kim, S., Bae, S., Cho, K., Chung, T., Mundt, L. E., Lee, S., Park, S., Park, H., Schubert, M.C., Glunz, S.W., Ko, Y., Jun, Y., Lee, H.S. and Kim, D. (2016). UV degradation and recovery of perovskite solar cells. *Scientific Reports*. **6**: 38150
- Leijtens, T., Eperon, G. E., Pathak, S., Abate, A., Lee, M. M. and Snaith, H. J. (2013). Overcoming ultraviolet light instability of sensitized TiO_2 with meso-superstructured organometal tri-halide perovskite solar cells. *Nature communications*. **4**: 2885.
- Li, Y., Xie, H., Wang, J. and Chen, L. (2011). Preparation and electrochemical performances of $\alpha\text{-MnO}_2$ nanorod for supercapacitor. *Materials Letters*. **65(2)**: 403-405.
- Liang, J., Zhao, P., Wang, C., Wang, Y., Hu, Y., Zhu, G., Ma, L., Liu, J. and Jin, Z. (2017). $\text{CsPb}_{0.9}\text{Sn}_{0.1}\text{IBr}_2$ Based All-Inorganic Perovskite Solar Cells with Exceptional efficiency and stability. *Journal of The American Chemical Society*. **139(40)**: 14009-14012.

- Lim, Y. S., Lim, H. N., Lim, S. P. and Huang, N. M. (2014). Catalyst-assisted electrochemical deposition of graphene decorated polypyrrole nanoparticles film for high-performance supercapacitor. *RSC Advances*. **4(99)**: 56445-56454.
- Lim, Y. S., Tan, Y. P., Lim, H. N., Huang, N. M. and Tan, W. T. (2013). Preparation and characterization of polypyrrole/graphene nanocomposite films and their electrochemical performance. *Journal of Polymer Research*. **20(6)**: 1-10.
- Lim, Y. S., Tan, Y. P., Lim, H. N., Huang, N. M., Tan, W. T., Yarmo, M. A. and Yin, C.Y. (2014). Potentiostatically deposited polypyrrole/graphene decorated nano-manganese oxide ternary film for supercapacitors. *Ceramics International*. **40(3)**: 3855-3864.
- Lim, Y. S., Tan, Y. P., Lim, H. N., Tan, W. T., Mahnaz, M. A., Talib, Z. A., Huang, N.M., Kassim, A. and Yarmo, M. A. (2013). Polypyrrole/graphene composite films synthesized via potentiostatic deposition. *Journal of Applied Polymer Science*. **128(1)**: 224-229.
- Lin, T.W., Dai, C.S., & Hung, K.C. (2014). High energy density asymmetric supercapacitor based on NiOOH/Ni₃S₂/3D graphene and Fe₃O₄/Graphene composite electrodes. *Scientific Reports*. **4**: 7274.
- Liu, J., Jiang, J., Cheng, C., Li, H., Zhang, J., Gong, H. and Fan, H. J. (2011). Co₃O₄ nanowire@MnO₂ ultrathin nanosheet core/shell arrays: a new class of high-performance pseudocapacitive materials. *Advanced Materials*. **23(18)**: 2076-2081.
- Liu, L., Jiang, J., Jin, S., Xia, Z. and Tang, M. (2011). Hydrothermal synthesis of β-bismuth oxide nanowires from particles. *CrystEngComm*. **13(7)**: 2529-2532.
- Liu, M., Johnston, M. B. and Snaith, H. J. (2013). Efficient planar heterojunction perovskite solar cells by vapour deposition. *Nature*. **501(7467)**: 395-398.
- Liu, T., Zhao, Y., Gao, L. and Ni, J. (2015). Engineering Bi₂O₃-Bi₂S₃ heterostructure for superior lithium storage. *Scientific Reports*. **5**: 9307.
- Liu, W., Yan, X., Lang, J. and Xue, Q. (2012). Effects of concentration and temperature of EMIMBF₄/acetonitrile electrolyte on the supercapacitive behavior of graphene nanosheets. *Journal of Materials Chemistry*. **22(18)**: 8853-8861.
- Lu, X., Zheng, D., Zhai, T., Liu, Z., Huang, Y., Xie, S. and Tong, Y. (2011). Facile synthesis of large-area manganese oxide nanorod arrays as a high-performance electrochemical supercapacitor. *Energy & Environmental Science*. **4(8)**: 2915-2921.
- Luan, F., Wang, G., Ling, Y., Lu, X., Wang, H., Tong, Y., Liu, X.X. and Li, Y. (2013). High energy density asymmetric supercapacitors with a nickel oxide nanoflake cathode and a 3D reduced graphene oxide anode. *Nanoscale*. **5(17)**: 7984-7990.
- Lv, H., Ji, G., Liang, X., Zhang, H. and Du, Y. (2015). A novel rod-like MnO₂@Fe loading on graphene giving excellent electromagnetic absorption properties. *Journal of Materials Chemistry C*. **3(19)**: 5056-5064.

- Ma, J., Zhu, S., Shan, Q., Liu, S., Zhang, Y., Dong, F. and Liu, H. (2015). Facile synthesis of flower-like $(\text{BiO})_2\text{CO}_3@\text{MnO}_2$ and $\text{Bi}_2\text{O}_3@\text{MnO}_2$ nanocomposites for supercapacitors. *Electrochimica Acta*. **168**: 97-103.
- Ma, M.G., Zhu, J.F., Sun, R.C. and Zhu, Y.J. (2010). Microwave-assisted synthesis of hierarchical Bi_2O_3 spheres assembled from nanosheets with pore structure. *Materials Letters*. **64(13)**: 1524-1527.
- Marchioro, A., Teuscher, J., Friedrich, D., Kunst, M., van de Krol, R., Moehl, T., Grätzel, and Moser, J.E. (2014). Unravelling the mechanism of photoinduced charge transfer processes in lead iodide perovskite solar cells. *Nat Photon*. **8(3)**: 250-255.
- Masarapu, C., Zeng, H. F., Hung, K. H. and Wei, B. (2009). Effect of temperature on the capacitance of carbon nanotube supercapacitors. *ACS Nano*. **3(8)**: 2199-2206.
- Meher, S. K., Justin, P. and Rao, G. R. (2010). Pine-cone morphology and pseudocapacitive behavior of nanoporous nickel oxide. *Electrochimica Acta*. **55(28)**: 8388-8396.
- Miao, Y.X., Ren, L.H., Shi, L. and Li, W.C. (2015). Hydrothermal synthesis of manganese oxide nanorods as a highly active support for gold nanoparticles in CO oxidation and their stability at low temperature. *RSC Advances*. **5(77)**: 62732-62738.
- Murakami, T. N., Kawashima, N. and Miyasaka, T. (2005). A high-voltage dye-sensitized photocapacitor of a three-electrode system. *Chemical Communications*. **26**: 3346-3348.
- Ng, C. H., Lim, H. N., Hayase, S., Harrison, I., Pandikumar, A. and Huang, N. M. (2015). Potential active materials for photo-supercapacitor: A review. *Journal of Power Sources*. **296**: 169-185.
- Ng, C. H., Lim, H. N., Hayase, S., Zainal, Z., Shafie, S. and Huang, N. M. (2017). Capacitive performance of graphene-based asymmetric supercapacitor. *Electrochimica Acta*. **229**: 173-182.
- Ng, C. H., Lim, H. N., Lim, Y. S., Chee, W. K., & Huang, N. M. (2015). Fabrication of flexible polypyrrole/graphene oxide/manganese oxide supercapacitor. *International Journal of Energy Research*. **39(3)**, 344-355. doi: 10.1002/er.3247
- Niezgoda, J. S., Foley, B. J., Chen, A. Z. and Choi, J. J. (2017). Improved charge collection in highly efficient CsPbBr_2 solar cells with light-induced dealloying. *ACS Energy Letters*. **2(5)**: 1043-1049.
- Nithya, V. D. and Sabari Arul, N. (2016). Progress and development of Fe_3O_4 electrodes for supercapacitors. *Journal of Materials Chemistry A*. **4(28)**: 10767-10778.
- Noh, J. H., Im, S. H., Heo, J. H., Mandal, T. N. and Seok, S. I. (2013). Chemical management for colorful, efficient, and stable inorganic-organic hybrid nanostructured solar cells. *Nano Letters*. **13(4)**: 1764-1769.
- O'regan, B. and Grätzel, M. (1991). A low-cost, high-efficiency solar cell based on dye-sensitized colloidal TiO_2 films. *Nature*. **353(6346)**: 737-740.

- Ou, B., Huang, R., Wang, W., Zhou, H. and He, C. (2014). Preparation of conductive polyaniline grafted graphene hybrid composites via graft polymerization at room temperature. *RSC Advances*. **4(81)**: 43212-43219.
- Park, N.G. (2015a). Perovskite solar cells: an emerging photovoltaic technology. *Materials Today*. **18(2)**: 65-72.
- Park, N.G. (2015b). Perovskite solar cells: Switchable photovoltaics. *Nat Mater*. **14(2)**: 140-141.
- Park, N., Van de Lagemaat, J. and Frank, A. (2003). Effect of morphology on electron transport in dye-sensitized nanostructured TiO₂ Films. *Journal of PhotoScience*. **10(2)**: 199-202.
- Pascoe, A. R., Duffy, N. W., Scully, A. D., Huang, F. and Cheng, Y.B. (2015). Insights into planar CH₃NH₃PbI₃ perovskite solar cells using impedance spectroscopy. *The Journal of Physical Chemistry C*. **119(9)**: 4444-4453.
- Pei, S., Zhao, J., Du, J., Ren, W. and Cheng, H.M. (2010). Direct reduction of graphene oxide films into highly conductive and flexible graphene films by hydrohalic acids. *Carbon*. **48(15)**: 4466-4474.
- Protesescu, L., Yakunin, S., Bodnarchuk, M. I., Krieg, F., Caputo, R., Hendon, C. H., Yang, R.X., Walsh, A. and Kovalenko, M. V. (2015). Nanocrystals of cesium lead halide perovskites (CsPbX₃, X = Cl, Br, and I): Novel optoelectronic materials showing bright emission with wide color gamut. *Nano Letters*. **15(6)**: 3692-3696.
- Qiu, K., Lu, Y., Zhang, D., Cheng, J., Yan, H., Xu, J., Xu, J., Liu, X., Kim, J.K. and Luo, Y. (2015). Mesoporous, hierarchical core/shell structured ZnCo₂O₄/MnO₂ nanocone forests for high-performance supercapacitors. *Nano Energy*. **11(0)**: 687-696.
- Qiu, L., Yang, X., Gou, X., Yang, W., Ma, Z. F., Wallace, G. G. and Li, D. (2010). Dispersing carbon nanotubes with graphene oxide in water and synergistic effects between graphene derivatives. *Chemistry-A European Journal*. **16(35)**: 10653-10658.
- Rahman, M. M., Khan, S. B., Asiri, A. M., Alamry, K. A., Khan, A. A. P., Khan, A., Rub, M.A. and Azum, N. (2013). Acetone sensor based on solvothermally prepared ZnO doped with Co₃O₄ nanorods. *Mikrochimica Acta*. **180(7-8)**: 675-685.
- Ray, C., Dutta, S., Roy, A., Sahoo, R. and Pal, T. (2016). Redox mediated synthesis of hierarchical Bi₂O₃/MnO₂ nanoflowers: a non-enzymatic hydrogen peroxide electrochemical sensor. *Dalton Transactions*. **45(11)**: 4780-4790.
- Ray, S. C., Saha, A., Basiruddin, S. K., Roy, S. S. and Jana, N. R. (2011). Polyacrylate-coated graphene-oxide and graphene solution via chemical route for various biological application. *Diamond and Related Materials*. **20(3)**: 449-453.
- Ripolles, T. S., Nishinaka, K., Ogomi, Y., Miyata, Y. and Hayase, S. (2016). Efficiency enhancement by changing perovskite crystal phase and adding a charge extraction interlayer in organic amine free-perovskite solar cells based on cesium. *Solar Energy Materials and Solar Cells*. **144**: 532-536.

- Roiati, V., Colella, S., Lerario, G., De Marco, L., Rizzo, A., Listorti, A. and Gigli, G. (2014). Investigating charge dynamics in halide perovskite-sensitized mesostructured solar cells. *Energy & Environmental Science*. **7(6)**: 1889-1894.
- Rühle, S., Segal, A., Vilan, A., Kurtz, S. R., Grinis, L., Zaban, A., Lubomirsky, I. and Cahen, D. (2009). A two junction, four terminal photovoltaic device for enhanced light to electric power conversion using a low-cost dichroic mirror. *Journal of Renewable and Sustainable Energy*. **1(1)**: 013106.
- Ryu, S., Noh, J. H., Jeon, N. J., Chan Kim, Y., Yang, W. S., Seo, J. and Seok, S. I. (2014). Voltage output of efficient perovskite solar cells with high open-circuit voltage and fill factor. *Energy & Environmental Science*. **7(8)**: 2614-2618.
- Sabba, D., Mulmudi, H. K., Prabhakar, R. R., Krishnamoorthy, T., Baikie, T., Boix, P. P., Mhaisalkar, S. and Mathews, N. (2015). Impact of anionic Br⁻ substitution on open circuit voltage in lead free perovskite (CsSnI_{3-x}Br_x) Solar Cells. *The Journal of Physical Chemistry C*. **119(4)**: 1763-1767.
- Saga, T. (2010). Advances in crystalline silicon solar cell technology for industrial mass production. *NPG Asia Mater*. **2**: 96-102.
- Salazar-Pérez, A., Camacho-López, M., Morales-Luckie, R., Sánchez-Mendieta, V., Ureña-Núñez, F. and Arenas-Alatorre, J. (2005). Structural evolution of Bi₂O₃ prepared by thermal oxidation of bismuth nano-particles. *Superficies y vacío*. **18(3)**: 4-8.
- Saliba, M., Matsui, T., Seo, J.-Y., Domanski, K., Correa-Baena, J.-P., Nazeeruddin, M. K., Zakeeruddin, S.M., Tress, W., Abate, A., Hagfeldt, A. and Gratzel, M. (2016). Cesium-containing triple cation perovskite solar cells: improved stability, reproducibility and high efficiency. *Energy & Environmental Science*. **9(6)**: 1989-1997.
- Salunkhe, R. R., Lee, Y.H., Chang, K.H., Li, J.M., Simon, P., Tang, J., Torad, N.L., Hu, C.C. and Yamauchi, Y. (2014). Nanoarchitected graphene-based supercapacitors for next-generation energy-storage applications. *Chemistry – A European Journal*. **20(43)**: 13838-13852.
- Salunkhe, R. R., Tang, J., Kamachi, Y., Nakato, T., Kim, J. H. and Yamauchi, Y. (2015). Asymmetric supercapacitors using 3D nanoporous carbon and cobalt oxide electrodes synthesized from a single metal-organic framework. *ACS Nano*. **9(6)**: 6288-6296.
- Sarma, B., Jurovitzki, A. L., Smith, Y. R., Mohanty, S. K. and Misra, M. (2013). Redox-induced enhancement in interfacial capacitance of the titania nanotube/bismuth oxide composite electrode. *ACS Applied Materials & Interfaces*. **5(5)**: 1688-1697.
- Sharma, R. K., Rastogi, A. C. and Desu, S. B. (2008). Manganese oxide embedded polypyrrole nanocomposites for electrochemical supercapacitor. *Electrochimica Acta*. **53(26)**: 7690-7695.
- Shockley, W. and Queisser, H. J. (1961). Detailed balance limit of efficiency of p-n junction solar cells. *Journal of Applied Physics*. **32(3)**: 510-519.

- Skunik-Nuckowska, M., Grzejszczyk, K., Kulesza, P. J., Yang, L., Vlachopoulos, N., Häggman, L., Johansson, E. and Hagfeldt, A. (2013). Integration of solid-state dye-sensitized solar cell with metal oxide charge storage material into photoelectrochemical capacitor. *Journal of Power Sources*. **234(0)**: 91-99.
- Snaith, H. J. (2013). Perovskites: The emergence of a new era for low-cost, high-efficiency solar cells. *The Journal of Physical Chemistry Letters*, *4(21)*, 3623-3630. doi: 10.1021/jz4020162
- Snook, G. A., Kao, P. and Best, A. S. (2011). Conducting-polymer-based supercapacitor devices and electrodes. *Journal of Power Sources*. **196(1)**: 1-12.
- Sowri Babu, K., Ramachandra Reddy, A., Sujatha, C., Venugopal Reddy, K. and Mallika, A. N. (2013). Synthesis and optical characterization of porous ZnO. *Journal of Advanced Ceramics*. **2(3)**: 260-265.
- Stoller, M. D. and Ruoff, R. S. (2010). Best practice methods for determining an electrode material's performance for ultracapacitors. *Energy & Environmental Science*. **3(9)**: 1294-1301.
- Stoumpos, C. C., Malliakas, C. D. and Kanatzidis, M. G. (2013). Semiconducting tin and lead iodide perovskites with organic cations: phase transitions, high mobilities, and near-infrared photoluminescent properties. *Inorganic Chemistry*. **52(15)**: 9019-9038.
- Stoumpos, C. C., Malliakas, C. D., Peters, J. A., Liu, Z., Sebastian, M., Im, J., Chasapis, T.C, Wibowo, A.C, Chung, D.Y, Freeman, A.J, Wessels, B.W. and Kanatzidis, M. G. (2013). Crystal growth of the perovskite semiconductor CsPbBr₃: A new material for high-energy radiation detection. *Crystal Growth & Design*. **13(7)**: 2722-2727.
- Stranks, S. D., Eperon, G. E., Grancini, G., Menelaou, C., Alcocer, M. J., Leijtens, T., Herz, I.M, Petrozza, A. and Snaith, H. J. (2013). Electron-hole diffusion lengths exceeding 1 micrometer in an organometal trihalide perovskite absorber. *Science*. **342(6156)**: 341-344.
- Suarez, B., Gonzalez-Pedro, V., Ripolles, T. S., Sanchez, R. S., Otero, L. and Mora-Sero, I. (2014). Recombination study of combined halides (Cl, Br, I) perovskite solar cells. *The Journal of Physical Chemistry Letters*. **5(10)**: 1628-1635.
- Subhan, M. A. and Ahmed, T. (2014). Synthesis, characterization and spectroscopic investigations of novel nano multi-metal oxide Co₃O₄·CeO₂·ZnO. *Spectrochimica Acta Part A: Molecular and Biomolecular Spectroscopy*. **129**: 377-381.
- Subramanian, V., Zhu, H., Vajtai, R., Ajayan, P. and Wei, B. (2005). Hydrothermal synthesis and pseudocapacitance properties of MnO₂ nanostructures. *The Journal of Physical Chemistry B*. **109(43)**: 20207-20214.
- Sun, H., Deng, J., Qiu, L., Fang, X. and Peng, H. (2015). Recent progress in solar cells based on one-dimensional nanomaterials. *Energy & Environmental Science*. **8(4)**: 1139-1159.
- Sun, Y., Wu, Y., Fang, X., Xu, L., Ma, Z., Lu, Y., Zhang, W.H., Yu, Q., Yuan, N. and Ding, J. (2017). Long-term stability of organic-inorganic hybrid perovskite solar cells with high

- efficiency under high humidity conditions. *Journal of Materials Chemistry A*. **5(4)**: 1374-1379.
- Sun, Y. and Yan, X. (2017). Recent advances in dual-functional devices integrating solar cells and supercapacitors. *Solar RRL*. **1(3-4)**: 1700002-n/a.
- Sutton, R.J., Eperon, G.E., Miranda, L., Parrott, E.S., Kamino, B.A., Patel, J.B., Horantner, M.T., Johnston, M.B., Haghighirad, A.A., Moore, D.T. and Snaith, H.J. (2016). Bandgap-tunable cesium lead halide perovskites with high thermal stability for efficient solar cells. *Advanced Energy Materials*. **6(8)**: 1502458-n/a.
- Tang, C.H., Yin, X. and Gong, H. (2013). Superior performance asymmetric supercapacitors based on a directly grown commercial mass 3D $\text{Co}_3\text{O}_4@\text{Ni}(\text{OH})_2$ core-shell electrode. *ACS Applied Materials & Interfaces*. **5(21)**: 10574-10582.
- Tang, J. and Yamauchi, Y. (2016). Carbon materials: MOF morphologies in control. *Nat Chem*. **8(7)**: 638-639.
- Tu, Y., Wu, J., Zheng, M., Huo, J., Zhou, P., Lan, Z., Lin, J. and Huang, M. (2015). TiO_2 quantum dots as superb compact block layers for high-performance $\text{CH}_3\text{NH}_3\text{PbI}_3$ perovskite solar cells with an efficiency of 16.97%. *Nanoscale*. **7(48)**: 20539-20546.
- Tu, Y., Wu, J., Zhang, L., He, X., Dong, J., Jia, J., Guo, P., Lin, J., Huang, M. and Huang, Y. (2017). Modulated $\text{CH}_3\text{NH}_3\text{PbI}_{3-x}\text{Br}_x$ film for efficient perovskite solar cells exceeding 18%. *Scientific Reports*. **7**:44603.
- Unnikrishnan, B., Wu, C.W., Chen, I. W. P., Chang, H.T., Lin, C.H. and Huang, C.C. (2016). Carbon dot-mediated synthesis of manganese oxide decorated graphene nanosheets for supercapacitor Application. *ACS Sustainable Chemistry & Engineering*. **4(6)**: 3008-3016.
- Vidyadharan, B., Aziz, R. A., Misnon, I. I., Kumar, G. M. A., Ismail, J., Yusoff, M. M. and Jose, R. (2014). High energy and power density asymmetric supercapacitors using electrospun cobalt oxide nanowire anode. *Journal of Power Sources*. **270**: 526-535.
- Wang, B., Xiao, X. and Chen, T. (2014). Perovskite photovoltaics: a high-efficiency newcomer to the solar cell family. *Nanoscale*. **6(21)**: 12287-12297.
- Wang, F., Xiao, S., Hou, Y., Hu, C., Liu, L. and Wu, Y. (2013). Electrode materials for aqueous asymmetric supercapacitors. *RSC Advance*. **3(32)**: 13059-13084.
- Wang, G., Zhang, L. and Zhang, J. (2012). A review of electrode materials for electrochemical supercapacitors. *Chemical Society Reviews*. **41(2)**: 797-828.
- Wang, H. and Hu, Y. H. (2012). Graphene as a counter electrode material for dye-sensitized solar cells. *Energy & Environmental Science*. **5(8)**: 8182-8188.
- Wang, J.G., Kang, F. and Wei, B. (2015). Engineering of MnO_2 -based nanocomposites for high-performance supercapacitors. *Progress in Materials Science*. **74**: 51-124.

- Wang, J.G., Yang, Y., Huang, Z.H. and Kang, F. (2013). Effect of temperature on the pseudo-capacitive behavior of freestanding MnO₂@carbon nanofibers composites electrodes in mild electrolyte. *Journal of Power Sources*. **224**: 86-92.
- Wang, J., Gao, Z., Li, Z., Wang, B., Yan, Y., Liu, Q., Mann, T., Zhang, M. and Jiang, Z. (2011). Green synthesis of graphene nanosheets/ZnO composites and electrochemical properties. *Journal of Solid State Chemistry*. **184(6)**: 1421-1427.
- Wang, J., Khoo, E., Ma, J. and See Lee, P. (2010). Room-temperature synthesis of MnO₂·3H₂O ultrathin nanostructures and their morphological transformation to well-dispersed nanorods. *Chemical Communications*. **46(14)**: 2468-2470.
- Wang, J., Liu, S., Zhang, X., Liu, X., Liu, X., Li, N., Zhao, J. and Li, Y. (2016). A high energy asymmetric supercapacitor based on flower-like CoMoO₄/MnO₂ heterostructures and activated carbon. *Electrochimica Acta*. **213**: 663-671.
- Wang, P., Wang, J., Wang, X., Yu, H., Yu, J., Lei, M. and Wang, Y. (2013). One-step synthesis of easy-recycling TiO₂-rGO nanocomposite photocatalysts with enhanced photocatalytic activity. *Applied Catalysis B: Environmental*. **132-133**: 452-459.
- Wang, S., Jiang, Y., Juarez-Perez, Emilio J., Ono, Luis K. and Qi, Y. (2016). Accelerated degradation of methylammonium lead iodide perovskites induced by exposure to iodine vapour. *Nature Energy*. **2**: 16195.
- Wang, S. X., Jin, C. C. and Qian, W. J. (2014). Bi₂O₃ with activated carbon composite as a supercapacitor electrode. *Journal of Alloys and Compounds*. **615**: 12-17.
- Wang, X., Bai, H., Yao, Z., Liu, A. and Shi, G. (2010). Electrically conductive and mechanically strong biomimetic chitosan/reduced graphene oxide composite films. *Journal of Materials Chemistry*. **20(41)**: 9032-9036.
- Wang, X., Sumboja, A., Lin, M., Yan, J. and Lee, P. S. (2012). Enhancing electrochemical reaction sites in nickel-cobalt layered double hydroxides on zinc tin oxide nanowires: a hybrid material for an asymmetric supercapacitor device. *Nanoscale*. **4(22)**: 7266-7272.
- Wang, Y., Li, S., Xing, X., Huang, F., Shen, Y., Xie, A., Wang, X. and Zhang, J. (2011). Self-assembled 3D flowerlike hierarchical Fe₃O₄@Bi₂O₃ core-shell architectures and their enhanced photocatalytic activity under visible light. *Chemistry – A European Journal*. **17(17)**: 4802-4808.
- Wei, W., Cui, X., Chen, W. and Ivey, D. G. (2011). Manganese oxide-based materials as electrochemical supercapacitor electrodes. *Chemical Society Reviews*. **40(3)**: 1697-1721.
- Wu, C., Shen, L., Huang, Q. and Zhang, Y.C. (2011). Hydrothermal synthesis and characterization of Bi₂O₃ nanowires. *Materials Letters*. **65(7)**: 1134-1136.

- Xia, H., Wang, Y., Lin, J. and Lu, L. (2012). Hydrothermal synthesis of MnO₂/CNT nanocomposite with a CNT core/porous MnO₂ sheath hierarchy architecture for supercapacitors. *Nanoscale Research Letters*. **7(1)**: 33.
- Xia, X., Tu, J., Zhang, Y., Wang, X., Gu, C., Zhao, X. and Fan, H. J. (2012). High-quality metal oxide core/shell nanowire arrays on conductive substrates for electrochemical energy storage. *ACS Nano*. **6(6)**: 5531-5538.
- Xiao, Y., Wu, J., Yue, G., Xie, G., Lin, J. and Huang, M. (2010). The preparation of titania nanotubes and its application in flexible dye-sensitized solar cells. *Electrochimica Acta*. **55(15)**: 4573-4578.
- Xie, L.J., Wu, J.F., Chen, C.M., Zhang, C.M., Wan, L., Wang, J.L., Kong, Q.Q., Lv, C.X., Li, K.K. and Sun, G.H. (2013). A novel asymmetric supercapacitor with an activated carbon cathode and a reduced graphene oxide–cobalt oxide nanocomposite anode. *Journal of Power Sources*. **242**: 148-156.
- Xing, G., Mathews, N., Sun, S., Lim, S. S., Lam, Y. M., Grätzel, M., Mhaisalkar, S. and Sum, T. C. (2013). Long-range balanced electron-and hole-transport lengths in organic-inorganic CH₃NH₃PbI₃. *Science*. **342(6156)**: 344-347.
- Xiong, J., Yang, B., Cao, C., Wu, R., Huang, Y., Sun, J., Zhang, J., Liu, C., Tao, S., Gao, Y. and Yang, J. (2016). Interface degradation of perovskite solar cells and its modification using an annealing-free TiO₂ NPs layer. *Organic Electronics*. **30**: 30-35.
- Xu, J., Gao, P. and Zhao, T. S. (2012). Non-precious Co₃O₄ nano-rod electrocatalyst for oxygen reduction reaction in anion-exchange membrane fuel cells. *Energy & Environmental Science*. **5(1)**: 5333-5339.
- Xu, J., Ku, Z., Zhang, Y., Chao, D. and Fan, H. J. (2016). Integrated photo-supercapacitor based on PEDOT modified printable perovskite solar cell. *Advanced Materials Technologies*. **1(5)**: 1600074-n/a.
- Xu, J., Wu, H., Lu, L., Leung, S.F., Chen, D., Chen, X., Fan, Z., Shen, G. and Li, D. (2014). Integrated photo-supercapacitor based on bi-polar TiO₂ nanotube arrays with selective one-side plasma-assisted hydrogenation. *Advanced Functional Materials*. **24(13)**: 1840-1846.
- Xu, K., Li, W., Liu, Q., Li, B., Liu, X., An, L., Chen, Z., Zou, R. and Hu, J. (2014). Hierarchical mesoporous NiCo₂O₄@MnO₂ core-shell nanowire arrays on nickel foam for aqueous asymmetric supercapacitors. *Journal of Materials Chemistry A*. **2(13)**: 4795-4802.
- Xu, P., Chen, S., Xiang, H.J., Gong, X.G. and Wei, S.H. (2014). Influence of defects and synthesis conditions on the photovoltaic performance of perovskite semiconductor CsSnI₃. *Chemistry of Materials*. **26(20)**: 6068-6072.
- Xu, X., Li, S., Zhang, H., Shen, Y., Zakeeruddin, S. M., Grätzel, M., Cheng, Y.B. and Wang, M. (2015). A Power Pack Based on Organometallic Perovskite Solar Cell and Supercapacitor. *ACS Nano*. **9(2)**: 1782-1787.

- Xu, Y., Gong, T. and Munday, J. N. (2015). The generalized Shockley-Queisser limit for nanostructured solar cells. *Scientific Reports*. **5**: 13536.
- Yakunin, S., Protesescu, L., Krieg, F., Bodnarchuk, M. I., Nedelcu, G., Humer, M., De Luca, G., Fiebig, M., Heiss, W. and Kovalenko, M. V. (2015). Low-threshold amplified spontaneous emission and lasing from colloidal nanocrystals of caesium lead halide perovskites. *Nat Commun*. **6**: 8056.
- Yan, W., Li, Y., Li, Y., Ye, S., Liu, Z., Wang, S., Bian, Z. and Huang, C. (2015). High-performance hybrid perovskite solar cells with open circuit voltage dependence on hole-transporting materials. *Nano Energy*. **16**: 428-437.
- Yan, W., Li, Y., Ye, S., Li, Y., Rao, H., Liu, Z., Wang, S., Bian, Z. and Huang, C. (2016). Increasing open circuit voltage by adjusting work function of hole-transporting materials in perovskite solar cells. *Nano Research*. **9(6)**: 1600-1608.
- Yang, P., Xiao, X., Li, Y., Ding, Y., Qiang, P., Tan, X., Mai, W., Lin, Z., Wu, W., Li, T., Jin, H., Liu, P., Zhou, J., Wong, C.P. and Wang, Z. L. (2013). Hydrogenated ZnO core-shell nanocables for flexible supercapacitors and self-powered systems. *ACS Nano*. **7(3)**, 2617-2626.
- Yella, A., Lee, H.W., Tsao, H. N., Yi, C., Chandiran, A. K., Nazeeruddin, M. K., Diao, E.W.G., Yeh, C.Y., Zakeeruddin, S.M. and Grätzel, M. (2011). Porphyrin-sensitized solar cells with cobalt (II/III)-based redox electrolyte exceed 12 percent efficiency. *Science*. **334(6056)**, 629-634.
- You, B., Wang, L., Li, N. and Zheng, C. (2014). Improving the energy storage performance of graphene through insertion of pristine CNTs and ordered mesoporous carbon coating. *ChemElectroChem*. **1(4)**: 772-778.
- Yu, L., Zhang, G., Yuan, C. and Lou, X. W. D. (2013). Hierarchical NiCo₂O₄@MnO₂ core-shell heterostructured nanowire arrays on Ni foam as high-performance supercapacitor electrodes. *Chemical Communications*. **49(2)**: 137-139.
- Yuan, C., Zhang, X., Wu, Q. and Gao, B. (2006). Effect of temperature on the hybrid supercapacitor based on NiO and activated carbon with alkaline polymer gel electrolyte. *Solid State Ionics*. **177(13-14)**: 1237-1242.
- Yuan, L., Lu, X.-H., Xiao, X., Zhai, T., Dai, J., Zhang, F., Hu, B., Wang, X., Gong, Li., Chen, J., Tong, Y., Zhou, J. and Wang, Z. L. (2011). Flexible solid-state supercapacitors based on carbon nanoparticles/MnO₂ nanorods hybrid structure. *ACS Nano*. **6(1)**: 656-661.
- Zhang, C., Xie, L., Song, W., Wang, J., Sun, G. and Li, K. (2013). Electrochemical performance of asymmetric supercapacitor based on Co₃O₄/AC materials. *Journal of Electroanalytical Chemistry*. **706**: 1-6.
- Zhang, L. L. and Zhao, X. S. (2009). Carbon-based materials as supercapacitor electrodes. *Chemical Society Reviews*. **38(9)**: 2520-2531.
- Zhang, Q. and Cao, G. (2011). Nanostructured photoelectrodes for dye-sensitized solar cells. *Nano Today*. **6(1)**: 91-109.

- Zhao, X., and Park, N.G. (2015). Stability issues on perovskite solar cells. *Photonics*. **2(4)**: 1139-1151.
- Zhou, H., Chen, Q., Li, G., Luo, S., Song, T. b., Duan, H. S., Hong, Z., You, J., Liu, Y. and Yang, Y. (2014). Interface engineering of highly efficient perovskite solar cells. *Science*. **345(6196)**: 542-546.
- Zhu, Q., Bao, X., Yu, J., Zhu, D., Qiu, M., Yang, R. and Dong, L. (2016). Compact layer free perovskite solar cells with a high-mobility hole-transporting layer. *ACS Applied Materials & Interfaces*. **8(4)**: 2652-2657.
- Zhu, Y., Murali, S., Stoller, M. D., Ganesh, K. J., Cai, W., Ferreira, P. J., Pirkle, A., Wallace, R.M., Cychosz, K.A., Thommes, M., Su, Dong., Stach, E.A. and Ruoff, R. S. (2011). Carbon-based supercapacitors produced by activation of graphene. *Science*. **332(6037)**: 1537-1541.
- Zuo, W., Zhu, W., Zhao, D., Sun, Y., Li, Y., Liu, J. and Lou, X. W. (2016). Bismuth oxide: a versatile high-capacity electrode material for rechargeable aqueous metal-ion batteries. *Energy & Environmental Science*. **9(9)**: 2881-2891.

APPENDICES

APPENDIX A: Electrochemical Performances of Super Capacitors for Photo-Super Capacitor Application

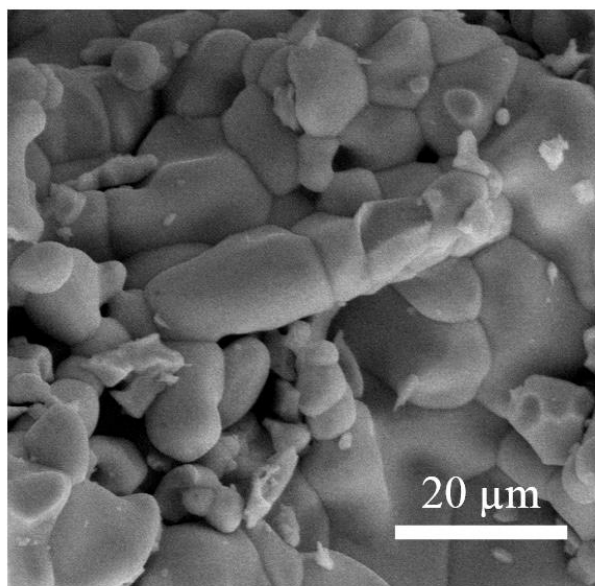


Figure A.1 FESEM image of Bi_2O_3 particle before hydrothermal process

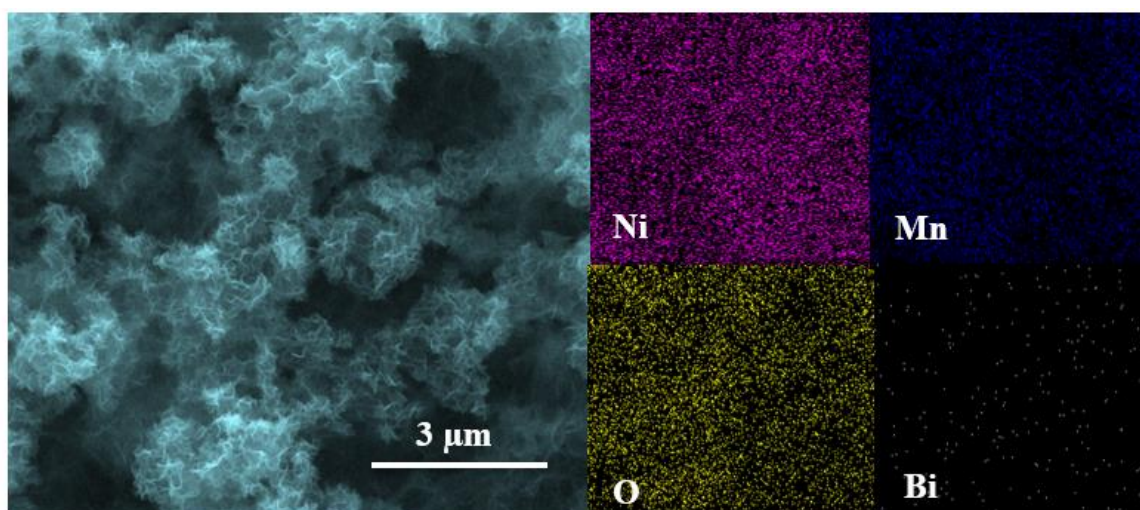


Figure A.2 Elemental maps of Ni, Mn, O, and Bi elements for $\text{Bi}_2\text{O}_3/\text{MnO}_2$

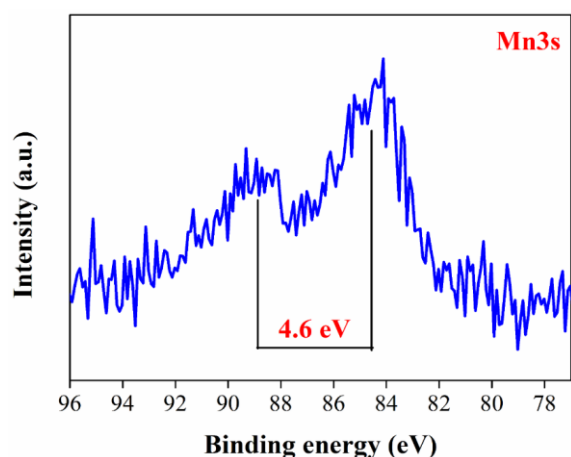


Figure A.3 XPS analysis: determination of oxidation state of MnO₂ from Mn3s plot

Table A.1 General information of a graphite sheet and a nickel foam

Substrate	Company	Specifications	Price (RM)
Nickel foam	GoodFellow	<ul style="list-style-type: none"> • Thickness: 1.6 mm • Bulk density: 0.45 g/cm³ • Pores/cm: 20 • Size: 300 x 300 mm 	2810.00/per unit
Graphite sheet	Latech Singapore	<ul style="list-style-type: none"> • Material: Natural graphite (>99.95%) • Thickness: 0.1 – 1 mm 	85.80/square meter

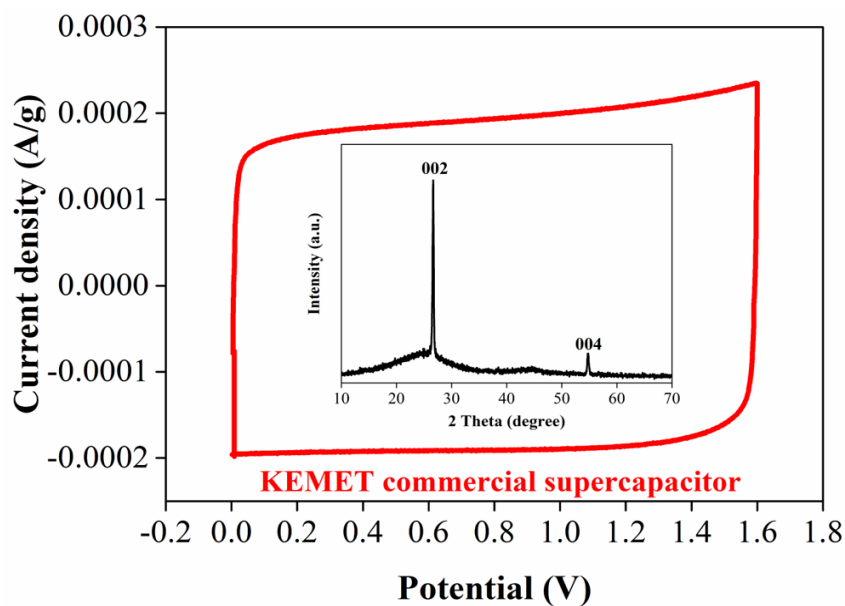


Figure A.4 The cyclic voltammogram of KEMET commercial super capacitor at 2 mV/s and the inset shows the XRD profile of KEMET commercial super capacitor. The XRD profile shows that the KEMET commercial super capacitor is composed of graphitic carbon based material.

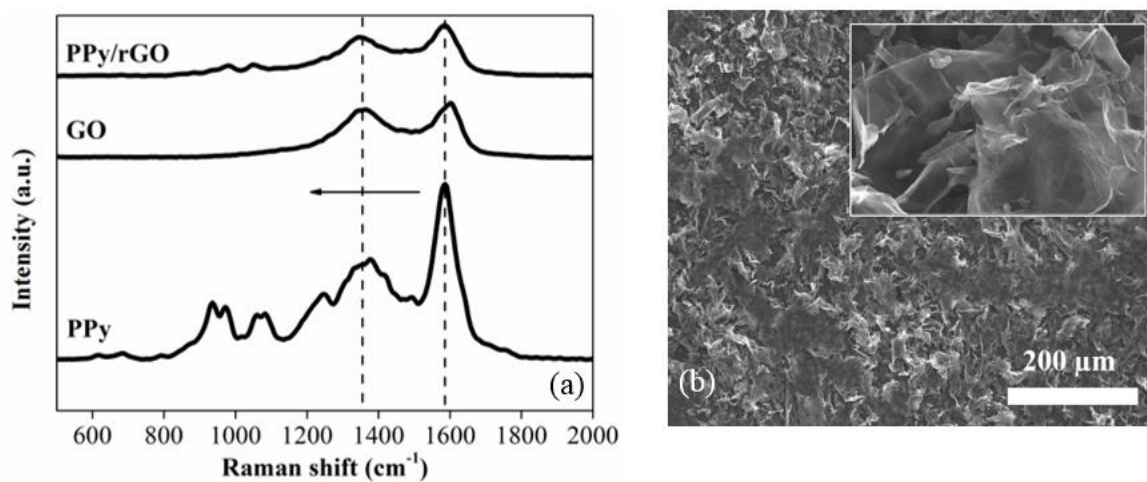


Figure A.5 (a) Raman spectroscopy and (b) FESEM images of polypyrrole/reduced graphene oxide (PyR) negative electrode. Inset shows the magnified PyR materials.

Table A.2 Electrochemical performances of Bi₂O₃/MnO₂ symmetrical super capacitor, Bi₂O₃/MnO₂//PyR and RZCo//PyR asymmetrical super capacitor. The Bi₂O₃/MnO₂ and RZCo are assigned as the positive electrode, while the PyR is the negative electrode for the asymmetric configured super capacitor. The specific capacitance is obtained from galvanostatic charge/discharge. (The bold column is the super capacitor used for photo-super capacitor).

Super Capacitors	Potential Window (V)	Specific Capacitance (F/g)	Energy Density (Wh/kg)	Power Density (W/kg)	Capacitive Retention (%)
Bi ₂ O ₃ /MnO ₂ //PyR (Asymmetrical)	1.6	89.4	25.6	115.3	60 after 1000 cycles
RZCo//PyR (Asymmetrical)	1.6	139.8	41.8	188.3	87 after 1000 cycles
Bi ₂ O ₃ /MnO ₂ (Symmetrical)	1.0	62.3	7.1	51.8	95 after 1000 cycles

Table A.3 General information and specifications of KEMET commercial super capacitor (KEMET Part Number: FT0H105ZF).

Specifications	
Description	Radial cylindrical double layer capacitor
Capacitance	0.1 F
Voltage	5.5 VDC
Temperature range	-40/+85 °C

APPENDIX B: Perovskite Solar Cell and Photo-Super Capacitor

Table B.1 Specifications and prices comparison between FTO and ITO conductive glass. Data were extracted from Techinstro®. TCO represents transparent conductive oxide.

TCO substrate	L x W x thickness	Resistance	Transmittance	Price (100 pack size)
ITO	25 mm x 25 mm x 1.1 mm	10 Ω /sq	>90%	\$ 283
FTO	25 mm x 25 mm x 1.1 mm	10 Ω /sq	>79%	\$ 316

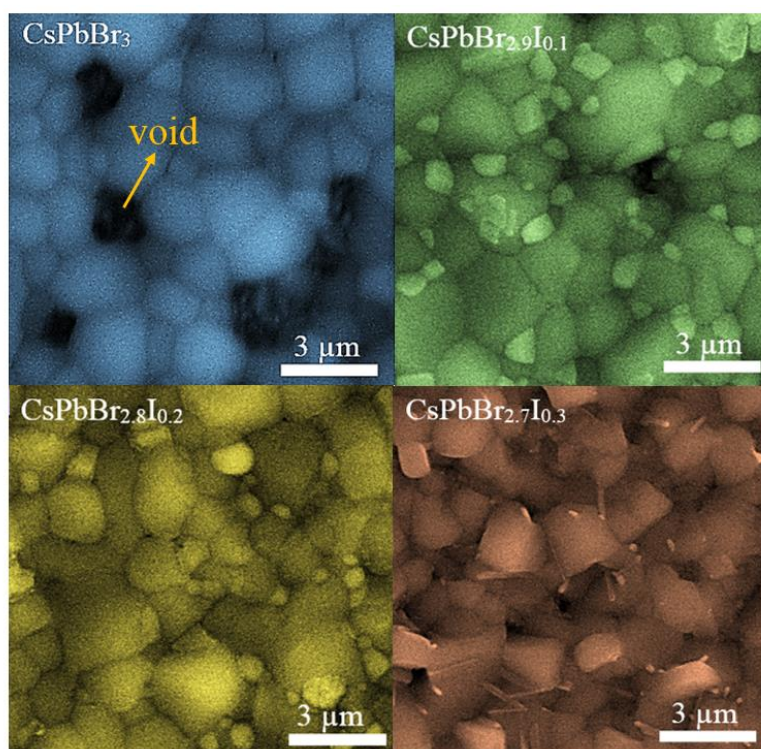


Figure B.1 Magnified FESEM images of CsPbBr_{3-x}I_x perovskite materials on ITO conductive glass, where x=0, 0.1, 0.2, and 0.3.

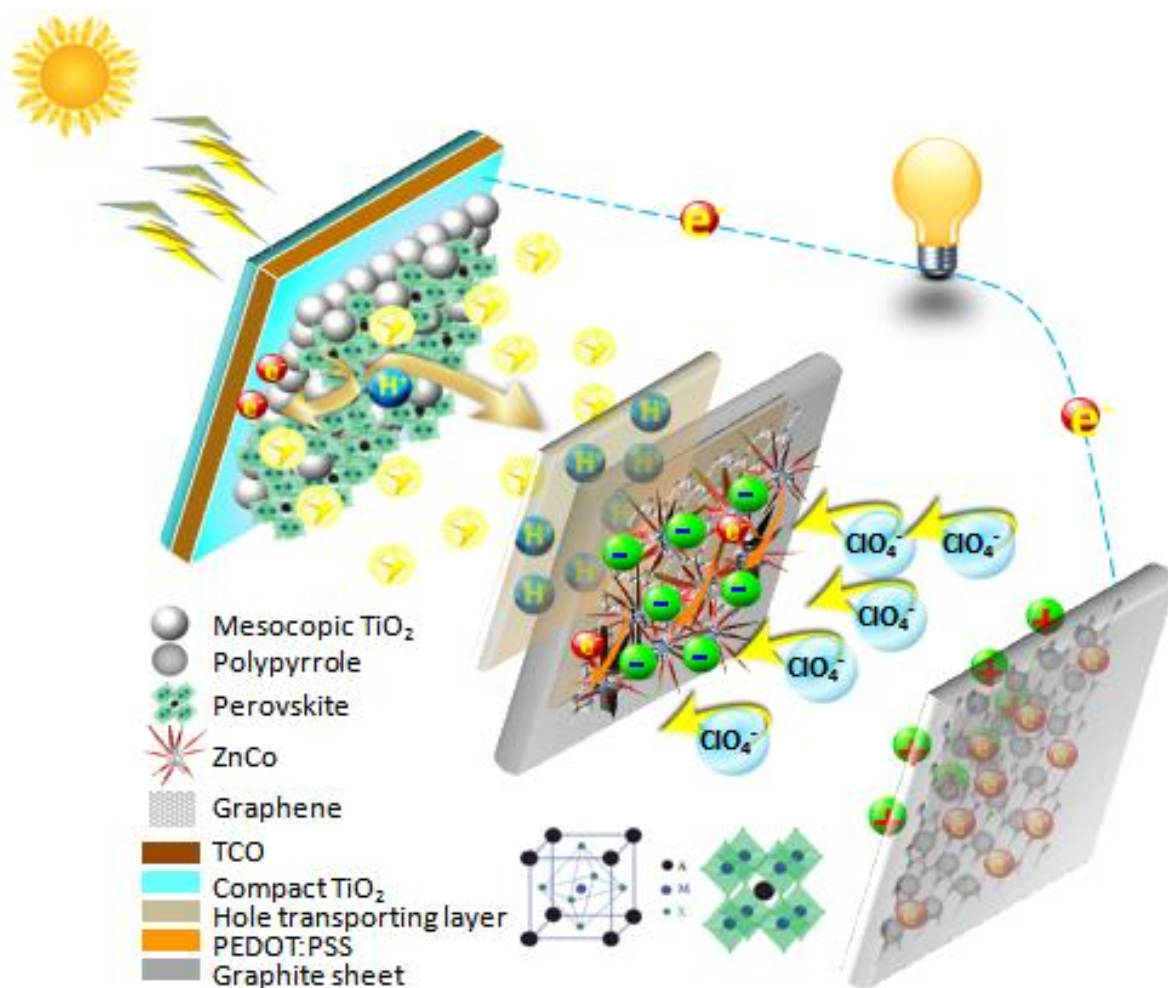


Figure B.2 A three electrodes coupled photo-super capacitor. The sharing electrode of PEDOT:PSS-assisted RZCo electrode is acted as the counter electrode for the perovskite solar cell and simultaneously being a positive electrode for the super capacitor.



UNIVERSITI PUTRA MALAYSIA

STATUS CONFIRMATION FOR THESIS/PROJECT REPORT AND COPYRIGHT

ACADEMIC SESSION: _____

TITLE OF THESIS/PROJECT REPORT:

FABRICATION OF SUPER CAPACITOR AND PEROVSKITE-SENSITIZED SOLAR CELL FOR THE ASSEMBLY OF PHOTO-SUPER CAPACITOR

NAME OF STUDENT:

NG CHI HUEY

I acknowledge that the copyright and other intellectual property in the thesis/project report belonged to Universiti Putra Malaysia and I agree to allow this thesis/project report to be placed at the library under the following terms:

1. This thesis/project report is the property of Universiti Putra Malaysia.
2. The library of Universiti Putra Malaysia has the right to make copies for educational purposes only.
3. The library of Universiti Putra Malaysia is allowed to make copies of this thesis for academic exchange.

I declare that this thesis is classified as

*Please tick (√)

CONFIDENTIAL

(Contain confidential information under Official Secret Act 1972).

RESTRICTED

(Contains restricted information as specified by the organization/institution where research was done)

OPEN ACCESS

I agree that my thesis/project report to be published as hard copy or online open access.

This thesis is submitted for:



PATENT

Embargo from _____ until _____
(date) (date)

(Signature of Student)

New IC No/Passport No.:

Date:

(Signature of Chairman of Supervisory
Committee)

Name: Associate Professor Dr. Janet Lim
Hong Ngee

Date:

[Note: If the thesis is CONFIDENTIAL or RESTRICTED, please attach with the letter from the organization/institution with period and reasons for confidentially or restricted.]